Fluorescent nanosensors for the monitoring of different intracellular reactive oxygen species (ROS)

Ratier Adrien

A thesis submitted in partial fulfilment of the requirements of Liverpool John Moores University for the degree of Doctor of Philosophy

July 2020

Acknowledgements

Table of content

4

Abbreviations

λ_{exc}: excitation wavelength

λ_{em}: emission wavelength

ADIBO: azadibenzocyclooctyne

ADPA: anthracene dipropionic acid

AIBN: azobisisobutyronitrile

APF: 2-[6-(4'-Amino)phenoxy-3H-xanthen-3-on-9-yl] benzoic acid

CAT: catalase

CPY: commercial peroxy yellow

CuAAC: copper(I)-catalyzed azide-alkyne cycloaddition

Cc: cytochrome c

DBZTC: 2-chloro-1,3-dibenzothiazo-linecyclohexene

DCM: dichloromethane

DCFH: 2,7-dichlorodihydrofluorescein

DCFDA: 2,7-dichlorodihydrofluorescein diacetate

DIBO: dibenzocyclooctyne

DIC: N,N′-diisopropylcarbodiimide

DIPEA: N,N-diisopropylethylamine

DMA: dimethyl anthracene

DMF: dimethylformamide

DMSO: dimethyl sulfoxide

DNA: deoxyribonucleic acid

DPA: diphenyl anthracene

EPR: enhanced permeability and retention

ESI: electron spray ionization

ESR: electron spin resonance

EtOH: ethanol

FTIR: Fournier transformed infra-red

GPx: peroxidase

GSH/GSSG: glutathione

HE: hydroethidine

HPF: 2-[6-(4'-hydroxy)phenoxy-3H-xanthen-3-on-9-yl] benzoic acid

HPLC: high performance liquid chromatography

MsCl: methanesulfonyl chloride

MS: mass spectra

MSN: mesoporous silica nanoparticles

MW: microwave

NADP: nicotinamide adenine dinucleotide phosphate

NBS: N-bromosuccinimide

NHS: N-hydroxysuccinimide

NMR: nuclear magnetic resonance

NOX: NADPH oxidase

NP(s): nanoparticles

PBS: phosphate buffer solution

PCC: pyridinium chlorochromate

PDT: photodynamic therapy

PEBBLE: photonic explorer for bioanalysis with biologically localised embedding

PEG: polyethylene glycol

PLGA: polylactic-co-glycolic acid

PMA: phorbol myristate acetate

PrxIII: peroxiredins

PVA: polyvinyl alcohol

POY: peroxy yellow

RhB: rhodamine B

RNS: reactive nitrogen species

ROS: reactive oxygen species

SOD: superoxide dismutase

SOSG: superoxide sensor green

TBAI: tetra-butylammonium iodide

TEA: triethylamine

TFA: trifluoroacetic acid

THF: tetrahydrofuran

ToF: time of flight

TPP: triphenyl phosphonium

Tpy-Cy: 2-{4-[4′-amino-methylphenyl)-2,2′:6′,2″-terpyridinyl]-7-(1-ethyl-3,3-dimethyl-(indolin-2-ylidene)}-3,5-(propane-1,3-diyl)-1,3,5-heptatrien-1-yl)-1-ethyl-3,3-dimethyl-3H-indolium

UV: ultra-violet

Xa: xanthine

XO: xanthine oxidase

Abstract

Reactive oxygen species (ROS) play important roles for the regulation of normal functions such as proliferation, differentiation, migration and cell death. At low doses they participate in the redox balance, but an excess of these species leads to damage to proteins, lipids or DNA. ROS are involved in the onset and progression of several degenerative diseases (*e.g.,* cancer, neurological disorder, etc). Cancer cells are highly susceptible to ROS-mediated damage and several chemotherapy agents achieve cytotoxicity by inducing oxidative stress.

Sensing the variations of different intracellular ROS is crucial for real time assessments of anticancer treatment efficiency. Yet, no sensor currently allows simultaneous and independent monitoring of different ROS live cells. Indeed, existing sensors monitor either the total levels of ROS or the levels of single species (i.e., sensors such as diphenylanthracene, peroxy yellow, anthrafluorescein, etc.).

The need to optimise and personalise treatment regimens and for unravelling the mechanisms underpinning ROS-induced cell death requires the introduction of a new set of tools able to provide a real-time report of intracellular ROS levels in response to a given intervention.

In this project we developed new fluorescent nanosensors able to respond to different ROS. This was achieved through the synthesis of three conjugatable molecular probes able to respond to individual ROS, namely; an anthrafluorescein-based probe for superoxide anion, a dimethylanthracene-based probe for singlet oxygen and a fluorescein-based probe for hydrogen peroxide. The new probes were grafted onto poly(lactic-*co*-glycolic acid) (PLGA) and formulated as nanoparticles containing either

10

conjugated or encapsulated sensors. We characterised the fluorescent response of the probes, conjugates and nanospecies in the presence of the target ROS analytes. Lastly, we demonstrated the ability of the nanosensors to enter cells and their potential of to be used as intracellular ROS sensors.

Chapter 1. *Introduction*

1.1. Reactive oxygen species (ROS)

1.1.1. What are ROS?

ROS are derivatives of molecular oxygen characterised by a high reactivity[1–3]. Different species of ROS exist: some have an unpaired electron and display the typical reactivity of radicals (*e.g.,* superoxide radical ($O_2^{\bullet-}$), hydroperoxyl radical ($HO_2^{\bullet}$), hydroxyl radical ($HO^{\bullet}$), peroxyl radical ($ROO^{\bullet}$) and alkoxyl radical ($RO^{\bullet}$)), wheras other species react as electrophiles (hydrogen peroxide (H_2O_2) and hypochlorous acid ($HOCl$)) and/or as oxidative agents (singlet oxygen ($^1O_2$)) (Fig. 1.1).
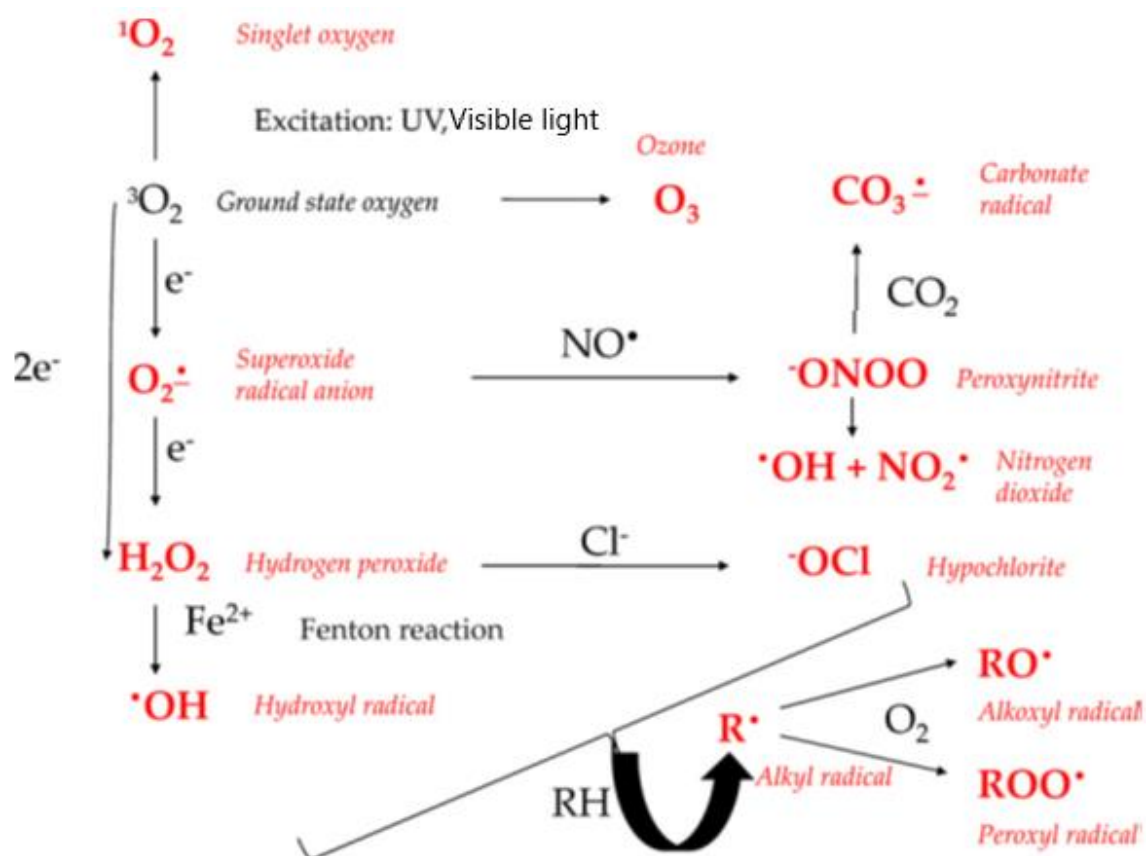
Figure 1.1: Different types of ROS[4]

1.1.2. Cell production of ROS

Between the 80% and 90% of the ROS produced by cells are formed in mitochondria during the electron transport chain [5–10] (Fig. 1.2 & 1.3). Superoxide anions are formed from molecular oxygen in the third compartment of the mitochondria. To prevent superoxide-mediated toxicity (see below), these anions are transformed into hydrogen peroxide by an antioxidant enzyme called superoxide dismutase (SOD). Due to its higher stability, hydrogen peroxide is a relatively long-lived ROS compared to superoxide anion and it can diffuse out of the mitochondria. In the cytosol, catalase (CAT) and other antioxidants such as glutathione peroxidase (GPx) or peroxiredins (PrxIII) can transform hydrogen peroxide into water. Ferrous ions can reduce hydrogen peroxide to form hydroxyl radicals. Hydroxyl radicals can in turn react with superoxide anions to form oxygen and water as a further detoxification step. NADPH oxidase (NOX)[11], present in the cell membrane, can also form superoxide anions outside the cell, which can be transformed into hydrogen peroxide and enter the cell. Superoxide anions and hydrogen peroxide can also be transformed into reactive nitrogen species (RNS) (nitric oxide ($^{\bullet}$NO), peroxynitrite (ONOO$^-$)) or chlorinated ROS (hypochlorous acid (HOCl)). A further ROS source is the degradation of lipids and alcohol in the peroxisome. ROS can also be formed as a result of external stimuli, for example, under ionizing UV radiation or from the metabolism of a wide range of drugs[8,10,12,13].
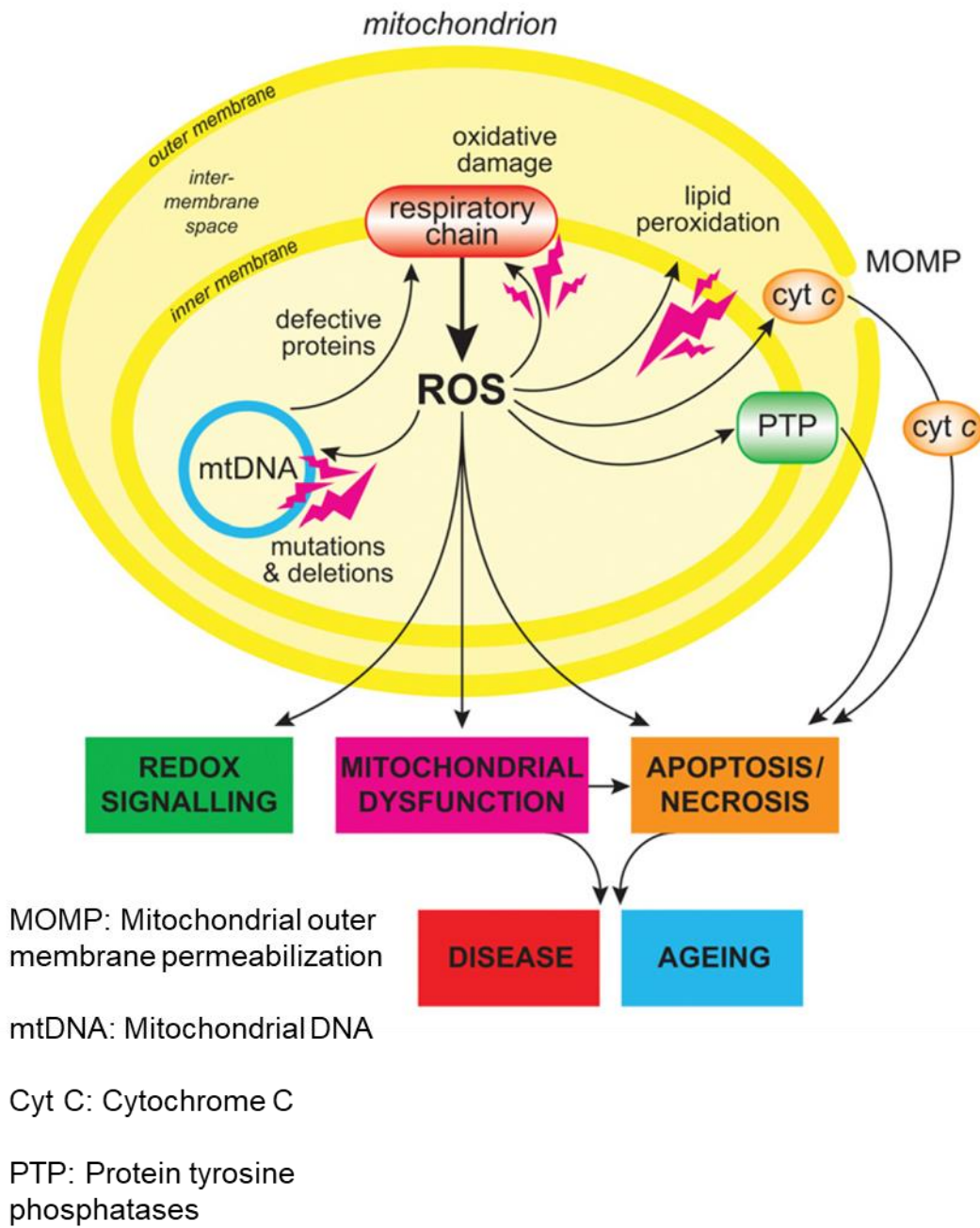
Figure 1.2: Overview of mitochondrial ROS production and impact of ROS on cell fate[10,14,15]

CAT : catalase
Gpx : glutathione peroxidase
GSH : glutathione
GR : glutathione reductase
MPO : myeloperoxidase
NADH : nicotinamide adénine dinucléotide
NADPH : nicotinamide adénine dinucléotide phosphate
NOS : nitric oxide synthases
NOX : NADPH oxydase
Prx : peroxiredin
SOD : superoxide dismutase
TTFA : thenoyltrifluoroacetone
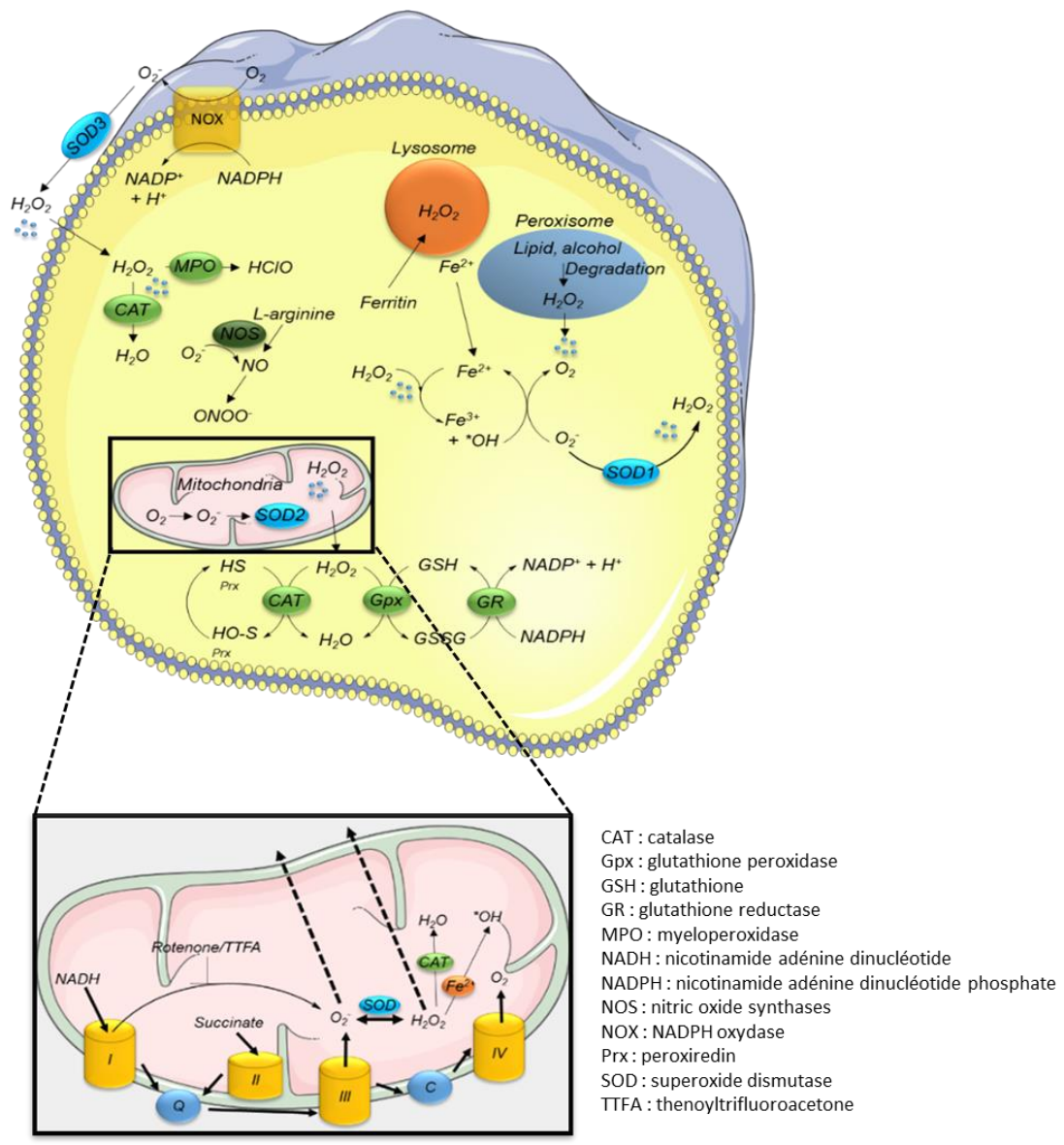
Figure 1.3: Transport of ROS in cells[12]

1.1.3. <u>Reactivity of ROS</u>

Electrons are more stable when they are paired, this gives radicals less stability compared to non-radical species and can explain their reactivity. Indeed, the two main features of ROS (*i.e.*, short lifetime and limited diffusion range) are more prominent for ROS radicals[16]. The less reactive a molecule is, the longer its lifetime and the farther it can move in the surrounding environment, with its reactivity profile having an impact

15

in a wider spatial range from the generation site (Tab. 1.1). The most reactive ROS is the hydroxyl radical followed by the superoxide radical and singlet oxygen. Compared to those three, hydrogen peroxide is less reactive and can diffuse over a longer distance.

Table 1.1: Reactivity and mobility of some ROS[16]

ROS	Half-life	Mean free path
Hydroxyl radical	1 ns	1 nm
Superoxide anion	1 µs	30 nm
Singlet oxygen	1 µs	30 nm
Hydrogen peroxide	1 ms	1 µm

ROS display different reactivity profiles, which in turn define the biomolecules they are able to modify[7,16–18]: superoxide radical reacts with double bond-containing compounds (*e.g.*, unsaturated fatty acids), while hydroxyl radicals will react with double bond-containing compounds as lipids[19] and DNA[20], but also with hetero-atoms (*e.g.*, sulfur or nitrogen) on proteins[21] leading to crosslinking, oxidation or hydrolysis. Hydrogen peroxide oxidizes proteins, whereas reactions of singlet oxygen with proteins, polyunsaturated acids or DNA often occur via Diels-Alder reaction. Some examples of reactions of ROS with biomolecules are reported in Table 1.2.

Table 1.2: Examples of the reactions of ROS with lipids, proteins and DNA

Lipids[10]	
Proteins[2,21–23] (Amino Acid)	
DNA[20,24]	
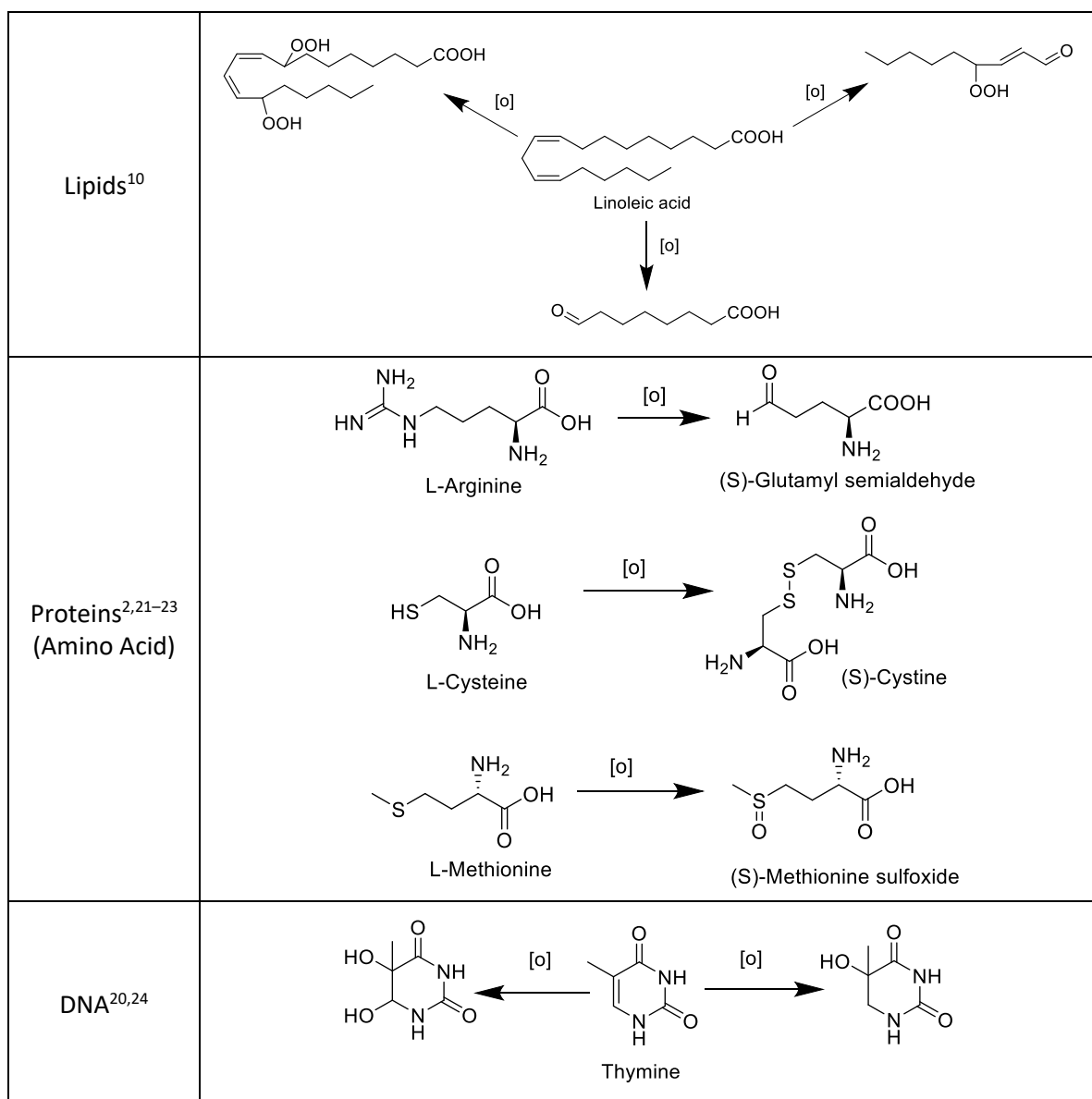
Reaction of ROS with biomolecules can lead to modification/damage of proteins, lipids and nucleic acids. In order to avoid these damages, the intracellular levels of ROS are carefully controlled by antioxidant species, such as SOD (Eq. 1.1)[25], CAT (Eq. 1.2)[26–29] GSH (Eq. 1.3) or NADPH (Eq. 1.4)[30].

Equation 1.1: SOD effect on superoxide[31]

$$2\ O_2^{\bullet-} + 2\ H^+ \xrightarrow{\text{SOD}} 2H_2O + O_2$$
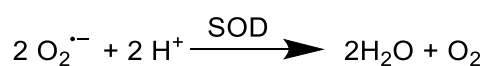
Equation 1.2: CAT effect on hydrogen peroxide[26]

$$2H_2O_2 \xrightarrow{\text{CAT}} 2H_2O + O_2$$
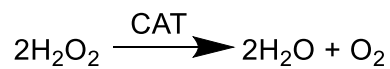
Equation 1.3: Glutathione effect on hydrogen peroxide[30]

$$2GSH + H_2O_2 \longrightarrow GSSG + 2H_2O \qquad (1)$$

$$2GSH + ROOH \longrightarrow GSSG + ROH + H_2O \qquad (2)$$

Equation 1.4: NADPH effect on oxygen[30]

$$NADPH + 2O_2 \longrightarrow NADP^+ + 2O_2^{\bullet-} + H^+$$

1.1.4. <u>ROS participation in cell homeostasis and oxidative stress</u>

At low or moderate levels, ROS participate in the physiological homeostasis of the cell[9,32–34]. ROS are involved in regulating development, differentiation, stress signalling and cell death[7,32,33,35–38] (Fig. 1.4). For example, ROS are linked with the proliferation and survival of cells by mitogen-activated protein kinase cascades or phosphoinositide 3-kinase pathway, with iron homeostasis or with homeostasis and antioxidant gene regulation by Nrf2 and Ref1-mediated redox cellular signaling[39]. One example of the implication of ROS in cell survival processes is the activation of the tumour suppressor protein p53[34,40,41]. p53 is extremely important in the control of cellular stress responses, inducing either cell cycle arrest in order to promote DNA repair and survival, or cell death by apoptosis[42], depending on the context.

An imbalance between ROS and antioxidants can have various consequences. If an excess of antioxidant exists, the cell proliferation pathway is affected and this can lead to malformation or dysfunction such as cardiomyopathies[43] or neurodegenerative disorders[44]. An excess of ROS causes a phenomenon called oxidative stress, which was found to be linked to several diseases[39,45] (*e.g.* cancer[18,46–48], obesity[49],

neurodegenerative diseases[17], diabetes[50,51], aging[52–54], hypertension[55,56]) (Fig. 1.4 and 1.5).
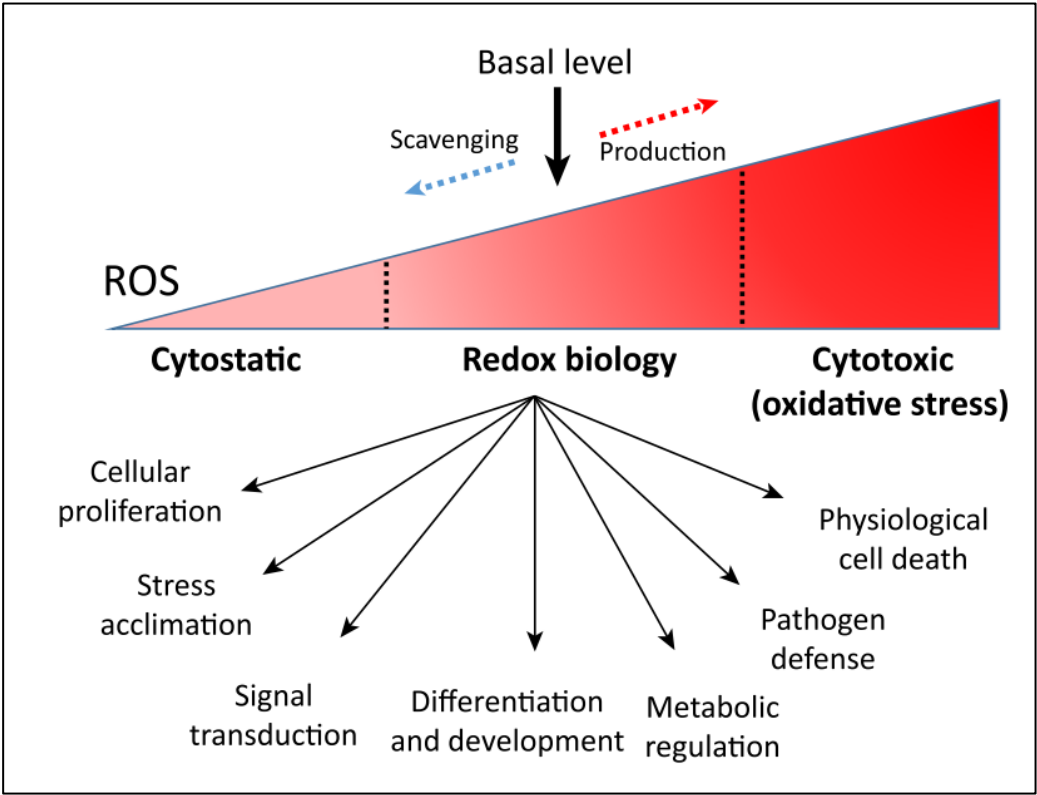
Figure 1.4: Redox balance in cells[35]
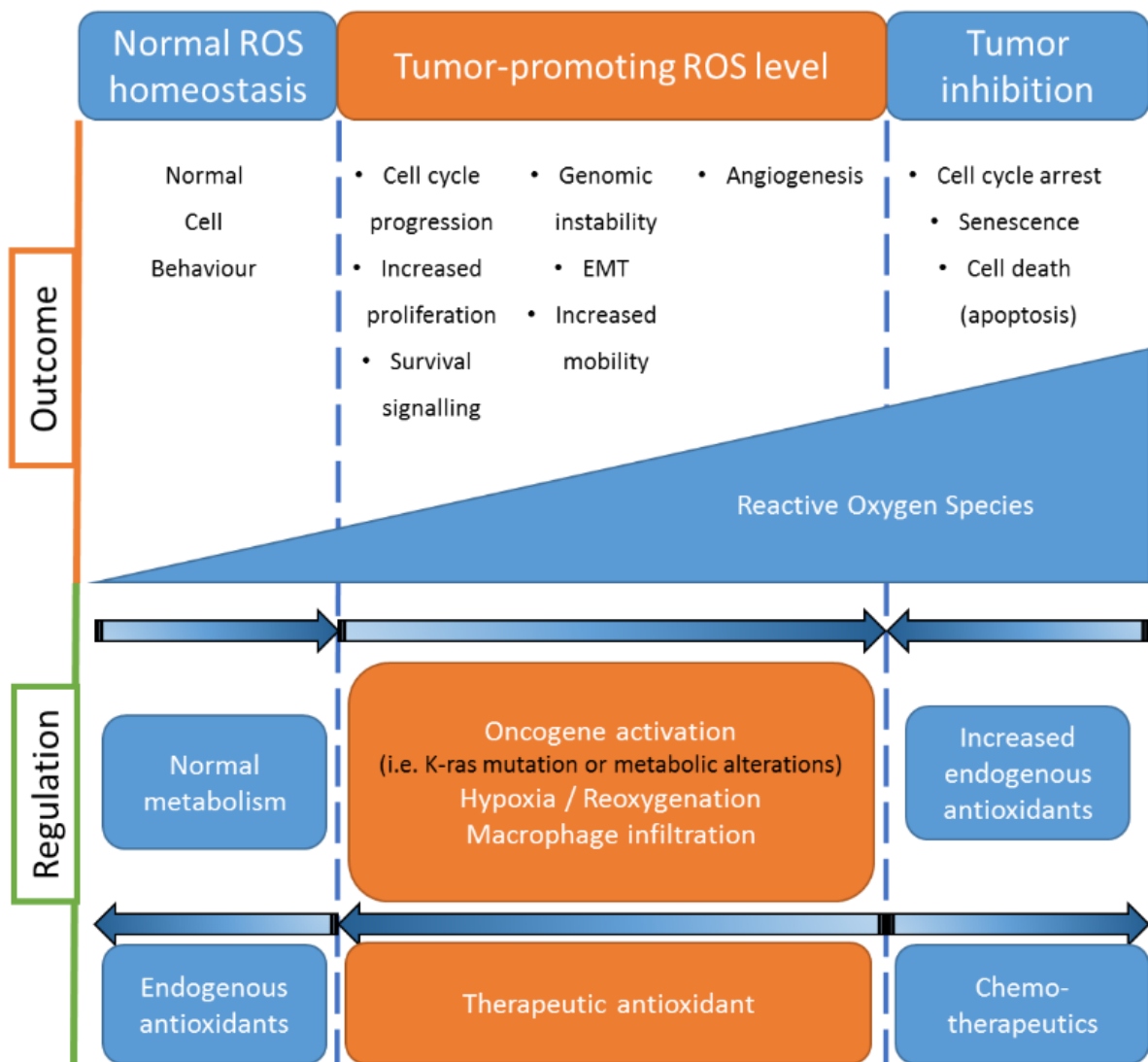
Figure 1.5: Impact on cancer of different level of ROS and ROS-related gene regulation[57]

Oxidative stress occurs when the balance between antioxidants species such as glutathione (GSH/GSSG)[58] (Eq. 1.3) or (NADPH/NADP$^+$) ratios (Eq. 1.4) and ROS shift in favour of ROS. This imbalance results in the damages to biomolecules discussed in Section 1.1.3[25].

Cancer cells display a high susceptibility to oxidative stress, an effect known under the name of "the Warburg effect"[8]. This behaviour is exploited by several therapeutic approaches that aim at inhibiting tumour growth by increasing ROS concentration in

cancer cells. Externally induced production of ROS is the warhead of a therapeutic approach called photodynamic therapy (PDT) (Fig. 1.6)[8,59–62]. This therapy relies on the generation of ROS through the irradiation of a photosensitizing chemical compound with non-toxic visible light to inactivate target cell (*e.g.*, cancer cells or microorganisms) and eradicate infections or ablate cancer and precancerous tissue[63]. PDT leads to cell death either *via* apoptosis[34,37,40,64], which is called programmed cell death or necrosis[62], which is due to outside trauma or depletion of vital substances.
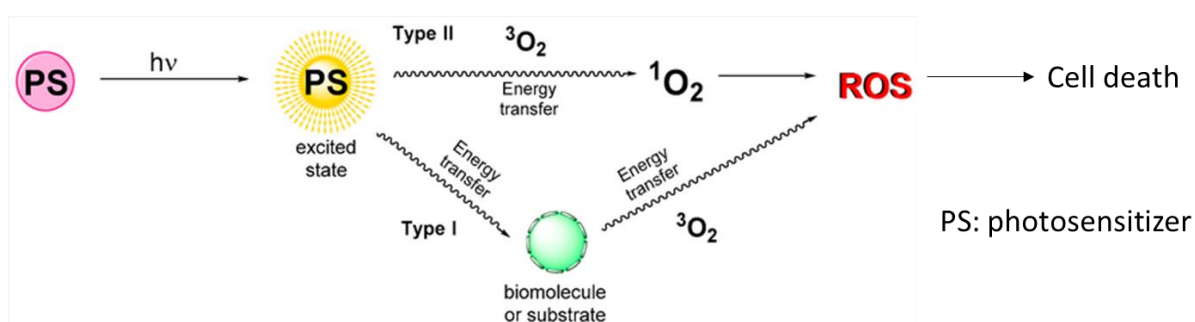
Figure 1.6: PDT process[65]

Apoptosis[66] is morphologically characterized by chromatin condensation, cleavage of chromosomal DNA into internucleosomal fragments, cell shrinkage, membrane blebbing and formation of apoptotic bodies without plasma membrane breakdown. Typically, apoptotic cells release "find me" and "eat me" signals required for the clearance of the remaining debries by phagocytic cells. At the biochemical level, apoptosis entails the activation of caspases, a highly conserved family of cysteine-dependent aspartate-specific proteases. Necrosis[66] is morphologically characterized by vacuolization of the cytoplasm, swelling and breakdown of the plasma membrane resulting in an inflammatory reaction due to release of cellular contents and pro-inflammatory molecules. Necrosis is thought to be the result of pathological insults or be caused by a bio-energetic catastrophe, or ATP depletion to a level incompatible

with cell survival. The biochemistry of necrosis is characterized mostly in negative terms by the absence of caspase activation, cytochrome c release and DNA oligonucleosomal fragmentation.

1.1.5. <u>Approaches for the detection and quantification of ROS</u>

The importance of ROS in the redox homeostasis of the cell and their role in triggering toxicity and potentially cell death (see previous sections) compelled scientists to develop viable approaches for ROS detection and quantification in biological environment. Because of their short life and their short range of action, the detection and quantification or ROS had to rely on the development of bespoke analytical tools[67,68].

Electron spin resonance (ESR) is a technique that permits the direct identification of oxygen free radicals. Because of their short lifetime, specific reagents are used to stabilize these radicals, either by addition of a covalent bond (the molecule is called a spin trap)[69] or by oxidation of the molecule (the molecule is called a spin sensor)[68]. Spin traps are more often used than spin sensors. The most popular spin trap is 5,5-dimethyl-1-pyrroline-N-oxide[70,71], which is useful in solution but has limited applicability in most biological systems due to competing reactivity with SOD and ascorbate that partially inhibits formation of product. Furthermore, its range of efficient concentration is limited, as it must be used with ROS concentrations between 20 and 100 mM[72,73], which do not make it a sensitive technique. Another spin trap is 5-diethoxyphosphoryl-5-methyl-1-pyrroline N-oxide[74], which can be modified to have a triphenylphosphonium group to promote its selective uptake by mitochondria[75]. The main limitations of this species are its poor sensitivity (i.e., concentrations under 50 mM of ROS cannot be

detected), its toxicity to cells and non-specificity to superoxide [76–79]. Moreover, this this spin trap does not allow quantification of ROS and is also expensive[68].

Chemiluminescent sensors are high potential tools for ROS detection, in particular for superoxide anion, for their sensitivity and ease of use[16]. The principle is that the sensor reacts with the ROS and the reaction leads to the release of a photon that is detected by a photometer without excitation by a light source[68,71]. Lucigenin is one the sensors used for superoxide anion measurement in macrophages and neutrophils[69,80]. One drawback of lucigenin is the susceptibility of the chemiluminescent species to reduction in the presence of flavoprotein reductase[81], which in turn increases the level of superoxide anions. In addition, the chemiluminescent species can react with other molecules such as hydrogen peroxide[68], reducing the specificity of the detection. Luminol is also used but is less selective because it reacts with hydrogen peroxide, hydroxy radicals and peroxynitrite and increases the level of those ROS (Eq. 1.5)[82–84]. This represents a serious drawback for the accurate quantification of ROS.

Equation 1.5: Lucigenin intermediate reduction
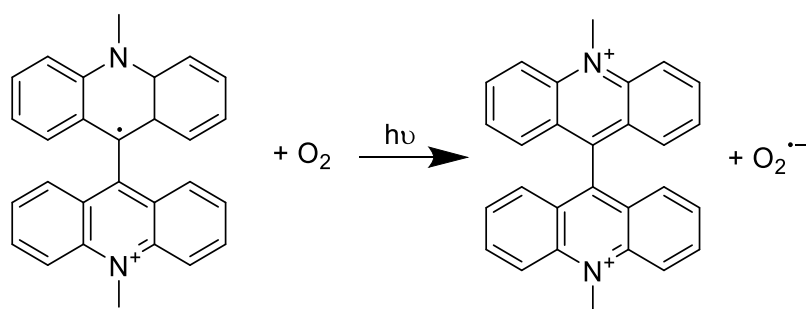
Superoxide is also detected by cytochrome c (Cc) reduction coupled with spectrophotometry [67,68]. Cc can be reduced by superoxide anions from the ferri- to the ferro- form, causing an alteration of the absorbance at 550 nm, which can be detected spectrophotometrically. Its specificity is relatively low due to the cross-reactivity of

superoxide anion with enzymes or reductants as xanthine oxidase, ascorbate or glutathione, which in turns hampers its quantification with this method[68].

Last but not least, fluorescent sensors can be used to detect different types of ROS. Two types of fluorescent sensors exist: protein-based sensors and small organic molecules. Protein-based sensors are designed through the combination of fluorescent proteins and prokaryotic redox sensitive proteins[67,68]. These sensors can provide real-time and dynamic detection of redox state change. Sensors of different colours are available, for example green (redox-sensitive green fluorescent protein[85] type 1 or 2), yellow (redox-sensitive yellow fluorescent protein[86] combined with glutaredoxin-1[87] or charged with 3 residues[88]) or red (redox-sensitive red fluorescent protein[89]). These species are biocompatible but slow-reacting and not very sensitive, which does not allow accurate quantification of ROS[68]. Organic sensors are species whose fluorescent behaviour is modified following reaction with ROS. A large panel of fluorescent sensors exists with different properties, such as wavelengths of emission and excitation, selectivity, and ability to enter cells or selectively accumulate in intracellular organelles (*e.g.*, mitochondria)[3]. These species are summarised in Table 1.3.

Method	Reaction	Advantages	Limitations
ESR	(DMPO) / (DEPMPO)	- Stabilize ROS by addition of covalent bond or by oxidation - Modified DEPMPO can enter selectively in mitochondria with triphenylphosnium group attached on	- Limit of range of ROS - DEPMPO is more toxic - Need of an external analysis (as NMR) - Non specific
Chemiluminescence	(Lucigenin) / (Luminol)	- Sensitive and easy to operate - Detectable by photometer without excitation by a light source	- Can be reduced by flavoprotein reductase: this reduced form can generate more superoxide anion - Less selective than Lucigenin - Increases the level of ROS
Cytochrome C	$Fe^{3+}\text{-}Cc + O_2^{\bullet-} \longrightarrow Fe^{2+}\text{-}Cc + O_2$	- Form a ferro-form that can be observed using a spectrophotometer - Specific to superoxide anion	- Low specificity due to the cross-reactivity with enzymes or reductants
Fluorescence	Protein-based sensors ⟶ Oxidised protein-based sensor	- Biocompatible	- Slow-reacting - Not very sensitive
	Organic-based sensors ⟶ Oxidised organic-based sensors		Options, advantage and limitations discussed in the following sections

1.1.6. Fluorescent sensors for ROS

The possibility of correlating the fluorescence intensity with the concentration of the ROS makes fluorescent sensors particularly attractive for the quantification of reactive oxygen species concentration in cells[67,68,90]. The vast array of sensors developed to detect and quantify ROS are discussed in the following sections.

1.1.6.1. <u>Superoxide anion sensors</u>

As previously described, the superoxide anion is the first ROS generated by the mitochondrial electron transport chain. Even if this ROS is unstable because of its radical nature, some sensors can successfully detect and quantify it (Tab. 1.4)[3]. Most selective sensors developed can only be used in a limited range of pH.

1.1.6.2. <u>Hydrogen peroxide sensors</u>

Hydrogen peroxide is the most stable ROS, therefore easier to detect and quantify. However, the sensors designed to detect hydrogen peroxide often react with other more reactive ROS, leading to lack of selectivity of the sensors themselves. (Tab. 1.5)[3]. Most of the selective sensors developed have a lack of selectivity.

1.1.6.3. <u>Singlet oxygen sensors</u>

Singlet oxygen is not directly created by cells. The formation of this ROS is induced by an endogenous or exogenous photosensitiser following irradiation during PDT[59–61,91–93]. Given its importance for ROS-based therapeutic approaches such as PDT, some sensors have been developed to detect and quantify singlet oxygen (Tab. 1.6). Sensors for singlet oxygen tend to be quite selective and they respond to the analyte by either increasing (turn-on sensors) or decreasing (turn-off sensors) their fluorescence emission intensity; the main difference is the analysis, whether measuring an increasing or decrease in the fluorescence.

1.1.6.4. <u>Hydroxyl radical sensors</u>

The hydroxyl radical is the most reactive ROS, yet a number of sensors for its detection have been developed (Tab. 1.7). Most of these are selective to the hydroxyl radical, but they can be used only over a limited range of pH.

Table 1.4: Fluorescent sensors for superoxide anion
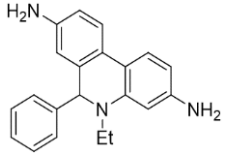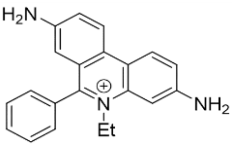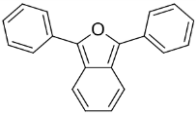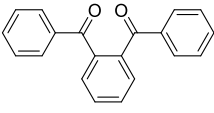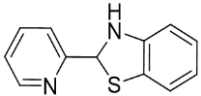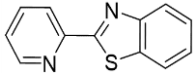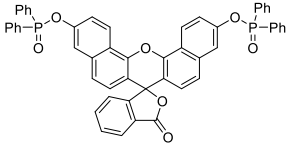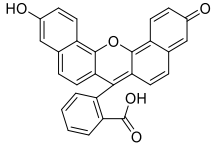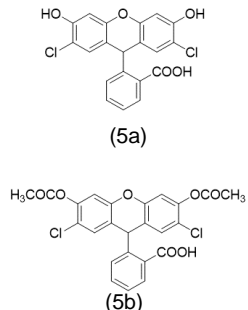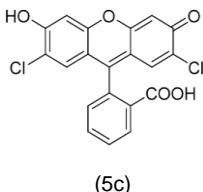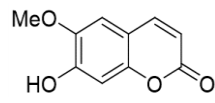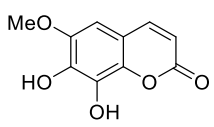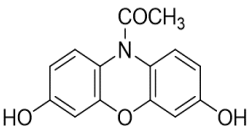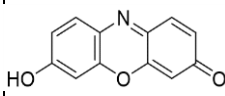
Name	Molecule	Reaction product	$\lambda_{exc}/\lambda_{em}$ (nm)	Advantages	Limitations
Hydroethidine (HE)[3,90,94–105]	(1a)	(1b)	520 / 610	•Cross cellular membrane •Useful for monitoring the oxidative burst in cells	•Cytochrome *c* can oxidize it •High (1a) concentrations increase fluorescence because of connection with DNA •(**1a**) increases superoxide dismutation to peroxide •(**1a**) can be oxidized by peroxide via non-specific peroxidase catalysis and make some interference •Possibility to be oxidized by other reactivity species
1,3-Diphenyliso benzofuran[106]	(2a)	(2b)	410/455 or 477	•Good indicator in phospholipid liposomes	•Non-selective (react with singlet oxygen) •Fluorescence by decrement
2-(2-Pyridil)-benzothiazoline[3]	(3a)	(3b)	377/528	•No interaction with other ROS •Determination of SOD activity	• Emission is optimal at pH between 8.9 and 10
3'-oxo-3'H-spiro[dibenzo[c,h]xanthene-7,1'-isobenzofuran]-3,11-diyl bis(diphenylphosphinate) (Phosphinated dianthrafluorescein)[107]	(4a)	(4b)	602/662[108] 490/ 530[109]	• Selective • Can be selective to hydrogen peroxide by replacing phosphinated group into sulfonyl[110]	• Emission is optimal at pH between 7.4 and 8

Table 1.5: Fluorescent sensors for hydrogen peroxide

Name	Molecule	Reaction product	λexc/λem (nm)	Advantages	Limitations
2,7-Dichlorodihydrofluorescein (DCFH) [3,67,99,100,102,111–114]	(5a) (5b)	(5c)	498/522	•Diacetate (1b) form can be applied in cell studies (DCFDA) •Useful marker of oxidative stress	•Non-selective •Cellular peroxidase important for oxidation or catalase and SOD •Cytochrome c, peroxidases, hematin increase formation of DCF •Photo reduction of DCF by visible light or UVA radiation
Scopoletin (7-hydroxy-6-methoxy-coumarin) [115–117]	(6a)	(6b)	360/460	•Widely used as a hydrogen peroxide monitoring sensor, either isolated in mitochondria or in stimulated neutrophils and eosinophils	•Decrease of fluorescence •Low selectivity •Low extinction coefficient •Interference from autofluorescence •Need amplification •Low stability in biological media (pH and temperature) •Interference from reductive compound (NADPH, NADH, ascorbic acid and Glutathione)
Amplex Red (N-acetyl-3,7-dihydroxyphenoxanine) [115,118,119]	(7a)	(7b)	563/587	•Can measure superoxide anion if use of SOD •Small autofluorescence •Stable from pH 7.5 to 8.5	• Low selectivity •At high HOCl concentration, fluorescence increases
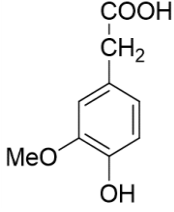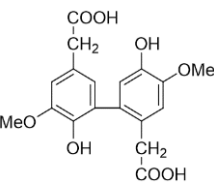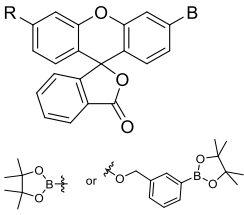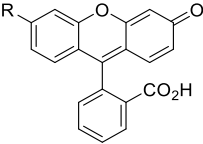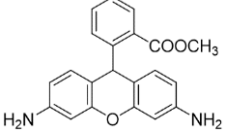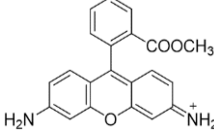
			Excitation/Emission		
Homovanillic Acid (4-hydroxy-3-methoxy-phenylatic acid)[116,120,121]	 (8a)	 (9b)	312/420	•Useful to detect the production of hydrogen peroxide in isolated mitochondria of various tissues	•Low selectivity
Boronated fluorescein based sensors[95,98,102,103,111,114,122,123]	 (10a & 10b)	 (10b)	510/528	•Useful to detect the production of hydrogen peroxide in mitochondria depending on the R variety (as triphenylphosphonium group in MitoPY1) •Selective	•Can react with peroxynitrite
Dihydrorhodamine 123 [124,125]	 (11a)	 (11b)	505/529	• Evaluation of scavenging activity. •Cationic and lipophilic sensors	•Non-selective •Not oxidised directly

29
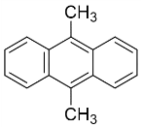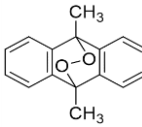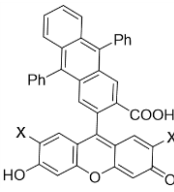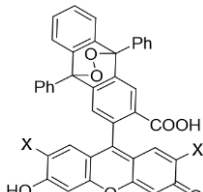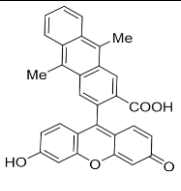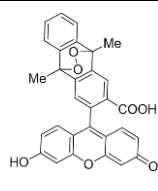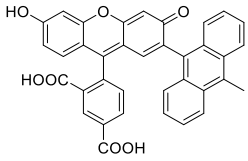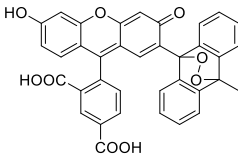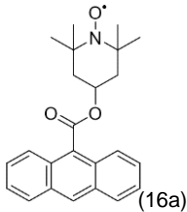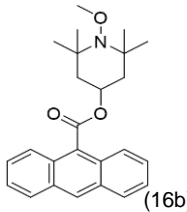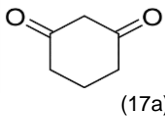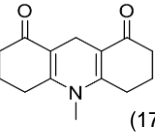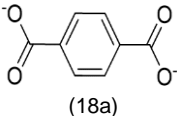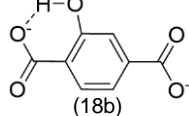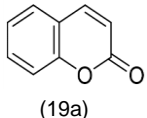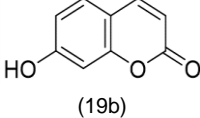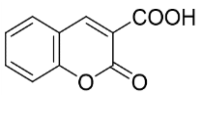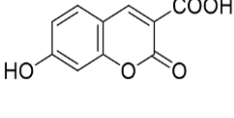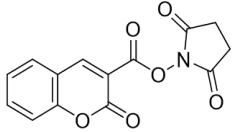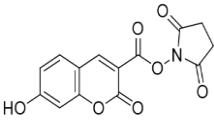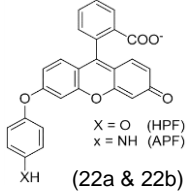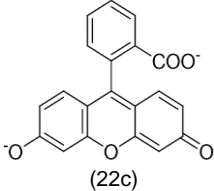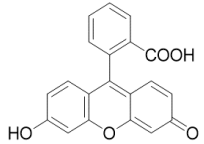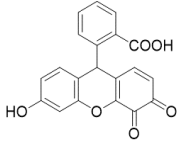
Name	Molecule	Reaction product	λexc/λem (nm)	Advantages	Limitations
9,10-Dimethylanthracene (DMA)[3,126–128]	(12a)	(12b)	375/463	•Very specific •Quick	•Extinction of fluorescence •Hard to pass through the membrane
9- [2-(3-Carboxy-9,10-diphenyl)anthryl]-6-hydroxy-3H-xanthen-3-ones (DPAXs)[3,102,107,111,129,130]	(13a, 13b & 13c)	(13d)	X = H 494/515 X = Cl 506/527 X = F 494/515	•Very specific •Quick •Membrane-permeable	•Initial reactive is fluorescent too and with the same wavelength •Extinction of fluorescence in acid conditions (Cl or F are added to decrease the pKa)
9- [2-(3-Carboxy-9,10-methyl)anthryl]-6-hydroxy-3H-xanthen-3-ones (DMAX)[3,102,107,131]	(14a)	(14b)	492/515	•Very specific •Quick •Less hydrophobicity than DPAX	•Less hydrophobicity than DPAX •Initial molecule has a low fluorescence
Singlet oxygen sensor green (SOSG)[60,63,90,107,130–134]	(15a)	(15b)	504/525	•Very specific •Quick	

Table 1.7: Fluorescent sensors for hydroxyl radical

Name	Molecule	Reaction product	λexc/λem (nm)	Advantages	Limitations
4-(-Anthroyloxy)-2,2,6,6-tetramethyl piperidine-1-oxyl[135–137]	(16a)	(16b)	377/427	•Specific	•Initial molecule has a low fluorescence •Need DMSO to generate $CH_3^\bullet$ •Coupling with other carbon-centre radicals
1,3-Cyclohexanedione [138]	(17a)	(17b)	400/452	•Specific	•Need DMSO to make HCOH and not possible for cell
Sodium terephtalate[139]	(18a)	(18b)	310/430	•Specific	•pH optimum 6.80-7.90
Coumarin[140,141]	(19a)	(19b)	350 & 395/450	•Specific	•Fluorescence depends on the pH •Depends on where hydroxylation is situated
Coumarin-3-carboxilic acid [142,143]	(20a)	(20b)	351 & 395/450	•Specific •COOH increase the fluorescence at 7 position •Accurate, reproducible, performed real-time	•Fluorescence depends on the pH •Depends on where hydroxylation is less 1 position

N-hydroxysuccinimidyl ester of coumarin-3-carboxylic acid[144–146]	(21a)	(21b)	352 & 395/450	•Specific •COOH increase the fluorescence at 7 position •Accurate, reproducible, performed real-time •Linear fluorescence	•Fluorescence depends on the pH
2-[6-(4'-Hydroxy or Amino)phenoxy-3H-xanthen-3-on-9-yl] benzoic acid (HPF or APF)[147]	(22a & 22b)	(22c)	500/520	•HPF is selective	•Fluorescence is suppressed in presence of DMSO •APF reactive with HOCl •Less sensitive than DCFH
Fluorescein[148]	(23a)	(23b)	495/515	•Form oxidized Fluorescence with HO$^•$	•Loss of fluorescence •Not selective

1.2. <u>Nanosensors</u>

1.2.1. <u>Nanoparticles</u>

Nanoparticles (NPs)[149] are a family of particles characterised by their size: regardless of shape, a particle is defined as a "nanoparticle" if one of its dimensions is from 1 to 100 nm[150,151].

One of the many classifications of NP is based on their composition:

- **Carbon-based NPs** such as fullerenes and carbon nanotubes. Fullerenes[152,153] are football-shaped cages made of sp^2 hybridized carbon. Fullerenes C_{60} and C_{70} have diameters of 7.114 and 7.648 nm respectively. Carbon nanotubes[154] have a tubular structure with a diameter between 1 and 2 nm.

- **Metal NPs** are mostly made of copper, silver or gold. Gold NPs[155] have been obtained in a variety of shapes, such as nanospheres, nanorods, nanoshells and other geometric shapes (tetrahedra, octahedra, cubes, icosahedra). Depending on their shapes, gold NPs have different sizes. For example, nanorods have a cross-section of around 50 nm in nanocages, but a nanoshell will have a diameter of around 140 nm. Depending on their shape and size, gold silver and copper NPs will have different optical properties.

- **Ceramic NPs** are inorganic non-metallic species. They can have different forms, ranging from amorphous to dense solids with different ranges of porousity[156]. One of the most widely inorganic NPs is made of silicon[157–160].

- **Semiconductor NPs** are made of metallic and non-metallic materials such as for example a mixture of nickel and platinum on carbon nanotubes[161].

- **Polymeric NPs** (or PNPs) are organic NPs. They often appear as nanospheres or nanocapsules. They can be functionalised on the surface to conjugate a variety of species. Examples of polymers used to obtain nanoparticles are polylactic-co-glycolic acid (PLGA), polyethylene glycol (PEG), poly(methyl methacrylate), poly(N,N-dimethylacrylamide) [151,162–165], and polysaccharides[166].

- **Lipid-based NPs** are NPs with lipid moieties. They form spheres with a diameter between 10 and 1000 nm[167].

The approaches to make NPs can be divided in two broad classes [168,169]:

- bottom-up synthesis, producing nanoparticles from small molecules or atoms

- top-down synthesis, producing nanoparticles from larger species.

As shown in Figure 6, because of their size, morphology and properties (optical[170], thermal[171,172], magnetic[173,174] or mechanical[175]) NPs are suitable for a wide array of applications. Their use is still a controversial matter because of their potential toxicity[154,176,177]: for example, their absorption by inhalation, their distribution in the body and long exposure effects are not fully characterised or known and their long-term effect in the environment is also still the object of debate[149]. Numerous applications of NPs in the therapeutic and diagnostic fields have been explored[178–180]. NPs are regarded as advantageous drug delivery agents because they can increase drug efficiency and reduce side effects on patients[181]. NPs are also used in manufacturing processes in several sectors (medical, commercial, ecological, microelectronics, aerospace or pharmaceutic sector[182–185]), in environmental applications (evaluation of their risk [186] or absorption of contaminants[187,188]), as well as in the electronic fields (new semiconductor, transistor[189–191]) and mechanical industries (lubrication effect[175]).

1.2.2. <u>NPs as a support for sensors</u>

A prominent biomedical application of nanoparticle relies on their potential for the development of nanosensors. The advantages of using a NP as the support for a sensor are listed below[192–195]:

- The use of molecular sensors exhibiting unfavourable properties for biological measurements (*e.g.*, poor aqueous solubility, uneven distribution due to sequestration, chemical interference, or toxicity) can be enabled by encapsulating them in a nanoparticle.

- The NP protects the sensing component from interference caused by species present in biological environments (*e.g.*, undesirable enzymatic reactions and nonspecific uptake by proteins).

- Nano-sized structures have a high surface-area-to-volume ratio, which determines a higher probability for analyte detection.

- Because a single nanosensor can carry a large number of molecular sensors, NPs can increase the local concentration of the sensor, thereby enhancing the intensity of the response signal.

- Because of their size, which is much smaller than the size of biological cells, NPs cause minimal physical perturbations to cells or tissues while measurements are undertaken. Also, this favours the detection of unstable analytes with limited diffusion distances as ROS.

- ROS sensitive molecular sensors are chemically unstable and encapsulating them into NPs can improve their stability.

- Nanosensors can be provided with different reactive functional groups (multifunctionality), thereby enabling conjugation with different species.

35

- Nanosensors can be targeted to specific cells or tissues of interests by conjugating target-specific ligand moieties onto the NP surface.

These advantages, combined with the potential offered by fluorescent sensing to quantify ROS level, fostered the development of fluorescent nanosensors for one or more ROS. Thus, a wide array of nanosensors were developed, exploiting different methods to generate a fluorescent signal following the reaction with the target analyte(s). Thus, ROS nanosensors based were described[194], based on a polymeric or micelle matrix (for fluorescent dyes[196–200] or chemiluminescent dyes[201–204]) or metallic matrix (for fluorescence quenching[205–207], NP surface energy transfer[208] or surface enhanced Raman scattering/spectroscopy[209]).

The first report of this application concerned the synthesis of a Photonic Explorer for Bioanalysis with Biologically Localised Embedding (PEBBLE)[200]. This nanosensor consists of DCFDA encapsulated in hydrophobic ORMOSIL (ORganic MOdified SILica) NPs[194–196,210,211]. DCFDA, a derivative of DCFH, is a sensor for hydrogen peroxide. As discussed above, DCFDA suffers lack of selectivity, and responds to other ROS and to species such as peroxidase. The presence of the hydrophobic ORMOSIL nanoparticles greatly enhances the selectivity of the sensor by creating different barriers for non-target analytes (*i.e.,* a *size* barrier, which prevent large species like peroxidase and esterase from reaching the sensor; a *time* barrier, which prevents access of highly reactive hydroxyl radicals; and *hydrophobic energy* barrier for most other ROS). Thanks to the presence of the NP, the fluorescent sensor DCFDA gains selectivity and efficiency (Fig. 1.7).
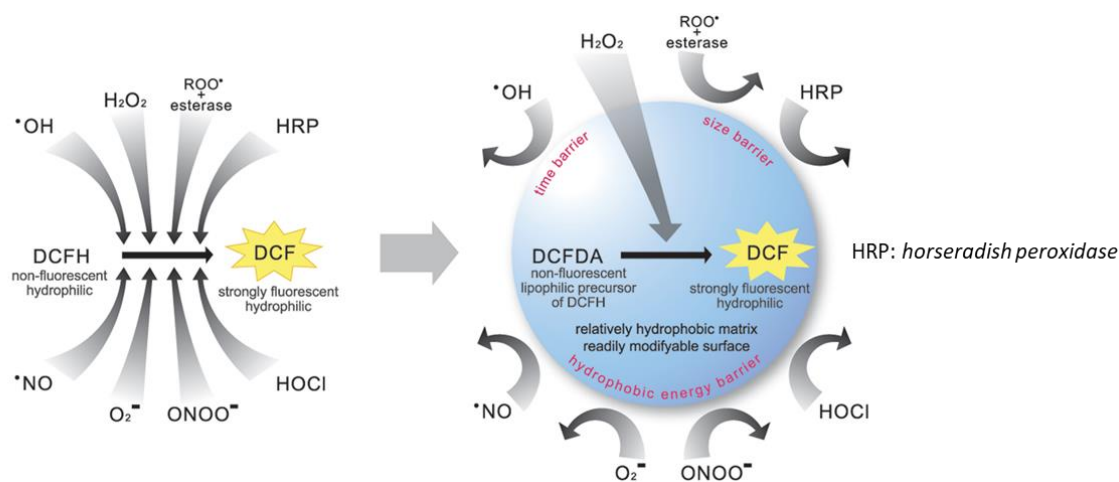
Figure 1.7: Schematic representation of induced H_2O_2 selectivity by encapsulating DCFDA into relatively hydrophobic ORMOSIL NPS[196]

SOSG[133] and anthracene dipropionic acid (ADPA)[134], used to detect singlet oxygen, were covalently linked to polyacrylamide NPs without linkers (A), with linkers (B), or with trimethylphosphonium groups (C) which were introduced to enhance the penetration in mitochondria[96,212].(Fig. 1.8). This study demonstrated that the nanosensor was more effective in detecting singlet oxygen compared to the stand-alone sensor[134]. It was also shown that the nanosensors (nanoSOSG) could detect singlet oxygen within *Escherichia Coli* without causing toxicity to the cell[133].
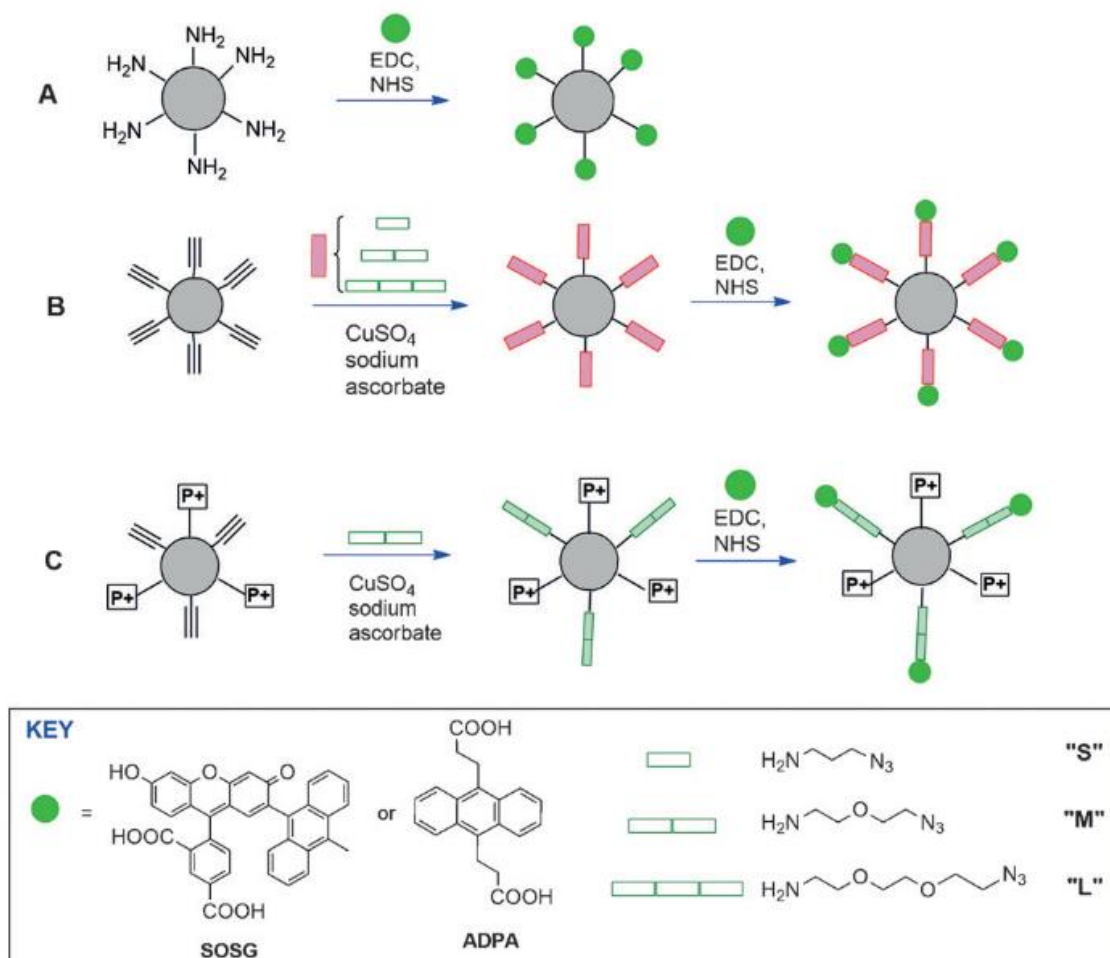
Figure 1.8: Conjugation of ADPA or SOSG to functionalized polyacrylamide NPs directly (A), via a spacer (B) and with positively-charged trimethylphosphonium groups (C)[133]

Nanosensors for superoxide were also reported, describing the encapsulation of RhB, DBZTC or Tpy-Cy in mesoporous silica nanoparticles (MSN)[213] (Fig. 1.9). In these ratiometric sensors, rhodamine B was used to localise NPs because its emission is not affected by the fluctuation of pH or levels of superoxide anion, and its signal can be used as reference. DBZTC is used to sense superoxide levels and Tpy-Cy for pH sensing. These nanosensors proved useful to study the influence of superoxide and pH on autophagy and apoptosis in various pathological conditions. As previously

described, triphenylphosphonium (TPP) groups were included to improve the ability of the sensor to enter mitochondria.
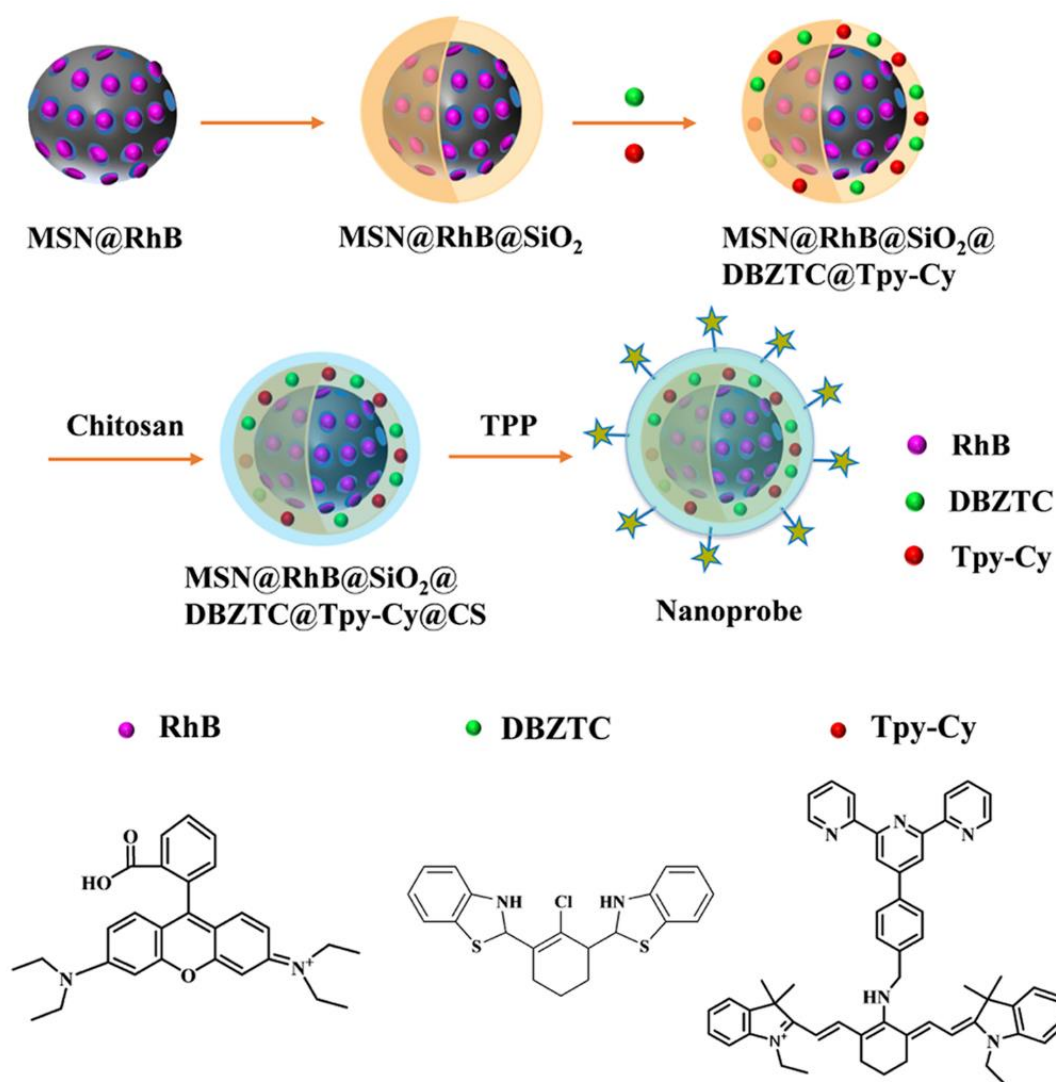
Figure 1.9: Illustration of the nanosensor formation and the structures of RhB, DBZTC, and Tpy-Cy[213]

PEBBLE nanosensors with a matrix of amine-functionalized polyacrylamide and CCA covalently attached on the surface were synthesised[198]. Because of the short range and lifetime of this ROS, the fluorescent molecular sensor was positioned on the surface of the nanoparticle, and Texas Red-Dextran was encapsulated in the matrix to make this nanosensor ratiometric and a more reliable tool to measure this highly

reactive ROS (Fig. 1.10). This study showed that the large surface-to-volume ratio of the nanoparticle allowed a greater sensing area for this ROS.
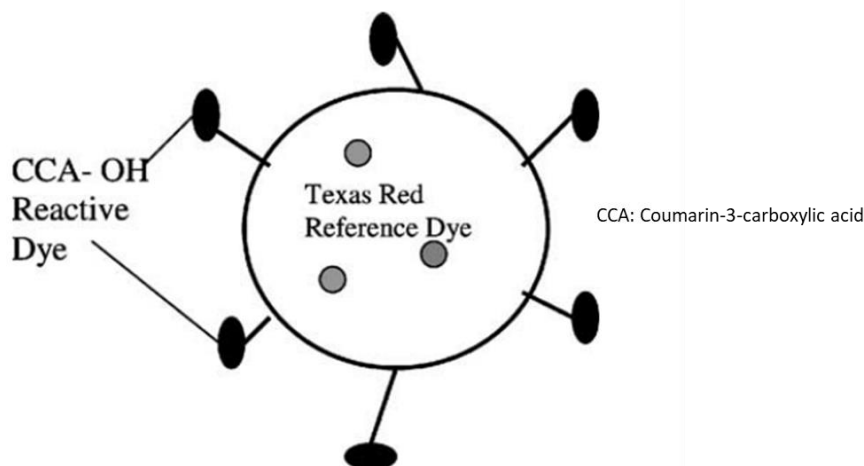
Figure 1.10: Hydroxyl radical PEBBLE sensor[198]

1.2.3. Summary

the involvement of ROS in biological processes fuelled the development of analytical tools to identify and quantify these short-lived species. Amongst the various approaches, the use of fluorescent labels holds a great potential because of their specificity and their ability to quantify ROS concentration. The potential of fluorescent sensors was further expanded by the development of nanosensors. The use of nanoparticles proved useful to detect and quantify ROS made impressive progresses since its inception, providing further confirmation that the use of a nanoparticle support greatly broadens the applicability of fluorescence ROS sensing.

This work aims at contributing to its field by exploring the possibility of sensing simultaneously different ROS types, as detailed in the following sections.

Aim of the work

As discussed in the introduction, the use of a NP as a support for ROS fluorescent can have real advantages to address and overcome of the lack of selectivity, potential toxicity and instability of some of the fluorescent ROS molecular sensors[194]. The involvement of ROS in homeostatic processes in the cell needs to be fully characterised, especially the role of different ROS and how their levels fluctuate in the cells in different physio-pathologic conditions. To the best of our knowledge, a sensing device that allows this kind of analysis has not been described so far, and this project will address this knowledge gap.

The aim of this project is to design and synthesise novel polymeric nanosensors to monitor, in real time and concurrently, the levels of different ROS, in order to further the understanding of the impact of ROS on the homeostatic or pathological state of cells.

The works will be articulated along the following objectives:

1) synthesis of the sensors

2) synthesis of the nanosensors

3) investigation of the sensing response in the presence of the target analytes

To achieve the project aim, the choice of the fluorescent sensors is crucial. When using multiple sensors, wavelengths of excitations and emissions need to be carefully chosen, so that they do not overlap, leading to signal interference. In order to covalently link the sensors to the polymeric nanoparticle matrix, they also need to bear a suitable functional group for conjugation with the NPs structure.

The structure of the target nanosensor is illustrated in Figure 1.11. The support of the nanosensor is a PLGA-based NPs with three orthogonal functional groups that are able to react with three conjugation partners on the fluorescent sensors (A). The choice of the structures of the fluorophores comprises:

- Novel modified boronated fluorescein (yellow fluorescent) for hydrogen peroxide detection with a carboxylic group that can react on an amine on the NPs (B).
- Novel modified hydroethidine (red fluorescent) for super oxide anion detection with an azide group that can react on a terminal alkyne on the NPs (C),
- Novel modified DPAX (green fluorescent) for singlet oxygen detection with an aldehyde group that can react on a hydroxylamine on the NPs (D),
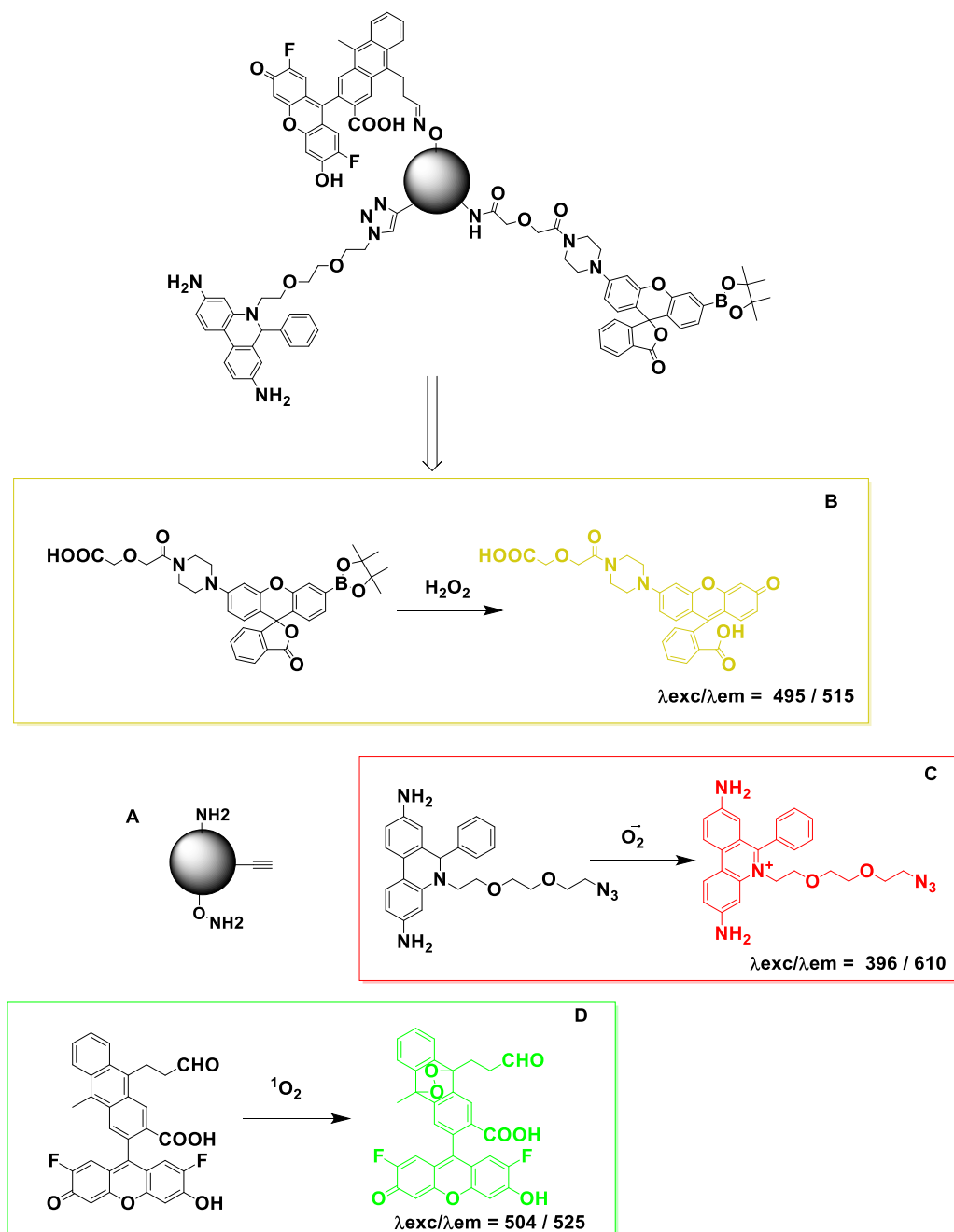
Figure 1.11: Target nanosensors design. Modified HE (A), DMAX (B), fluorescein (C) on nanosensor (D).

Chapter 2. *Synthesis and fluorescence behaviour of new functionalized molecular sensors*

As described in the previous chapter, the selection of the three sensors was made on the basis of their reported selectivity toward the target analyte, their wavelengths of excitation and emission, and on the potential to introduce suitable functional groups. We chose known ROS probes selective towards different ROS that emit with light at different wavelength (i.e., different colour) and we devised a strategy to insert a functional group to allow conjugation. For those reasons, we selected structures of HE (**1a**) for superoxide, DMAX (**14a**) for singlet oxygen and peroxy yellow (POY) (**23a**) for hydrogen peroxide.

2.1. Superoxide sensor

2.1.1. Hydroethidine

2.1.1.1. Synthetic approach

Zielonka and collaborators described and approach to introduce a substituent bearing a phosphonium group onto hydroethidine to obtain a species able to target mitochondria[96,100]. As discussed in the previous section, we aimed at providing hydroethidine with an azide group to exploit CuAAC chemistry for conjugation to alkyne-derivatised nanoparticle (Fig 2.1). We reasoned that choosing either a carboxylic group or an aldehyde group as the conjugation handle would potentially lead to unwanted cross-reactions with the primary amino groups on hydroethidine under conjugation conditions.

44
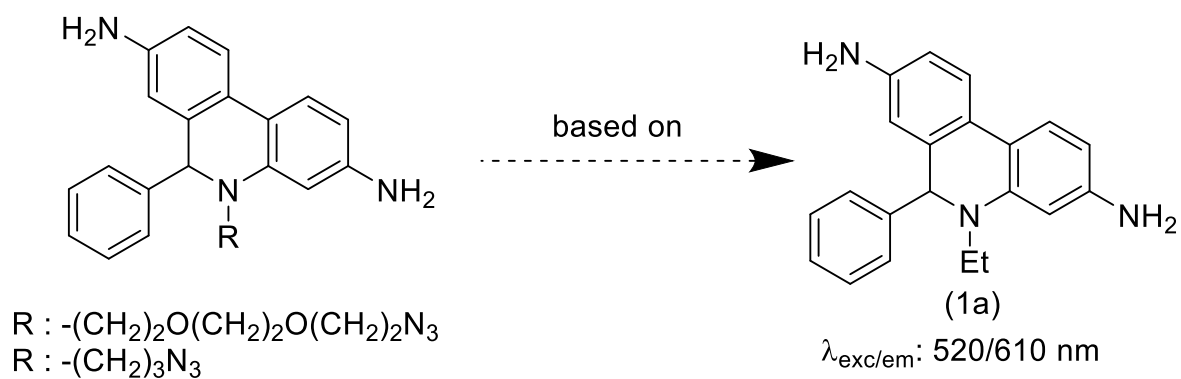
*Figure 2.1: Design of desired molecule from (**1a**)*

To obtain the target superoxide sensor we followed the synthetic strategy reported by Chu *et al.* (Scheme 2.1). According to this approach, the aromatic amino groups on hydroethidine are protected with a Boc group to avoid reaction with the alkyl halide in the following steps. Alkylation of the endocyclic nitrogen is then carried out with a suitable alkyl halide and lastly the protecting group is removed. The reduction of hydroethidium (**27**) into hydroethidine (**28**) is reported to occur in the presence of NaBH$_3$CN[96,97,214–219]. Considering the nature of our target side chain on hydroethidium (**27**), the use of a mild reducing agent such as NaBH$_3$CN seemed suitable, as it would avoid the unwanted reduction of the azide group.
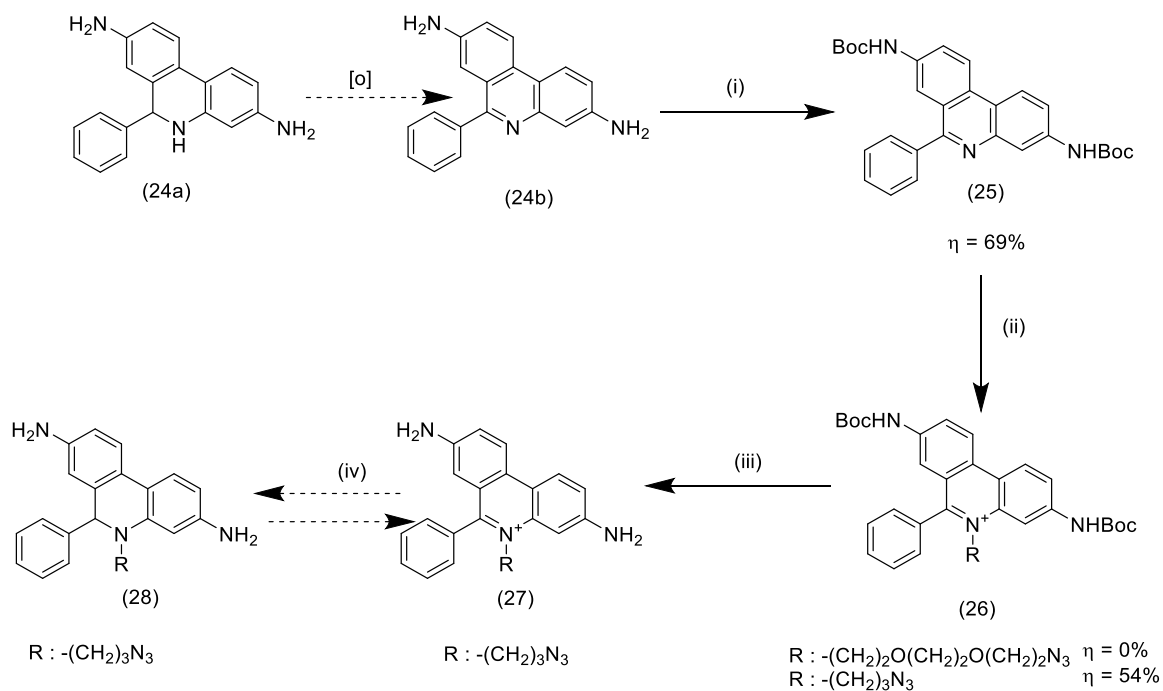
*Scheme 2.1: Synthetic approach for (**28**). (i) Boc$_2$O, THF, water, NaHCO$_3$; (ii) I-R; (iii) HCl 4M in 1,4 dioxane; (iv) NaBH$_3$CN, 0°C.*

2.1.1.2. <u>Boc protection of (24a or 24b)</u>

On analysing commercial hydroethidine (**24a**) by ^{1}H-NMR, we observed that this species is very quickly oxidised into (**24b**) in contact with air (Fig. 2.2). Although unexpected, this behaviour did not hamper our synthetic approach, because (**24b**) can be a substrate for the synthetic transformations we intended to carry out. Chu *et al.*, proposed a synthetic approach to protect (**24b**) primary amine group with a Boc group[220] (Sch. 2.1). The reaction was carried out by treating hydroethidine with 7 equivalents of Boc$_2$O in water and THF in an ice bath. The mixture was stirred at 0 °C for 30 minutes and at room temperature overnight. The desired compound was obtained as a yellow solid with a yield of 69%. Purification by column chromatography was not possible because the compound proved unstable on silica, so it was used for the following steps without further purification. We were unable to identify the products

of degradation, but we speculate that the acidity of silica may have led to the loss of Boc groups: following column chromatography we observed on the mass spectra the presence of hydroethidine (HE), and of the monoprotected derivative (1 BOC HE) and with two Boc groups (2 BOC HE) (Fig. 2.3).
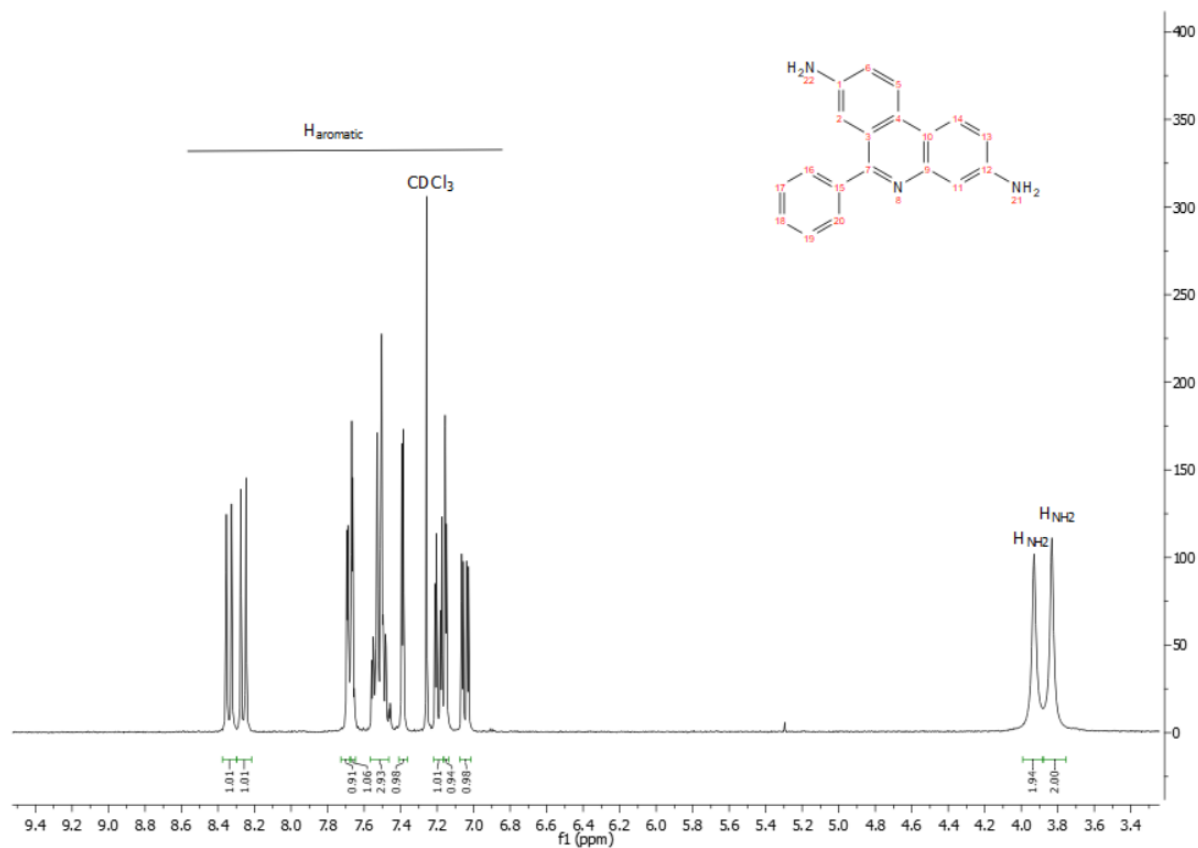
Figure 2.2: NMR of commercial HE with CDCl₃ at 300 MHz
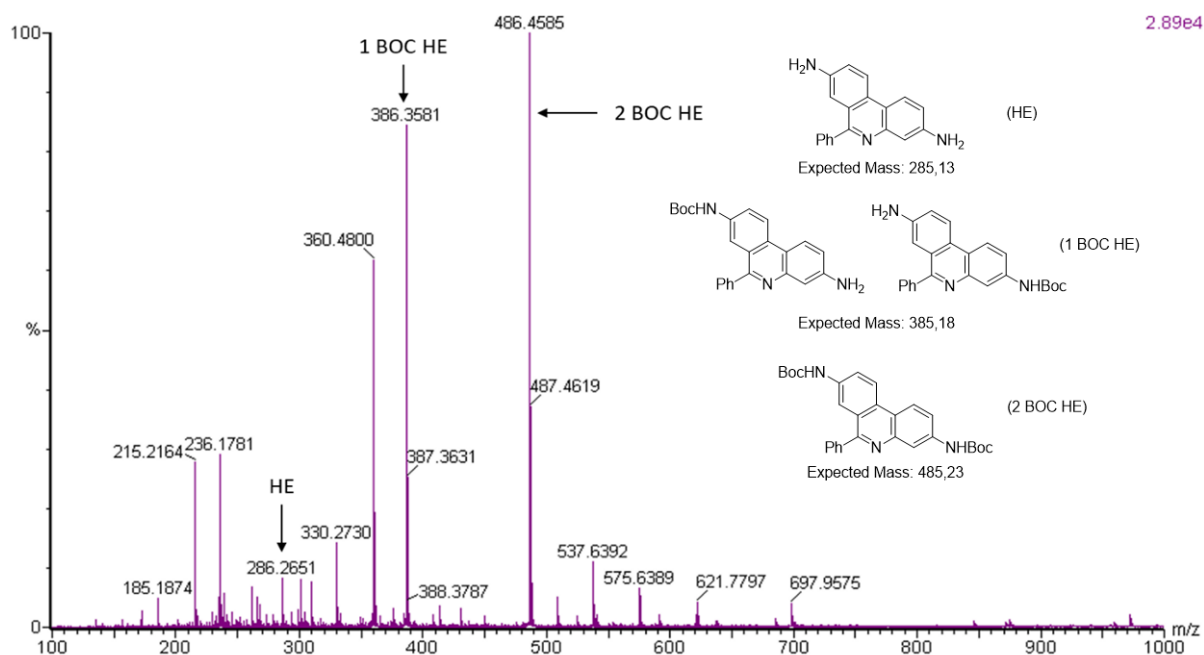
*Figure 2.3: Mass spectra of (**25**) after purification by column chromatography (ES+).*

2.1.1.3. Alkylation of side chain with functionalised moiety

2.1.1.3.1. Synthesis of chain (31)

In order to conjugate our sensor on NPs, a suitably functionalised linker must be introduced on the hydroethidine moiety. We decided to add a spacer between the hydroethidine and the azide to avoid interference of the latter with the sensing structure and to minimise the risk of steric hindrance during the conjugation to the nanoparticle. Our choice fell on 1-azido-2-(2-(2-ethoxy)ethoxy)ethane (Scheme 2.2), as it can be readily obtained from commercially available 2-(2-(2-chloroethoxy)ethoxy)ethanol (**29**). In addition, this linker displays a PEG-like structure that potentially improves the water solubility of the sensor, thereby facilitating the conjugation to the nanoparticle, which occurs in water[221]. The first step involves the replacement of the chloride on (**29**) with a iodide, a better leaving group, through a Finkelstein reaction[222]. This transformation,

which entails the nucleophilic displacement of a chloride with an iodide, is carried out in acetone. The insolubility of sodium chloride in acetone subtracts the chloride ions from the solution and drives the reaction to completion, affording the desired iodide in high yield. The second step of the synthesis involves the displacement of the iodide with azide, performed in boiling AcCN in the presence of NaN$_3$ as described by Kele *et al.*[223] (Sch. 2.2).
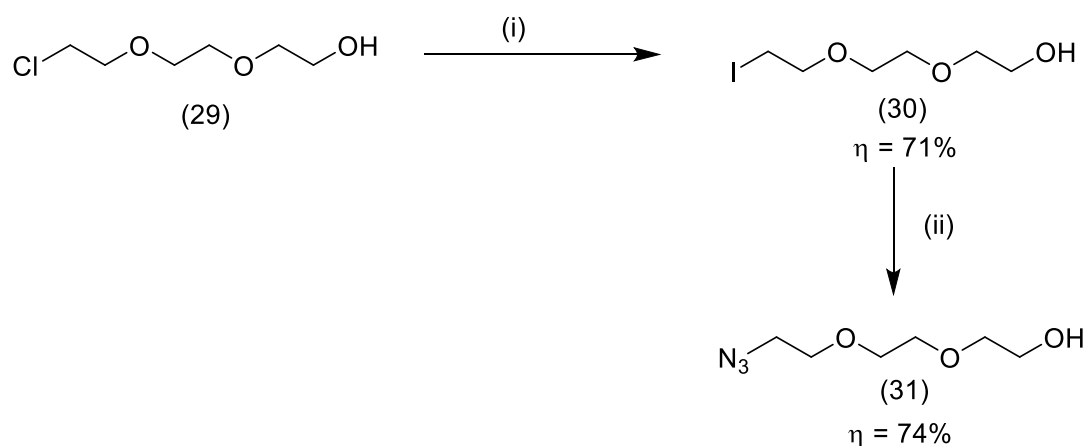
*Scheme 2.2: Synthesis of chain (**31**). (i) NaI, acetone, reflux; (ii) NaN$_3$, AcCN, reflux*

2.1.1.3.2. <u>Attachment of the chain (31) on (25)</u>

In order to attach the chain on the Boc-protected (**25**), we first explored the possibility of using the mesylate of alcohol (**31**) as a derivative that is easier to handle compared to the triflate used by Lee *et al.* [224]. The mesylate was obtained by treatment of (**31**) with MsCl in the presence of TEA, in DCM at 0°C (Sch. 2.3). Reaction of the mesylate (**32**) with (**25**) was attempted in refluxing acetonitrile: we verified that under these conditions no formation of the desired species took place. We speculated that the lack of reactivity we observed could be either due to the moderate nucleophilicity of the phenanthroline nitrogen of (**25**), making the mesylate insufficiently electrophilic for this reaction, or to steric hindrance caused by the relatively bulky mesylate group.
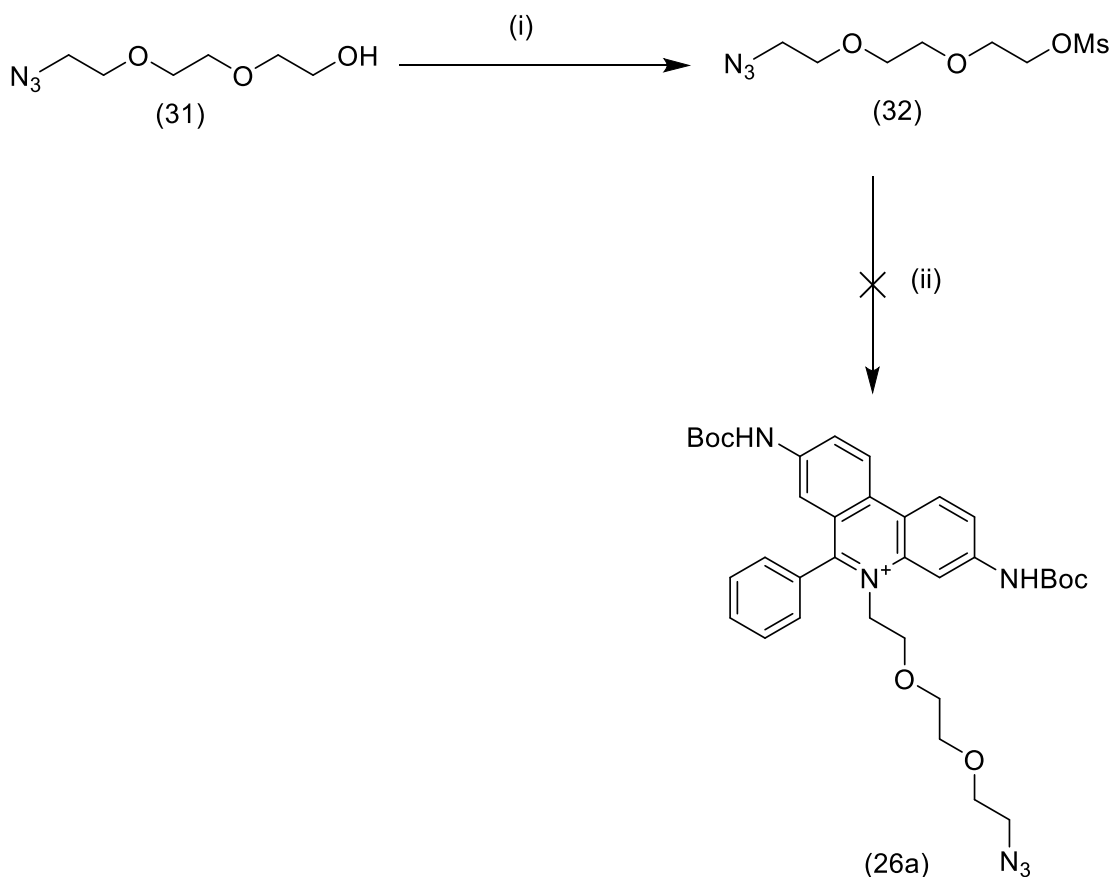
Scheme 2.3: Alkylation of (25) by (31). (i) MsCl, TEA, DCM, 0°C; (ii) (25), AcCN, reflux.

We attempted to circumvent this problem by using an iodide as the alkylating reagent, as outlined below.

2.1.1.3.3. Synthesis of chain (34)

In order to obtain the target iodide, (29) was transformed into 1-azido-(2-(2-chloroethoxy)ethoxy)ethane (33). To this end, the hydroxyl group was mesylated as indicated above. Then, the mesylate was treated with TBAI and NaN$_3$ and refluxed in toluene until TLC indicated complete conversion (2 days)[225,226] (Sch. 2.4). Replacement of the chloride by an iodide, was carried out in the same conditions described above for (30), to afford the desired product (34).
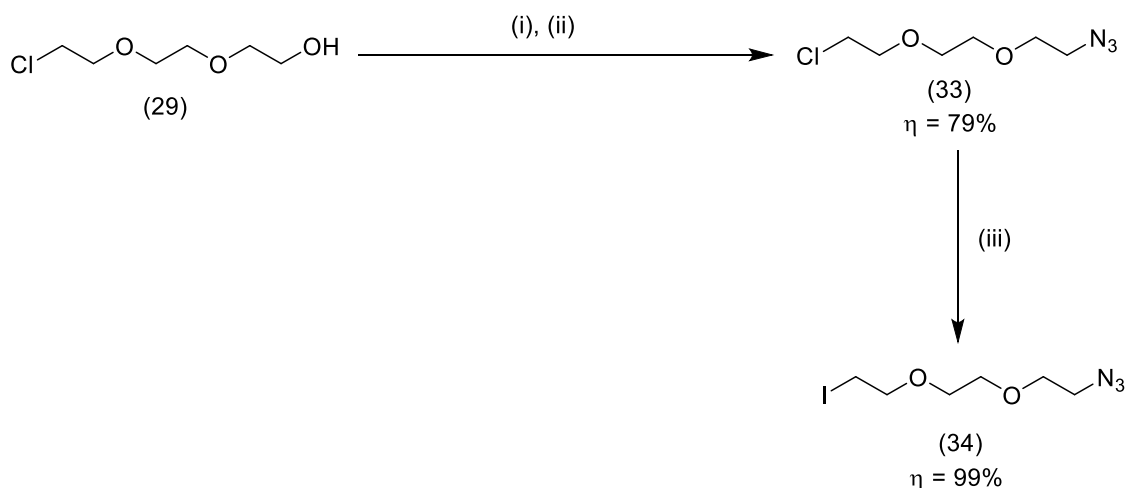
*Scheme 2.4: Synthesis of chain (**34**). (i) MsCl, TEA, toluene, 0°C; (ii) TBAI, NaN₃, toluene, reflux; (iii) NaI, acetone, reflux.*

2.1.1.3.1. <u>Attachment of the chain (34) on (25)</u>

To attach the chain on the Boc-protected hydroethidine (**25**), similar conditions to the ones described above were adopted (Sch. 2.5). Unfortunately, after 2 weeks of reflux conditions, the desired molecule was not obtained as verified by mass spectra (Fig. 2.4). The peak at 486.1351 shows that the starting material was still present in the reaction mixture.
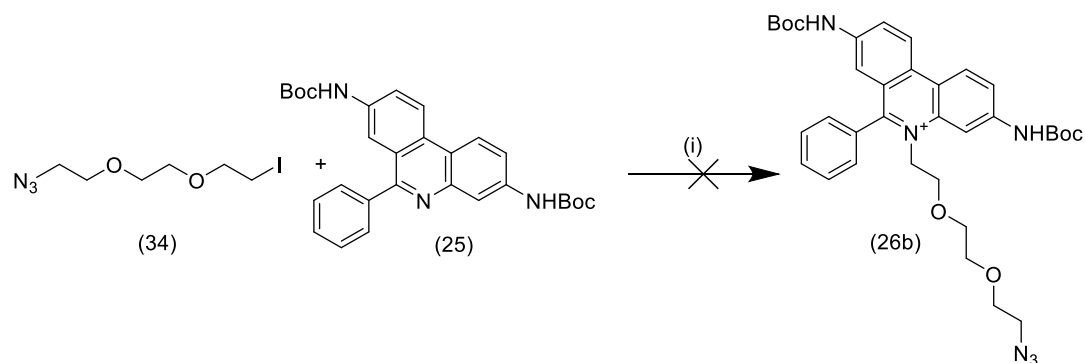
*Scheme 2.5: Alkylation of (**25**) by (**34**). (i) AcCN, reflux.*
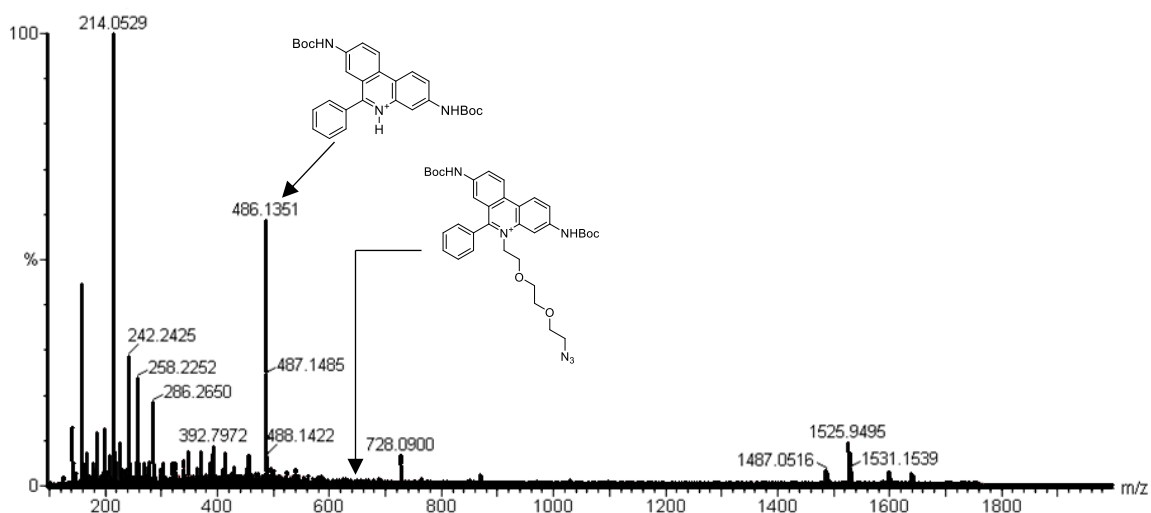
*Figure 2.4: Mass spectra of (**26**)*

Our hypothesis to explain the failure of this reaction is the choice of the chain. N-alkylated heterocycles such as phenanthroline can lose the alkyl group under various conditions, including heating[227]. In our case, the loss of the alkoxyethylene chain can be tentatively rationalised with the formation of an alkyloxyranium intermediate, which would facilitate the elimination (sch. 2.6).
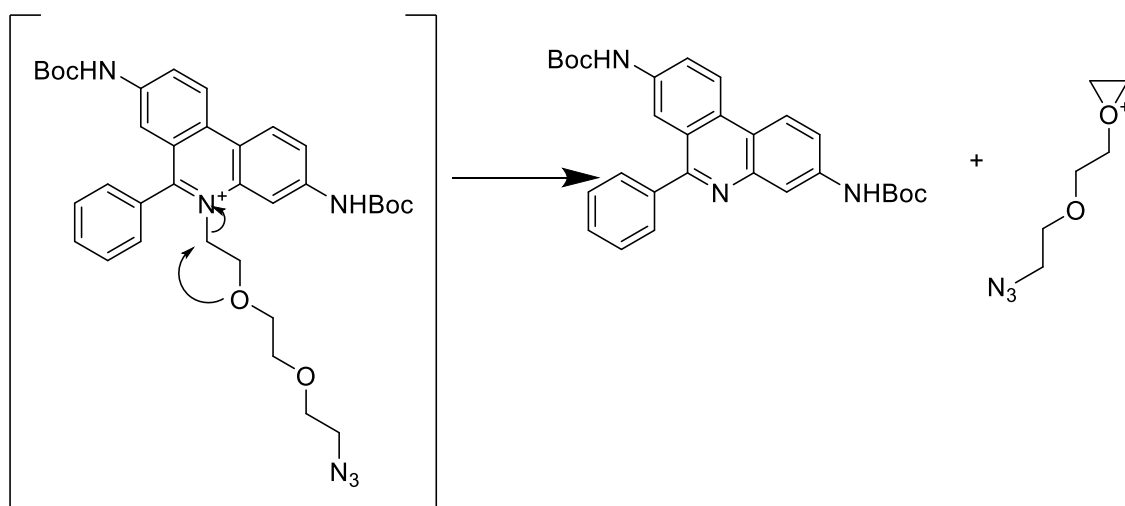
*Scheme 2.6: Speculative explanation for the failed reaction between (**34**) and (**25**).*

2.1.1.3.2. <u>Alkylation and azidation using 1,3-diidodopropane</u>

In the first instance, we attempted the incorporation of an azide group using a shorter chain without oxygen. As shown by Huber *et al.*, the alkyl chain is introduced on hydroethidine first and the azide moiety is added later (Sch. 2.7).1,3-diidodopropane (**35**) was refluxed in the presence of hydroethidine (**25**) in THF for 5 days[216]. Unfortunately, no reaction was observed after 5 days but it eventually progressed to completion in 2 months (monitored by MS). The procedure reported in the literature does not mention this extremely long reaction time, therefore we concluded that the use of the Alloc group has a considerable effect on the reactivity of the pyridine nitrogen. This might be due to its stability in acidic and basic conditions[228]. After the completion of the reaction, a yellow solid (**36**) was collected with 61% of yield.

For the introduction of the azide group, the alkylated protected hydroethidine was refluxed with sodium azide in a mixture of acetone and distilled water in proportion 3 for 1 to give a yellow solid (**26c**) with 89% yield[96].
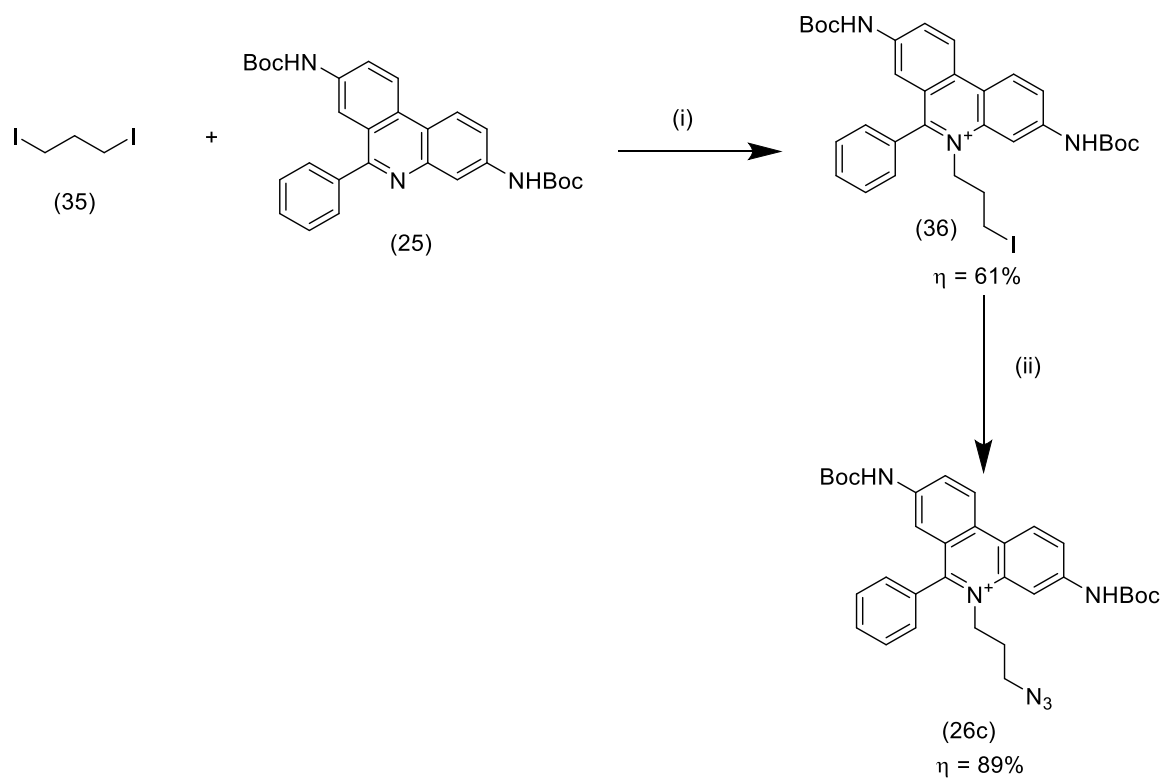
*Scheme 2.7: Synthesis of (**26c**). (i) THF, reflux, (ii) NaN₃, acetone/water (3:1), reflux.*

2.1.1.4. Reduction and deprotection

According to the procedure reported by Chu *et al*., the reduction step was carried out at 0°C in THF using NaBH₃CN as the reducing agent. Subsequent treatment with 4 M HCl in dioxane was employed to remove the Boc protecting group (Sch.2.8) to give (**28a**)[220].
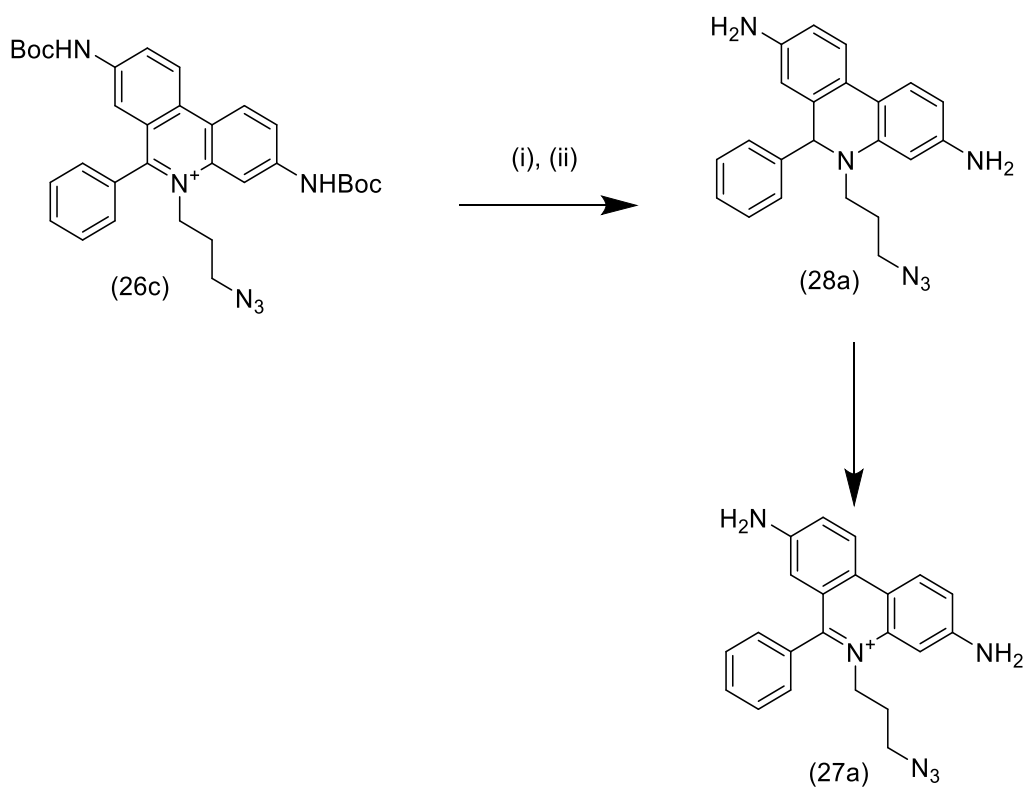
*Scheme 2.8: Reduction and deprotection of (**26c**). (i) NaBH₃CN, THF, 0°C; (ii) 4M HCl in 1,4-dioxane.*

After reduction and deprotection of (**26c**)[220], the mass spectra shows that the reaction struggled to reach completion. On one hand, Boc deprotection was not completed as indicated by the peaks at [M+100] and [M+200] for one or two Boc protecting groups, respectively, on the mass spectrum (Fig. 2.5). On the other hand, the oxidized molecule was still present in the solution. Two additional treatments with NaBH₃CN were made following the previous procedure to reduce the oxidised species. Unfortunately, the reaction was not complete and after few days, the reduced molecule (mass 369.4046) reverted to its oxidised form (mass 371.3177) (Fig. 2.5). The apparent lack of stability of alkylated hydroethidine led us to conclude that its use as a ROS sensor would be severely affected. In fact, the reduced form of (**28a**) is non-fluorescent whereas the oxidised form is. If (**28a**) is unstable and oxidises without the target

analyte, the detection and eventual quantification of superoxide anion would be biased[94,218]. In addition, the lengthy reaction times necessary for its synthesis contributes to making the use of alkylated hydroethidine unviable.
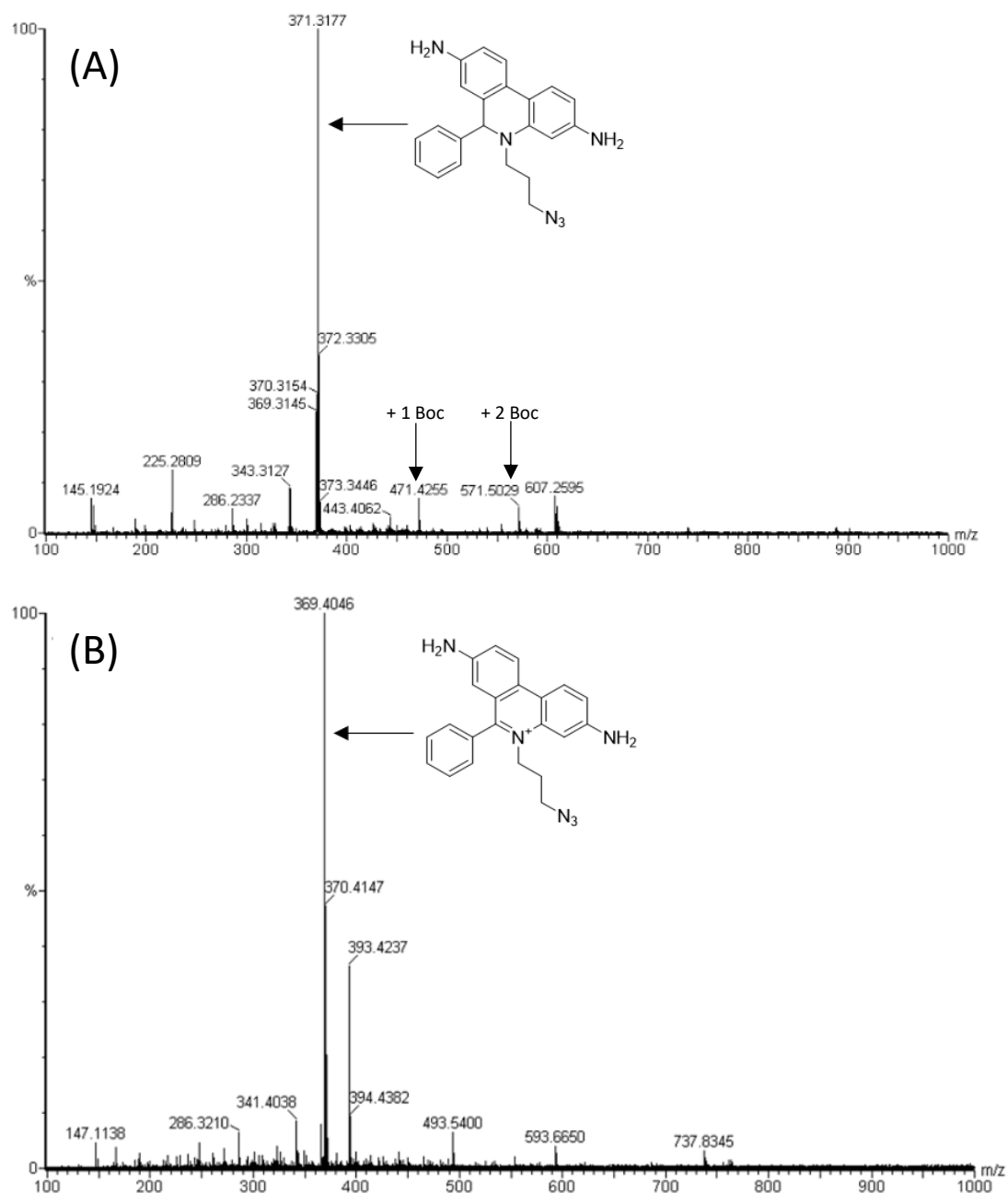
*Figure 2.5: Mass spectra of (**28a**) after reduction (A) and one day later (B) (ES+)*

2.1.2. Dianthrafluorescein

As discussed in the introduction alternative probes exist to detect superoxide anion. One of them is phosphinated dianthrafluorescein (**4a**). Although the literature reports conflicting information on the absorption/emission wavelengths ($\lambda_{exc}/\lambda_{em}$ = 602/662 nm[108] or $\lambda_{exc}/\lambda_{em}$ = 490/530 nm[109]) we selected phosphinated dianthrafluorescein because it is reported to emit in the red window of the spectrum and synthetic approaches to introduce functional groups amenable to conjugation are relatively straightforward (Fig 2.6).
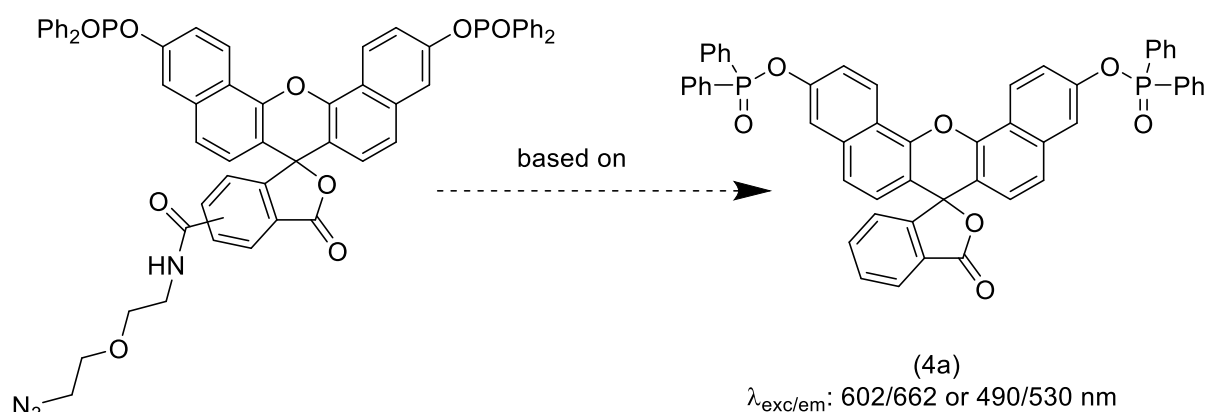
*Figure 2.6: Design of desired molecule from (**4a**)*

2.1.2.1. Synthetic approach

The dianthrafluorescein sensors described in the literature do not bear a functional group that allows their conjugation; therefore, we needed a synthetic strategy to obtain a phosphinated dianthrafluorescein derivative suitable for this project. Our approach, depicted in (Sch. 2.9), started with a Friedel-Craft reaction followed by ring closure to give the dianthrafluorescein scaffold. The insertion of the azide group on the chain would be then achieved by amidation of the activated carboxylic group.
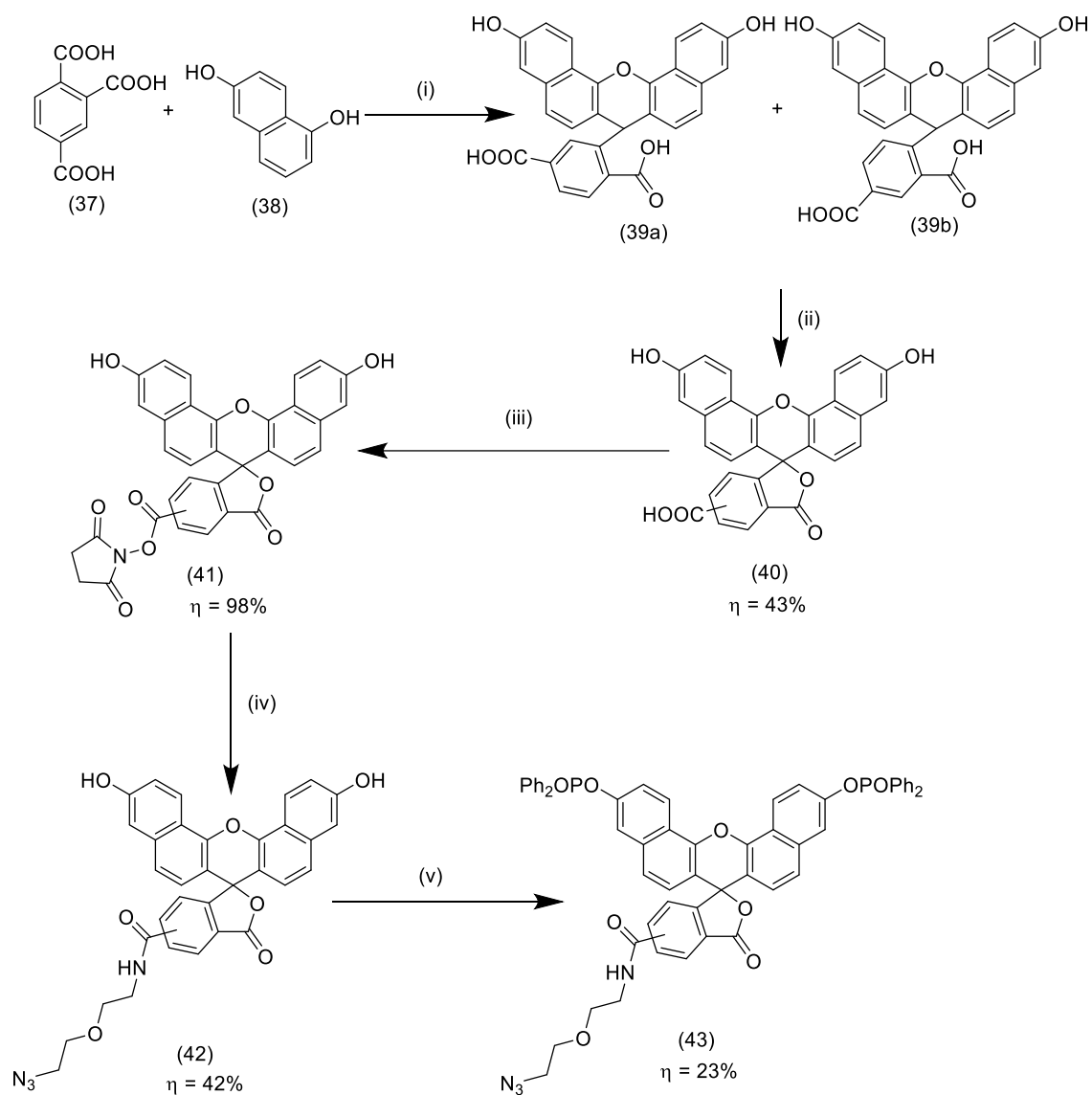
Scheme 2.9: Synthetic approach for (43). (i) CH₃SO₃H, 100°C (ii) CuCl₂, Na₂S₂O₈, 90°C; (iii) DIC, NHS, THF at rt; (iv) 2-(2-azidoethoxy)ethan-1-amine, TEA, DCM/DMF at rt; (v) P(O)Ph₂Cl, TEA, THF at rt.

Benzene-1,2,4-tricarboxylic acid and naphthalene-1,6-diol reacted in methanesulfonic acid in a tandem Friedel-Craft acylation and ring closure[110] to afford the target product (**39a** and **39b**) (Sch. 2.10) as a mixture of isomers that are not readily separable by column chromatography but that can be resolved by analytical HPLC (Fig. 18).
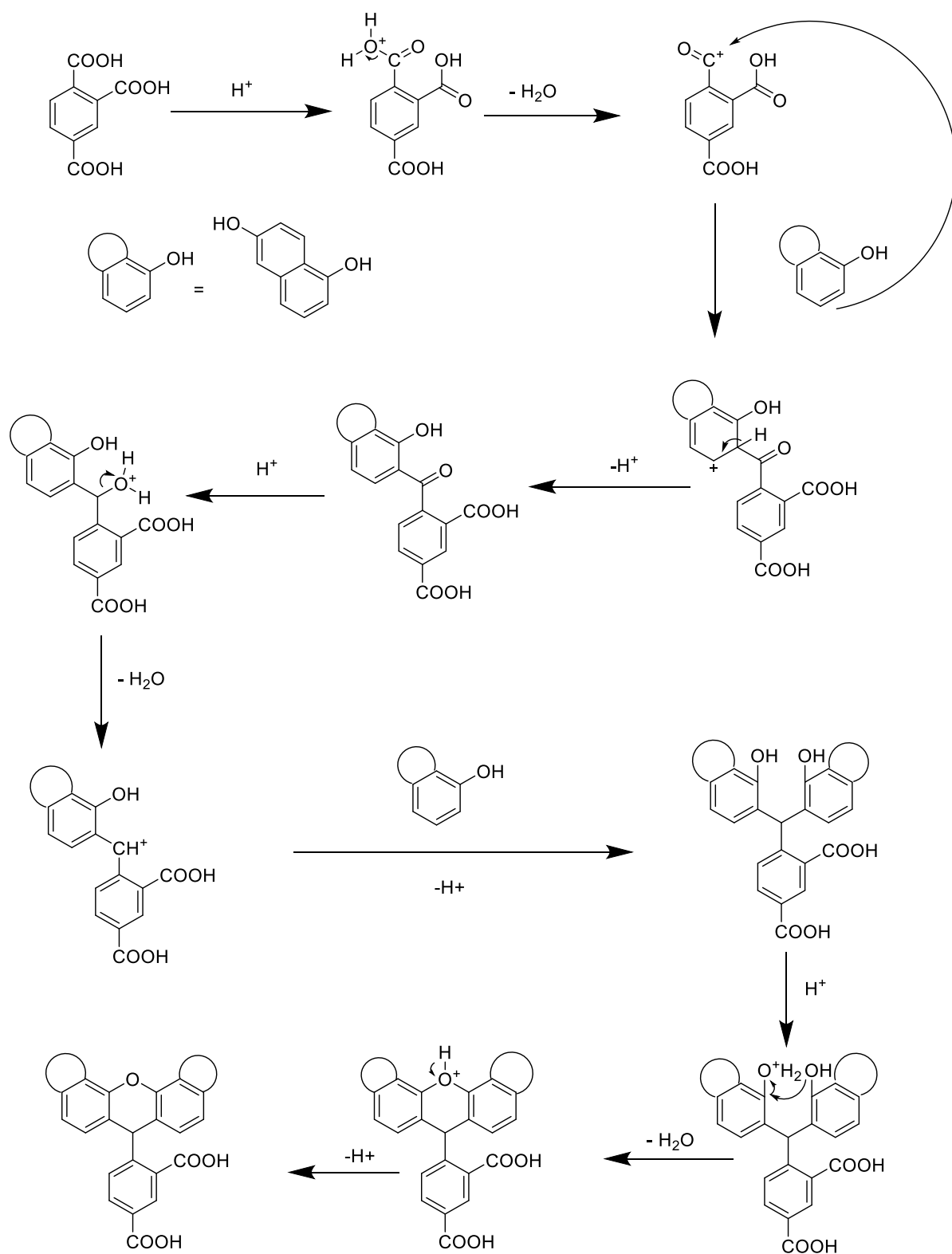
*Scheme 2.10: Friedel and Craft mechanism for the formation of dianthrafluorescein (only isomer **39b** is shown)*
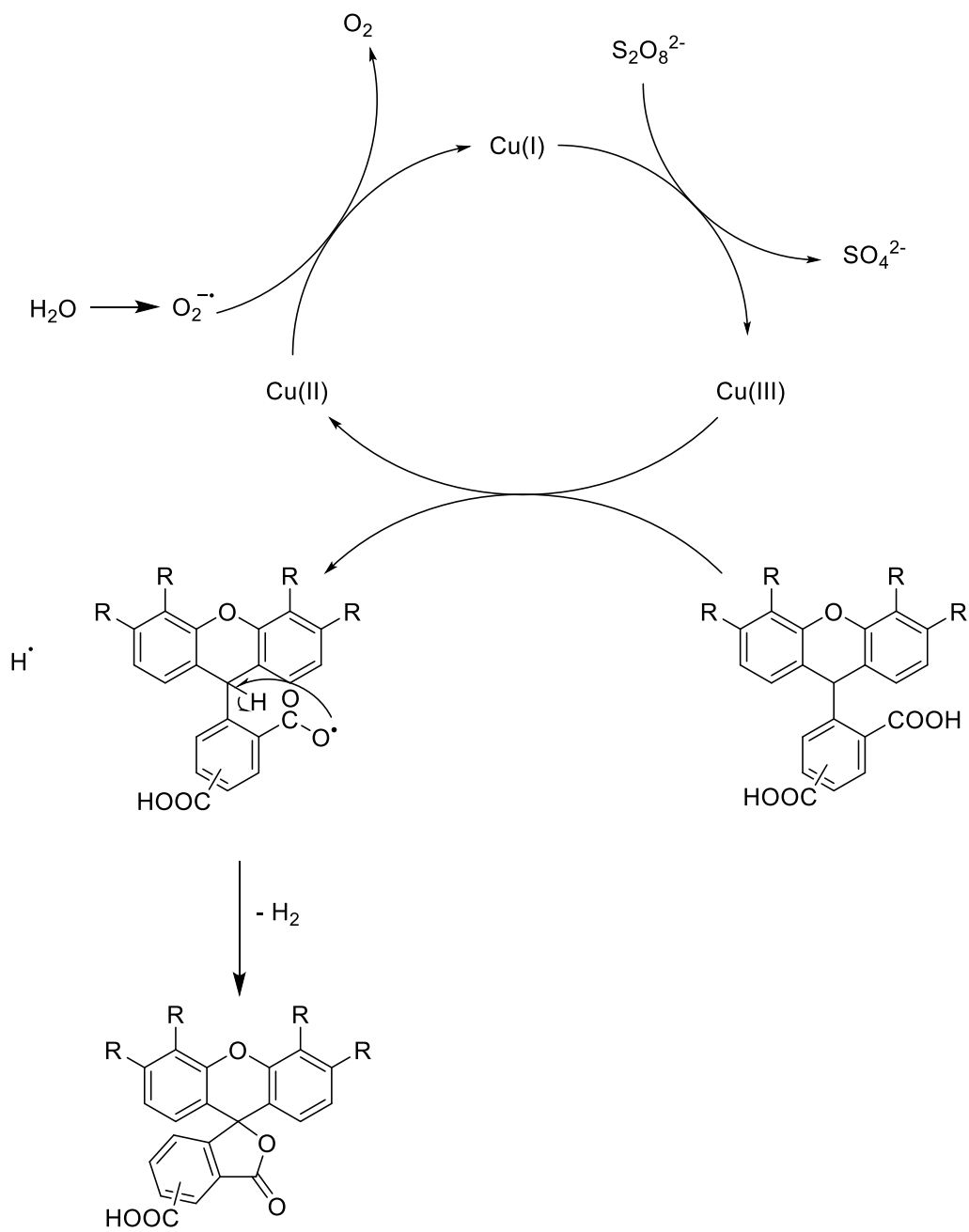
*Scheme 2.11: Ring closure mechanism to synthesise (**40**)*
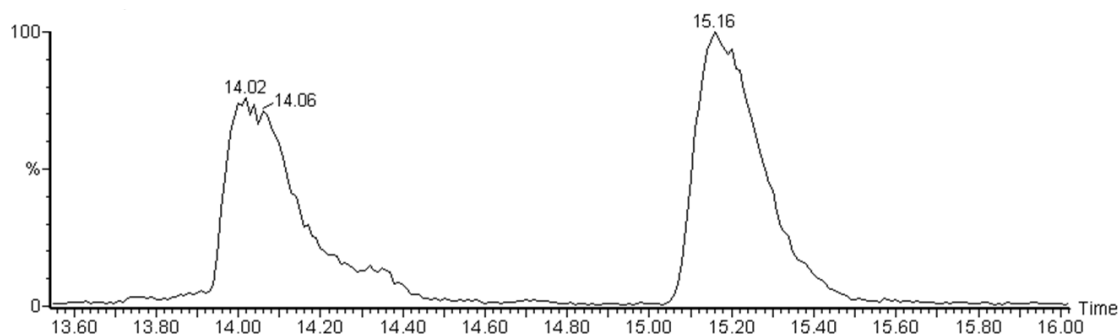
Figure 2.7: Separation of the two isomers (20a) and (20b) by LC

The closure of the 5-membered lactone was achieved by oxidation with copper chloride and sodium persulfate (Sch. 2.11)[229] to form a red solid (**40**) in 69% yield.
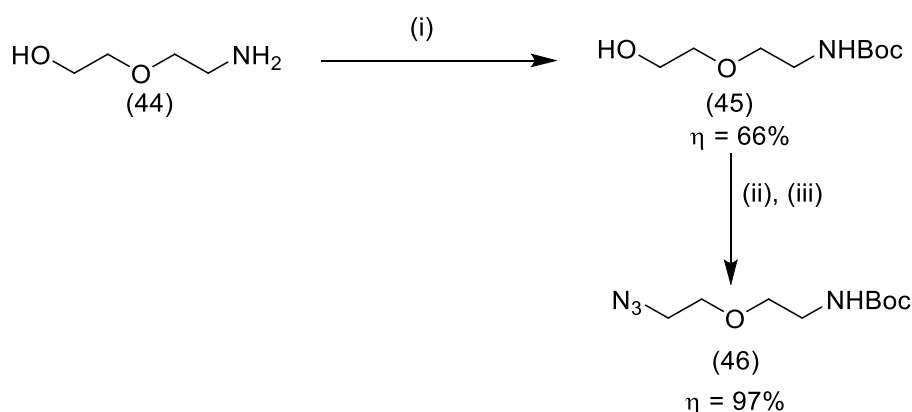
*Scheme 2.12: Synthesis of the alkyl chain (**46**). (i) Boc$_2$O, THF, water, NaHCO$_3$; (ii) MsCl, TEA, DCM, 0°C; (iii) (5), AcCN, reflux.*

As planned for hydroethidium, we aimed to insert an azide group on the fluorophore to conjugate it to the polymer via a CuAAC "click" reaction. To make the alkyl chain (**46**), 2-(2-aminoethoxy)ethan-1-ol (**44**) was Boc-protected as previously described for hydroethidine (**25**)[220]. The following step is a mesylation as described for species (**31**) and lastly the displacement of the mesylate by azide was carried out with sodium azide in DMF[230] to give a yellow viscous liquid (**46**) in 97% yield (Sch. 2.12).

61

The carboxylic group in dianthrafluorescein (**40**) was activated with NHS (Sch. 2.9)[231,232] in the presence of DIC to give a red solid (**41**) in 98% yield.

To obtain the target amide, (**46**) was treated with TFA in DCM (2:5) to remove the Boc protecting group and the resulting amine (**46a**) was coupled with (**41**)[233] in presence of TEA[234,235] to give a red solid (**42**) with 62% of yield (Sch. 2.13).
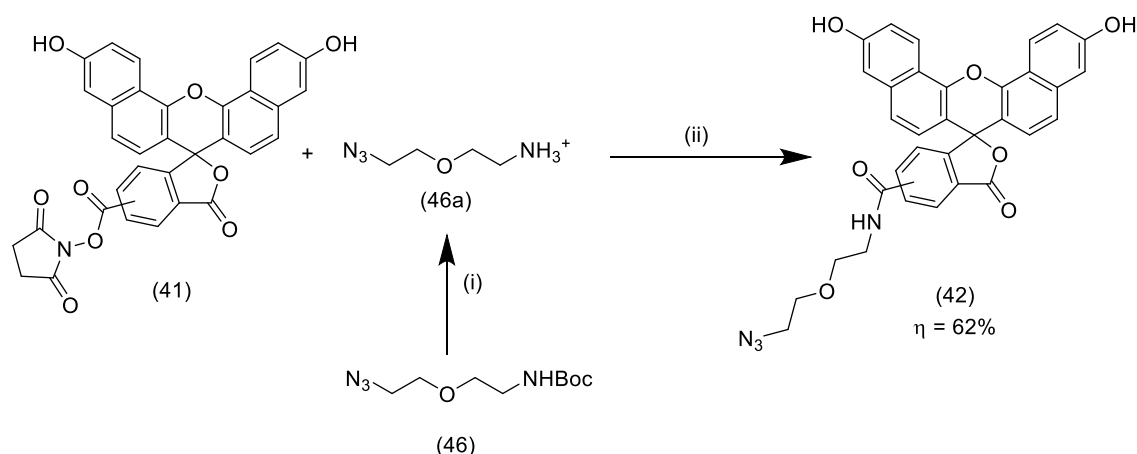
*Scheme 2.13: Alkylation of (**41**) by (**46**). (i) TFA/DCM, (ii) TEA, DCM/DMF.*

The phosphination of (**42**) was carried out with (Ph$_2$P(O)Cl)[108] (Sch. 2.9) in THF. We verified that the addition of Ph$_2$P(O)Cl must be carried out at 0°C and the reaction performed at room temperature in order to avoid the degradation of the chain and the recovery of dianthrafluorescein, which was indicated by the presence of a peak at 477.0754 on the MS (Fig. 2.8). These conditions led to the desired product (**43**) in 23% yield. The molecule must be stored in freezer under nitrogen as a precaution against potential degradation.
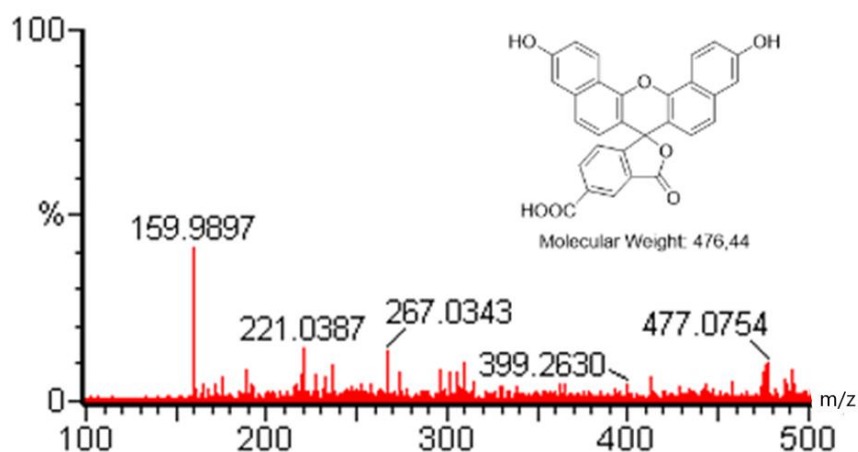
*Figure 2.8: Mass spectra of (**43**) after room temperature reaction (ES+)*

2.1.2.2. <u>Spectroscopic characterisation</u>

(**43**) has an absorption maximum at 490 nm and an emission maximum at 540 nm (Fig. 2.9), as expected from the literature (490 and 530 nm)[109]. This value is rather close to the emission of the POY sensor for hydrogen peroxide (see section 1.2) and could lead to signal interference.
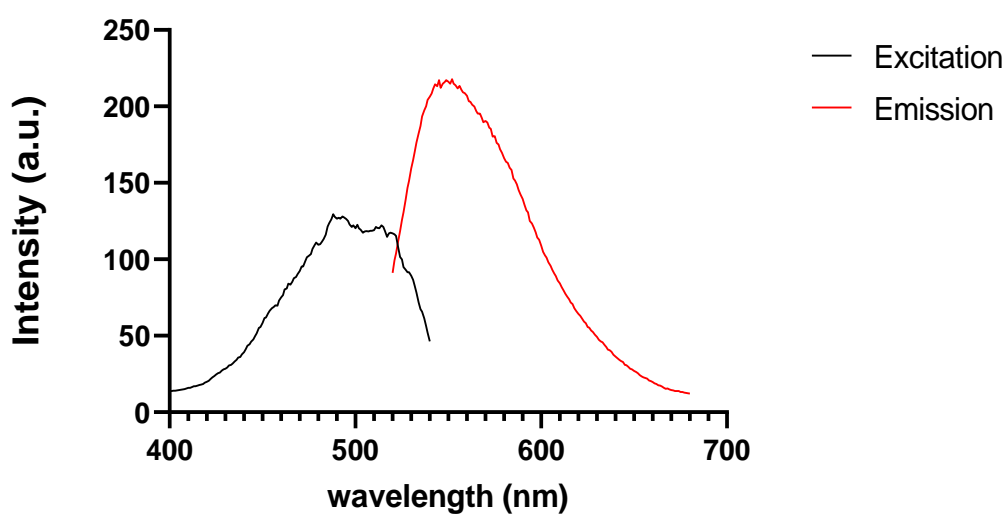
*Figure 2.9: Excitation and emission of the sensor (**43**)*

As a preliminary exploration of the efficiency of this sensor (**43**), its reactivity with superoxide anions was tested in aqueous solution. Superoxide anions were generated with xanthine (Xa) and xanthine oxidase (XO)[13,96,100,107,109]. The sensor was dissolved in DMSO and the resulting solution was diluted in PBS. PBS has been chosen because its pH (7.4) is similar to the pH of the cytoplasm in the cells (7.2). To this solution Xa and catalase solutions were added. Then different volumes of XO solution were added. Fluorescence spectra of the samples were recorded at 560 nm (Fig. 2.10a) and the intensity of the maximum of emission was plotted versus the added volume of XO (Fig. 2.10b).
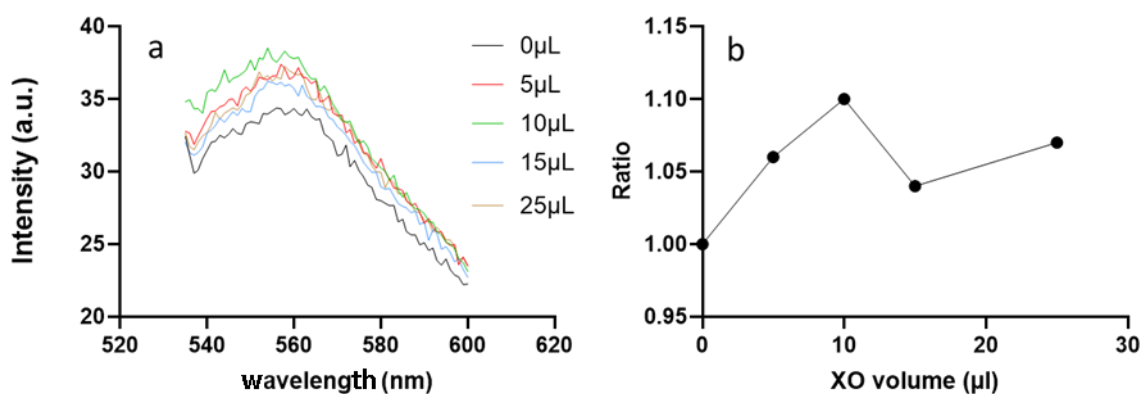
Figure 2.10: Example of fluorescence emission of (43) depending on XO volume. Fluorescence spectra of the samples (a), plot of normalised fluorescence versus added volume of XO (b).

As shown in Fig. 2.10 the fluorescence intensity increases between 0 and 15 μL and decreases from 15 μL. We speculated that this decrease could be due to the change of pH of the medium, which has is reported to have a considerable effect on the intensity of fluorescence emission of fluorescein-based species. As our experiments were performed in buffered solutions, we were inclined to rule out a pH effect in the efficiency of emission; yet, we wanted to verify whether we could observe the pH

dependence reported for dianthrafluorescein. As shown in Figure 2.11, dianthrafluorescein emits efficiently between 7.4 and 8.0[108].

A further possible explanation for the unexpected variation of emission intensity lies in the changes of emissive behaviour due to the interactions of the fluorophores with proteins and other biomacromolecules[196], which has been observed for SOSG[133]: the XO enzyme in our solution can bind with our sensor and alter its fluorescence. In this case the use of NPs can be advantageous as it will help to protect our sensor from interaction with the enzyme, as is reported for as for NanoPEBBLE[196] or NanoSOSG[133].
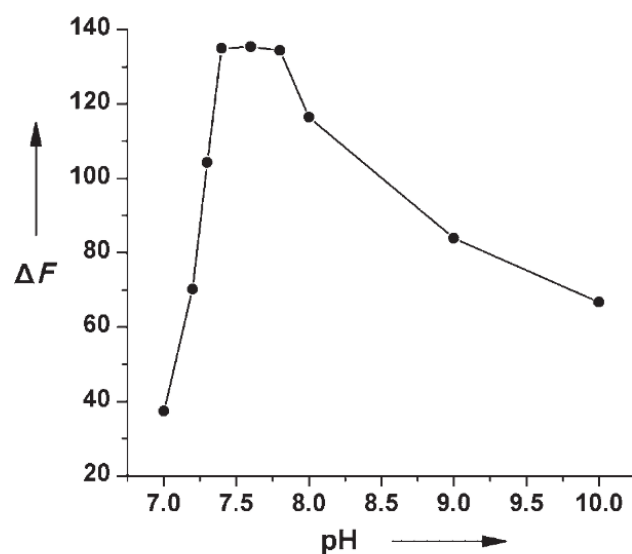
*Figure 2.11: Effect of the pH on (**43**)[108]*

Our work aimed at the synthesis of a superoxide sensor bearing an azide group for conjugation on polymeric nanoparticle led us to explore the functionalisation of a hydroethidine-based structure, which we subsequently discarded on the account of its

lack of stability. As an alternative sensing moiety, we selected dianthrafluorescein. The synthesis of the target species was successful, and the sensor showed a promising superoxide-dependent emissive behaviour, although we observed some unexpected variation of fluorescence emission. This behaviour was tentatively attributed to the interaction of the sensing moiety with the protein in the system (XO), an issue that will be potentially circumvented by the conjugation of the sensor with the NPs.

2.2. <u>Hydrogen peroxide</u>

2.2.1. <u>Modified peroxy yellow sensor: boronated group directly attached to the fluorescein</u>

As discussed in the introduction, POY is a useful sensor used for hydrogen peroxide detection. Peroxy yellow is based on fluorescein with a boronated group that reacts selectively with this ROS. A peroxy yellow sensor substituent bearing a phosphonium moiety that enhances the ability of the sensor to enter mitochondria has been reported and is referred to as mitoPY (Fig. 2.12)[101,236–238]. This species inspired us to synthesise a peroxy yellow with a substituent bearing a conjugatable group for conjugation to the polymeric matrix of the nanoparticle. We chose to introduce a carboxylic group on the peroxy yellow scaffold because of its versatility towards conjugation *via* amidation and orthogonality to the azide/alkyne reaction pair.
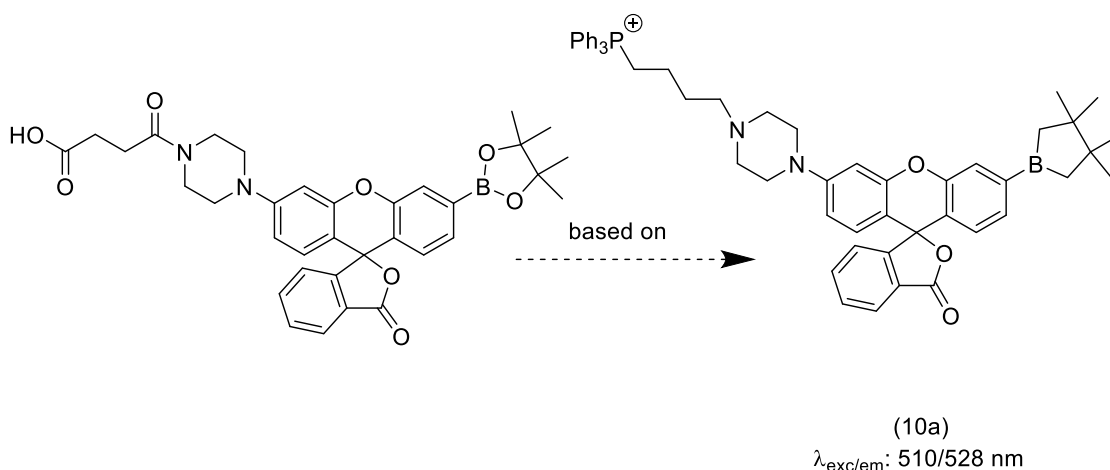
Figure 2.12: Design of desired molecule from (**10a**)

The reaction scheme was adapted from an approach described in the literature[101]. The main challenge was to adapt it to insert another side chain with a carboxylic group (Sch. 2.12).

The synthetic approach proposed by Dickinson *et al.* starts with a Friedel-Craft reaction to make 2-(2,4-dihydroxybenzoyl)benzoic acid (**49**).Species (**49**) then reacts with 3-(piperazin-1-yl)phenol to form the fluorescein moiety (**51**). Then, the nitrogen on the piperazine is protected with an Fmoc group and the free phenolic OH is transformed in the corresponding triflate. Finally, boronate is added to replace the triflate, Fmoc group is removed and the desired carboxylic group is introduced by acylation of the piperazine nitrogen (Sch. 2.14).
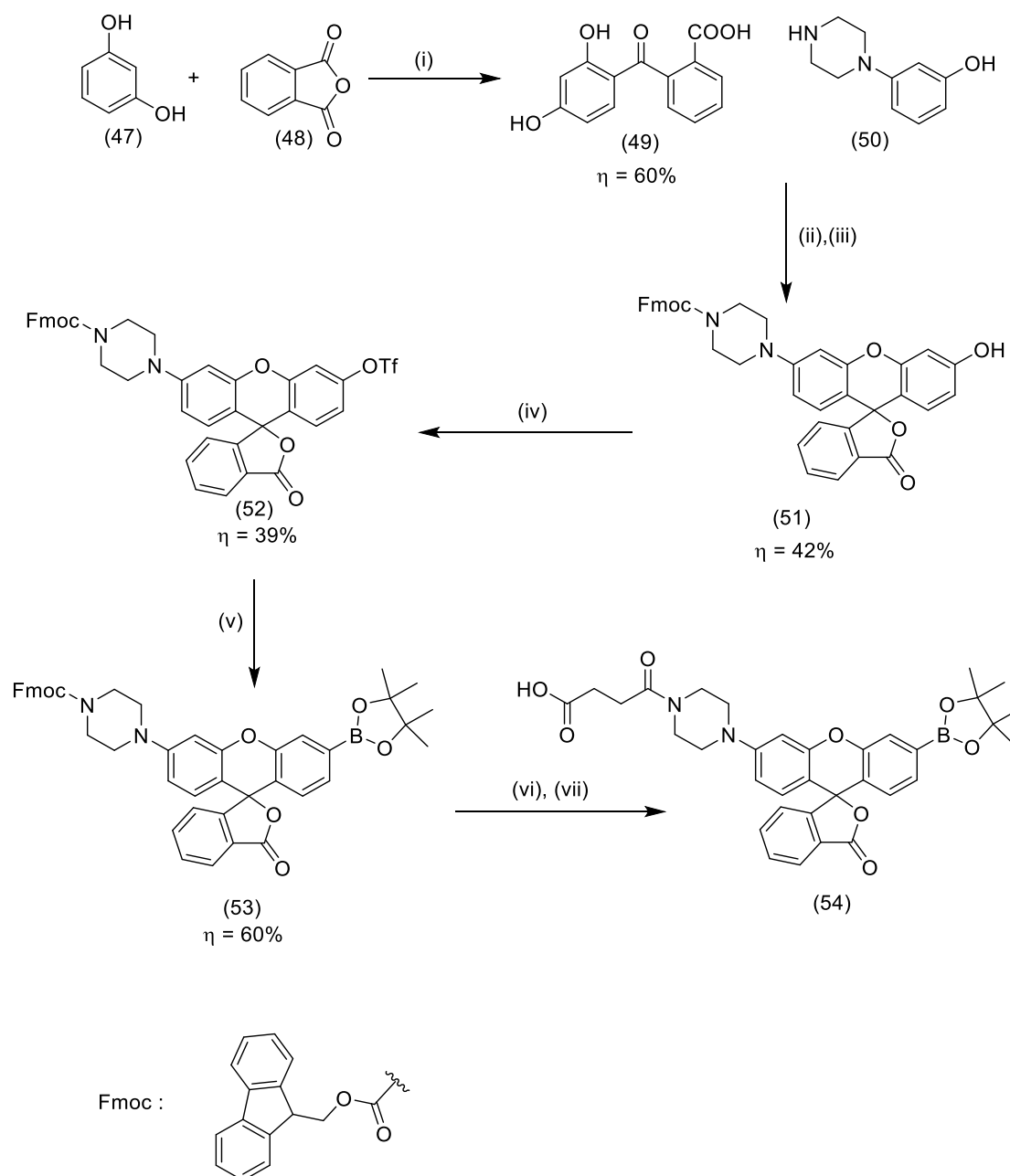
Scheme 2.14: Reaction scheme for (**54**), (i) AlCl₃, nitrobenzene; (ii) TFA; (iii) Fmoc-Cl, NaHCO₃, AcCN; (iv) N-phenyl bis(trifluoromethanesulfonamide) NaHCO₃, DMF; (v) Boron pinacol ester, Pd(dppf)Cl₂· CH₂Cl₂, sodium acetate, toluene; (vi) Piperidine, AcCN, (vii) Succinic acid, DIPEA.

Isobenzofuran-1,3-dione (**48**) and resorcinol (**47**) react under Friedel-Craft conditions in the presence of AlCl$_3$[239] (Sch. 2.15). After recrystallisation, benzophenone (**49**) was obtained as a pale green powder with 60% of yield.
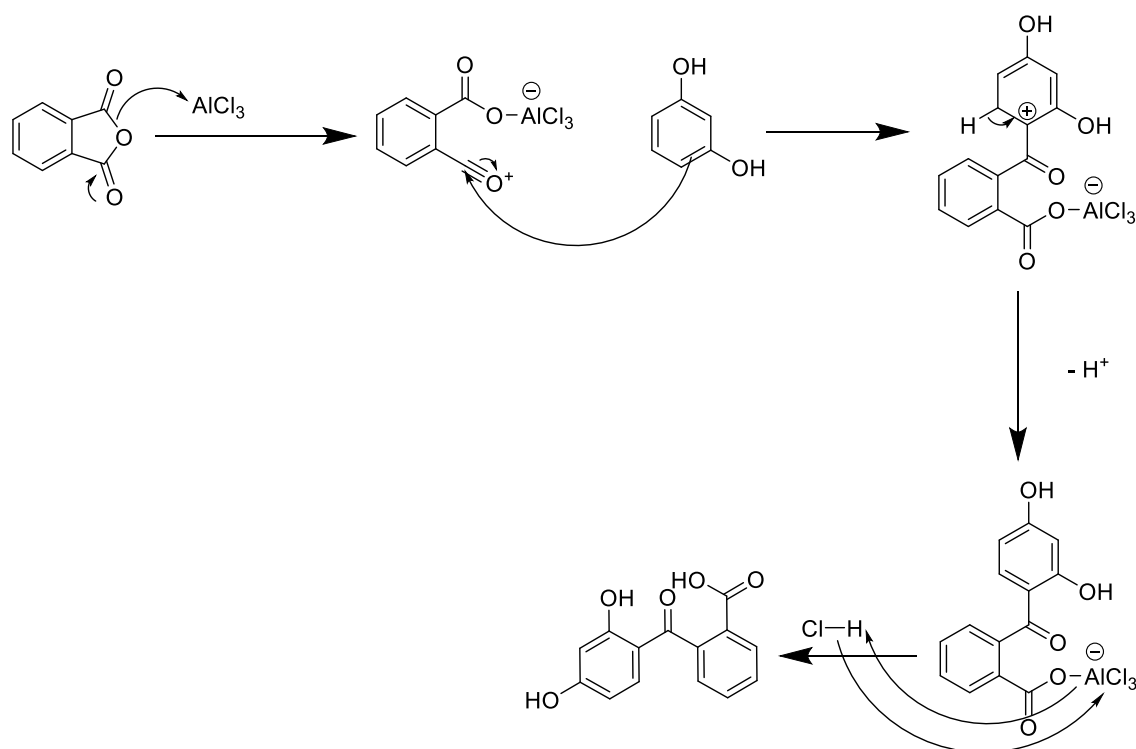
*Scheme 2.15: Friedel and Craft to obtain (**49**)*

Cyclization to the fluorescein derivative was performed using TFA (Sch 2.16). In the following steps of the synthesis, the -NH on piperazine ring is protected with a Fmoc group (Fig. 30)[101]. Dickinson *et al.* rationalise their choice of the Fmoc as a protecting group because its removal with piperidine does not damage the structure of the probe. Thus, 2,4-dihydroxybenzoyl)benzoic acid (**49**) and 1-(3-hydroxyphenyl)-piperazine (**50**) were treated in TFA under anhydrous conditions under a flow of argon. The desired product was precipitated by addition of diethyl ether and careful fast filtration to maintain the product as a solid and prevent the formation of a sticky residue. The crude was dissolved in methanol and evaporated to dryness to remove any residual TFA, affording (**51**) as a red solid in 42% yield.
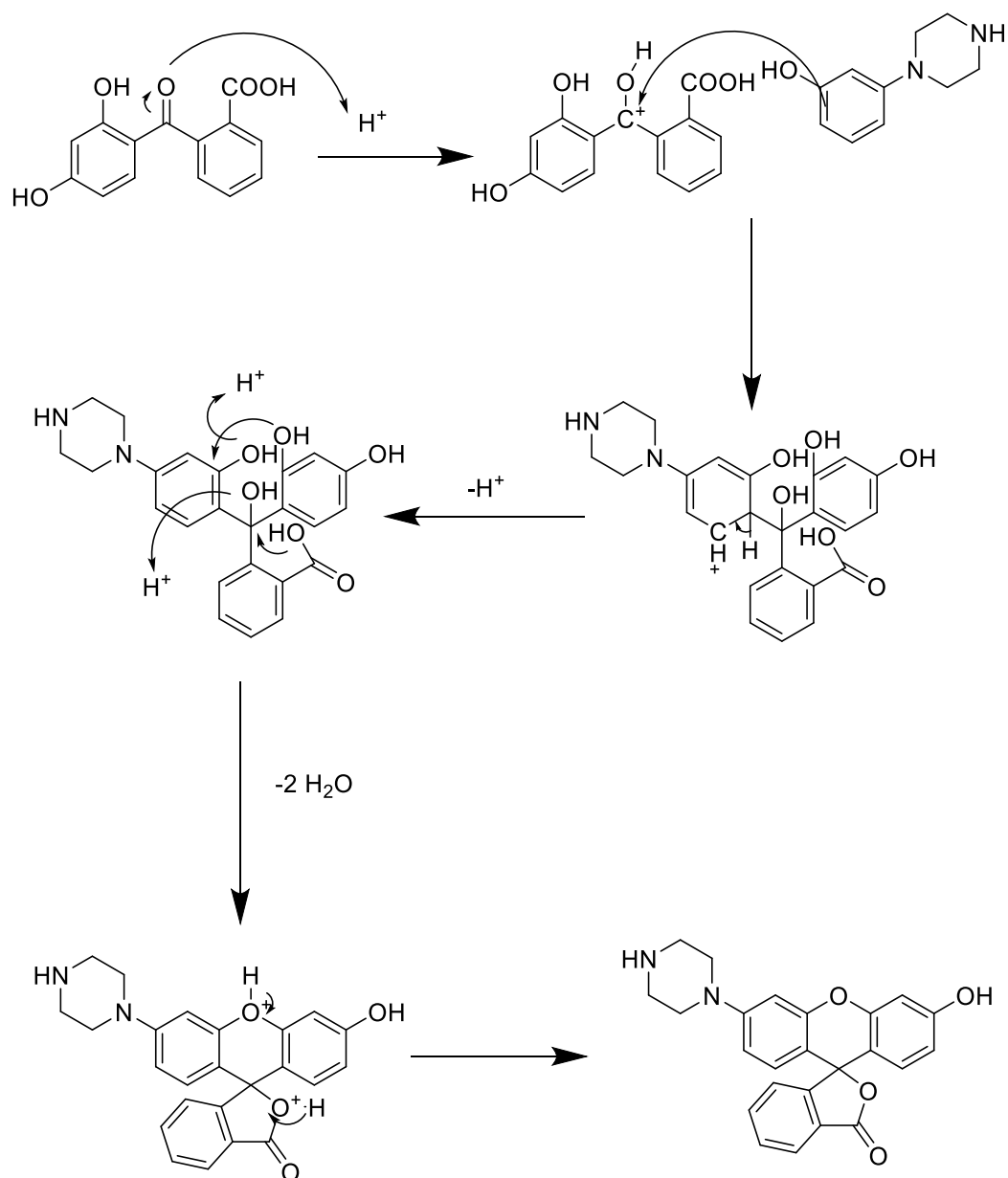
Scheme 2.16: Mechanism of fluorescein "body"

The following step consisted in the triflation of the hydroxyl group (Sch. 2.14)[101,240].

This reaction was necessary for the subsequent palladium-catalysed Suzuki coupling

between the boron pinacol ester and aryl triflate, which gives a one-step entry to

organoboronates from organic electrophiles. To this end, (**51**) was allowed to react with

N-phenyl bis(trifluoromethanesulfonamide) in the presence of sodium carbonate at

room temperature overnight to give a white solid (**52**) in 39% yield.

The mechanism of the palladium-catalysed coupling reaction between the diboron pinacol ester and aryl triflate[101,238] starts with the oxidative addition of the aryl triflate (**52**) to the palladium catalyst to give aryl palladium(II) species R-Pd(II)-Tf (Sch. 2.17). Then, a ligand exchange takes place between Tf of R-Pd(II)-Tf and the boronate to produce the R-PdII-B(OR)$_2$ intermediate during the transmetallation step and the subsequent reductive elimination affords the arylboronate along with the regeneration of the catalyst (Sch. 2.17). The reaction was performed in toluene in a microwave sealed tube for 4 hours[101] using [1,1′-bis(diphenylphosphino)ferrocene]dichloropalladium(II) complex with dichloromethane (Pd(dppf)Cl$_2$·CH$_2$Cl$_2$) as the catalyst. Flash chromatography afforded the desired species (**53**) in 60% yield.
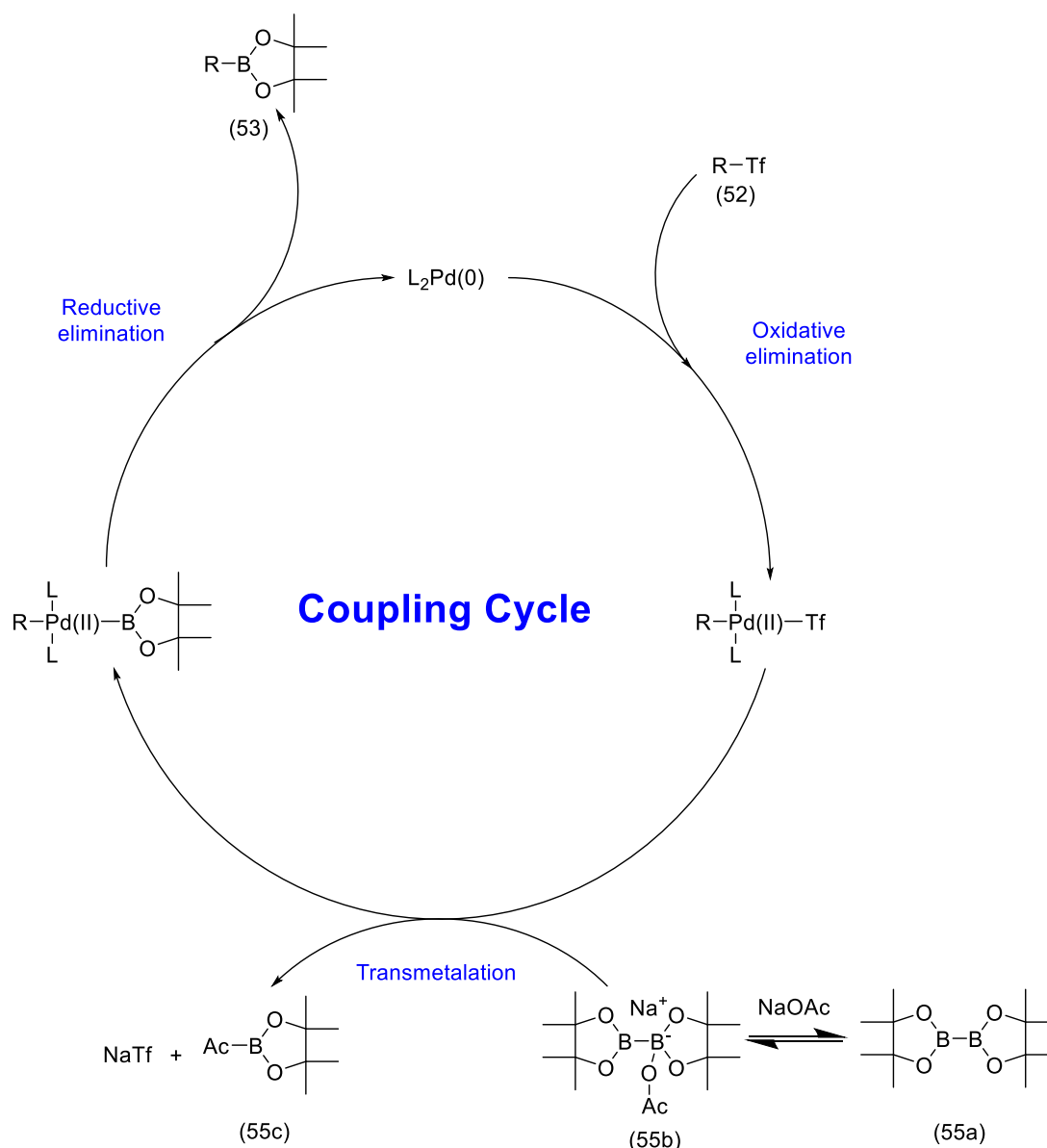
Scheme 2.17: Mechanism of coupling cycling using Pd(II)

Species (**53**) needed to be modified to introduce a carboxylic group to allow conjugation to the NP. To make this possible, the -NH on piperazine was deprotected[101] and then acylated with succinic anhydride[241] (Sch. 2.14). The reactivity of the anhydride allows the acylation to occur with no need for activation of the carboxylate with NHS and DIC. The boronated derivative (**53**) was treated with a solution of 15% of piperidine in acetonitrile at room temperature for 40 minutes. The deprotected species was dried under Ar and then chloroform and DIPEA were added

and the solution was cooled to 0°C. Succinic anhydride was added slowly. The reaction mixture was warmed to room temperature and stirred overnight. The solvent was removed under reduced pressure to give a pink solid. The desired product could not be purified from piperidine-Fmoc adduct (Fig. 2.13), as it decomposed on silica during column chromatography. The instability of the product on silica is also suggested by the 2D TLC shown in Fig. 2.14.
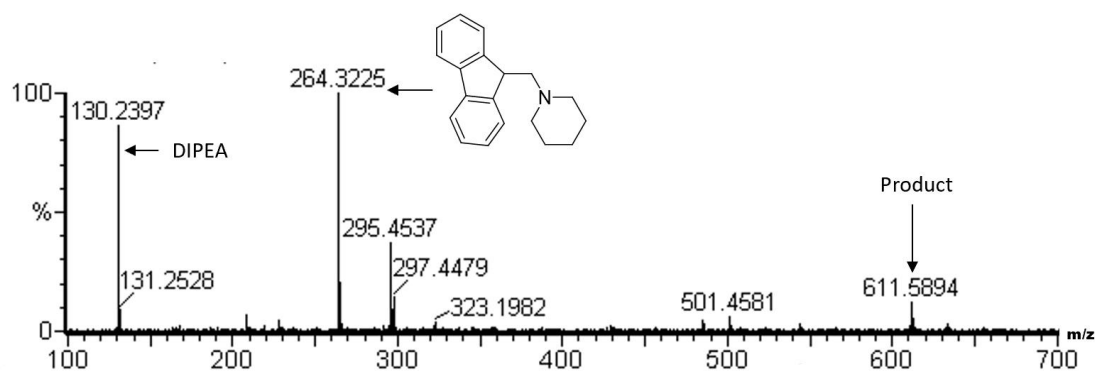
Figure 2.13: Mass spectra of crude (**54**) (ES+)
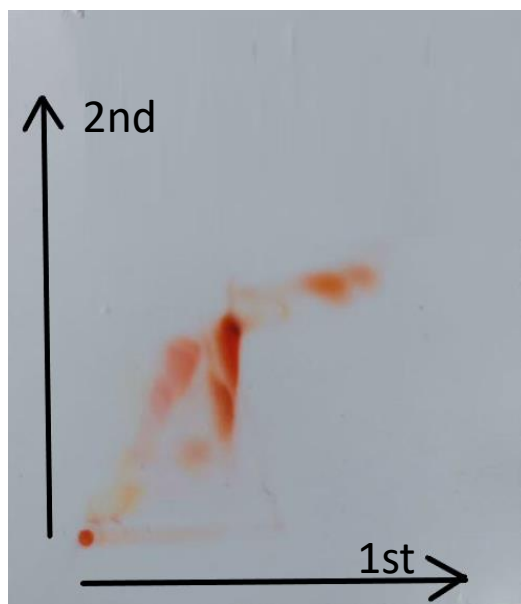
Figure 2.14: Bidimensional TLC of (**54**) with DCM/MeOH (9.5/0.5)

The unexpected instability of (**54**) on silica was inconvenient as it prevented us from purifying the final fluorescent sensor[101]. We set out to devise an alternative approach to add the boronated group and obtain the desired product as a pure species.

2.2.2. Modified peroxy yellow with a linker between boronated group and fluorescein

2.2.2.1. Synthetic approach
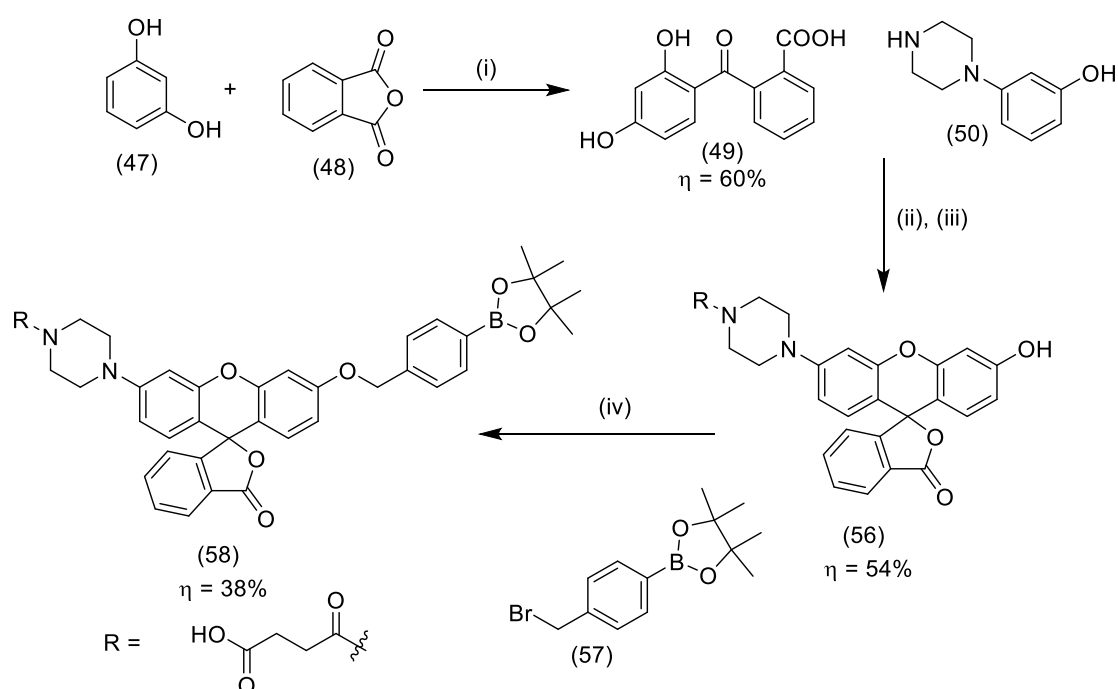
*Scheme 2.18: Reaction scheme for (**58**), (i) AlCl₃, nitrobenzene; (ii) TFA; (iii) succinic acid, DIPEA, DMF; (iv) (57), K₂CO₃, DMF.*

Following the challenges posed by the purification of (**55**) from the Fmoc and DIPEA adduct, we devised a variation on the previous synthetic approach that avoids Fmoc protection and deprotection steps (Sch. 2.18). The first step proceeds through a Friedel-Craft acylation as previously described[239], then the nitrogen on the piperazine is acylated with succinic anhydride to introduce the desired carboxylic group[101,241]. In

this approach the boronate group is introduced by nucleophilic substitution, attached to a benzoyl moiety, as outlined in Scheme 2.18. The boronate group guarantees that the molecule displays the desired reactivity towards hydrogen peroxide to reveal fluorescein (Sch.2.19)[242–244]. In addition, this synthetic approach has the advantage of being shorter with fewer steps and avoid the triflation and palladium catalysed coupling steps.
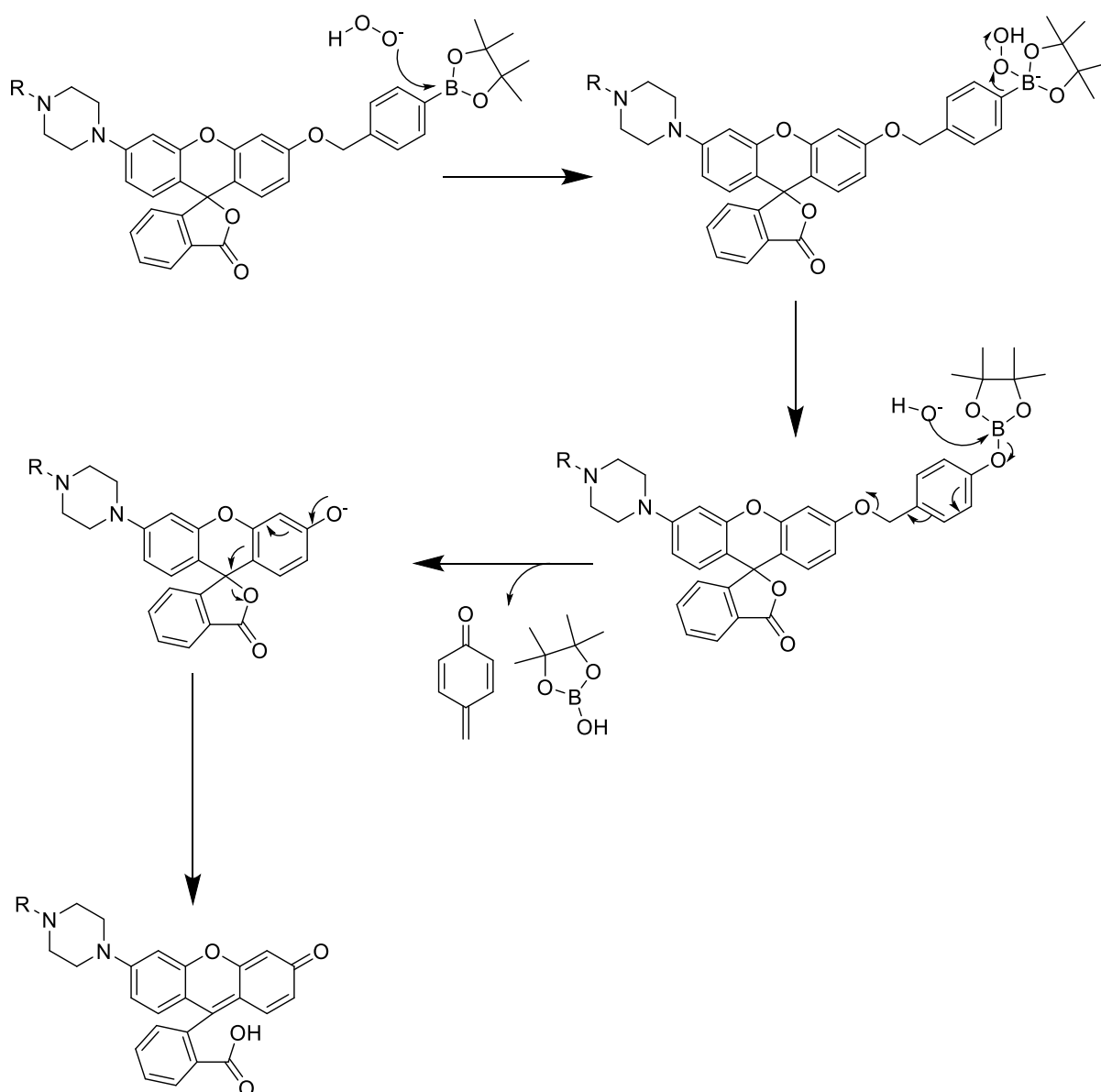
*Scheme 2.19: Mechanism of reaction of (**58**) with hydrogen peroxide[243]*

The Friedel-Craft adduct (**49**) reacts with phenol (**50**) in TFA as described previously[101] to give the fluorescein scaffold. Acylation with succinic anhydride in the presence of DIPEA led to the formation of (**56**) as a red solid in a yield of 54%. This synthetic approach was higher yielding than the one leading to (**51**), which afforded the target compound in 42% yield. Introduction of the boronate was achieved through a nucleophilic substitution of the phenolic oxygen in (**56**) on boronated benzyl bromide (**57**). The reaction was carried out in DMF in the presence of potassium carbonate at room temperature to give a red sticky solid (**58**) in 38% yield.

Although compound (**58**) showed sign of degradation on silica (*e.g.,* multiple spots on TLC), its isolation from the reaction mixture is easier and the whole process is higher yielding (overall 12% yield *vs.* 6% to obtain (**54**)). The molecule was stored in freezer under nitrogen to minimise exposure to air and potential degradation at room temperature.

2.2.2.2. <u>Spectroscopic characterisation</u>

The absorption and emission behaviour of the sensor were investigated. The excitation and emission maxima are at 515 nm and 540 nm respectively, which are in line with those reported in the literature (518 nm and 548 nm for peroxy yellow) (Fig. 2.15)[238].
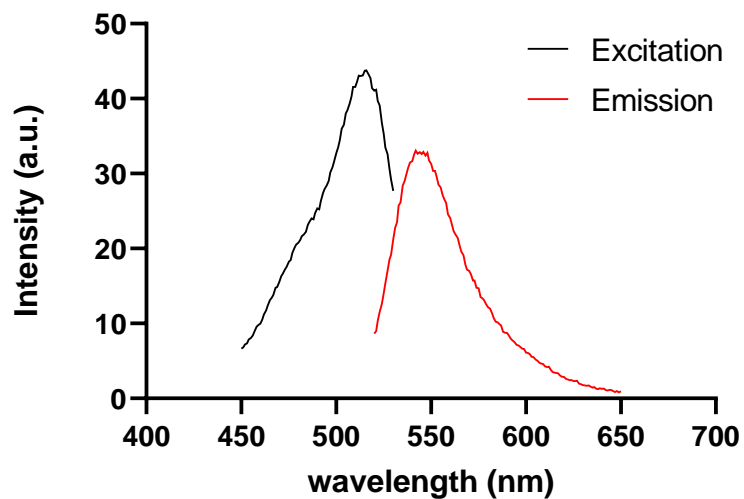
*Figure 2.15: Excitation and emission of sensor (**58**)*

A preliminary test of the responsiveness of this sensor (**58**) to hydrogen peroxide was carried out in the presence of different amounts of hydrogen peroxide in buffered aqueous solution (PBS, pH = 7.4)[242]. The fluorescence spectra at different concentrations of hydrogen peroxide were recorded at 544 nm (Fig. 2.16).
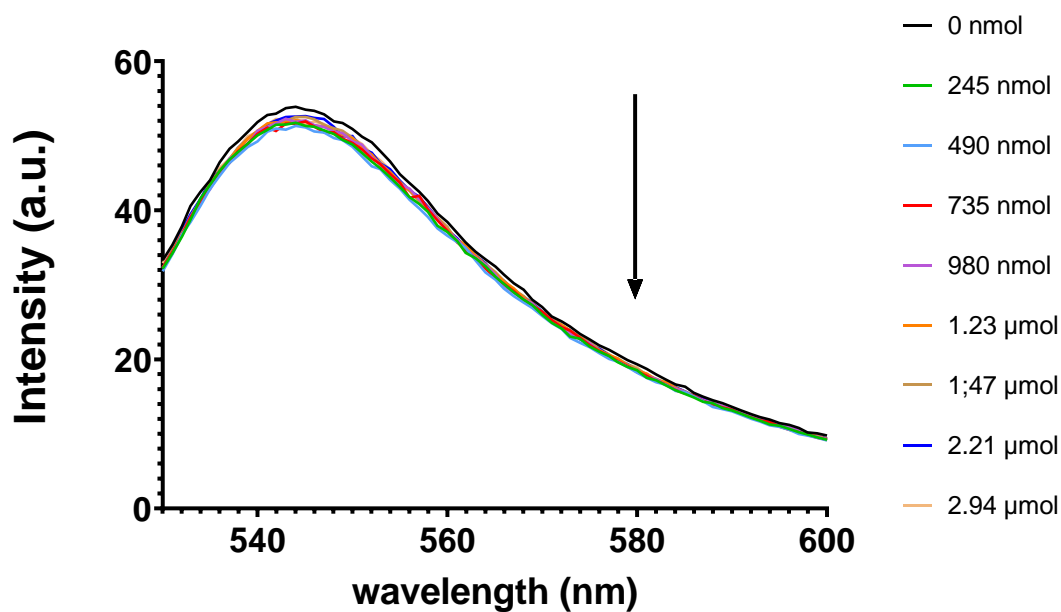
Figure 2.16: Example of the fluorescence emission with increasing hydrogen peroxide concentration

Unexpectedly, we observed a very slight decrease of the intensity of emission, which is in contrast with the behaviour reported in the literature[101].

It has been reported that pH has a considerable influence on fluorescein emissive behaviour, resulting in changes of both absorption/emission wavelengths and intensity of emission (Fig. 2.17)[245]; this is ascribed to the presence of the carboxylic group on the molecule. Because we carried out the experiments in buffered solution, we were able to rule out the influence of the pH on our measurement.
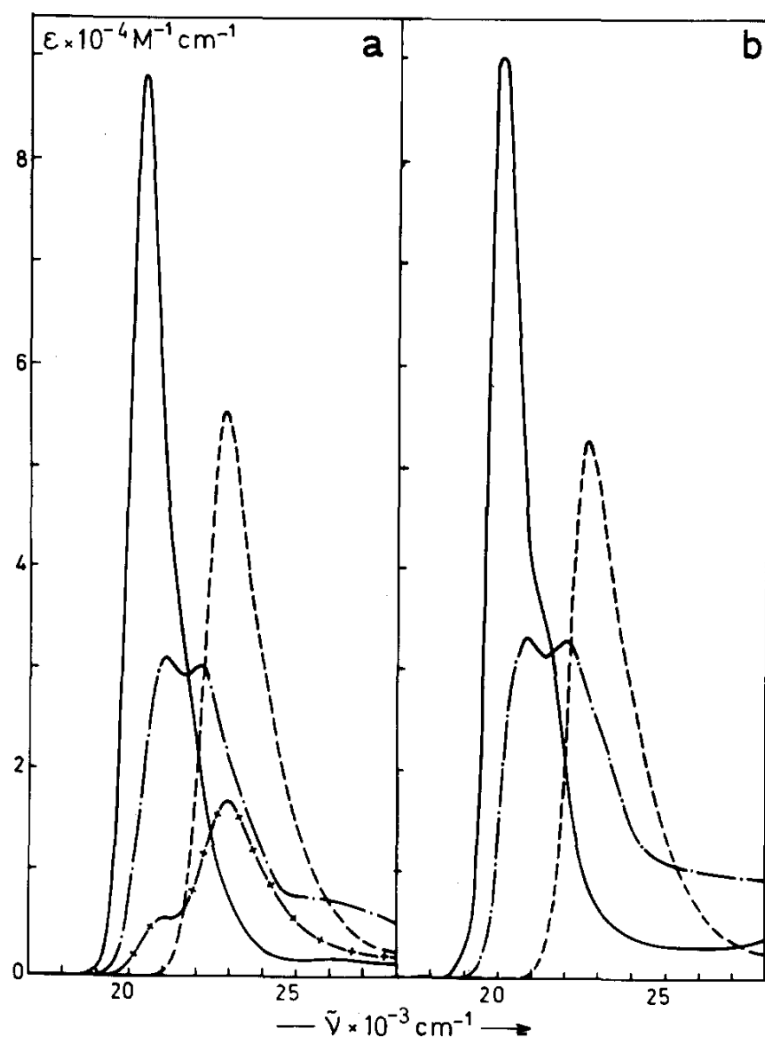
Fig. 1. (a) Absorption spectrum of fluorescein in aqueous solution: ——— pH 12, —·—·— pH 5.5, — x— x pH 3.3 and — — — — 1 M H_2SO_4. (b) Absorption spectrum of HPF in aqueous solution: ——— pH 10.2, —·—·— pH 4.8 and — — — — pH 1.6.

Figure 2.17: pH dependence of fluorescein (a) and HPF (b) absorption[245].

Crucially, performing repeated measurements on the same sample we observed a similar reduction of intensity of emission (Fig. 2.18)[101]. This led us to hypothesise that the decrease in emission intensity may arise from the tendency of fluorescein to bleach upon irradiation in the presence of hydrogen peroxide[246].
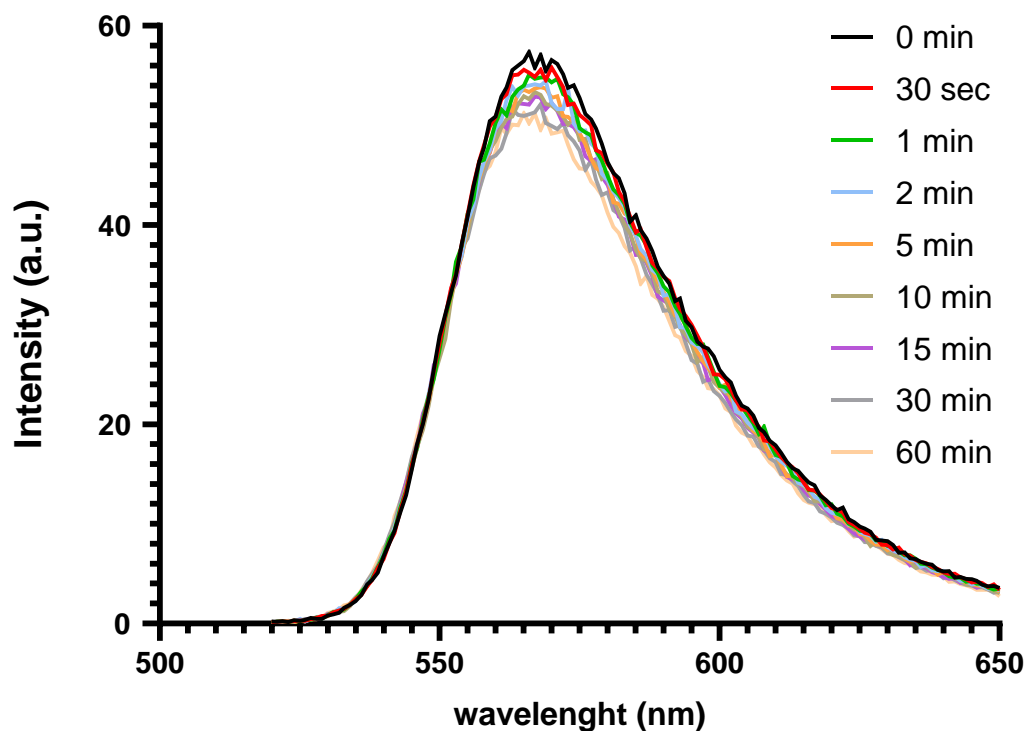
Figure 2.18: Example of the fluorescence emission with 980 nmol of hydrogen peroxide depending on time of exposure

Mass spectra (Fig. 2.19) taken before and after the reaction with a large excess hydrogen peroxide and shows that (**58**) has disappeared ([mass + K$^+$]: 753.3179) and rhodol ([M + Na$^+$]: 353.2903) has formed.
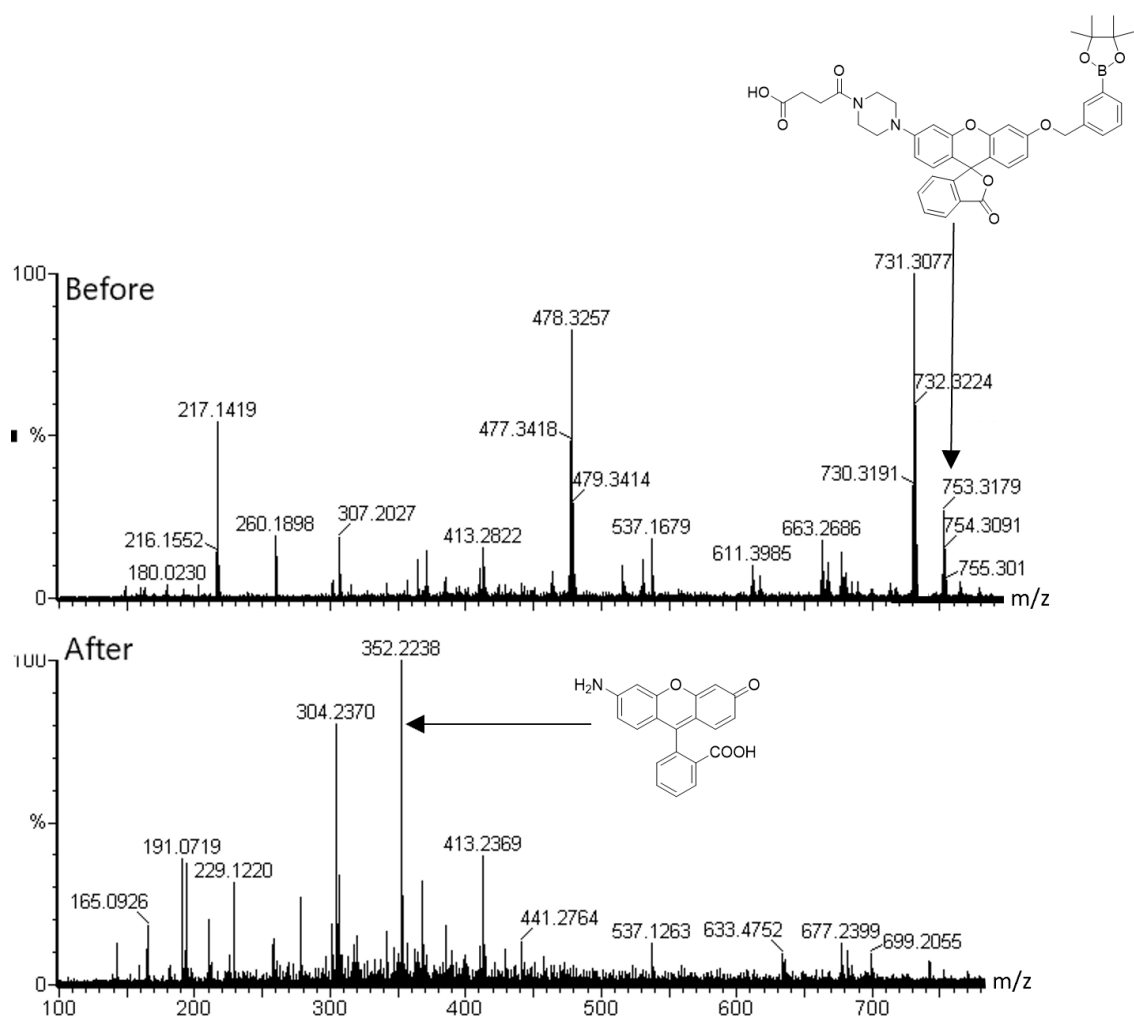
*Figure 2.19: Mass spectra of (**58**) before and after reaction with hydrogen peroxide (ES+)*

A further hypothesis to explain the degradation could involve the formation of a quinone structure from fluorescein, a behaviour that was reported in the literature (Fig. 2.20)[247], although we did not find evidence of the putative compound (**58a**) on the MS spectra. We were unable to isolate the individual components present in the solutions of probe and hydrogen peroxide, which prevented analysis by NMR to further elucidate the mechanism of degradation underpinning the decrease in fluorescence emission. Further mechanistic investigations were not pursued but the emissive behaviour in

81

response to hydrogen peroxide was evaluated for this sensor conjugated to a polymer, as discussed later in this work (chapter 3).
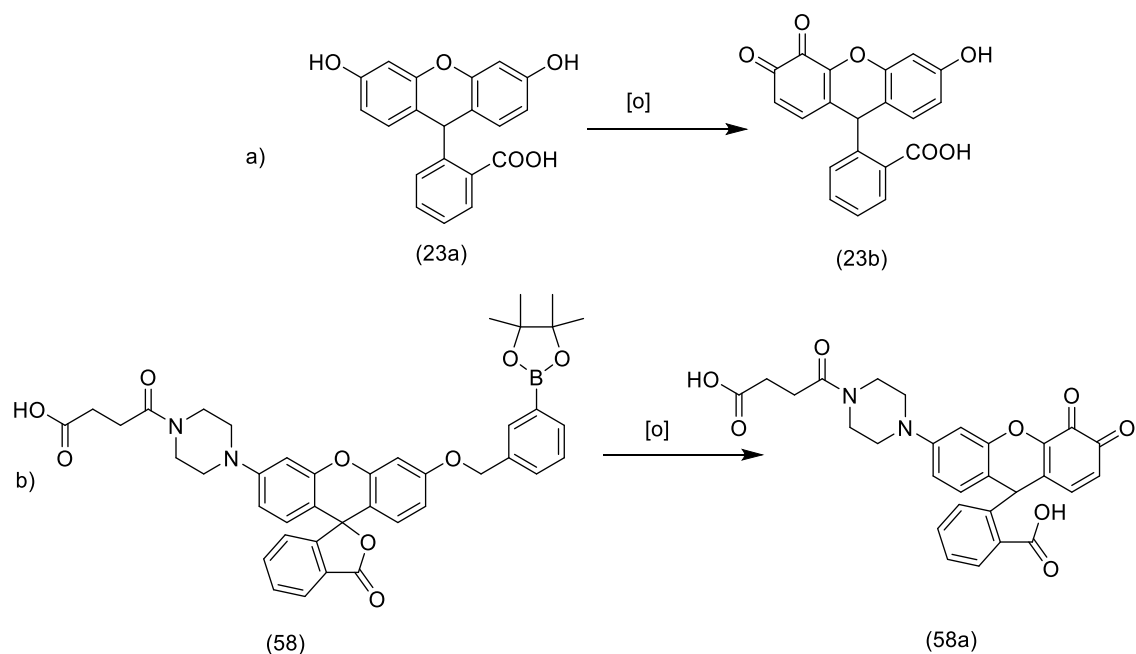
*Figure 2.20: Oxidation of fluorescein (a) and hypothesis for (**58**) (b)*

With compound (**58**) we achieved our goal to synthesise a boronated fluorescein probe endowed with a carboxylic group to allow conjugation to amino-functionalised polymeric nanoparticle matrices. Probe (**58**) was designed following the major shortcoming of the initial target probe (**54**), namely its instability on silica, which prevented its purification. Probe (**58**) offers the advantage of a shorter synthesis (three *vs.* five steps) and although it still displays an unsatisfactory stability on silica, it can be isolated and purified by crystallisation. In the presence of hydrogen peroxide, (**58**) displays an unexpected loss of intensity of fluorescence emission, a behaviour that could not be fully rationalised but that could be ascribed to degradation of the

fluorescein moiety. The conjugation of the sensor with the NPs could be advantageous to limit or slow down the degradation of the sensing moiety.

2.3. Singlet oxygen

As discussed in chapter 1 (section 1.1.6), DMAX was our initial target scaffold for singlet oxygen detection. The synthetic approach to obtain analogues of DMAX (DPAX[248] or Aarhus Sensor Green[130]) are reported in the literature, but the main challenge for us was to incorporate a functional group suitable for conjugation that display no cross-reactivity with ligation approaches involving the groups present on (**48**) and (**53**) (Fig 2.21). Our goal was to insert an aldehyde moiety to allow conjugation to NPs functionalised with an oxyamino group.
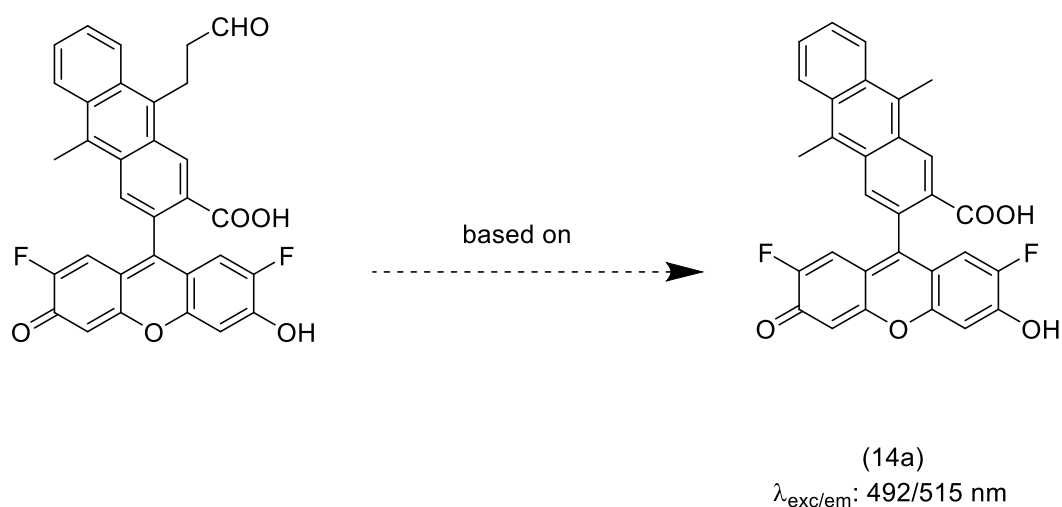
*Figure 2.21: Design of desired molecule from (**14a**)*

2.3.1. Modified DMAX

2.3.1.1. Synthetic approach

The synthetic strategy to obtain the target species is based on reported approaches to obtain DMAX-based sensors (Sch. 2.20). Although the synthetic route to DMAX-based species has been described by the Nagano group[129], our approach deviated

considerably from the published syntheses because of the need to introduce a conjugatable function. In particular, our challenge was to introduce two different groups on positions 9 and 10 of the anthracene moiety in DMAX.
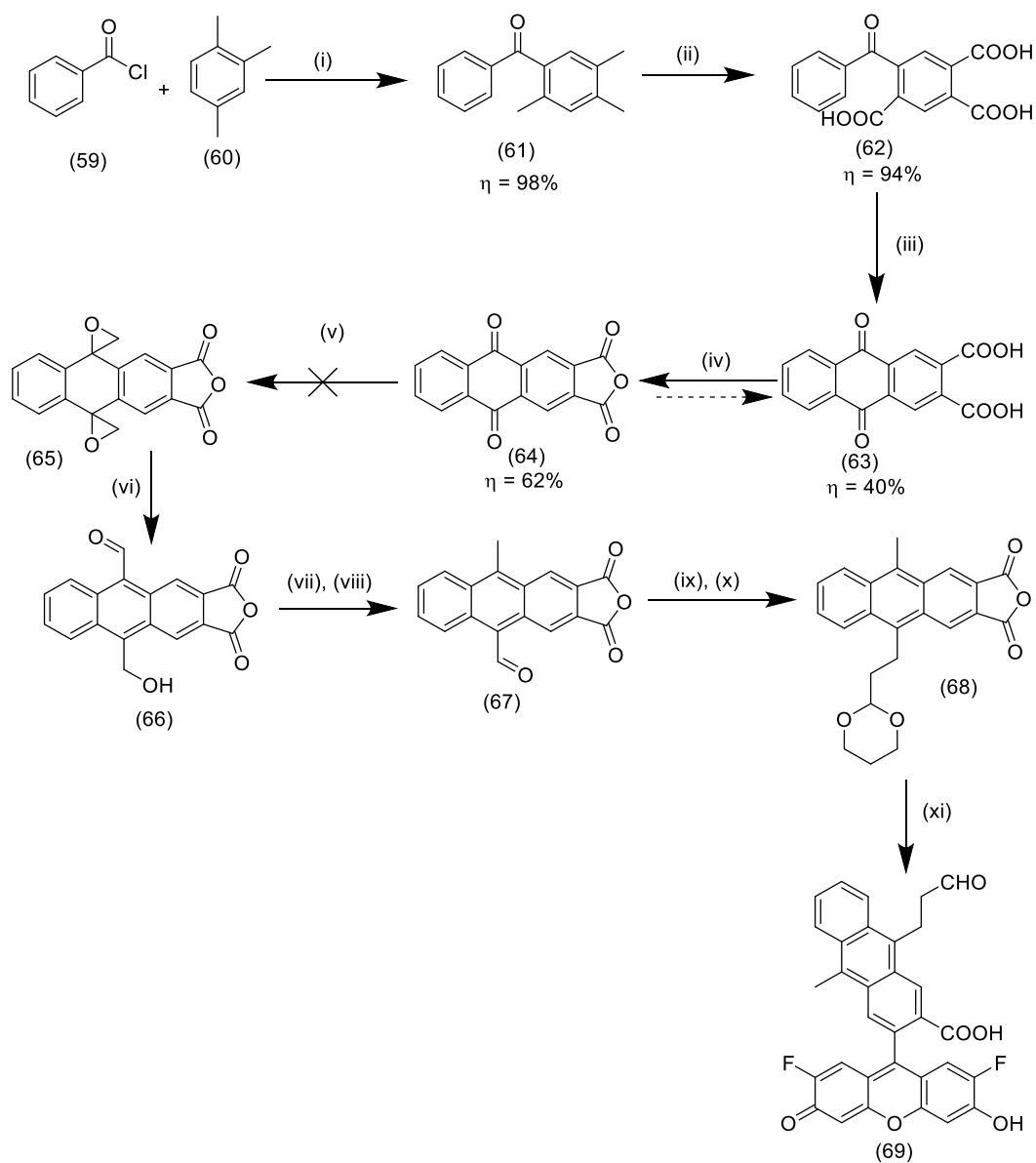
Scheme 2.20: Proposed synthetic approach for modified DMAX (69). (i) AlCl₃, DCM; (ii) KMnO₄; (iii) H₂SO₄; (iv) acetic anhydride; (v) SMe₃I, NaH, DMSO, THF; (vi) LiCl; (vii) Zn/HCl, (viii) PCC; (ix) diethyl (2-(1,3-dioxan-2-yl)ethyl)phosphonate; (x) H₂, Pd/C; (xi) 4-fluorobenzene-1,3-diol

Firstly, we envisaged to perform a Friedel-Craft acylation of benzoyl chloride (**59**) on trimethylbenzene (**60**) to obtain (**61**)[249]. The product would then be oxidized to the corresponding tricarboxylic derivatives[249] and treated with strong acid to give quinone (**63**)[249]. The two free carboxylic group would be transformed in the corresponding anhydride and treatment of the quinone anhydride with trimethylsulfonium iodide would afford the bis-epoxide in position 9 and 10[250,251]. Lithium chloride would then be used to open epoxide to form an anthracene bearing an aldehyde and an alcohol by Meinwald rearrangement[250]. This step would give the desired differentiation of reactivity of positions 9 and 10 on the anthracene. The aldehyde group would be then reduced to a methyl group *via* a Clemmensen reduction[252] and the primary alcohol would be oxidised to the corresponding aldehyde by treatment with pyridinium chlorochromate[253]. In order to increase the distance between the anthracene moiety and the conjugation site, which could sterically hinder the ligation to the nanoparticle, a Wittig-Horner would be carried out to install the desired protected aldehyde group farther away from the fluorophore[254]. Finally, the scaffold of DMAX would be obtained through a Friedel and Craft according to procedures described in the literature[130].

Following this strategy, benzoyl chloride and 1,2,4-trimethylbenzene were treated with AlCl$_3$ under Friedel and Craft conditions (Sch. 2.20)[248,249,255] to give the desired product (**61**) in 98% yield.

Different approaches to oxidise (**61**) are available (Sch. 2.21). The first we explored[256] relied on the use of KMnO$_4$ as the oxidant, which unfortunately gave a very low yield. A two-step method was then attempted, which relied on the reaction of (**61**) with HNO$_3$ in water at reflux for 5 days, followed by the treatment of the resulting yellow solid with KMnO$_4$[249,255]. This approach did not give the desired product. Finally, we were able to

achieve the target triacid by carrying out the oxidation with KMnO$_4$ in pyridine at 50°C for 5 days[257].
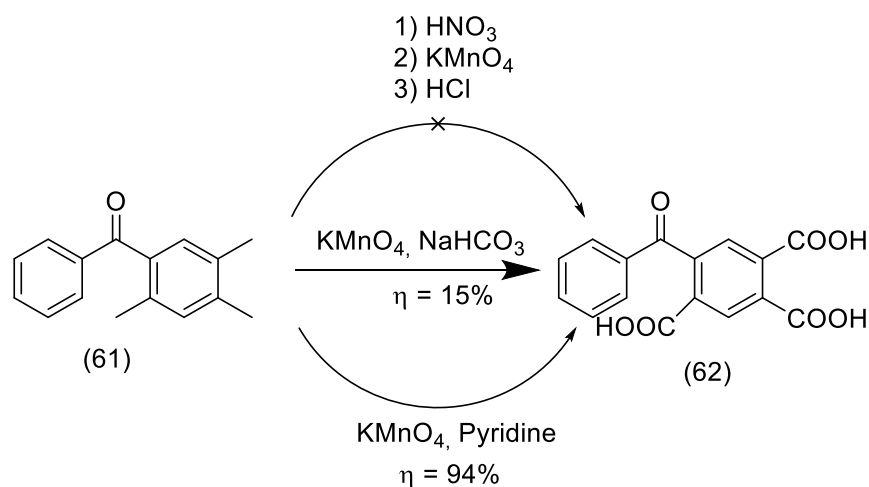
Scheme 2.21: Oxidation of (61)

Ring closure of (62) occurs *via* treatment with a strong acid: heating the starting material at reflux in concentrated H$_2$SO$_4$ for 3 hours afforded a brown solid from which the desired compound was isolated in 2% yield. We attributed this low yield to the fact that the previous steps were carried out on the crude products[248,249,255,258]. The highly hydrophilic products of the previous steps were challenging to purify due to the presence of two/three carboxylic groups, a considerable difference from the unsubstituted ring described in the literature[248,249]. A possible approach to overcome this challenge could involve the esterification of the carboxylic groups to make the products more amenable to purification by column chromatography on silica, followed by a base-catalysed hydrolysis on the purified species. Although this strategy would allow purification, we decided not to pursue it as it would add two synthetic steps and depending on the yields and could easily result in no overall advantage. We reasoned that despite the low yield, the approach we followed provided the desired compound (63) in sufficient amount to continue the synthesis. Before progressing further with the

synthesis, the carboxylic groups of (**63**) were protected as the phthalic anhydride (Sch. 2.20)[259] to avoid the reaction with sodium hydride and the methylating agent Me₃Si, as this would result in the formation of an ester. To perform this step (**63**) was treated with anhydrous acetic acid for different periods of time (1.5h, 4h and 1 day) in carefully dried glassware. After 24 hours, 62% of the desired species was obtained. We found that the hydrolysis to the parent dicarboxylic acid was very easy, so we stored the compound in vacuum at 35°C to ensure removal of water without causing degradation on the compound.

As mentioned above, epoxidation and treatment of the resulting species with LiCl is a viable strategy to differentiate the reactivity of the two carbonyl functions on the anthracene moiety. The epoxidation has been reported in the literature on non-substituted and dibromo-substituted anthracene quinones[250,251,260–264], and it occurs in the presence of SMe₃I following deprotonation with sodium hydride to give the sulfonium ylide (Sch. 2.22).
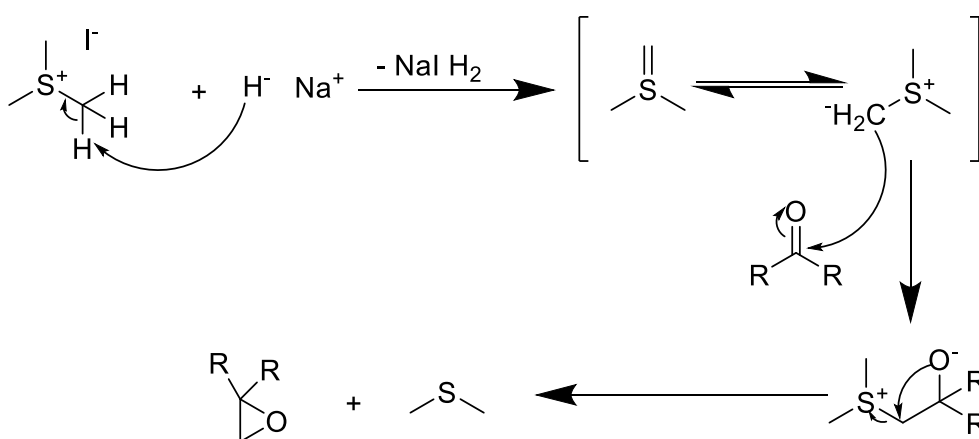
Scheme 2.22: Corey-Chaykovsky epoxidation mechanism[251]

We attempted the reaction on our substrate according to the procedure reported by Ciaccio *et al.*, which involves the treatment of anthraquinones with 3 molar equivalents

of NaH and SiMe₃I, but unfortunately the desired product was not obtained. This was deduced from the fact that the expected mass for the target species at 306 was not present on the mass spectra of the crude (Fig. 2.22): the presence of a peak at m/z = 281 indicated the reduction of the anthraquinone to anthracenediol. We speculate that it occurs by action of sodium hydride as a base, nucleophile and a reducing agent (Sch. 2.23)[265].
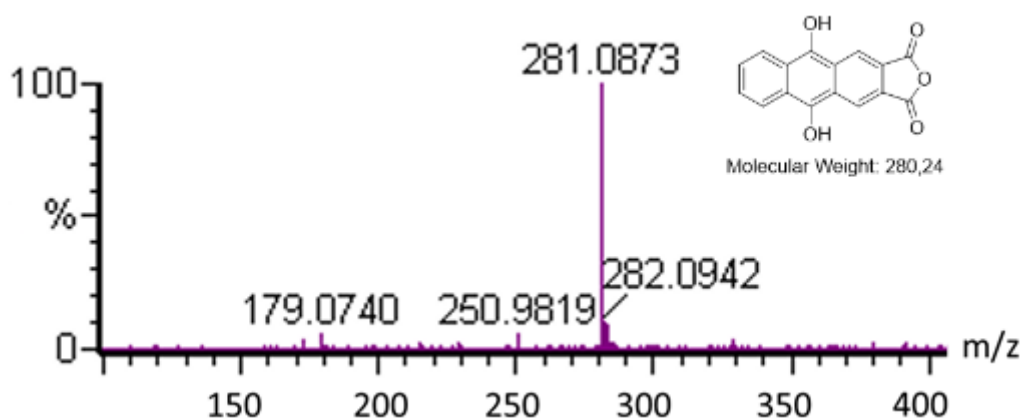
Figure 2.22: Mass spectra after epoxidation (ES+)
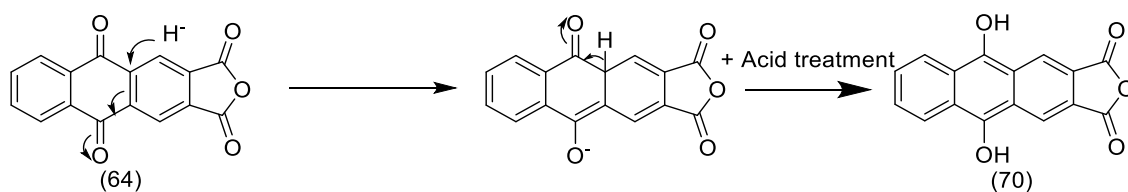
Scheme 2.23: Hypothetic reactional mechanism to form anthracenediol[265]

Repeated attempts to perform this reaction using different ratios and molar excess of the reagents led to the same results. We concluded that the presence of the two carboxylic functions alters the reactivity of the quinone groups compared to the one reported for the dibromoanthraquinone[248].

An alternative synthetic strategy to obtain the target structure would involve the use of 2,3-dibromo-9,10-anthraquinone to perform the functionalisation of positions 9 and 10

as indicated in Scheme 2.24, and subsequently introducing the carboxylic groups as cyanide group. We did not undertake the approach due to the Health and Safety implications of performing the reaction[248].
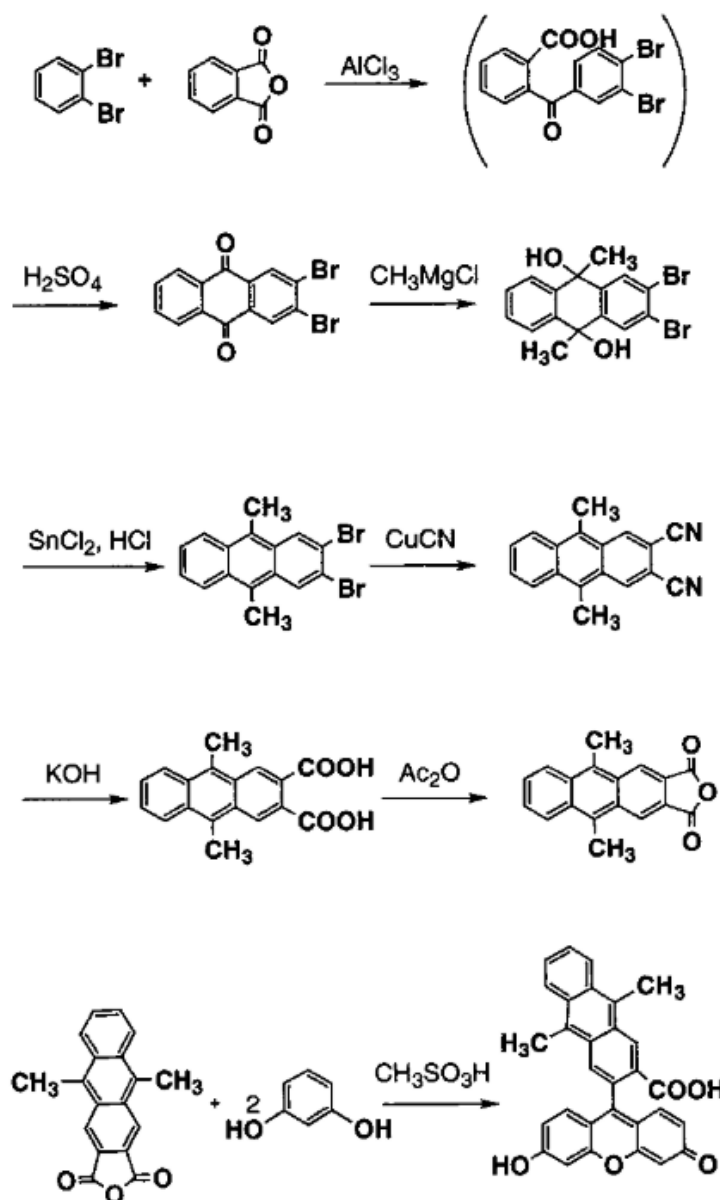
Scheme 2.24: Other synthetic approach to obtain DMAX[248]

We then explored the possibility of introducing the target aldehyde group on the anthraquinone through a Wittig reaction[266]. We treated (**63**) with potassium tert-butoxide and (4-carboxybutyl)triphenylphosphonium bromide. We used only one

equivalent of the latter reagent because our aim was to functionalise only one carbonyl group. Unfortunately, we observed no reaction and we were only able to recover unchanged (**63**) from the reaction mixture.

2.3.2. <u>Modified DMA</u>

In view of the challenges encountered in the synthesis of a functionalised DMAX derivative, we changed our target singlet oxygen sensor to a DMA derivative (Fig. 2.23). Keeping in mind that the target sensor should emit at a different wavelength as the other species so far obtained, (X) and (Y), and that it needs to bear a functional group suitable for conjugation, our choice for the fluorophore fell on 9,10-dimethylanthracene for both its reactivity and its blue fluorescence. A major difference between this sensor and the fluorescein-based sensors is that the intensity of its fluorescence emission decreases upon reaction with singlet oxygen[3]. As the reactive functionality for conjugation with the polymer we chose to insert a carboxylic group.
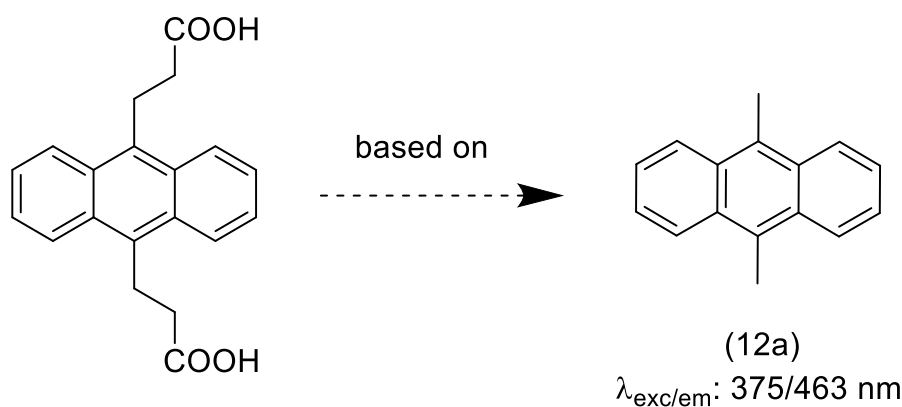
*Figure 2.23: Design of desired molecule from (**12a**)*

90

2.3.2.1. <u>Synthetic approach</u>

Although it would be possible to attempt the epoxidation on anthraquinone[263], we chose to follow a simpler synthetic approach because of time constraints. We envisaged introducing a carboxylic group as for the hydrogen peroxide sensor on only one or both methyl groups on the DMA. To achieve that, the methyl group(s) will be brominated[267] and then reacted with malonic acid[268] to give the modified DMA (Sch. 2.25).
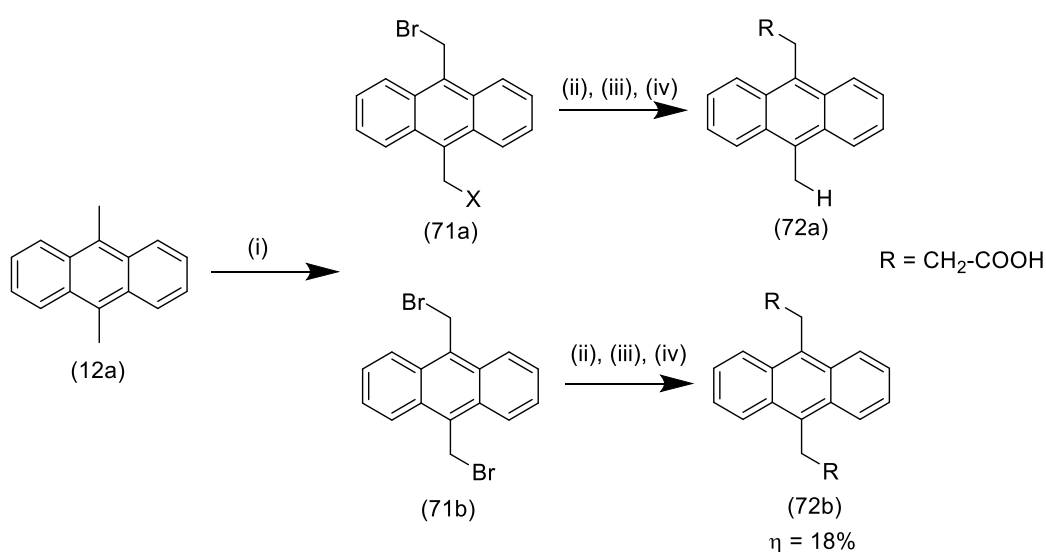
*Scheme 2.25: Synthetic approach for (**72a**) and (**72b**). (i) NBS, AIBN, AcCN; (ii) Na, EtOH, diethyl malonate; (iii) NaOH, MeOH, CHCl3, (iv) heat.*

Firstly, we attempted the bromination on only one of the methyl groups, using the conditions reported by Andrus *et al.*[267]. To this end, DMA was treated with one equivalent of NBS in presence of a catalytic amount of AIBN in AcCN at reflux. This approach led to the formation of mono- and di-substituted derivatives as well as unreacted DMA, in a mixture that proved laborious to resolve. To circumvent this problem, the reaction was modified by increasing the equivalent of NBS to 2.5 (Sch.

2.25) to favour the formation of the di-substituted derivative (**71b**), which was obtained with a yield of 98%.

Insertion of the carboxylic acid was carried out by displacement of the bromides with diethyl malonate. The reaction exploits the relative acidity of the alpha methylene to generate the corresponding carbanion. Following Martinez *et al.* procedure (Sch. 2.26)[268,269], diethyl malonate was treated with sodium ethoxide, generated from sodium in absolute ethanol. Following addition of the brominated DMA (**71b**) the mixture was refluxed for 4h. Saponification was carried out by NaOH in MeOH. After the reaction, the solution was acidified to pH = 1 by using concentrated HCl to precipitate the product. After filtration, spontaneous decarboxylation was achieved by maintaining compound (**76**) under vacuum at 120°C for 5 days to give a light green solid with 18% of yield. The sensor was stored under nitrogen in the freezer.
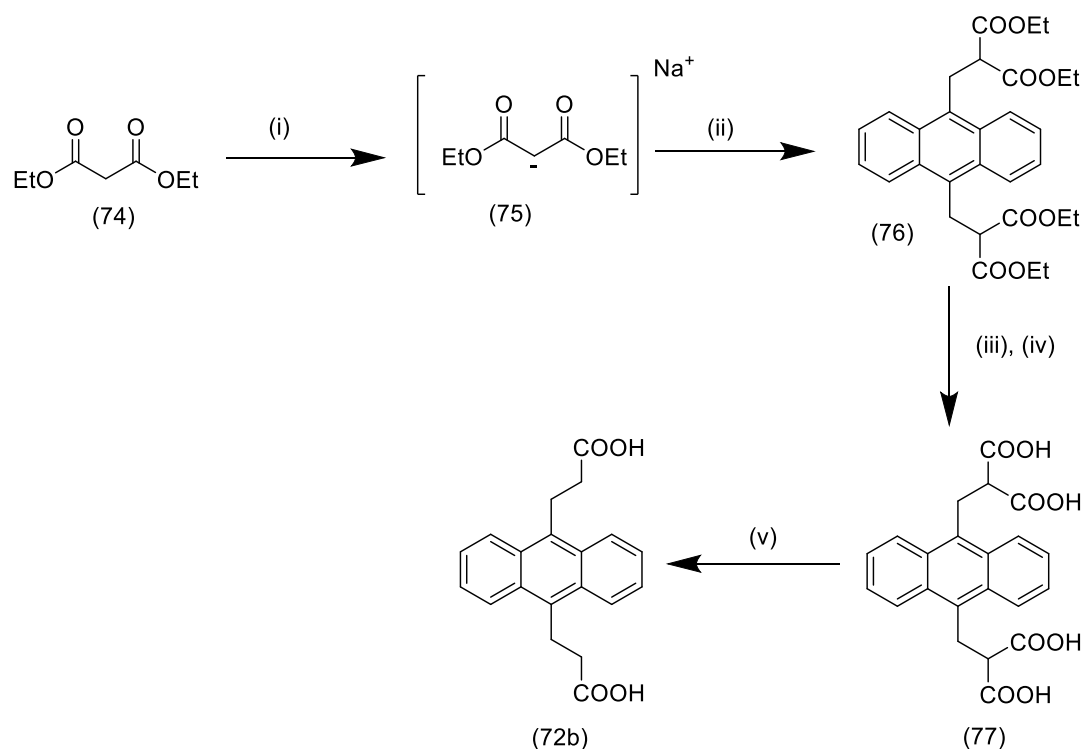
*Scheme 2.26: Malonic synthesis. (i) Na, EtOH; (ii) (**72b**), benzene; (iii) NaOH, MeOH, CHCl₃, (iv) HCl; (v) 120°C, under vacuum, 5h.*

2.3.2.2. <u>Spectroscopic characterisation</u>

The absorption and emission profile of compound (**72b**) were studied. Excitation and emission maxima were found at 325 nm and 425 nm (Fig. 2.24), which are in line with the values reported in the literature (375 and 436 nm)[3]. This molecule absorbs in UV and is blue fluorescent.
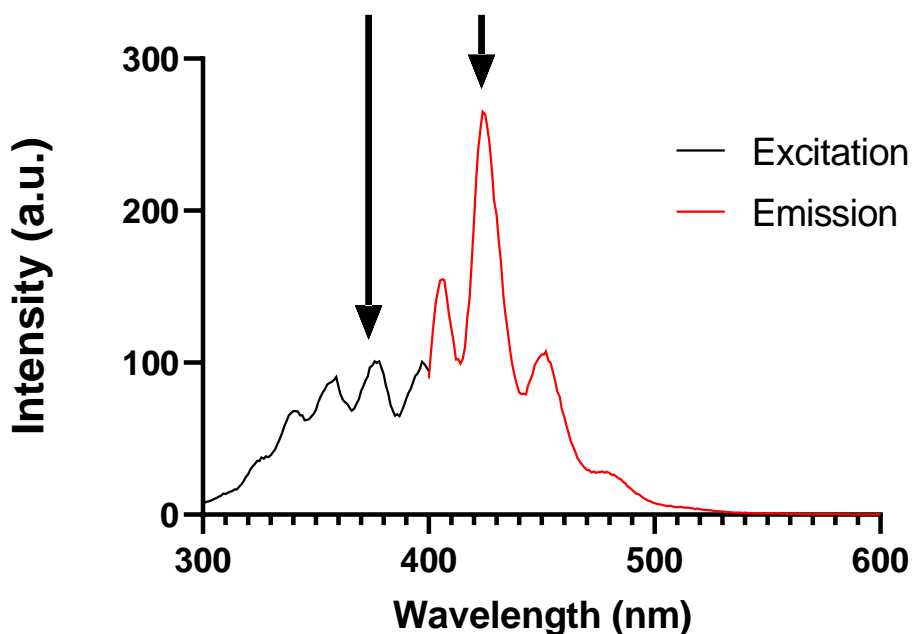
*Figure 2.24: Excitation and emission of sensor (**72b**)*

Preliminary studies of the responsiveness of this sensor to singlet oxygen were carried out in the presence of a photosensitiser with irradiation. Rose Bengal is often considered the photosensitiser of choice to perform these studies because of its high photodynamic efficiency[270]. In our case, though, Rose Bengal is not an ideal photosensitiser because it displays an absorbance band at 470 nm: as shown in figure 2.24, and DMA emits at this wavelength. A very efficient class of photosensitisers that absorb at favourable wavelengths are porphyrins. For this reason, we chose 5,10,15,20-*tetrakis*-(*N*-methylpyridinium-4-yl)porphyrin tetrachloride zinc(II) complex (Fig. 2.25), which has an intense absorption at *ca.* 400 nm and is efficient in promoting the generation of singlet oxygen[271].
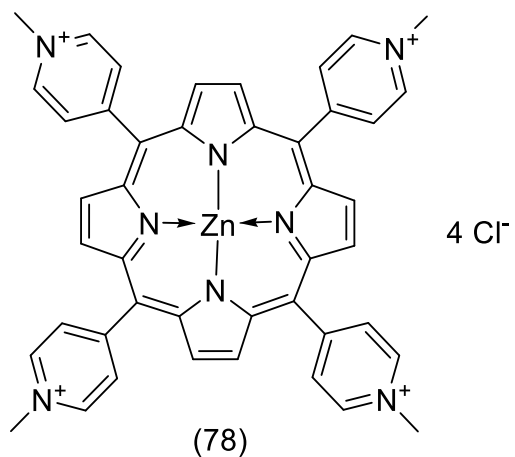
Figure 2.25: Zn-porphyrin complex

Thus, a solution containing both compound (**72b**) and the photosensitiser was irradiated with blue light (400 nm) and the emission spectrum of (**72b**) was recorded at 425 nm (Fig. 2.26a and 2.26b).
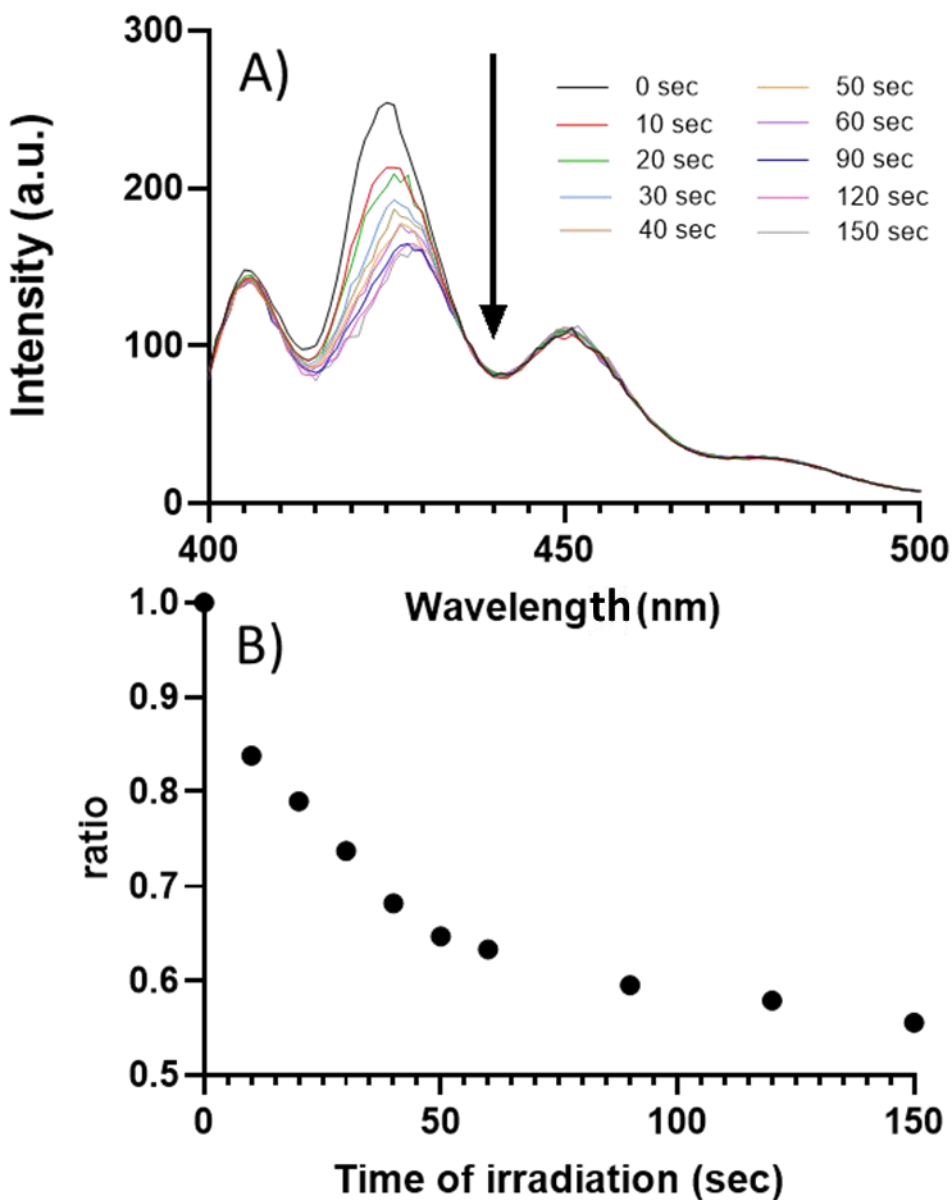
Figure 2.26: Example of fluorescence emission of sensor (73b) with singlet oxygen. Spectra (A) and plot of normalised fluorescence (B).

As expected, when exposed to singlet oxygen, the fluorescence intensity of (**72b**) decreases (Fig. 2.26a). Figure 2.26b, shows that the decrease is more marked at the beginning than at the end that is going to the limit of detection. This behaviour may be explained taking into account the consumption of DMA after 50 seconds[272].

2.4. <u>Chapter conclusion</u>

We successfully obtained two new species (**43**) and (**58**) and one known molecule (**72b**) with the structural features of ROS sensors and with suitable functional group to perform the conjugation to the polymers.

Attempts to obtain functionalised HE (**28**) failed, therefore an alternative dianthrafluorescein-based sensor for superoxide was designed and synthesised. Phosphonated dianthrafluorescein (**43**) was provided with an azide group to allow NPs conjugation based on the CuAAC reaction.

After a failed attempt to obtain a hydrogen peroxide sensor bearing a boronate group directly attached to the fluorescein skeleton (**54**), a suitable sensor bearing the boronate group attached to a benzoyl linker was obtained. This modified fluorescein sensor (**58**) was functionalised with a carboxylic acid.

The synthesis of a singlet oxygen sensor based on DMAX (**69**) was attempted but not achieved because of the difficulty to achieve reaction on a single carbonyl of the anthraquinone moiety (epoxidation or Wittig reaction). An alternative singlet oxygen responsive species based on dimethylanthracene derivative bearing a carboxylic group was obtained (**72b**).

The new sensors showed promising fluorescent behaviour. In fact, despite a dependency of the signal on pH, we observed for (**43**) an increase of the intensity of emission when the concentration of superoxide increased. But no major pH variations are expected in the cell, with or without ROS, so the impact of the pH dependency of the emission on the sensing process may be limited. The responsiveness of the sensor (**58**) to the target analyte was unexpected, as it resulted in a small decrease in emission

97

intensity, but conjugation to a polymer will be undertaken to study the behaviour of the conjugate in the presence of hydrogen peroxide. The expected fluorescent behaviour of the sensor (**72b**) was observed with the presence of singlet oxygen.

Fig 2.27 reports the excitation and emission profiles of (**43**), (**58**) and (**72b**). The emissions of (**43**) and (**58**) partially overlap and the emission spectra of (**72b**) is close to the excitation wavelength of (**43**), so (**43**) may absorb light emitted from (**72b**). This characteristic will be analysed in the next chapter.
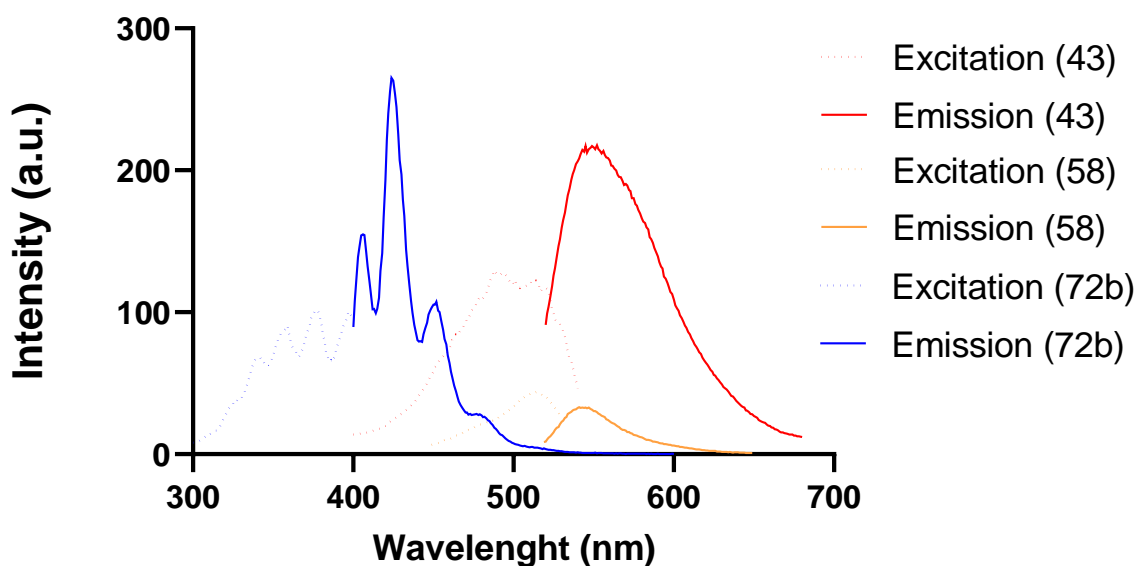
*Figure 2.27: Excitation and emission range of (**43**), (**58**) and (**72b**)*

Chapter 3. <u>Synthesis and fluorescence behaviour of nanosensors</u>

Following the synthesis of the molecular sensors, we turned our attention to the synthesis of polymer conjugates of the sensors to obtain the target NPs (nanosensors). The initial idea was to make PLGA NPs containing three different functionalities for orthogonal conjugation of the various sensors (**43**, **58** and **72b**) (Fig 3.1). As illustrated in Chapter 2 (section 2.1 and 3.1), both the modified DMA and the modified POY display carboxylic acid group. Although it would be possible to modify either of these by introducing a heterobifunctional linker[273], we chose to carry out the conjugation of each single sensor to the polymer and then use a mixture of the different conjugates to obtain the target nanoparticles. For the polymeric matrix of the nanoparticles we chose PLGA, a biocompatible and biodegradable polymer that allows straightforward functionalisation. This Chapter also discusses the analysis of the nanosensors responsiveness (fluorescence and selectivity) to the presence of the different ROS analytes.
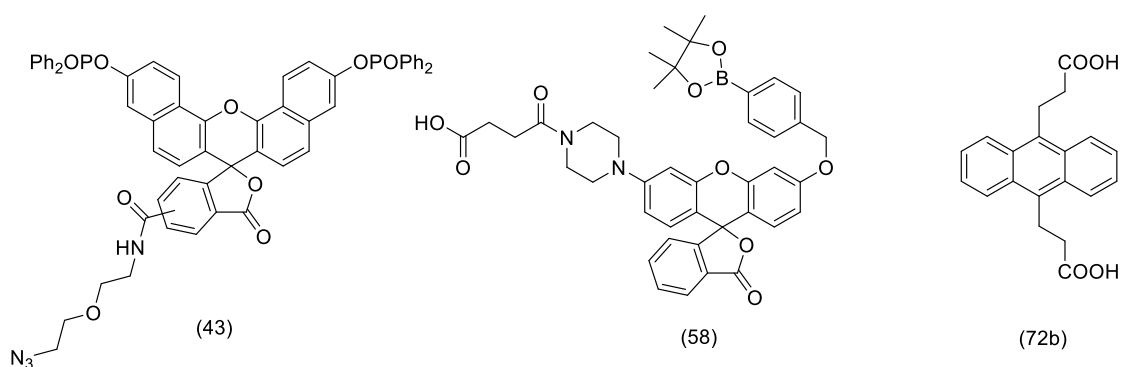
Figure 3.1: Three synthesised sensors used for conjugation with NPs

3.1. <u>Conjugation between PLGA and molecular sensors</u>

PLGA is a polymer commonly used in medicine and drug delivery as reviewed in the first chapter (Fig. 3.2)[151,159,164,165,274–277]. It is approved by the United States of America Food and Drug Administration (FDA) because of its biodegradability and biocompatibility. PLGA is a co-polymer composed of lactic acid and glycolic acid. Depending on the ratio of lactic-to-glycolic acid, the properties of PLGA can be tuned to meet the requirements of a variety of applications, giving this polymer a great versatility[162]. The end-groups of the PLGA chain are a carboxylic group and a primary alcohol, both of which can be exploited for conjugation. Strategies for the derivatisation of the single COOH on the chain are widely reported in the literature[274].
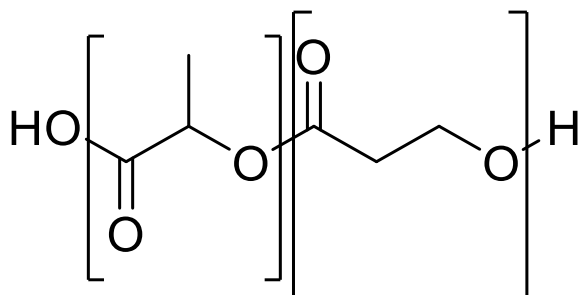
Figure 3.2: PLGA structure

3.1.1. <u>(58) and (72b) on PLGA</u>

Both (**58**) and (**72b**) have a carboxylic group as does PLGA, therefore a linker needs to be used to allow conjugation of these species. We chose 1,2-diaminoethane as a homo-bifunctional linker, as it can form amide bonds with both carboxylic groups. Because evidence of limited stability emerged during synthesis and purification of sensors, we performed the conjugation of the linker on the polymer first. The reaction was carried out in THF in the presence of *N*-hydroxysuccinimide and *N,N'*-diisopropylcarbodiimide were used as coupling activators[231,232], and of an excess of

1,2-diaminoethane to minimise the possibility of polymer cross-linking. The reaction was carried out overnight and the modified polymer was recovered by precipitation with diethyl ether and centrifugation. Sensors were added on the modified polymer using the same approach (Sch. 3.1). All steps were verified by Fourier-transform infrared spectroscopy (FTIR) by monitoring the appearance of the amide peaks following attachment of the linker and sensor[278] (amide C=O stretch between 1690 – 1630 cm^{-1} and amide N-H stretch between 3500 – 3180 cm^{-1}) (Fig. 3.3 & 3.4). Because of the variability of PLGA chain size and the important molecular weight compared to our molecule, experimental data (like NMR or MS) can't prove the conjugation of sensors to the polymer, but the polymer had the colour of the sensor and no washing removed the sensor.
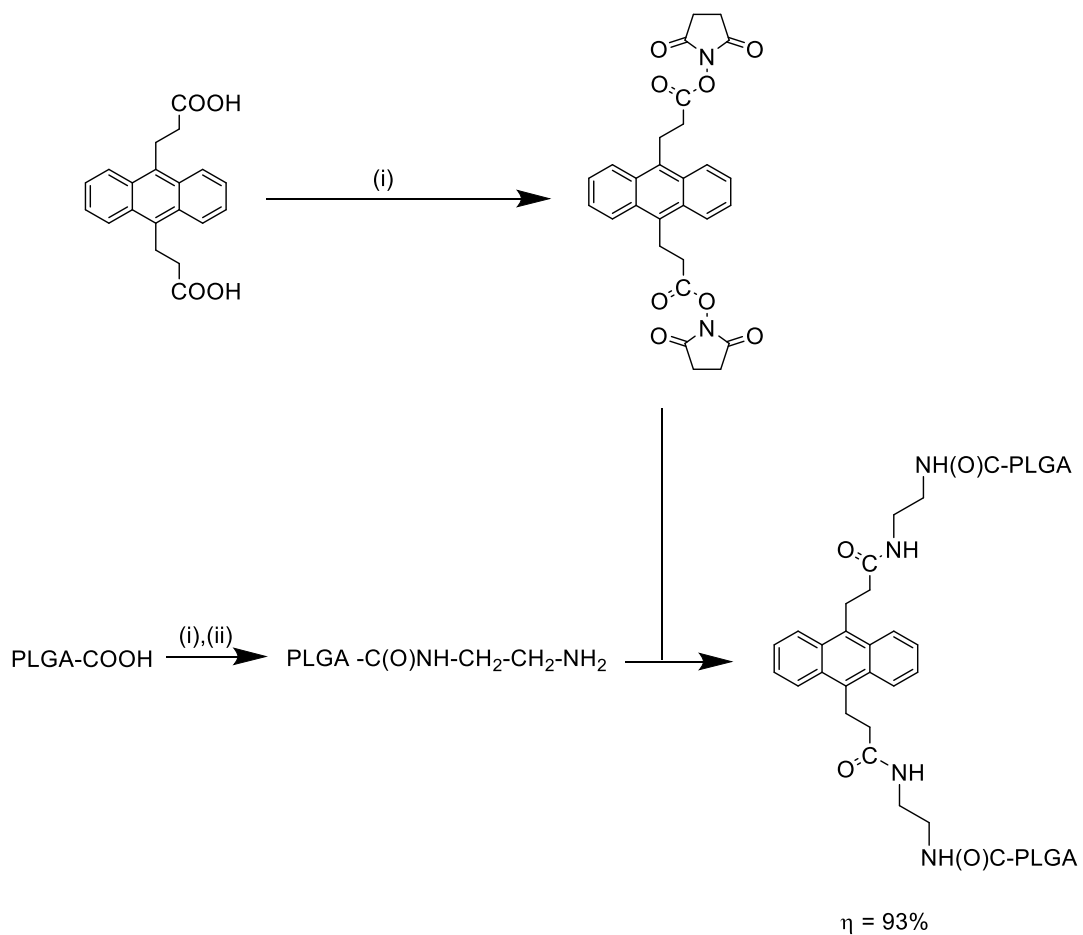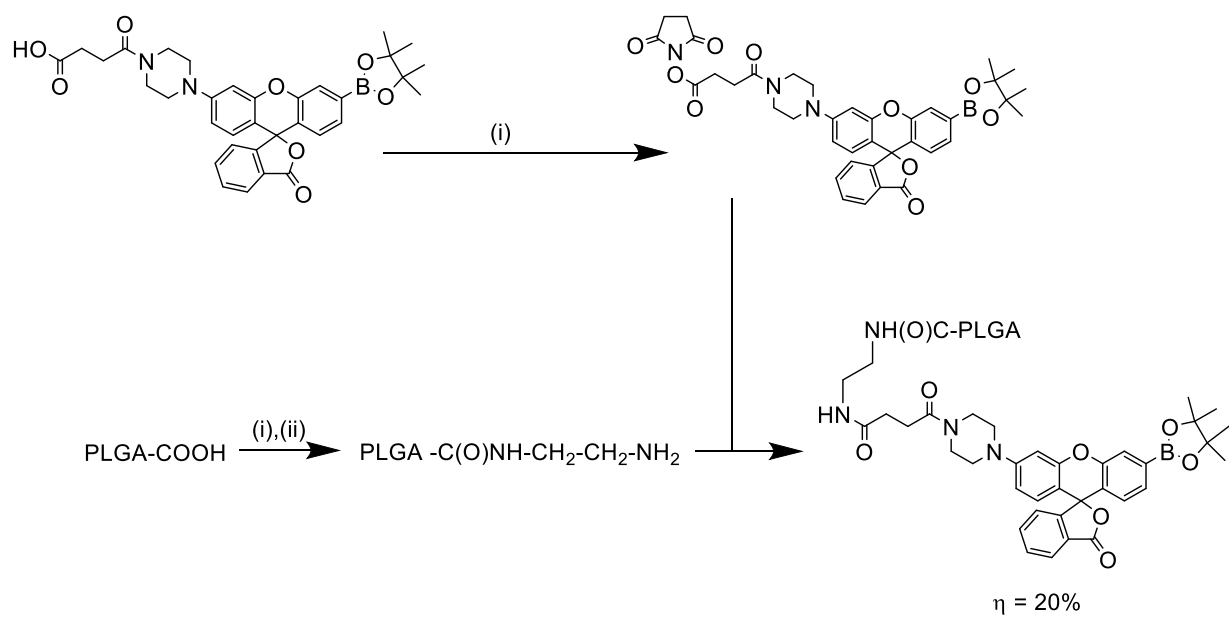
*Scheme 3.1: Scheme of addition of (**72b**) and (**58**) on PLGA. (i) NHS, DIC; (ii) excess*

1,2-diaminoethane.
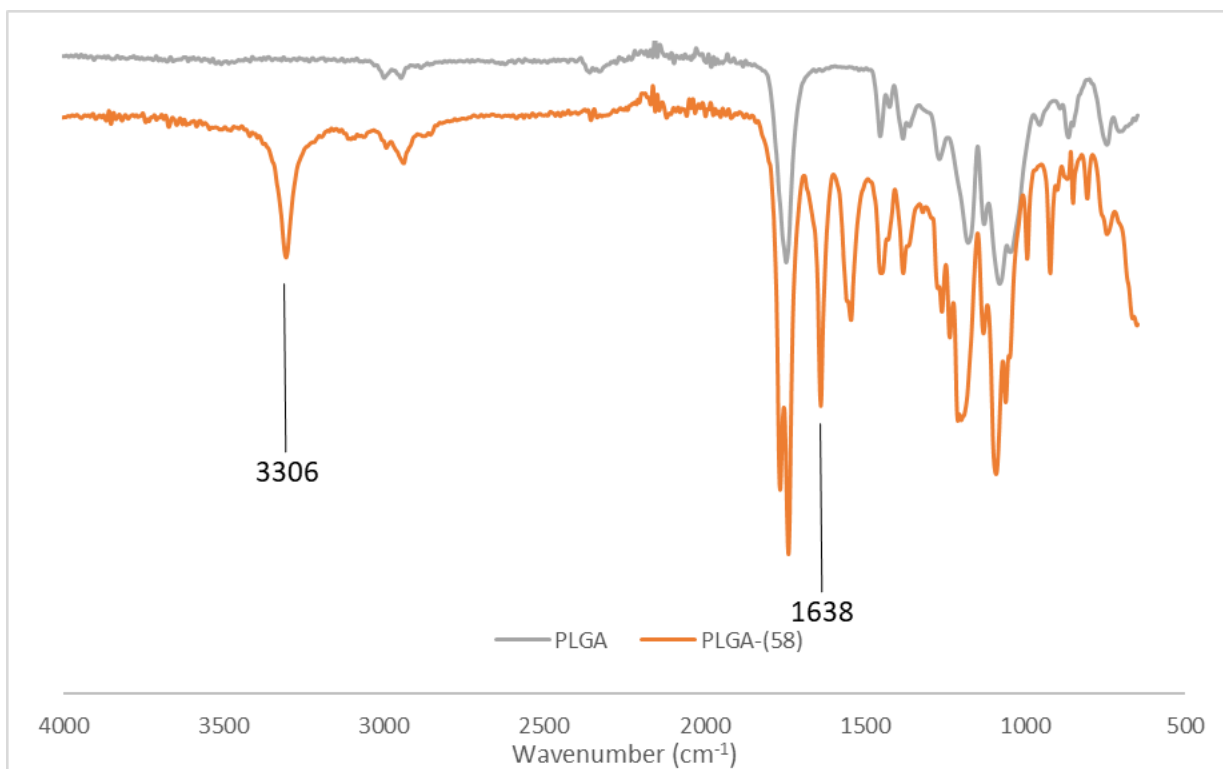
*Figure 3.3: Evolution of FTIR of formation of (**58**)-PLGA*
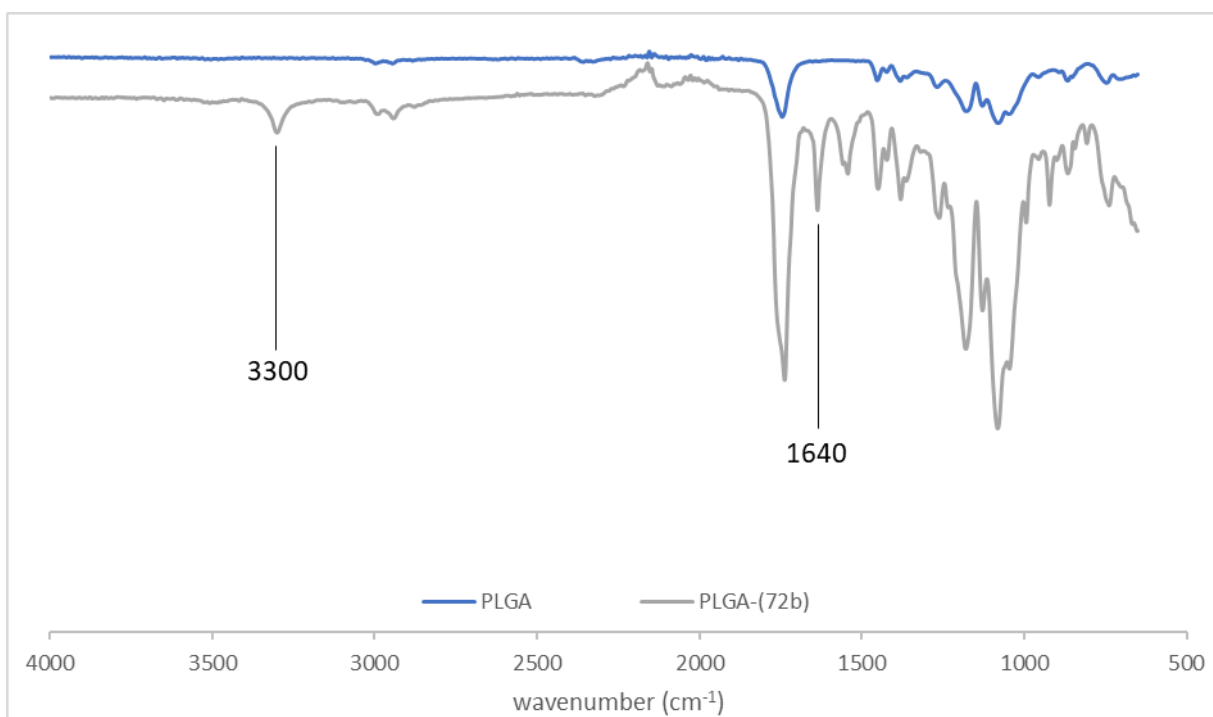
*Figure 3.4: Evolution of FTIR of formation of (**72b**)-PLGA*

3.1.2. **(43) on PLGA**

To allow conjugation with azide-bearing (**43**) the polymer needed to be functionalised with a triple bond. Azide can react with terminal alkynes in CuAAC with the presence of the pair Cu(I)/Cu(II)[91,217,279] (Sch 3.2) or with alkyne present on dibenzo-cyclooctyne (DIBO) which is driven by the loss of ring strain. Because the phosphinate are susceptible to reaction with radicals[280]. We chose the aza-dibenzocyclooctyne (ADIBO) amine[281] as heterobifunctional linker. On one side, DIBO is present to react with azide group on (**43**) and on the other side, a primary amine is present to react with the carboxylic acid moiety of PLGA. The linker was conjugated to the PLGA in the presence of DIC and NHS and the sensor was subsequently attached to the modified polymer in THF overnight (Sch. 3.3). All steps were monitored by FTIR, by following the appearance of the amide peaks when the linker is added (amide N-H stretch between 3500 – 3180 cm^{-1}) and a very small increment of alkene peak (alkene C-H stretch between 3100-3000 cm^{-1}) (Fig. 3.5). As previously, experimental data (like NMR or MS) can't prove the conjugation of sensors to the polymer, but the polymer had the colour of the sensor and no washing removed the sensor.
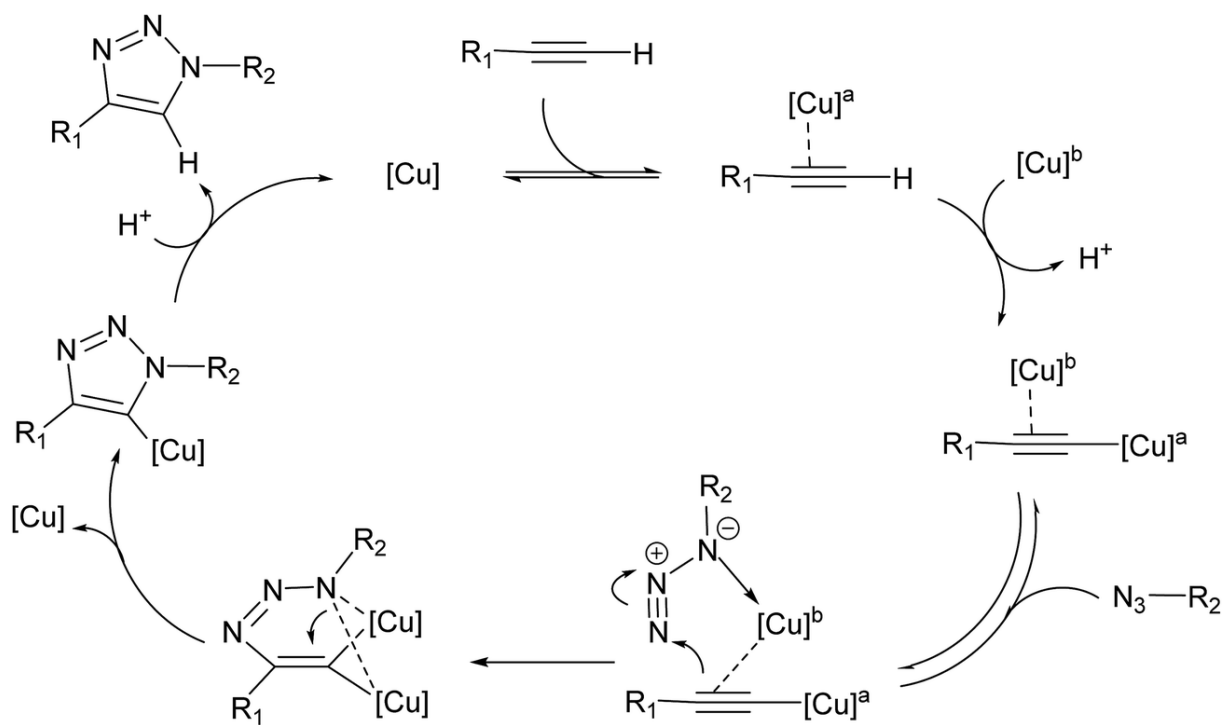
Scheme 3.2: CuACC mechanism[282]
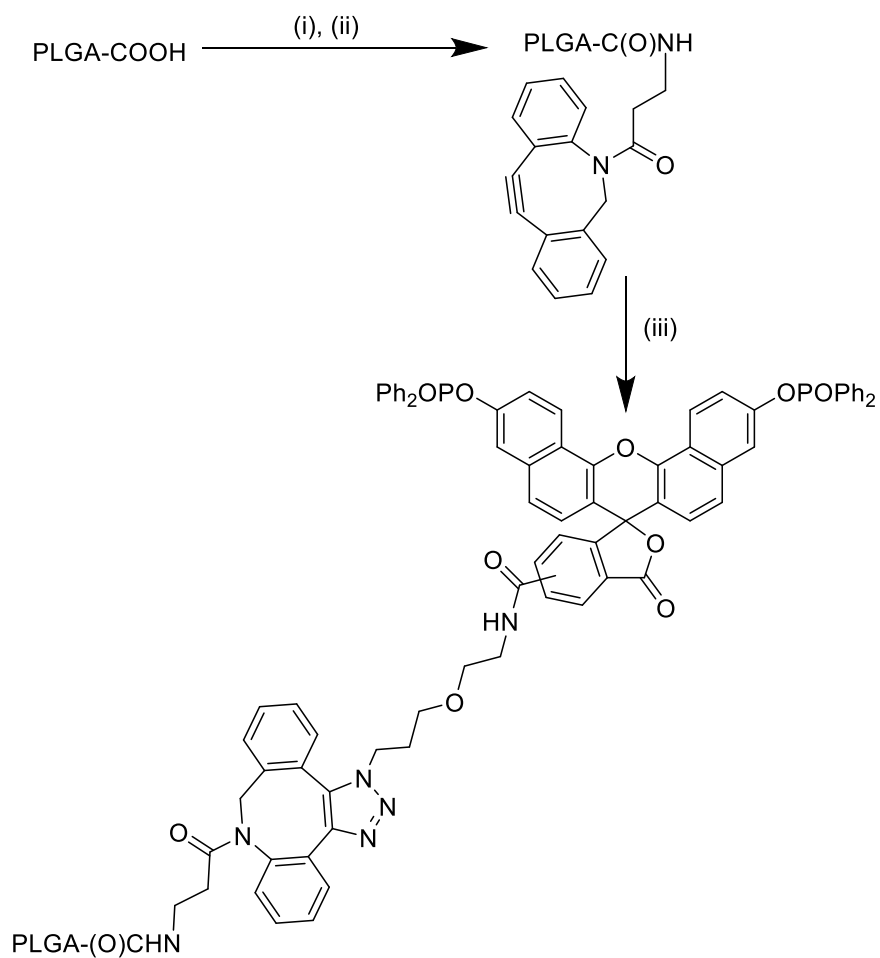
*Scheme 3.3: Addition of (43) on PLGA. (i) NHS, DIC; (ii) ADIBO amine; (iii) (**43**), DCM.*
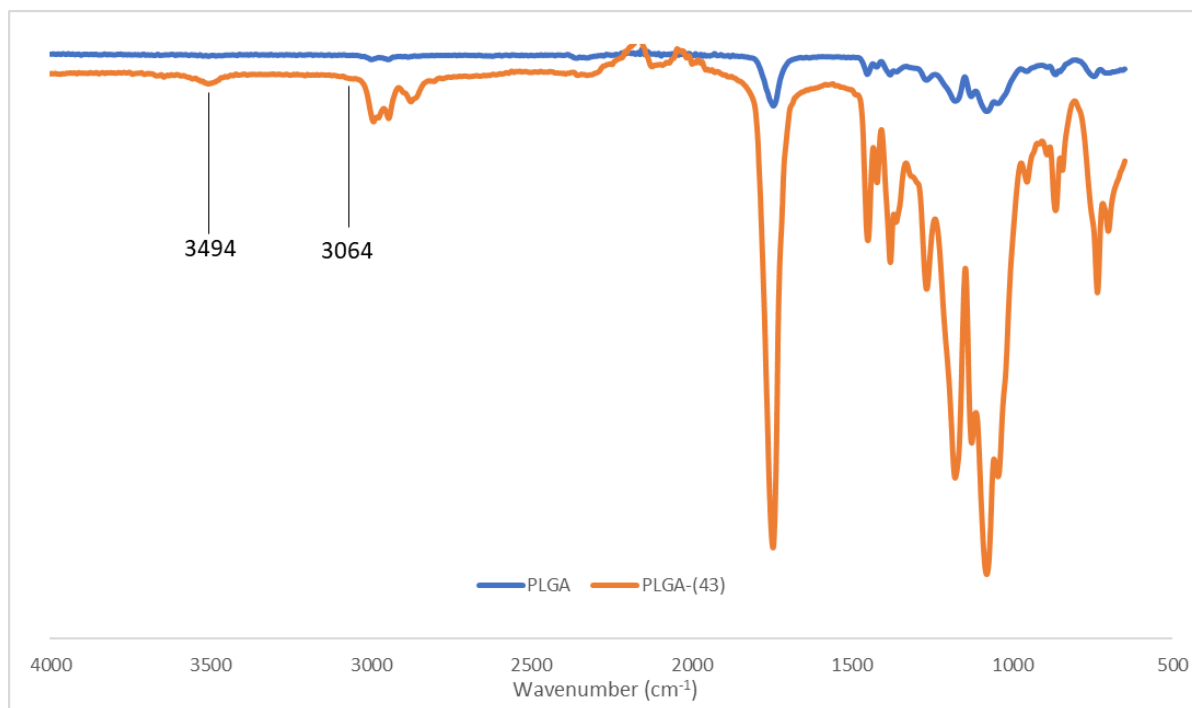
*Figure 3.5: Evolution of FTIR of formation of (**43**)-PLGA*

3.2. <u>Synthesis of NPs</u>

Two robust approaches to obtaining polymeric nanoparticles are double and single emulsion depending on the aqueous solubility of the material to be encapsulated. PLGA is a suitable material to be used in either of these approaches.

3.2.1. <u>Single emulsion</u>

To obtain NPs, PLGA or the desired polymer-sensor conjugate was dissolved in DCM and added dropwise to an aqueous solution of PVA under sonication. The mixture was left stirring to evaporate the DCM and then centrifuged. The resulted pellet was separated from the supernatant and the NPs suspended in PBS (Fig. 3.6)[277,283]. PLGA particles with a hydrodynamic radius of 143.53 ± 2.27 nm, measured by dynamic light scattering (see Experimental Section for details), were obtained.
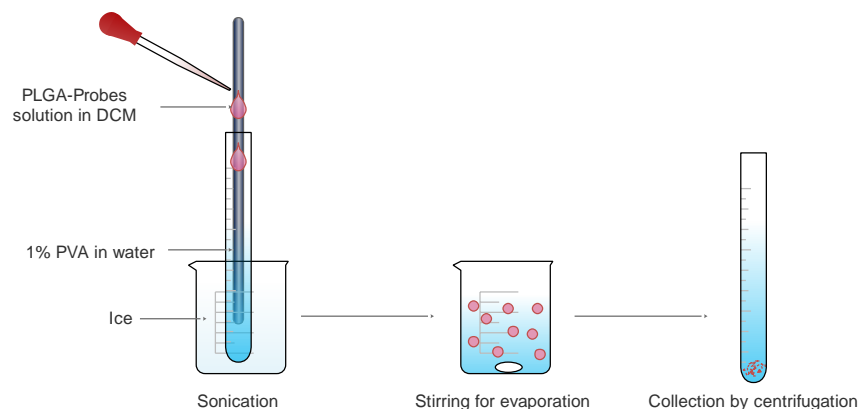
Figure 3.6: Single emulsion scheme

3.2.2. <u>Double emulsion</u>

The double emulsion technique is similar to the single emulsion with the only difference that a first emulsion of an aqueous PVA solution in the polymer solution is made. The first emulsion is prepared by slowly adding the PVA solution to a sonicating solution of DCM containing either PLGA. This water-in-oil emulsion is then added dropwise to an aqueous solution of PVA and stirred while the DCM evaporated. Thereafter the NPs are obtained and suspended in PBS as before[284,285]. Dynamic light scattering showed that this method afforded PLGA particles with an average hydrodynamic diameter of 151.10 ± 3.11 nm.

Both methods can be used to prepare NPs, suitable for cell penetration. The single emulsion has the advantage of being simpler and quicker whereas the double emulsion would be most suitable if there was a requirement to entrap a water-soluble molecule in the NPs. This is not required for this study, so, the single emulsion was chosen for NP formulation in this work.

3.2.3. <u>Results</u>

Following the method described above, NPs were prepared using PLGA and PLGA-conjugated with the different sensors to form nanosensors. The size and the zeta potential obtained for the different nanosensors are reported and compared with literature in Table 3.1.

Table 3.1: Size and zeta potential of nanosensors

Polymers	Size (nm)	Zeta (mV)
PLGA single emulsion	143.53 ± 2.27	/
PLGA double emulsion	151.10 ± 3.11	/
PLGA single emulsion (literature)[284,286]	60-200	-29 ± 0.18
PLGA double emulsion (literature)[283,287]	200	-23.3 ± 0.6
PLGA (**43**)	149.63 ± 5.64	-2.08 ± 0.32
PLGA (**58**)	155.83 ± 0.46	- 3.7 ± 0.78
PLGA (**72b**)	144.6 ± 0.30	-2.29 ± 0.43

The average hydrodynamic radius of the NPs obtained by single emulsion is consistent with the values reported in the literature, both when PLGA and PLGA conjugates are used. This can be explained considering that even in the case of polymer conjugates, the bulk of the nanoparticle is represented by PLGA, making it plausible that the minor component (the sensor) does not affect the formation and the properties of the particle.

Zeta potential measures the surface charge of the molecule (Fig. 3.7). The zeta potential of PLGA NPs in literature is *ca.* -26 ± 0.15 mV[286,287]. The negative value is due to the presence of carboxylic group and somewhat by the presence of alcohol.

The sensor-containing NPs display less negative values of zeta potential, which can be explained by the fact that the carboxylic groups are shielded by the presence of the sensor molecule.
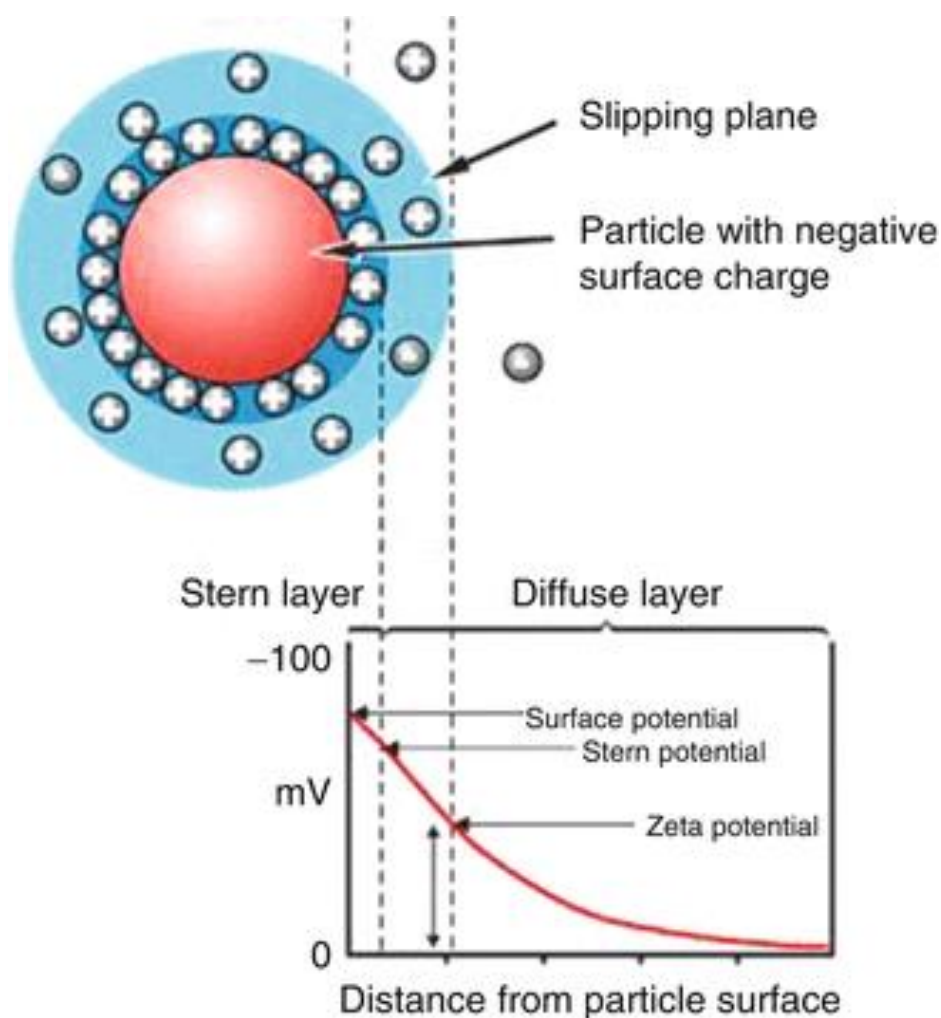
3.2.4. Stability of NPs

We next evaluated the stability of NPs in solution. This is an important parameter because the size of the NPs can increase due to irreversible aggregation and precipitation. NPs with small values of zeta-potential have a low surface charge, so they are prone to aggregation and precipitation because of the lack of electrostatic

repulsion between them. The stability of the NP suspensions was evaluated by storing the suspensions at room temperature and at 4 °C (in the fridge); the size and polydispersity of the NPs were monitored after one week, two weeks and a month. The behaviour of the size and polydispersity of nanosensors is shown in Fig 3.8 to 3.13. The values remain relatively stable for the time of the study, both at room temperature and at 4°C. Our NPs show a great stability after a month. In most of the samples (Fig 3.8 – 3.13), an increase in the average hydrodynamic radius and polydispersity index is observed after 7 days. In literature, NPs of PLGA keep a constant size the 21st days in general[289]. Our data suggests the formation of aggregates, but the apparent reversibility of the process, evidenced by the decrease of hydrodynamic radius and polydispersity index in subsequent measurements, indicates that flocculation rather than irreversible aggregation occurred[290]. Those variations can be due to external parameters (*e.g.,* atmospheric pressure, room temperature, humidity, etc.) or variations during sample handling (*e.g.,* how the sample is stirred before data acquisition). Their size remained under 200 nm which is the highest limit for the EPR effect[291] and their PdI stayed under 0.3 which is the highest limit too. EPR (i.e., enhanced permeability and retention) effect is a phenomenon caused by the altered microvasculature in tumour tissue that causes macromolecules and nanoparticles to accumulate and be retained in tumours more than in normal tissues.
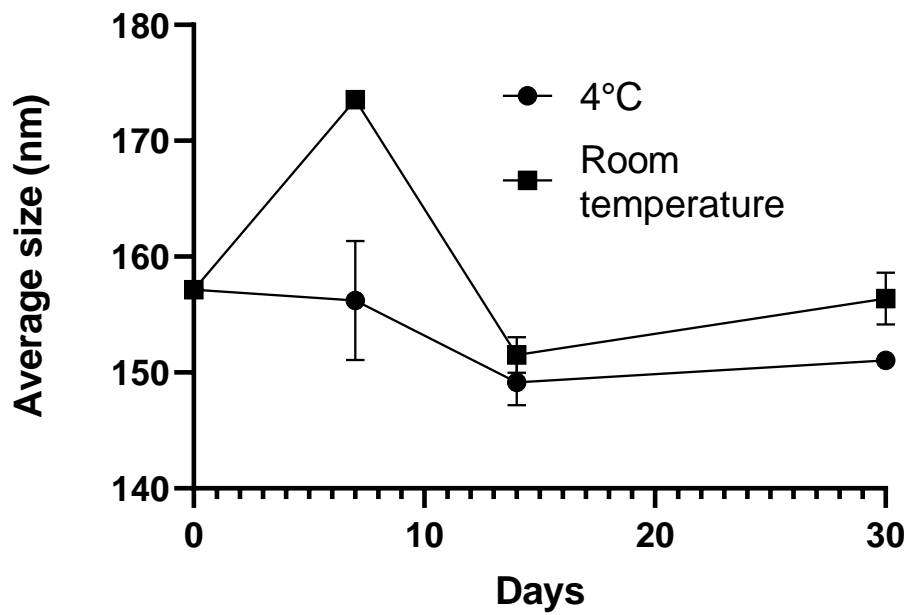
Figure 3.8: Size (hydrodynamic radius) *stability of (**43**)-functionalised PLGA NPs (N =*

3)
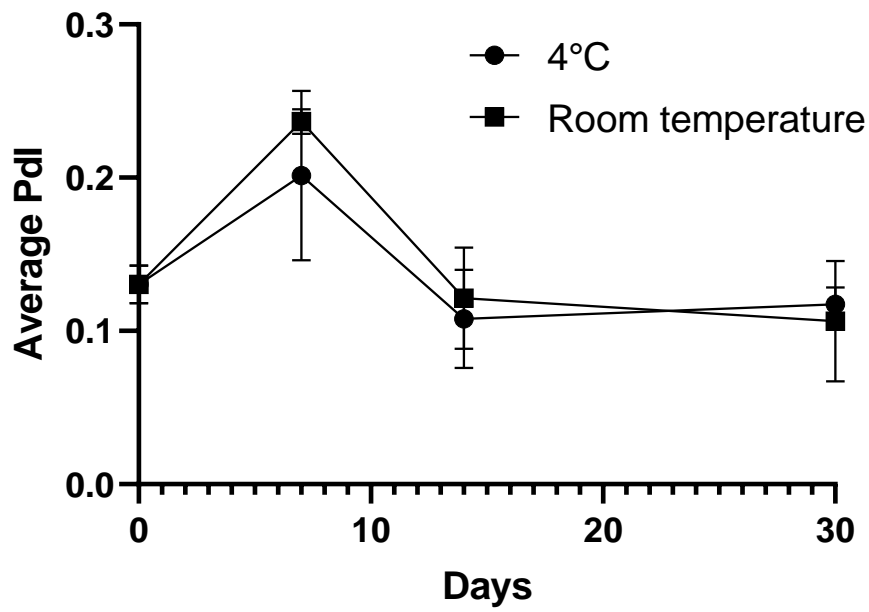
*Figure 3.9: Polydispersity index (PdI) stability of (**43**)-functionalised PLGA NPs (N =*

3)
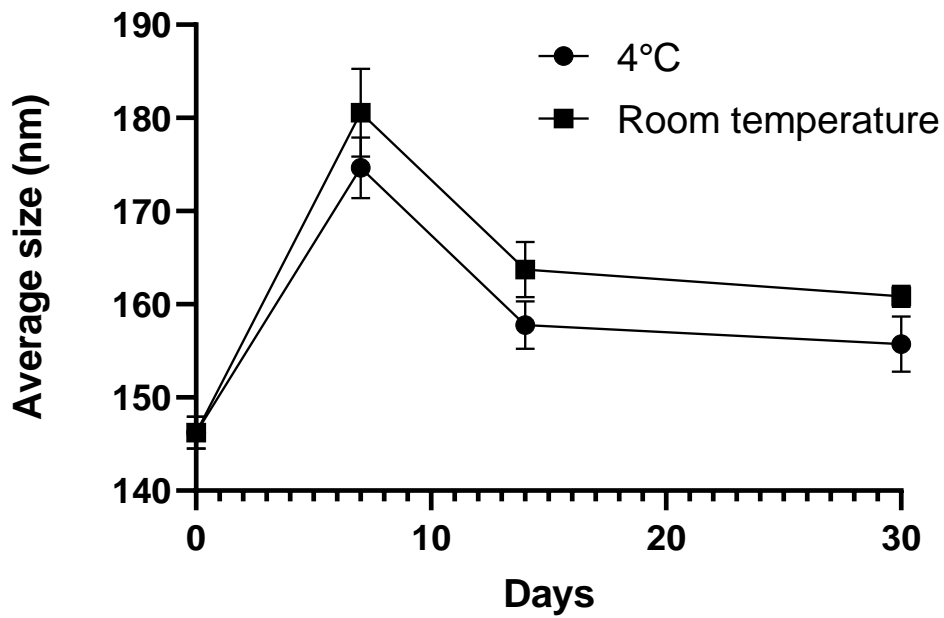
*Figure 3.10: Size stability of (**58**)-functionalised PLGA NPs (N = 3)*
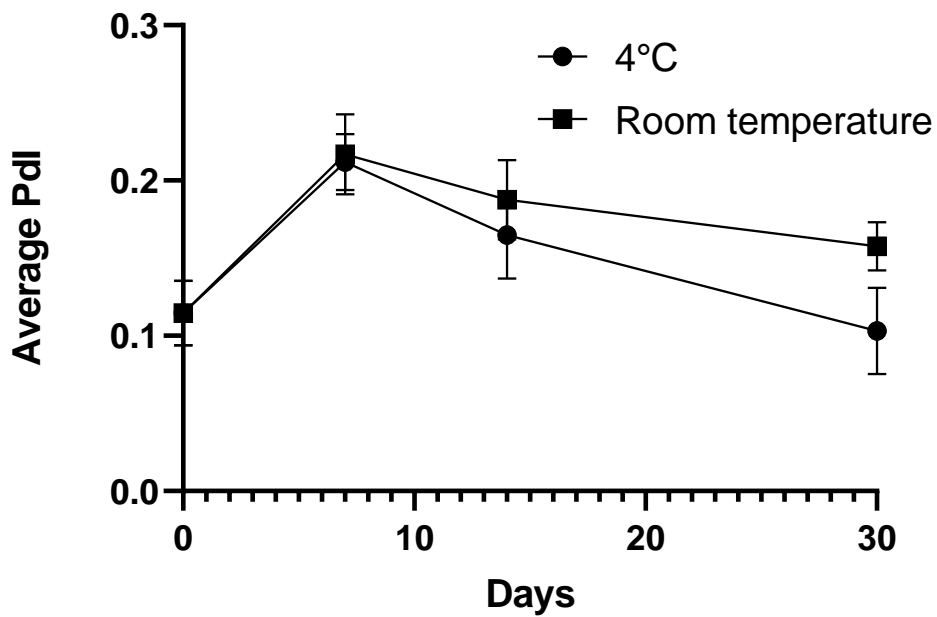
*Figure 3.11: PdI stability of (**58**)-functionalised PLGA NPs (N = 3)*
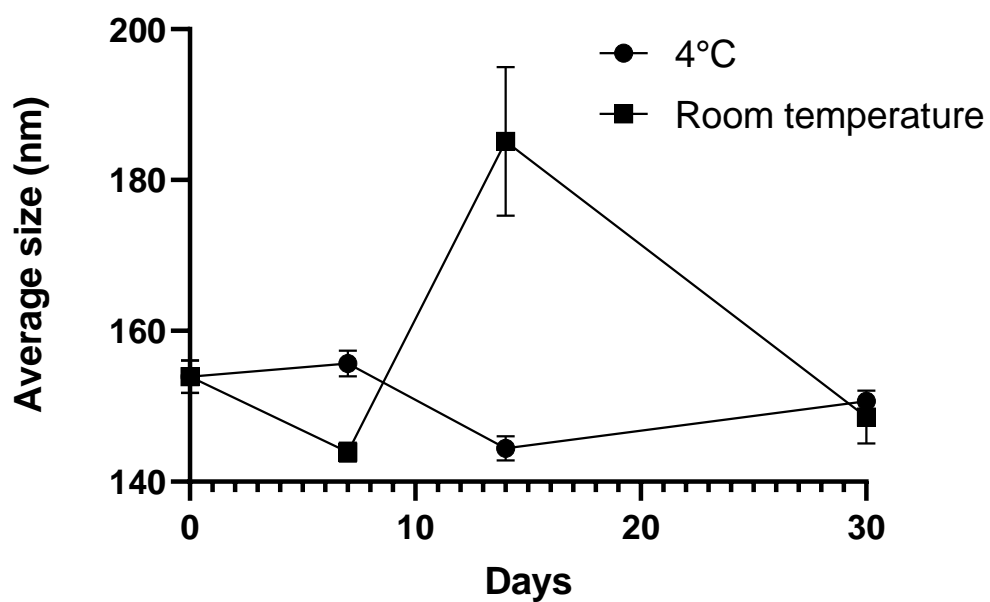
*Figure 3.12: Size stability of (**72b**)-functionalised PLGA NPs (N = 3)*
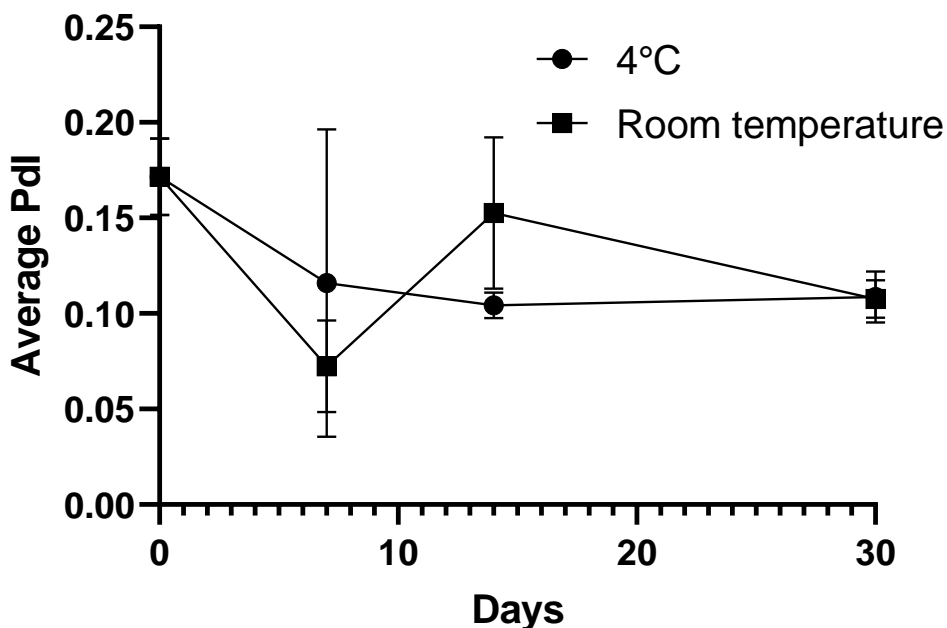
*Figure 3.13: PdI stability of (**72b**)-functionalised PLGA NPs (N = 3)*

3.2.5. <u>Responsiveness of the nanosensors to ROS analytes</u>

Lastly, we undertook the preparation of nanosensors containing different fluorescent probes to evaluate the possibility of monitoring different ROS species independently by evaluating their response in the presence of different kinds of ROS. The first studies were carried out by exposing 1 mg/mL suspensions of NPs to the target ROS analyte, generated with the methods reported in Chapter 2 (paragraphs 1.2, 2.2 and 3.2).

3.2.5.1. <u>Superoxide-responsive nanoparticles</u>

The fluorescent emission of the (**43**)-functionalised nanoparticles in the presence of different amount of XO is reported in Figure 3.14. Firstly, we observed that the shape of the emission spectrum had changed. This phenomenon is not uncommon for sensors associated to a polymer and this behaviour has been previously described for rhodol[238] and MitoPY1[101] which have similar shape but different emission wavelength

115

(519 nm and 530 nm respectively). In our case, two peaks of emission are visible, one at 530 nm and the other at 545 nm. The presence of two relative emission maxima can be ascribed to the presence of two "populations" of fluorophores, one embedded in the NP and others on the outer surface of the particles[103]. We verified that the increase in the fluorescence intensity is limited but more marked than the one observed in the stand-alone sensor. It is known that associating sensors with nanoparticles can protect the fluorophore from degradation caused by the surrounding environment, as reported for PEBBLE nanosensors[195,210]. Moreover, the evolution is linear between 0 and 15 µL (Fig. 3.15). This last property is important to calibrate our measure and to calculate the amount of ROS when we know fluorescence level.
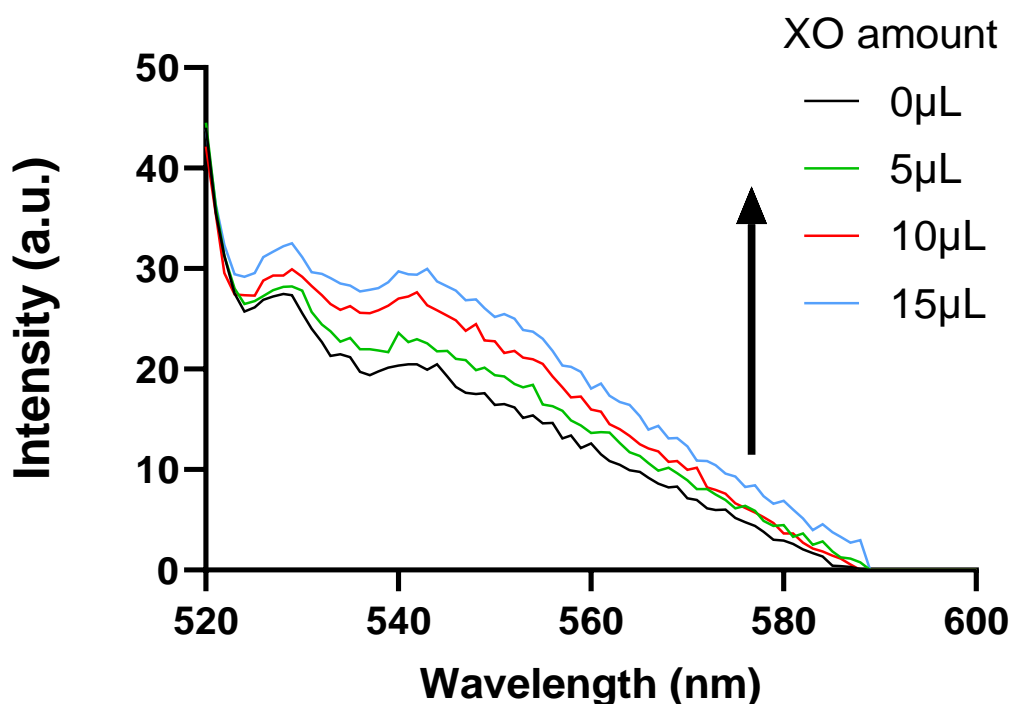
*Figure 3.14: Example of fluorescence emission spectra of (**43**) on PLGA NPs in the presence of super oxide*
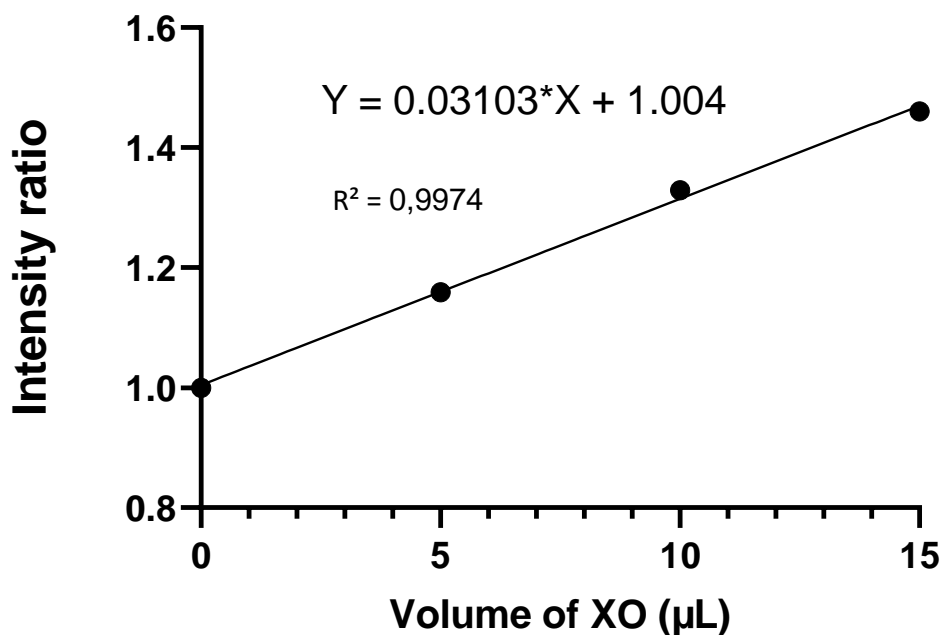
*Figure 3.15: Intensity ratio for (**43**)-PLGA NPs with superoxide anion (data are normalised with blank experiment: sensor without ROS)*

When we assessed the selectivity of the sensor towards other ROS, we observed an increase in the fluorescence emission in the presence of hydrogen peroxide but no increase in the presence of singlet oxygen (Fig. 3.16 & 3.17). These results show that the (**43**)-NP could be used to monitor superoxide and hydrogen peroxide jointly but not independently.
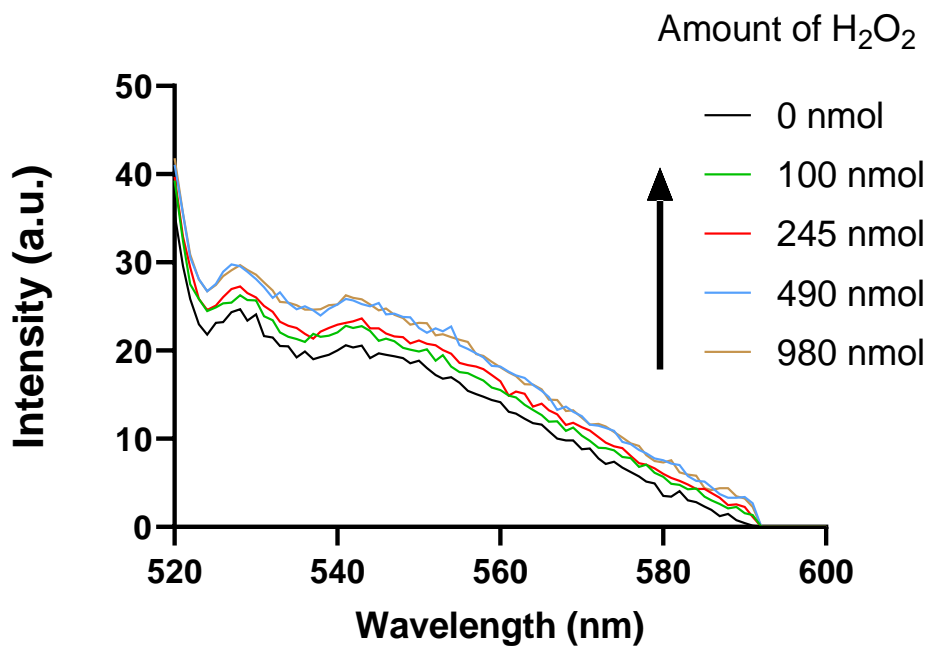
*Figure 3.16: Example of fluorescence emission spectra of (**43**) on PLGA NPs in the*

presence of hydrogen peroxide
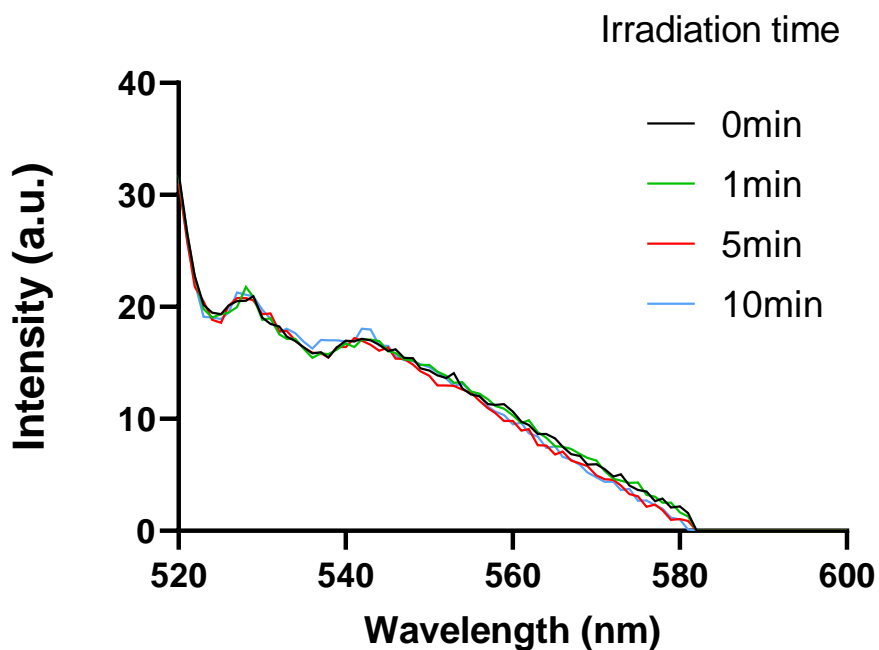
*Figure 3.17: Example of fluorescence emission spectra of (**43**) on PLGA NPs in the*

presence of singlet oxygen

3.2.5.2. <u>Hydrogen peroxide-responsive nanoparticles</u>

As reported in Chapter 2 (part 2.2.2.), we observed an unexpected decrease of intensity of fluorescence emission of (**58**) in the presence of increasing amounts of hydrogen peroxide. For (**58**) PLGA NPs the same behaviour was observed (Fig. 3.18). In addition, the same behaviour is observed in response to superoxide radical anions and singlet oxygen (Fig. 3.19 & 3.20). On the bases of these results, we concluded that (**58**) is neither an efficient nor a selective sensor for ROS.
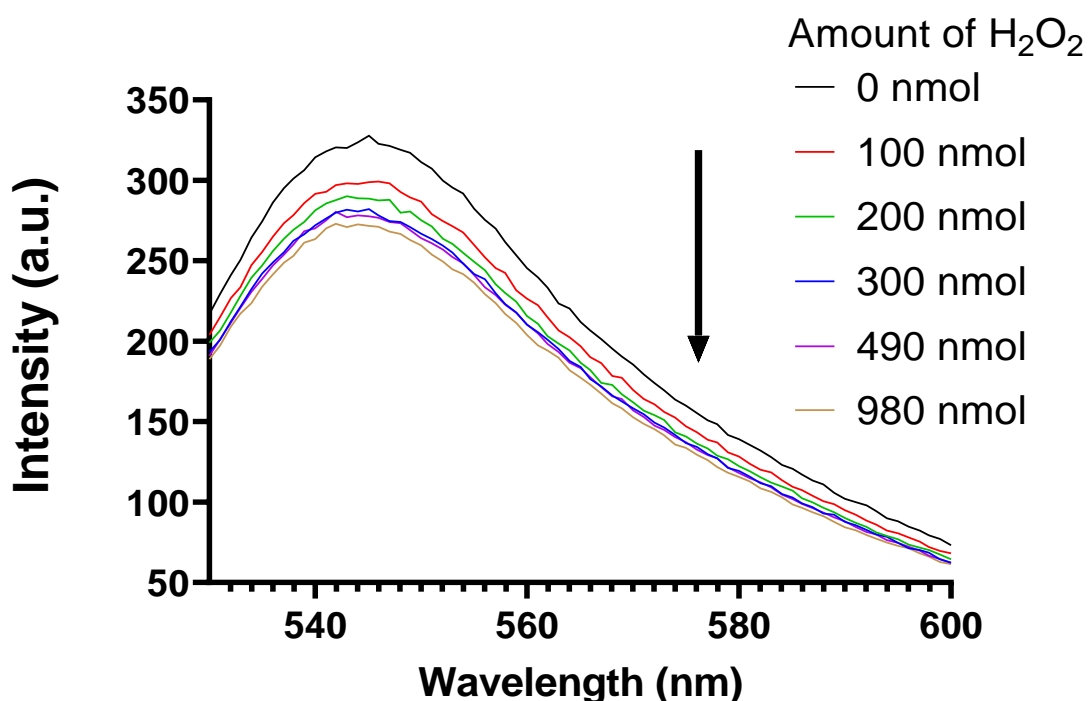
*Figure 3.18: Example of fluorescence emission spectra of (**58**) on PLGA NPs in the presence of hydrogen peroxide*

*Figure 3.19: Example of fluorescence emission spectra of (**58**) on PLGA NPs in the presence of superoxide anion*
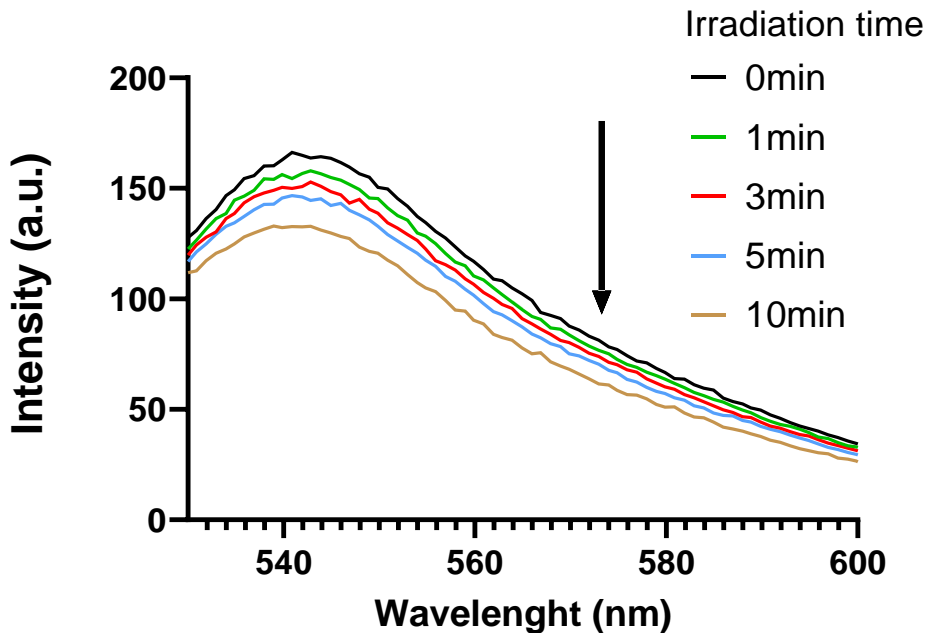
*Figure 3.20: Example of fluorescence emission spectra of (**58**) on PLGA NPs in the presence of singlet oxygen*

3.2.5.3. <u>Singlet oxygen-responsive nanoparticles</u>

In Chapter 2 we described how (**72b**) showed the expected decrease of fluorescence intensity in the presence of singlet oxygen. The behaviour is maintained with (**72b**)-PLGA conjugates, although the decrease is less pronounced (Fig. 3.21). As observed for the (**43**)-PLGA conjugates, the emission profile has changed.
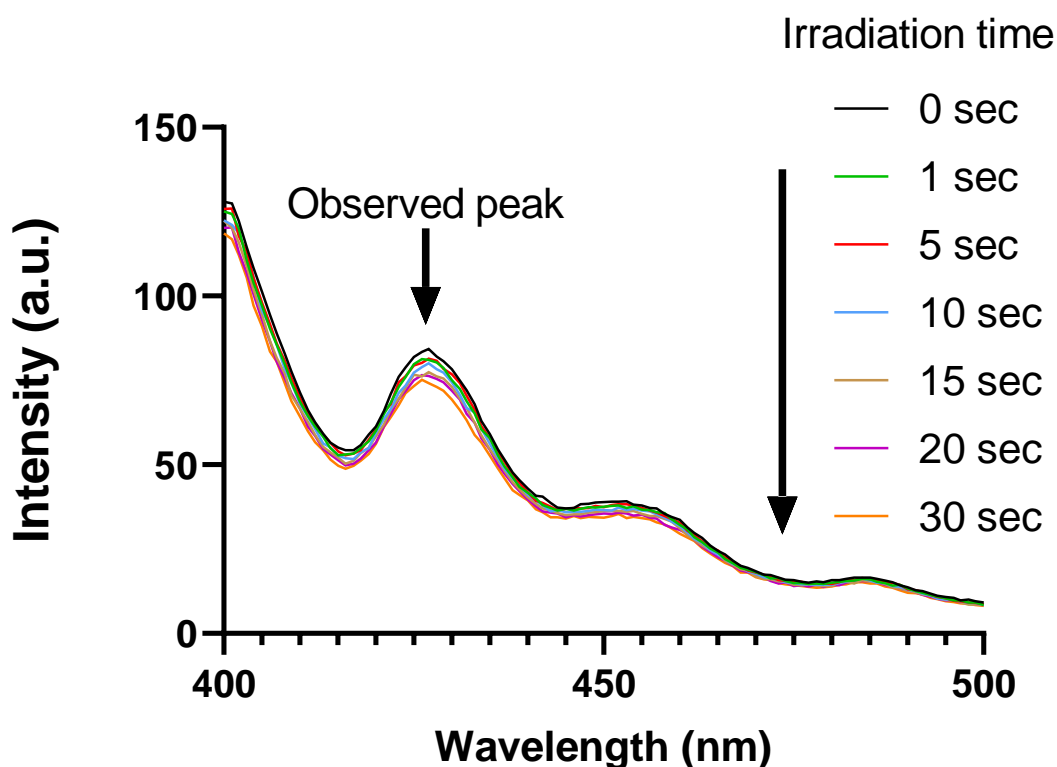
*Figure 3.21: Example of fluorescence emission spectra of (**72b**) on PLGA NPs in the presence of singlet oxygen*

Finally, (**72b**) show an interesting selectivity (Fig. 3.22 & 3.23): for low concentration of superoxide anion or hydrogen peroxide the intensity of emission is unaffected, whereas it starts to decrease at high concentration. This sensor is potentially useful to detect/quantify singlet oxygen, although the limited changes in the emission intensity may limit its applicability.

*Figure 3.22: Example of fluorescence emission spectra of (**72b**) on PLGA NPs in the*

presence of superoxide anion
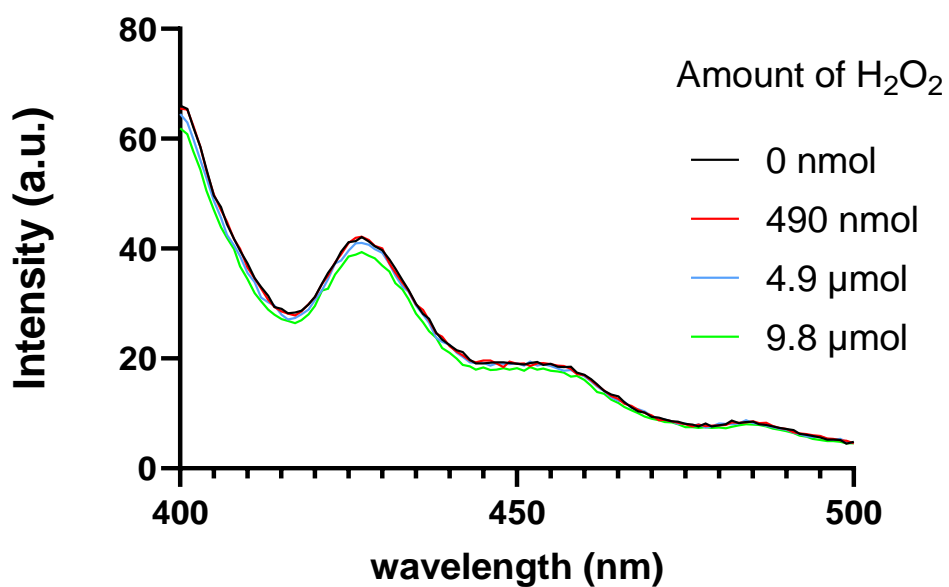
*Figure 3.23: Example of fluorescence emission spectra of (**72b**) on PLGA NPs in the*

presence of hydrogen peroxide

3.2.6. <u>Nanosensors containing (43) and (72b)</u>

Because of the encouraging responsive behaviour of (**43**)-PLGA NPs and (**72b**)-PLGA NPs with respectively superoxide anion and singlet oxygen reported in Chapter 3 (paragraph 3.2.5.), we attempted to evaluate whether the independent monitoring of ROS species was possible using (**43**)- and (**72b**)-conjugated polymers. A first experiment was carried out on a suspension of (**43**)-PLGA NPs and (**72b**)-PLGA NPs. A second experiment was carried out preparing a batch of (**43**)-PLGA and (**72b**)-PLGA NPs. The behaviour of the samples in the presence of superoxide and singlet oxygen is reported in figures 3.24 and 3.25.

3.2.6.1. <u>Combination of the two batches of NPs</u>

Figure 56 shows the fluorescence intensity variation when (**43**) and (**72b**) NPs are in the presence of singlet oxygen. The behaviour of (**43**) on PLGA is unexpected under this condition with an observed increase of fluorescence while (**72b**) on PLGA demonstrates an expected evolution with a decrease of fluorescence. The unexpected variation of fluorescence of (**43**) is not easy to explain. Although the absorption and emission spectra of (**72b**) (Chapter 2 part 3.2) and (**43**) (Chapter 2 part 1.2) on PLGA partially overlap, the two sensors are not close enough to give rise to FRET effect, where the energy emitted by (**72b**) would be absorbed by (**43**)[292].
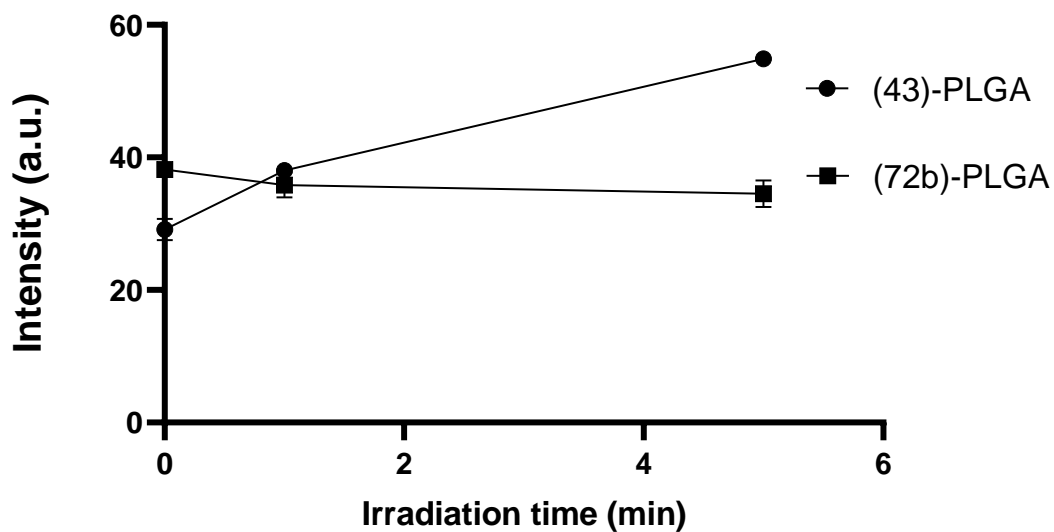
Figure 3.24: (**43**) *and* (**72b**) *NPs with singlet oxygen (N = 3)*

In the presence of superoxide radical anion (Fig. 57), the fluorescence intensity of (**43**) increases as expected, but a decrease of the intensity of (**72b**) fluorescence was also observed. Although the decrease is limited, it is of the same order as the one observed in the presence of singlet oxygen.
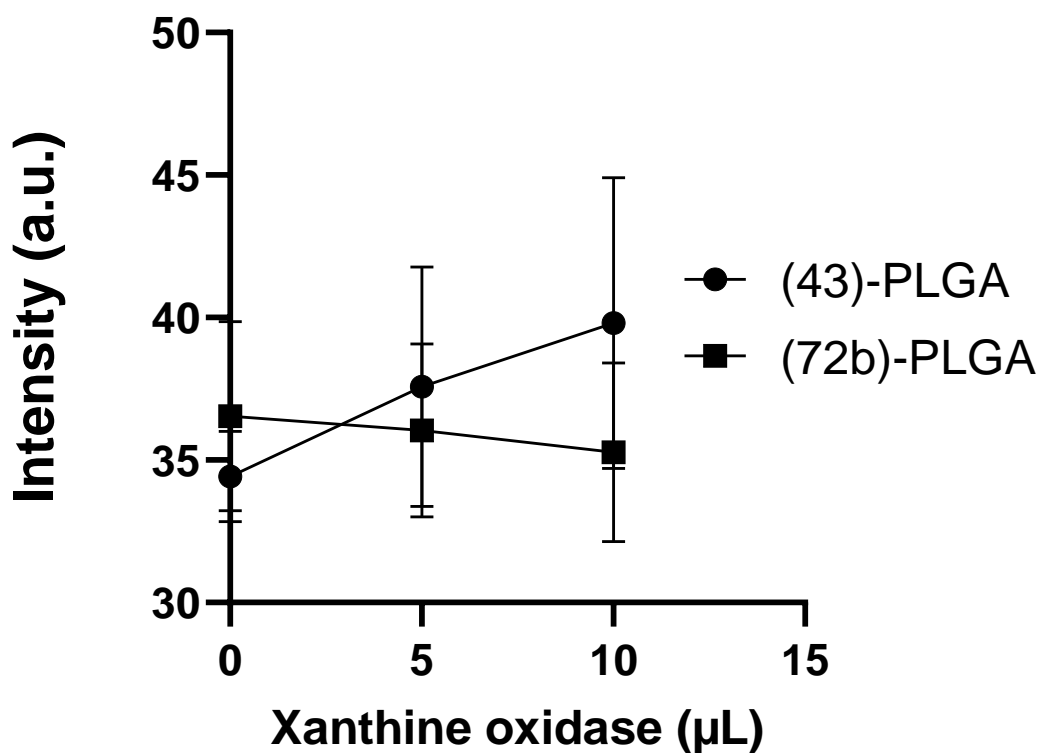
Figure 3.25: (**43**) *and* (**72b**) *NPs with superoxide (N = 3)*

3.2.6.2. <u>Two sensors on the NPs</u>

In the presence of singlet oxygen (Fig. 3.26), the fluorescence intensity of (**43**) increases to a lesser extent compared to what we observed in the experiment reported above. The fluorescence of (**72b**) decreases as expected and more markedly. It should be noted, however, that the error bars in the graph are large, which make it difficult to draw reliable conclusions on the selectivity of the sensors.
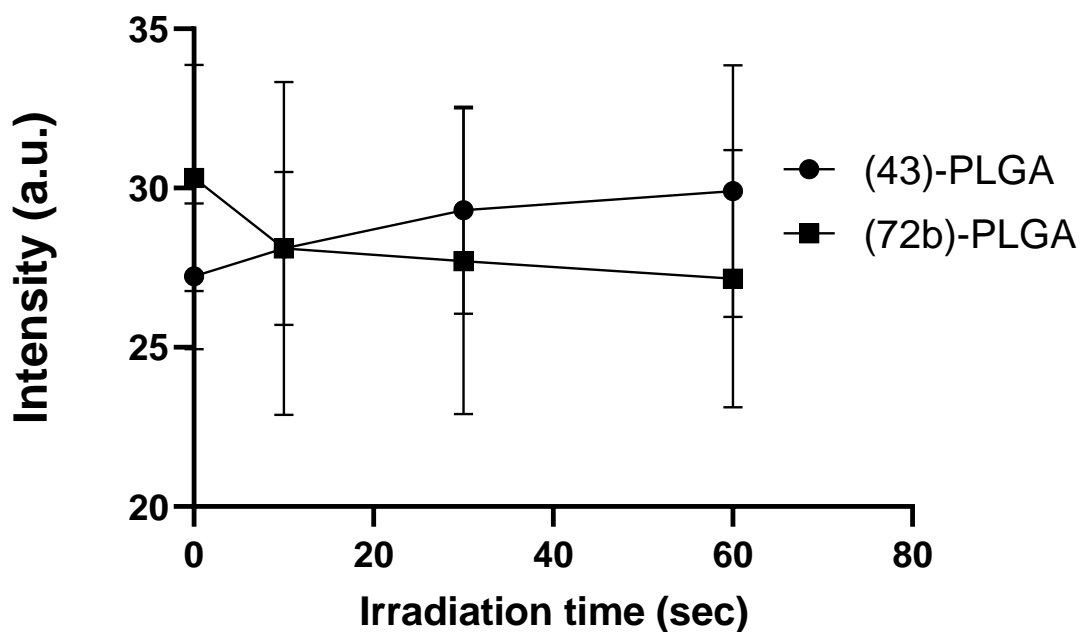
Figure 3.26: (**43**) *and* (**72b**) *in one pot with singlet oxygen (N = 3)*

The responsiveness of (**43**) and (**72b**) to superoxide anion are more promising than those obtained from the sample with the two populations of nanoparticles (Fig. 3.27). In the presence of superoxide radical anion, the intensity of the fluorescence of (**43**) increases while that of (**72b**) decrease only slightly at higher concentrations of superoxide, a similar behaviour was observed when (**72b**)-PLGA alone was exposed to superoxide. These results encouraged further experiments with dual NPs obtained from two or more polymer conjugates.
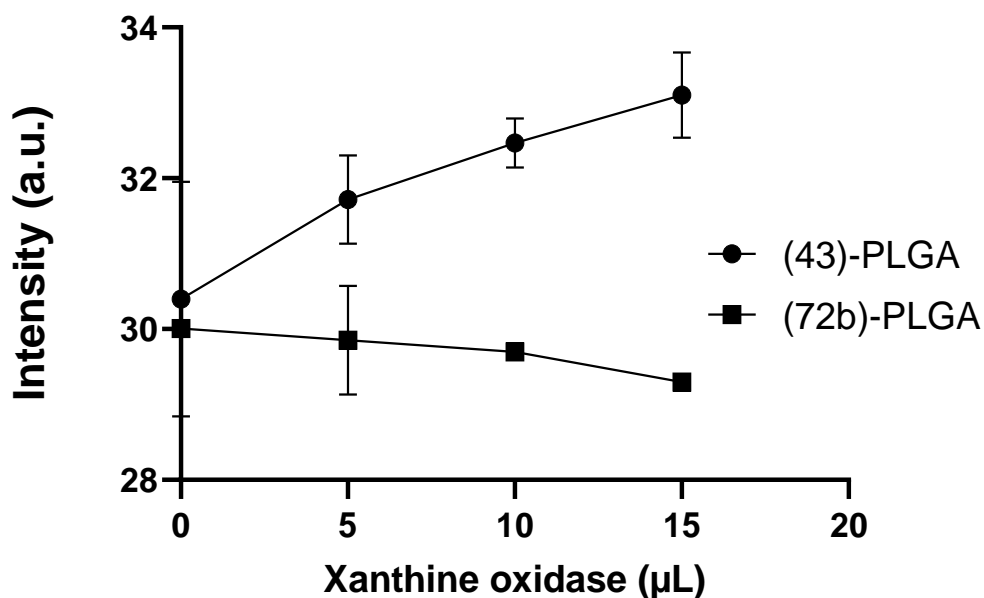
*Figure 3.27: (**43**) and (**72b**) in one pot with superoxide anion (N = 3)*

3.3. <u>Comparison with commercial sensors</u>

The non-optimal or unexpected behaviour of the NPs obtained could derive from the use of ROS sensors synthesised for this purpose but perhaps underperforming compared to more robust commercially available sensors. To prove the concept of dual independent sensing of ROS we decided to synthesise batches of sensors entrapping commercially available sensors: HE for superoxide anion (**1a**), peroxy yellow (**73**) for hydrogen peroxide and finally, SOSG (**15a**) for singlet oxygen (Fig. 3.28).
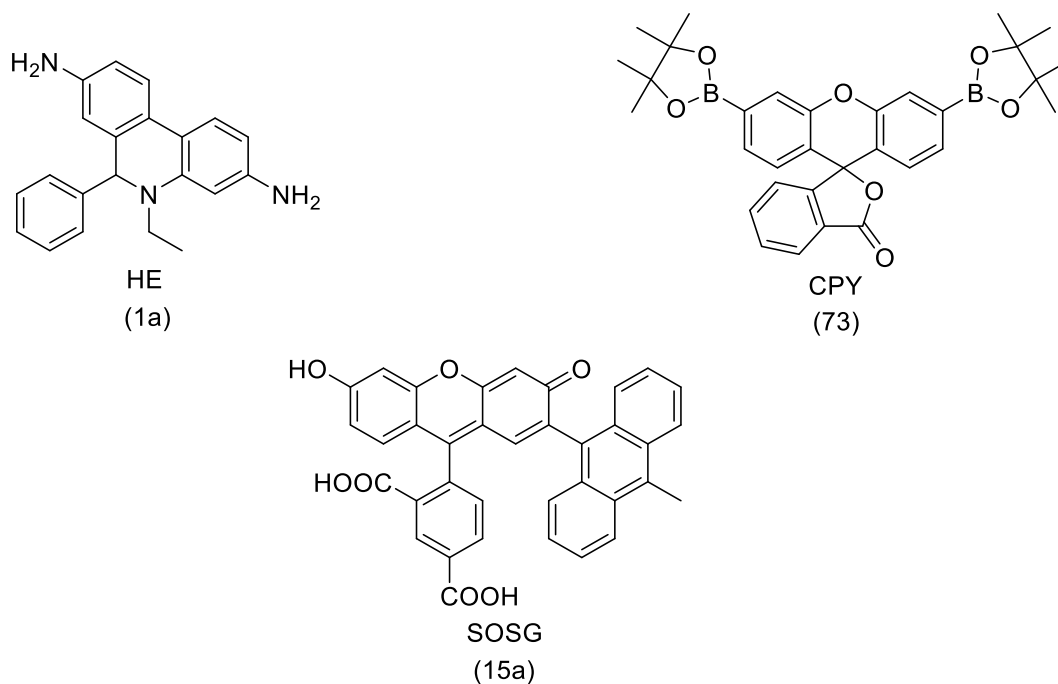
Figure 3.28: Commercial dyes used

3.3.1. <u>Synthesis of nanosensors with commercially available sensors</u>

3.3.1.1. <u>(15a)</u>

The synthesis of (**15a**)-containing nanosensors is reported in the literature using a polyacrylamide nanoparticle as the support[133]. For ease of comparison with our system, we synthesised PLGA nanoparticles containing (**15a**). Synthesis of (**15a**)-functionalised PLGA was carried out as reported in part 3 (section 1.1) and the NPs were obtained by single emulsion as reported in section 2.1.

3.3.1.2. <u>(1a) and (73)</u>

Due to the lack of suitable functional groups, (**1a**)[218] and (**73**)[236] cannot be linked on PLGA so we decided to encapsulate the sensors into the PLGA NPs using the single emulsion method described in section 2.1. adding (**1a**) or (**73**) to the reaction mixture.

128

3.3.1.3. <u>Size, zeta potential and stability</u>

Tab. 3.2 shows that the presence of sensors results in an increase of the size of the NPs. For (**15a**)-PLGA the new size is *ca.* 165 nm, but the incorporation of (**1a**) and (**73**) causes a marked increase, giving batches of particles with an average hydrodynamic radius of *ca.* 220 nm. NPs of this size may not be as readily internalised in cells or distributed selectively to tumour tissue via the EPR effect.

The stability and PdI of the sensor-encapsulating NPs were studied as reported in section 3 of this Chapter. The zeta potential of the NPs is negative with lower values for (**1a**)- and (**73**)-containing NPs probably because the non-covalent incorporation leaves carboxylate groups free.

Table 3.2: Size and zeta potential of nanosensors with commercial sensors

Polymers	Size (nm)	Zeta (mV)
PLGA single emulsion	143.53 ± 2.27	/
PLGA (**15a**)	164.93 ± 4.02	-1,24 ± 0.54
PLGA (**1a**)	220.53 ± 5.72	-5.6 ± 1.41
PLGA (**73**)	226.53 ± 6.43	-3.37 ± 1.36

Figures 3.29 & 3.30 show that suspensions of (**15a**)-NPs are stable both at room temperature and at 4 °C for up to 30 days, as the average hydrodynamic radius does not increase. The PdI is under 0.3 which means the dispersity is low and stays constant. A peak is still present after 7 days which can be due to the atmosphere conditions as above for our sensors.
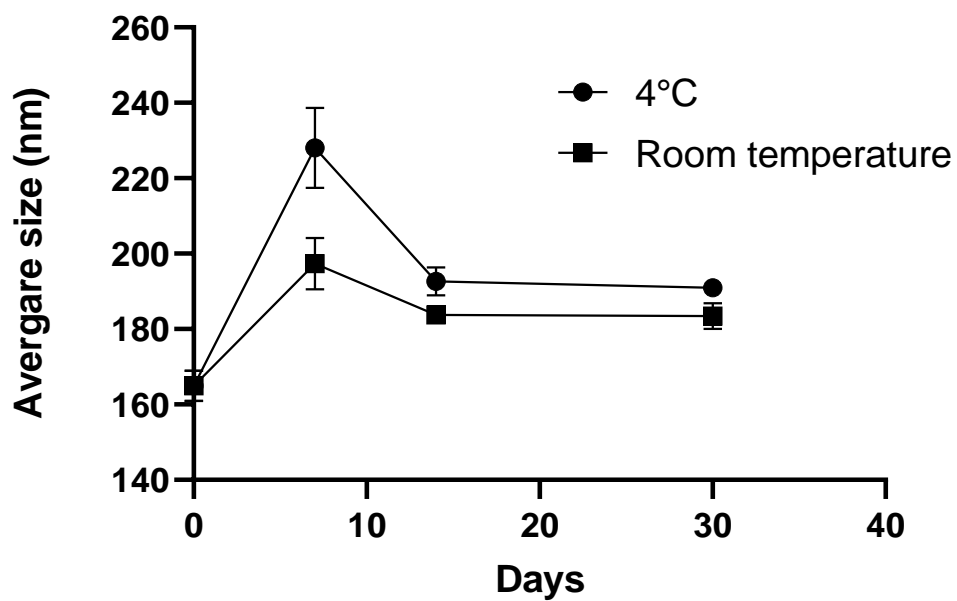
*Figure 3.29: Size stability of (**15a**) PLGA NPs (N = 3)*
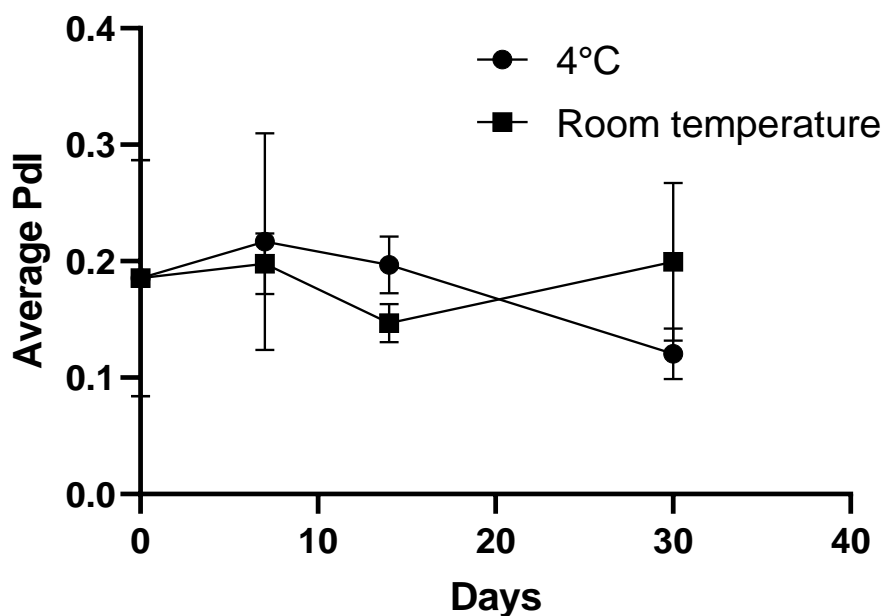
*Figure 3.30: PdI stability of (**15a**) PLGA NPs (N = 3)*

Figures 3.31 to 3.34 show evidence of aggregation for (**1a**)- and (**73**)-containing NPs

suspension at room temperature. On the contrary, at 4 °C the size of the suspended

NPs does not seem to vary with a definite trend. In both samples we observed a decrease of the average hydrodynamic radius after one week. This data suggests the formation of aggregates, but we observe a reversibility of the process, evidenced by the decrease of hydrodynamic radius and polydispersity index in subsequent measurements, indicates that flocculation rather than irreversible aggregation occurred[290] as previously discussed in Chapter 3 (Part 3.2.3).

The trend of the PdI supports what we observed for the size. The PdI index increases at room temperature but not at 4 °C (Fig. 3.31 and 3.34).
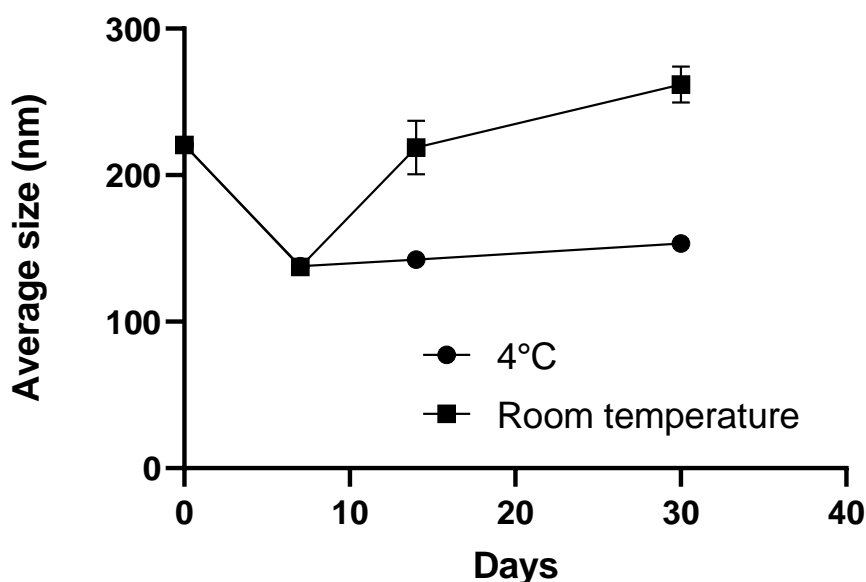
Figure 3.31: Size stability for (**1a**) PLGA NPs (N = 3)
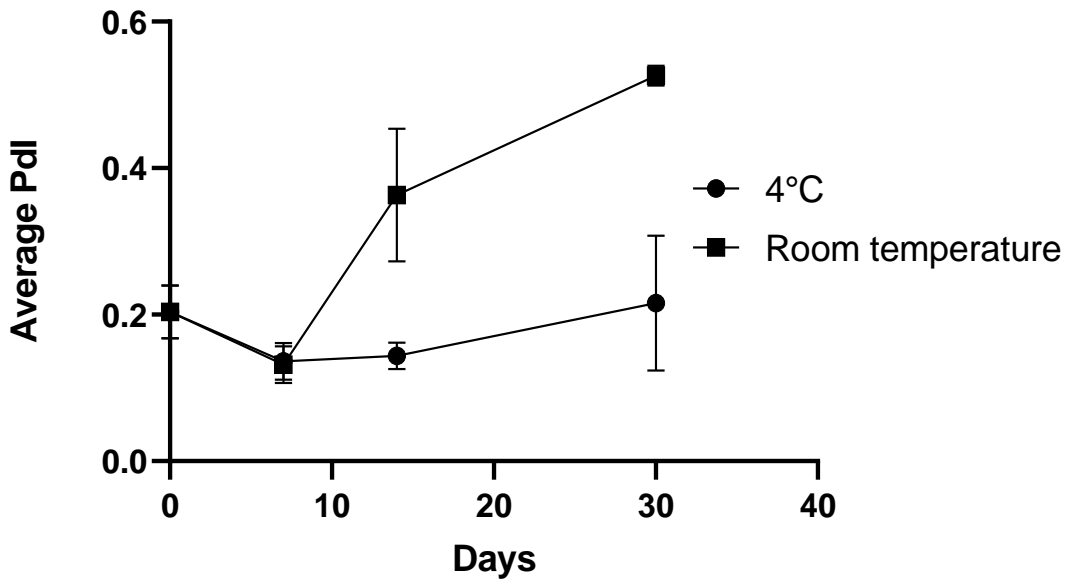
*Figure 3.32: PdI stability for (**1a**) PLGA NPs (N = 3)*
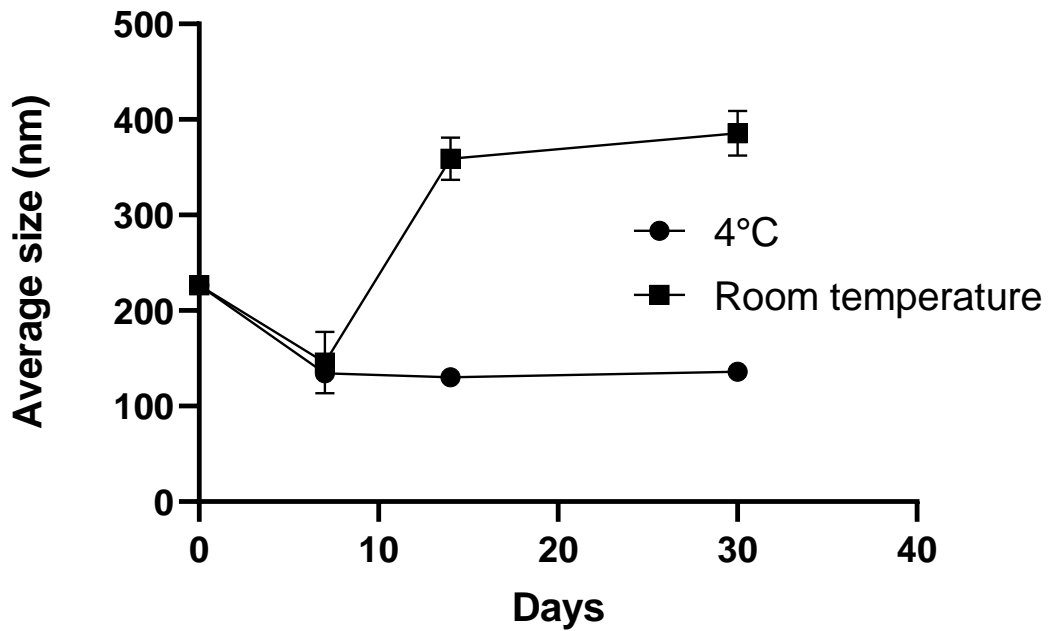
*Figure 3.33: Size stability of (**73**) PLGA NPs (N = 3)*

132
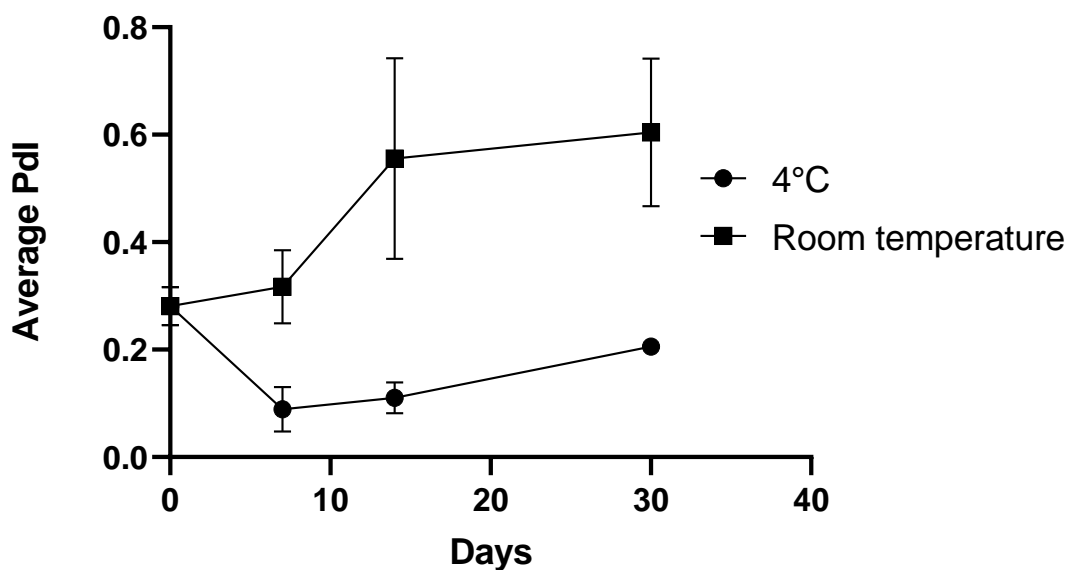
*Figure 3.34: PdI stability of (**73**) PLGA NPs (N = 3)*

3.3.2. <u>Responsiveness to target analytes</u>

The responsiveness of the new NPs to target ROS analytes was studied following the approaches described in section 3.2.5, namely, exposing the functionalised nanoparticles to xanthine/xanthine oxidase, hydrogen peroxide and photodynamically generated singlet oxygen.

3.3.2.1. <u>Superoxide-responsive nanoparticles</u>

The recommended excitation wavelength for (**1a**) is 535 nm, which causes an intense emission at 610 nm[3,104]. Disappointingly, we did not obtain any fluorescence emission in these conditions. The only very minor emission peak was registered at 527 nm following excitation at 485 nm (Fig. 3.35). Interaction with the polymer clearly affected the emissive behaviour of (**1a**)[293]. A very minor increment of the intensity of this band was observed in the presence of superoxide, but this would not be useful to monitor the target analyte.
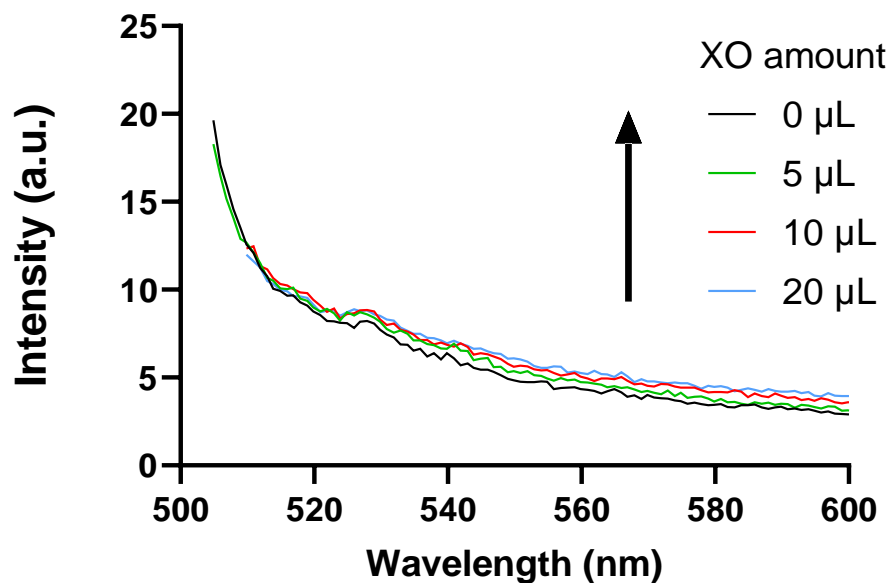
*Figure 3.35: Example of fluorescence emission spectra of (**1a**) on PLGA NPs in the presence of superoxide*

Fig 3.36 and 3.37 show that the presence of peroxide does not alter the profile of the emission spectrum of (**1a**) in NPs but very minor alterations are observed in the presence of singlet oxygen. The emissive profile of (**1a**) in nanoparticles indicate that it could not serve as a sensor.
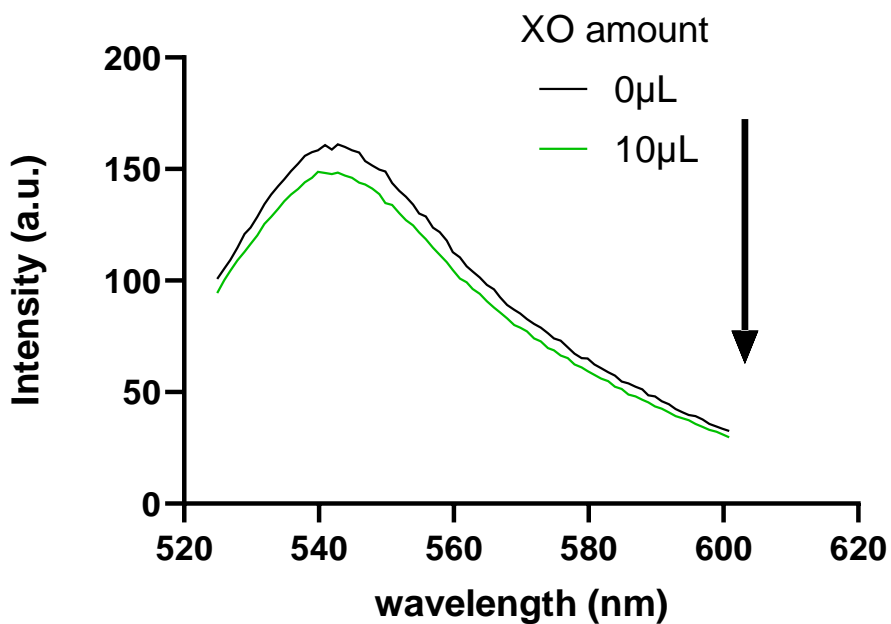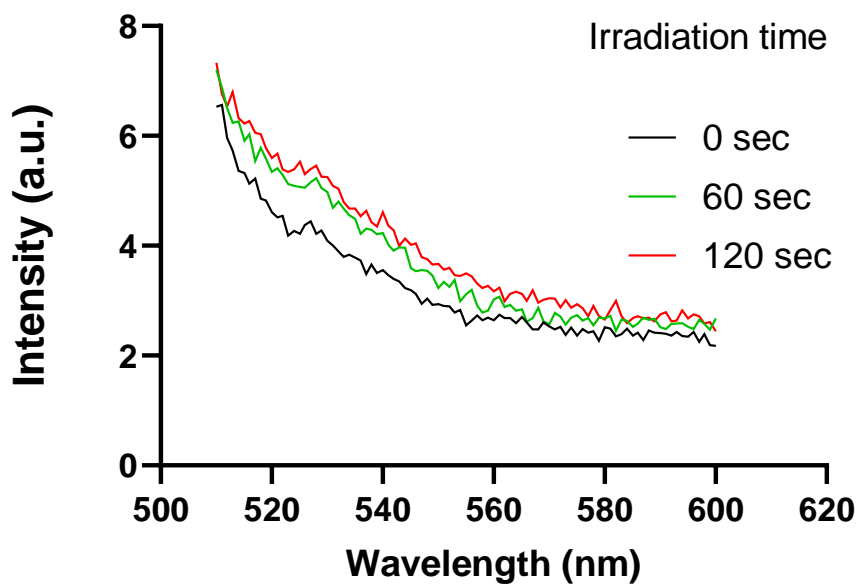
*Figure 3.36: Example of fluorescence emission spectra of (**1a**) on PLGA NPs in the presence of singlet oxygen*
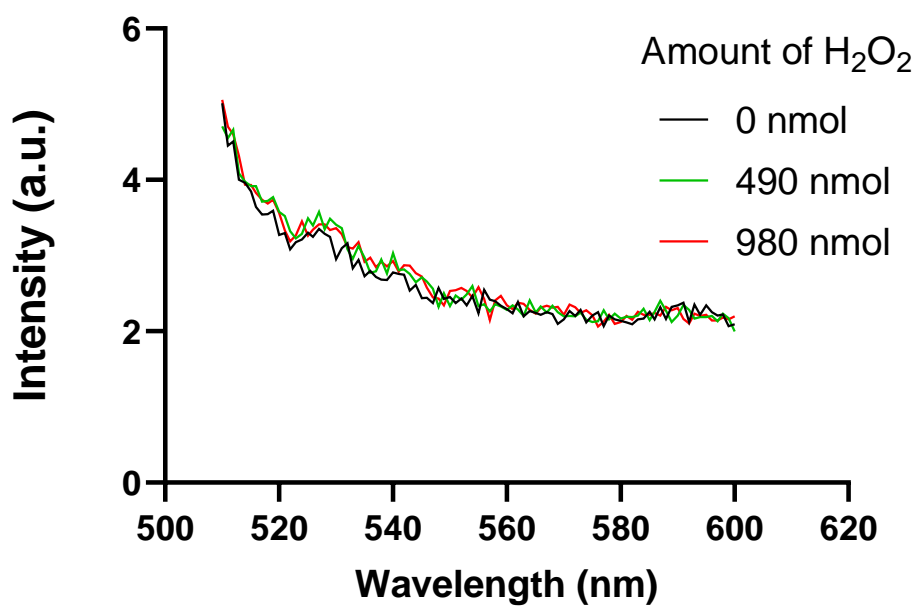
*Figure 3.37: Example of fluorescence emission spectra of (**1a**) on PLGA NPs in the presence of hydrogen peroxide*

3.3.2.2. Hydrogen peroxide-responsive nanoparticles

Unlike what we observed for (**1a**)-containing nanoparticle, (**73**) encapsulated in PLGA NPs maintains a similar behaviour with respect to excitation and emission as that described in the literature[3]. As expected, the fluorescence of (**73**) increases when it is exposed to hydrogen peroxide. Crucially, the fluorescence intensity reaches a maximum very quickly and the increase is not linear but asymptotic (Fig. 3.38 and 3.39). The system was probably saturated and no more sensor was available to react with hydrogen peroxide.
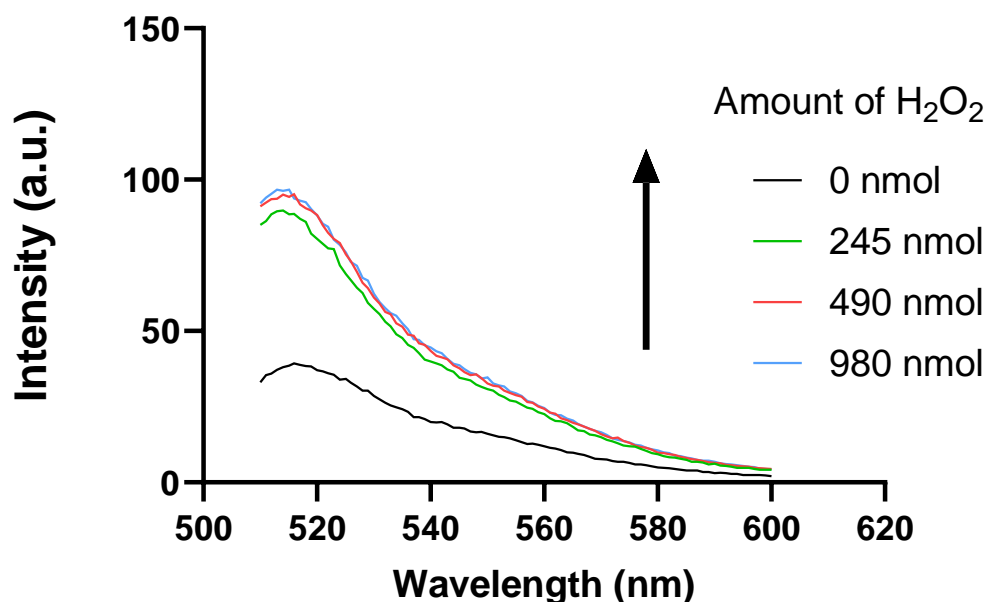
*Figure 3.38: Example of fluorescence emission spectra of (**73**) on PLGA NPs in the presence of hydrogen peroxide*
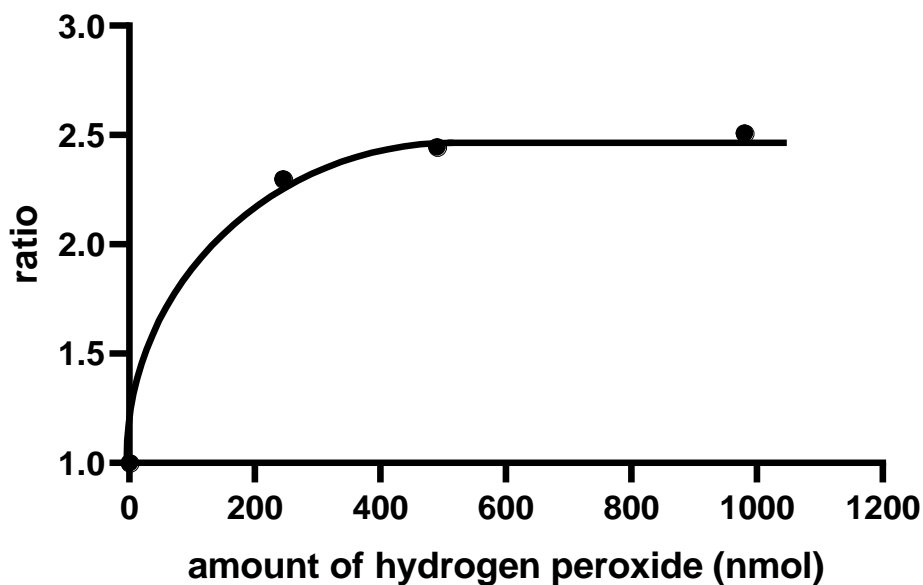
*Figure 3.39: (**73**) PLGA with hydrogen peroxide (ratio versus the amount of hydrogen) (data are normalised with blank experiment: sensor without ROS)*

(**73**) in PLGA shows good selectivity, as exposure to superoxide and singlet oxygen do not cause the fluorescence intensity to increase (Fig 3.40 and 3.41). The small increment observed with superoxide anion can be explained by the fact that superoxide can turn into hydrogen peroxide and not enough catalase was available for the highest concentration of superoxide anion.
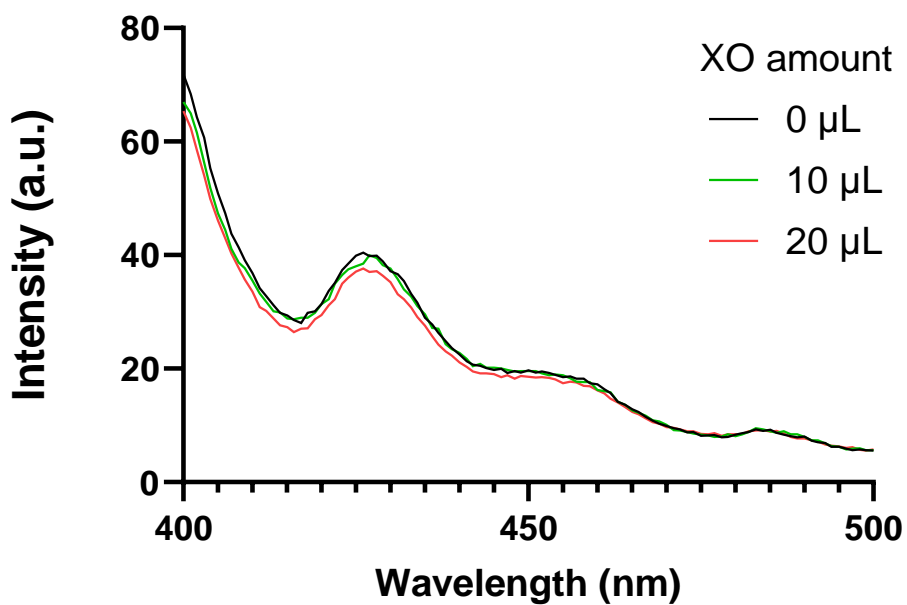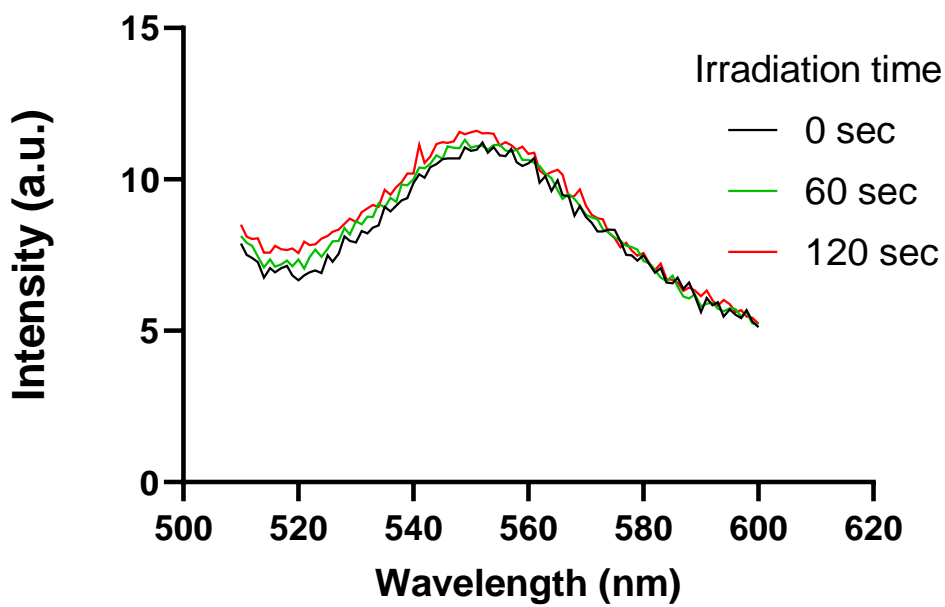
*Figure 3.40: Example of fluorescence emission spectra of (**73**) on PLGA NPs in the presence of singlet oxygen*
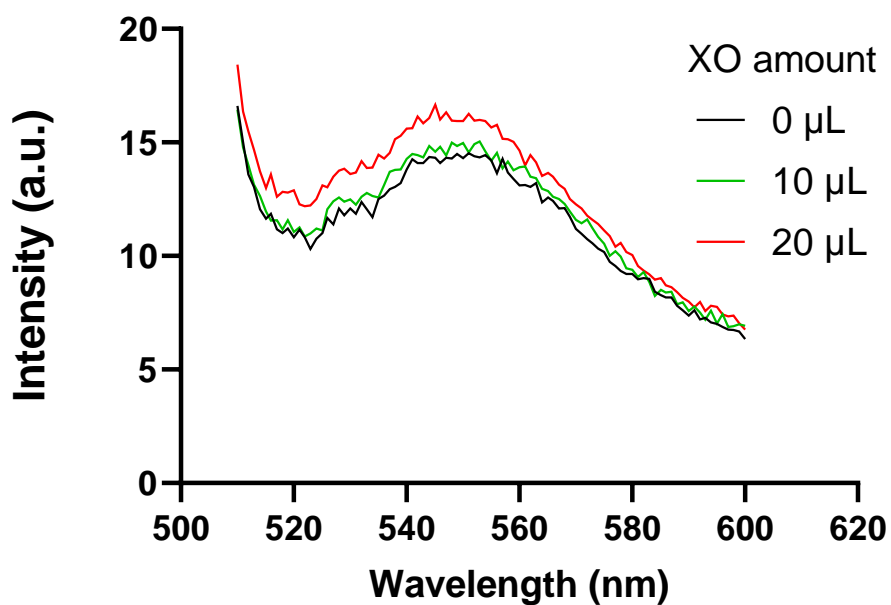
*Figure 3.41: Example of fluorescence emission spectra of (**73**) on PLGA NPs in the presence of superoxide anion*

3.3.2.3. Singlet oxygen-responsive nanoparticles

Compared to free (**15a**) with excitation at 505 nm and emission at 525 nm[63] or nano(**15a**) with excitation at 420 nm and emission at 525 nm[133], (**15a**) on PLGA NPs has an excitation at 474 nm and an emission at 540 nm. That means the PLGA has an influence on the emissive behaviour of the sensor. With singlet oxygen (Fig. 3.42), (**15a**) shows good responses as it was expected. The fluorescence intensity increase shows a good linearity, which could be useful to quantify singlet oxygen in the range observed (Fig. 3.43).
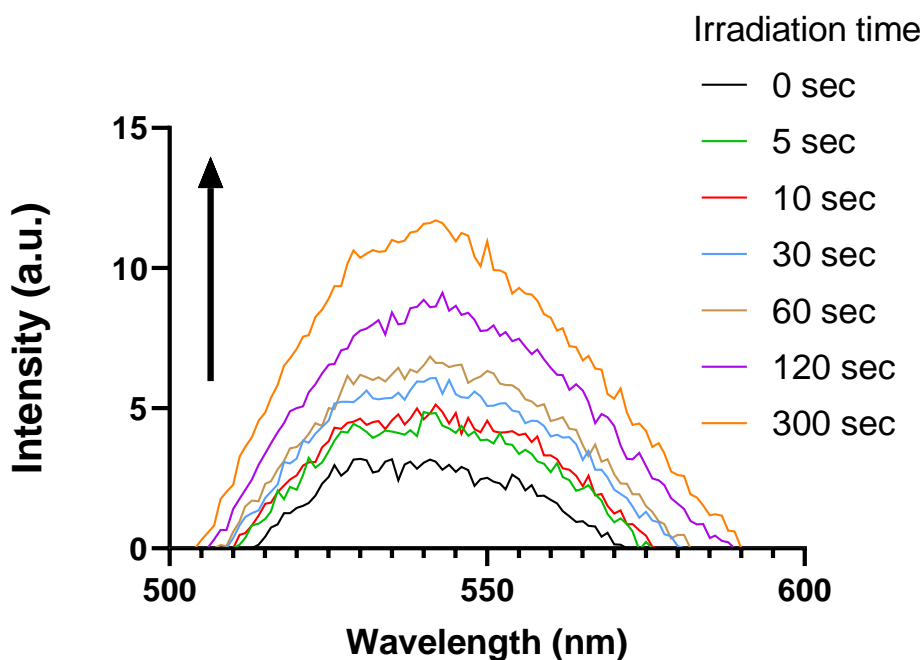
*Figure 3.42: Example of fluorescence emission spectra of (**15a**) on PLGA NPs in the presence of singlet oxygen*
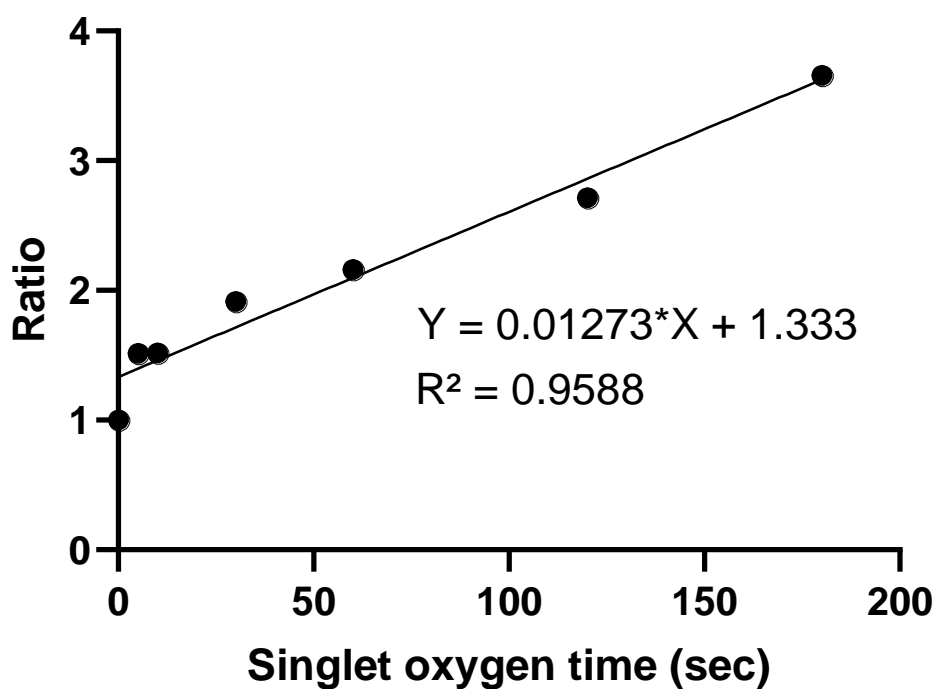
*Figure 3.43: Linear regression of ratio of (**15a**) PLGA (data are normalised with blank experiment: sensor without ROS)*

Unfortunately, in the presence of superoxide radical anion, (**15a**) displays an increase of fluorescence intensity, but to a lesser extent than in the presence of singlet oxygen (Fig. 3.44). No increase of intensity of emission was observed in the presence of hydrogen peroxide, indicating a promising, if partial, selectivity of response to the target analyte (Fig. 3.45).
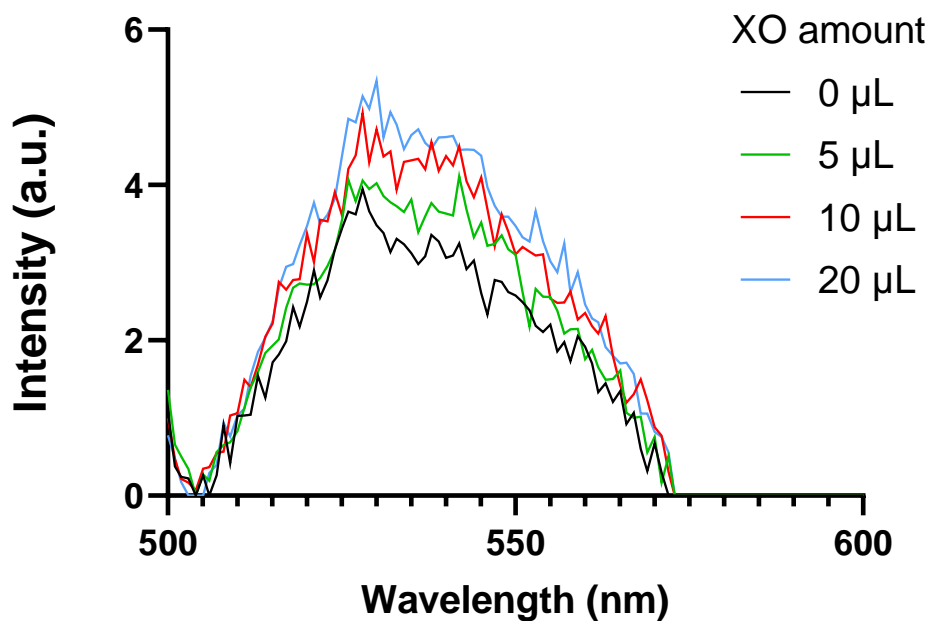
*Figure 3.44: Example of fluorescence emission spectra of (**15a**) on PLGA NPs in the*

presence of superoxide anion
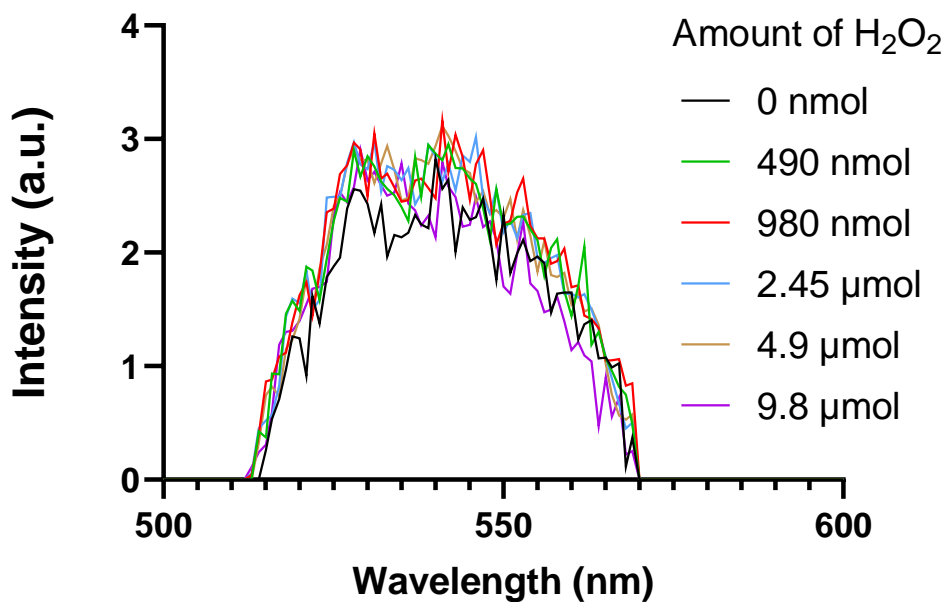
*Figure 3.45: Example of fluorescence emission spectra of (**15a**) on PLGA NPs in the*

presence of hydrogen peroxide

3.3.2.4. <u>Evaluation of individual responses in a nanosensors mixture</u>

The inability to covalently link (**1a**) and (**73**) to PLGA posed a challenge to the synthesis of dual sensors, via the strategy we previously adopted and described in section 3.3. This encouraged us to explore the responsiveness and the selectivity of the individual sensors as a mixture. Samples were prepared containing comparable amounts of nanosensors of each type ((**15a**)-PLGA, (**1a**)-PLGA, (**73**)-PLGA). Each sample was exposed to one particular ROS and the fluorescence of the three sensors was recorded. The ROS were generated according to the methods previously described (section 3.2).

The results of the experiment show that the performance of the single sensors decrease in the presence of other sensors (Fig. 3.46). Some of the selectivity observed with single sensors was lost and the responsiveness decreased. In short, we could not observe the target simultaneous and independent monitoring of ROS as we hoped. We speculate that in some cases interference may occur between the absorption/emission wavelength of the sensors[294,295].
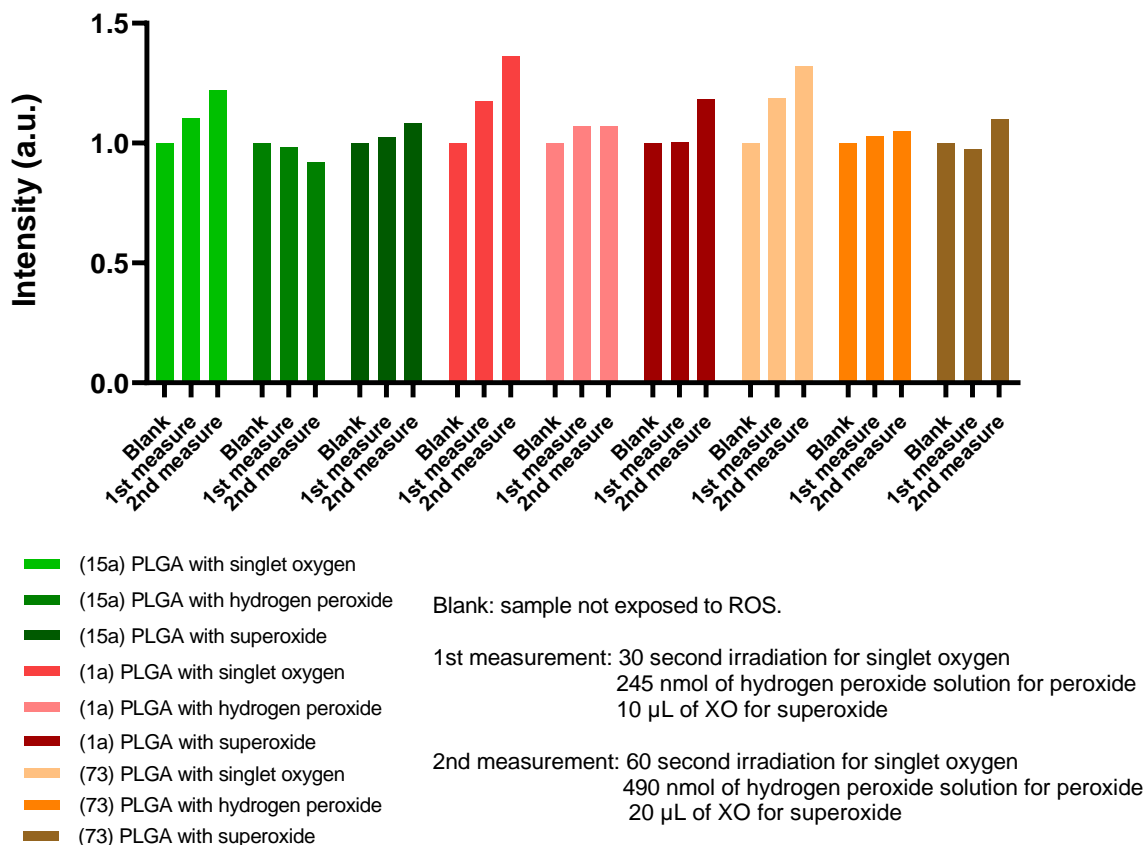
Figure 3.46: Results for commercial sensors on PLGA mixture with ROS (N = 1)

3.4. <u>Overview of the behaviour of the nanosensors</u>

In this section we intend to provide an overview of the behaviour of all the nanosensors generated in this work towards the different ROS analytes.

3.4.1. <u>Response to superoxide radical anion</u>

In the presence of superoxide anion (Fig. 3.47), (**43**)-PLGA and (**15a**)-PLGA increase their fluorescence, while (**1a**)-PLGA and (**73**)-PLGA are stable and (**58**)-PLGA an (**72b**)-PLGA slightly decrease. The behaviour of (**15a**) (fluorescence intensity should not to vary) and (**1a**) (should increase) nanosensors are unexpected. Notably, the

increment of (**43**) nanosensors is linear in this range of experiments, that means it is possible to quantify superoxide with this nanosensor.
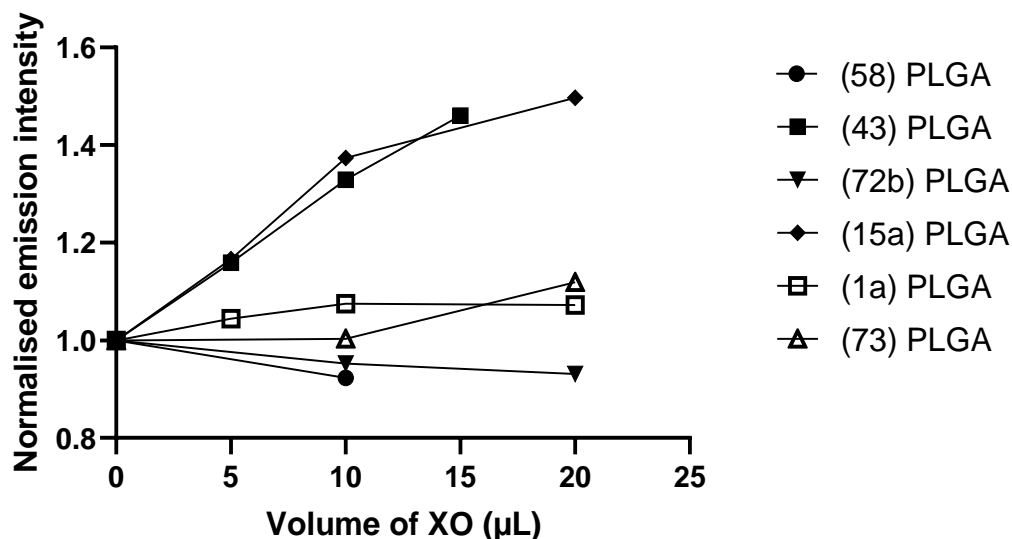
Figure 3.47: Nanosensors reactivity with superoxide anion (emission signals are normalised with blank experiment: sensor without ROS)

3.4.2. <u>Hydrogen peroxide</u>

In the presence of hydrogen peroxide (Fig. 3.48), the fluorescence emission of (**73**) NPs increase until it reaches a maximum, while (**58**) NPs show an unexpected decrease of fluorescence emission. The other nanosensors show the expected stability towards this analyte, indicating a lack of response.
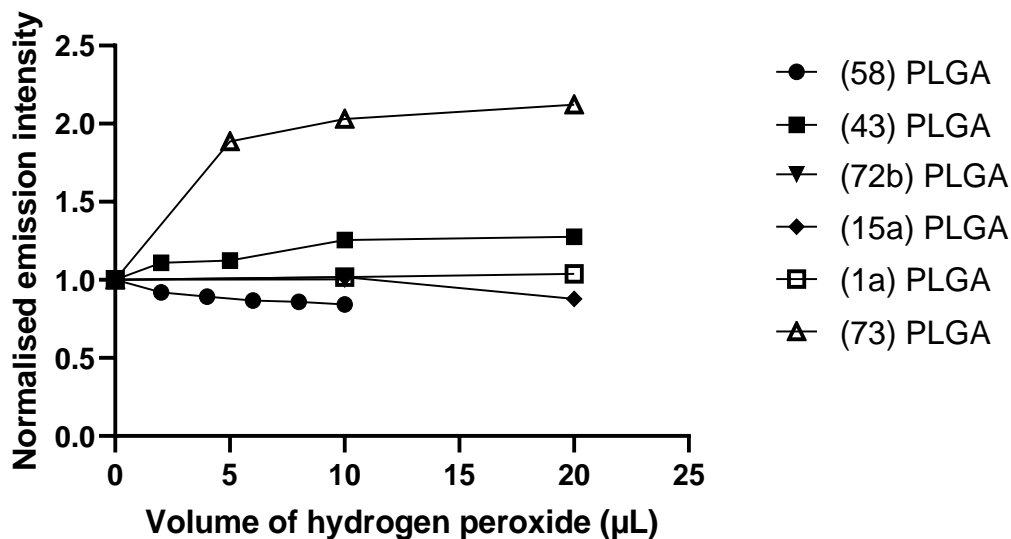
Figure 3.48: Nanosensors reactivity with hydrogen peroxide (emission signals are normalised with blank experiment: sensor without ROS)

3.4.3. <u>Singlet oxygen</u>

In the presence of singlet oxygen, (**15a**)-containing nanosensors show the expected increase of fluorescence emission (Fig. 3.49) (**72b**)-nanosensors show a decrease in fluorescence emission, as expected, but too limited to be useful in monitoring this analyte. The remaining nanosensors show lack of responsiveness to singlet oxygen, as their fluorescence intensity is unvaried. (**1a**)-PLGA displays a minor increase for long irradiation times.

145
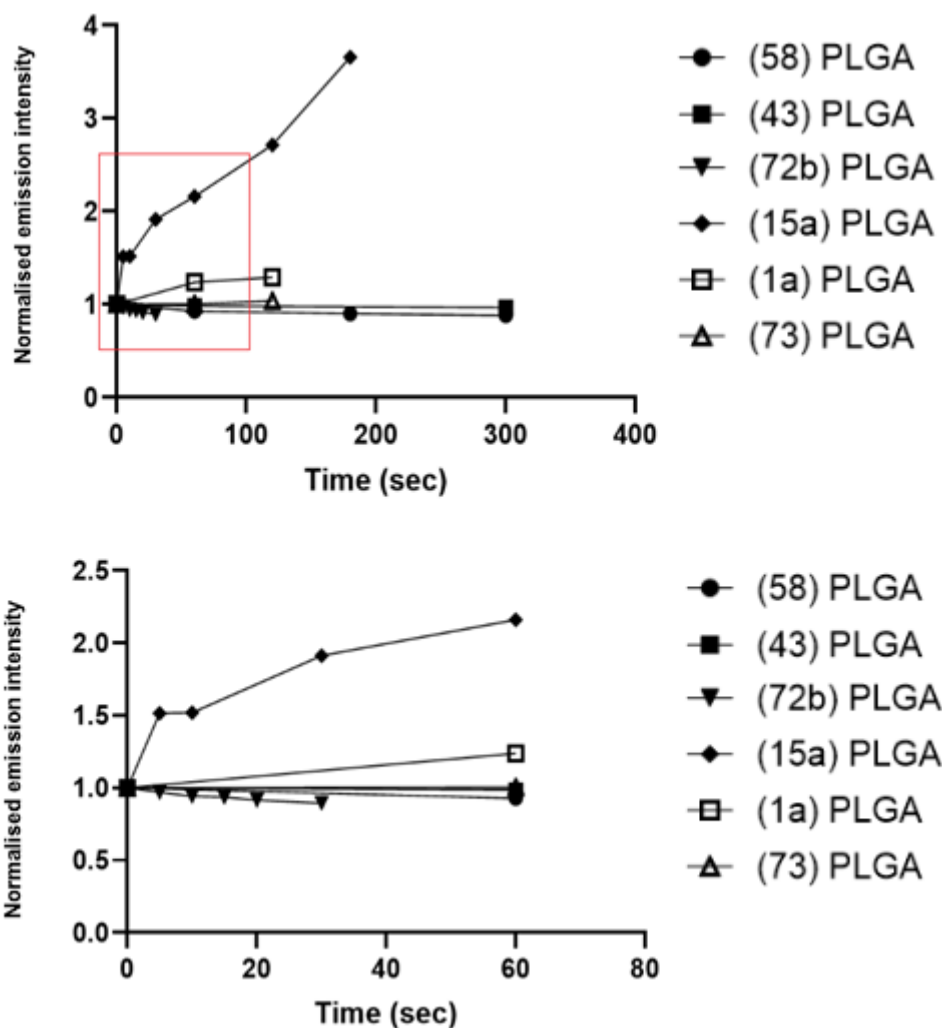
Figure 3.49: Nanosensors reactivity with singlet oxygen (emission signals are normalised with blank experiment: sensor without ROS)

3.5. Chapter conclusion

We obtained three target conjugates with our new sensors: (**43**)-PLGA, (**58**)-PLGA and (**72b**)-PLGA. By using the single emulsion method, stable nanosensors were obtained. The fluorescent behaviour the nanosensors are similar to those of the corresponding stand-alone probe and PLGA conjugate. A comparison of the response of the nanosensors grafted with the new molecular probes with similar nanospecies

containing encapsulated commercial probes (i.e., (**1a**), (**15a**) and (**73**)) showed interesting results.

Because of its linear response to superoxide anion and its good stability to the other ROS, (**43**)-PLGA is a good nanosensor for superoxide anion in comparison with (**1a**)-PLGA.

Because of its response to hydrogen peroxide and stability to various ROS, (**73**)-PLGA showed a more favourable behaviour as a sensor for hydrogen peroxide. One of its limitation is the lack of linearity for the quantification. (**58**)-PLGA showed an unexpected behaviour that does not encourage its use as a hydrogen peroxide sensor.

Lastly, (**15a**)-PLGA is a more promising sensor compared to (**72b**)-PLGA for singlet oxygen because of its higher sensitivity and linearity of answer, which gives the possibility to quantify ROS. The low stability of both singlet oxygen sensors towards superoxide anion seems to be the most important limitation.

Chapter 4. *Cell studies*

The species displaying the most promising behaviour in solution were studied as intracellular nanosensors. (**43**), (**15a**) or (**73**) responded as expected in the presence of superoxide, singlet oxygen and hydrogen peroxide, respectively. In this part, we report the results of our studies on the responsiveness of the sensors in the presence of subcellular components and biomacromolecules in order to assess the applicability of the nanosensors within cell. We focused on the ability of the nanosensors to enter cells, on their toxicity and efficiency as ROS sensors. The response of the nanosensors was compared with the response of the stand-alone sensors.

To study the responsiveness of sensors in cells, the choice of the cell line is crucial. THP1 is a monocytic cell line derived from leukaemia that is often used as *in vitro* cancer cell models and as representative of monocytes and macrophage immune cells[296–298]. The reactivity of THP1 with ROS to study the monocyte-macrophage differentiation[298] or apoptosis[297] makes this cell line a good candidate to study the responsiveness of our sensors.

ROS were generated by the addition of phorbol-12-myris-tate-13-acetate (PMA). PMA induces cell differentiation at a range from 20 ng/mL[299], which is a particular kind of cellular division that produces more specialised types of cells, by inducing oxidative stress[298,300–302]. Firstly, superoxide radical anion is generated and then other ROS as hydrogen peroxide are produced thanks to SOD present in cells (Chapter 1. Fig. 1.3). The extent of superoxide formation with PMA depends on the concentration and time of exposure. For example, cells exposed at more than 50 ng/mL for 3–4 days results in significant cell death, in contrary, cells differentiated in 20 ng/mL of PMA were more resistant to rapid cell death after 3-4 days[299]. For our study, the main limitation of this

procedure is the fact that it does not allow us to differentiate between superoxide or hydrogen peroxide because PMA will generate both.

High levels of singlet oxygen are not produced in the homeostatic conditions in the cells, so photosensitisers must be used to increase the levels of this ROS[59,303]. In this part of the work we used the water-soluble porphyrin photosensitiser described in Chapters 2 and 3. Following incubation with the sensors and the photosensitiser, cells were exposed to blue light (400 nm) for the generation of singlet oxygen.

4.1. <u>Flow cytometry</u>

Flow cytometry[304] measures optical and fluorescent characteristics of single cells. Physical properties, such as size (represented by forward angle light scatter (FSC-A)) and cytoplasmic complexity (*i.e.* granularity) (represented by right-angle scatter (SSC-A)) can resolve certain cell populations by autofluorescence. Flow cytometry can also evaluate the fluorescence of labelled cells.

Inside a flow cytometer, cells in suspension are drawn by a stream that allow the cells to pass individually through an interrogation point. At the interrogation point, a beam of monochromatic light, usually from a laser (488 nm, in our case), intersects the cells. Light is scattered off in all directions and is collected *via* optics that direct it to a series of filters (four filters are present on flow cytometer: 533/30, 585/40, 670LP and 675/25 nm). The light signals are then detected by photomultiplier tubes and digitized for computer analysis (Fig 4.1).
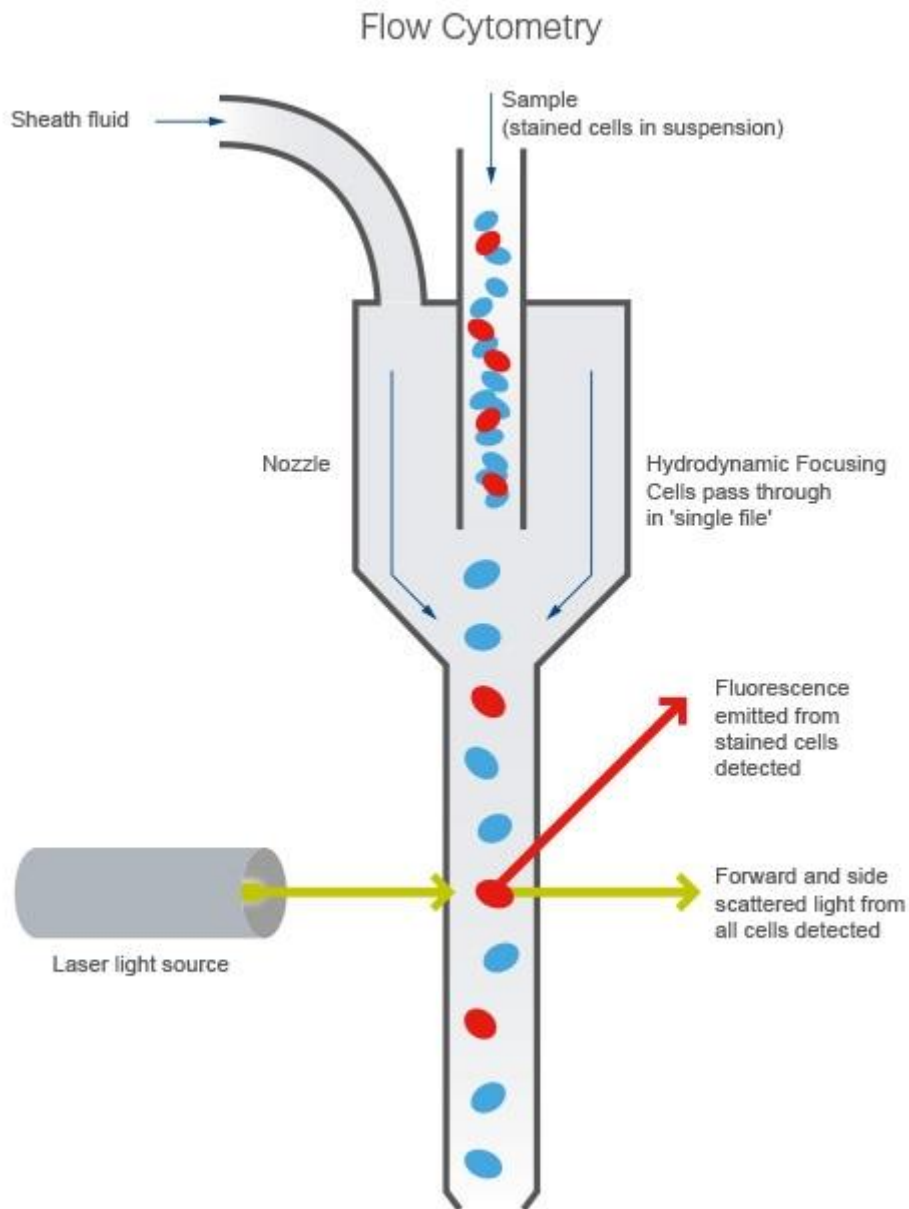
Flow Cytometry

Figure 4.1: Overview of the flow cytometer

The distribution of THP1 population on a flow cytogram is clear with area for apoptotic and viable cells (Fig. 4.2). Because of their smaller size due to their shrinking and to the formation of blebs and the fragmentation of organelles during the apoptosis[305], apoptotic cells are on the left side of the graph while viable cells stay at the bottom because of their bigger size and their lack of many fragmented organelles. This separation between both kind of cells and their distribution can give us an idea of the cytotoxicity of our NPs in cells.

We can see on figure 4.2 that apoptotic (in the left box) cells with all fragments are more complex (represented on SSC-A), than the viable cells (in the right box). Moreover, sizes (represented on FSC-A) are more important for viable cells than apoptotic one. Finally, viable cells are more represented with 91.2 % of them compared to 7.1 % for apoptotic cells.
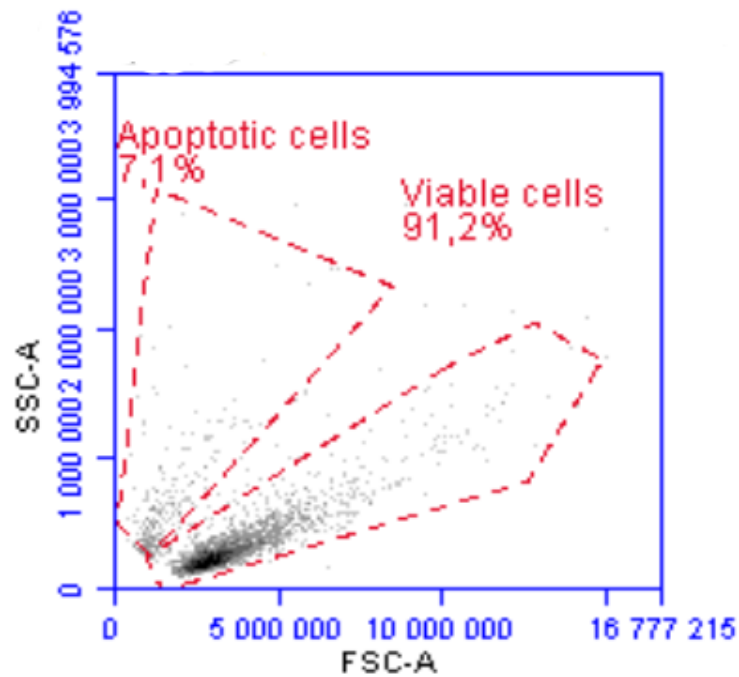
Figure 4.2: THP1 cells distribution

4.2. Microscopy

Flow cytometry is a method to quantify the fluorescence associated to a single cell, but it does not give any information about whether the fluorophore is inside the cell or about its intracellular localisation. The most suitable technique to obtain this kind of information is fluorescence microscopy.

Similar to the widefield microscope, the confocal microscope uses fluorescence optics[306]. Instead of illuminating the whole sample at once, laser light is focused onto

151

a defined spot at a specific depth within the sample. This leads to the emission of fluorescent light at exactly this point. A pinhole inside the optical pathway cuts off signals that are out of focus, thus allowing only the fluorescence signals from the illuminated spot to enter the light detector (Fig. 4.3).
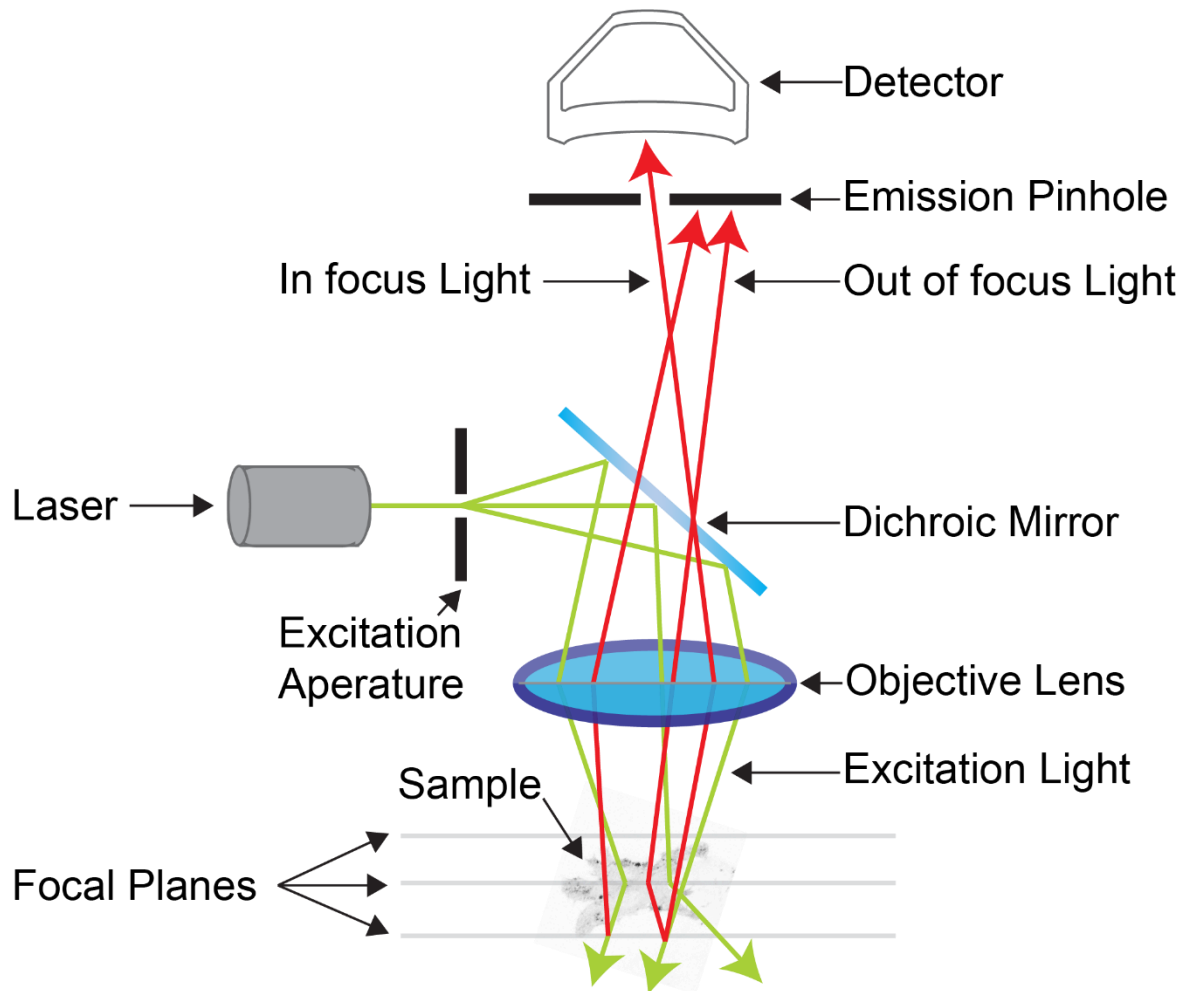
Figure 4.3: Confocal microscope principle

By scanning the specimen in a raster pattern, images of one single optical plane are created. 3D objects can be visualized by scanning several optical planes and stacking them using a suitable microscopy deconvolution software (z-stack). This last option allows us to study the presence and localisation of our sensor inside the cells.

152

4.3. Incubation time

To determine the optimal incubation time for maximum sensor internalisation and minimal damage to cells, THP1 were incubated with nanosensors solution at 1 mg/mL in PBS at different time at 37 °C with 5% of CO_2. Cell solutions were analysed by flow cytometry by following the evolution of the fluorescence. The incubation of sensors on PLGA is quick and after 30 min cells are mostly at their maximum signal (Fig. 4.4). This time was chosen for the rest of the studies.
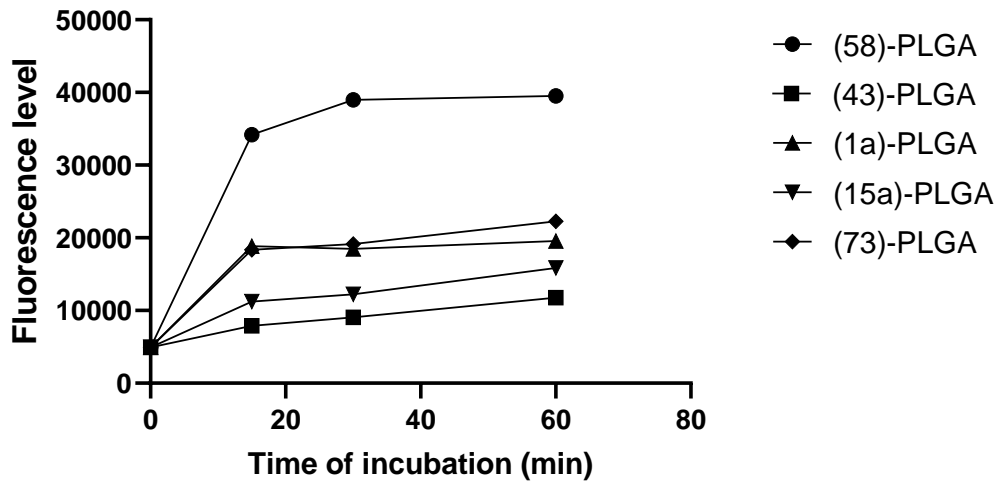
Figure 4.4: Determination of incubation time of sensors on PLGA

4.4. Cell internalisation of the sensors

To prepare cells for confocal microscopy, the literature encourages us to fixe THP1 cells to maintain cellular structure[307,308]. PMA is an agent that can induce ROS production and the cell differentiation generated is useful to fix cellular structure[302,309]. The cells were differentiated and exposed to a solution containing nanosensors and PMA for 30 minutes, they were isolated by centrifugation, washed with PBS solution

and examined on the confocal microscope (see experimental part). Parameters of microscope for the next figures are the same and described in the experimental part.

(**43**)-PLGA or stand-alone (**43**) were both observed to penetrate into the cells (Fig. 4.5), and the z-stack analysis shows that the sensors are inside the cell.
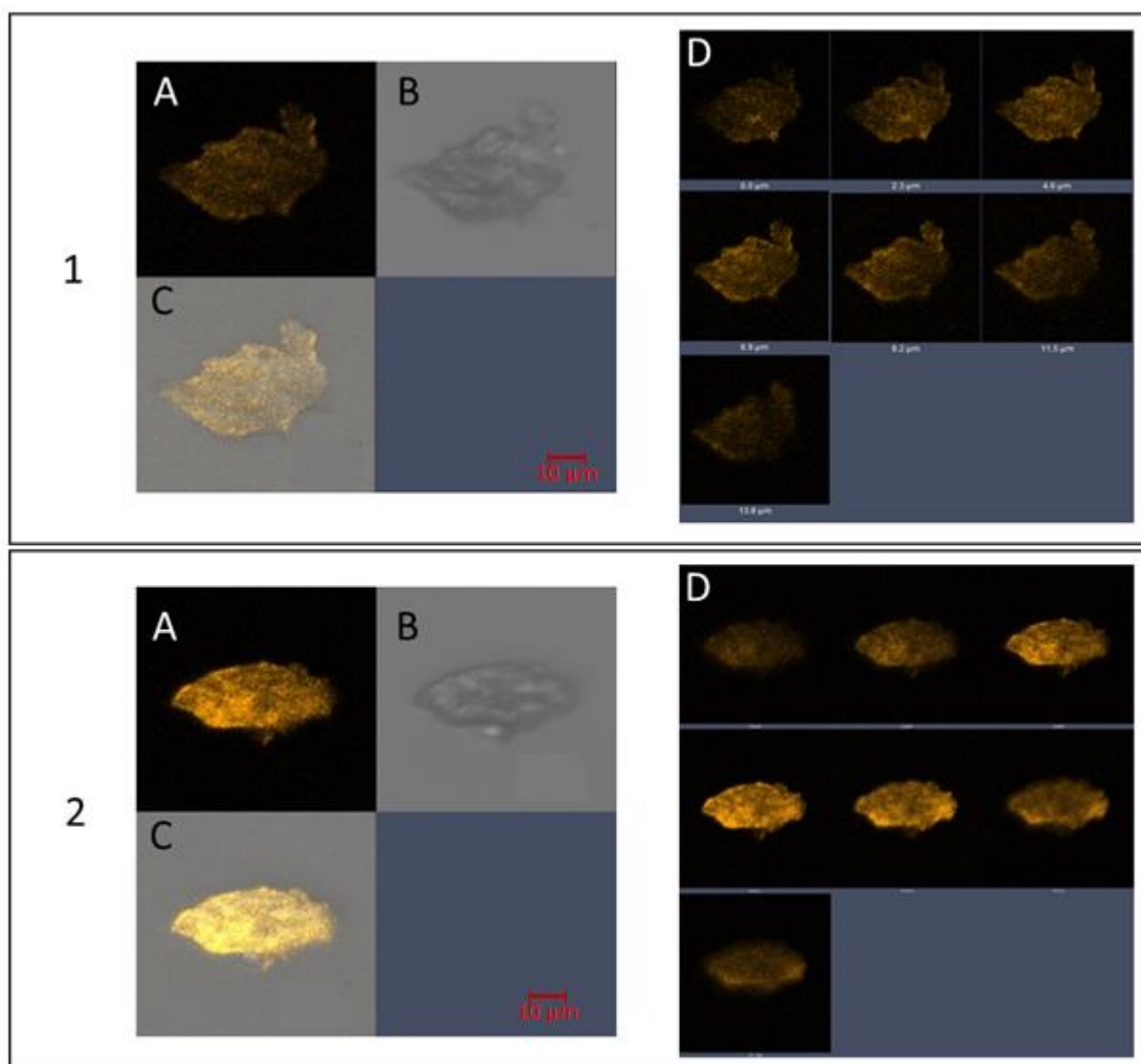
*Figure 4.5: Confocal microscopy pictures of THP1 incubated with (**43**) (1) and with (**43**)-PLGA (2). A) sensor fluorescence; B) white field; C) superposition of A and B; D) sensor fluorescence at different focal plans (0 µm, 2.3 µm, 4.6 µm, 6.9 µm, 9.2 µm, 11.5 µm and 13.8 µm).*

As above, both stand-alone (**58**) and (**58**)-PLGA NPs penetrate the cells (Fig. 4.6). No measurable difference was observed between the internalisation behaviour of sensors whether they are associated or not to PLGA NPs.
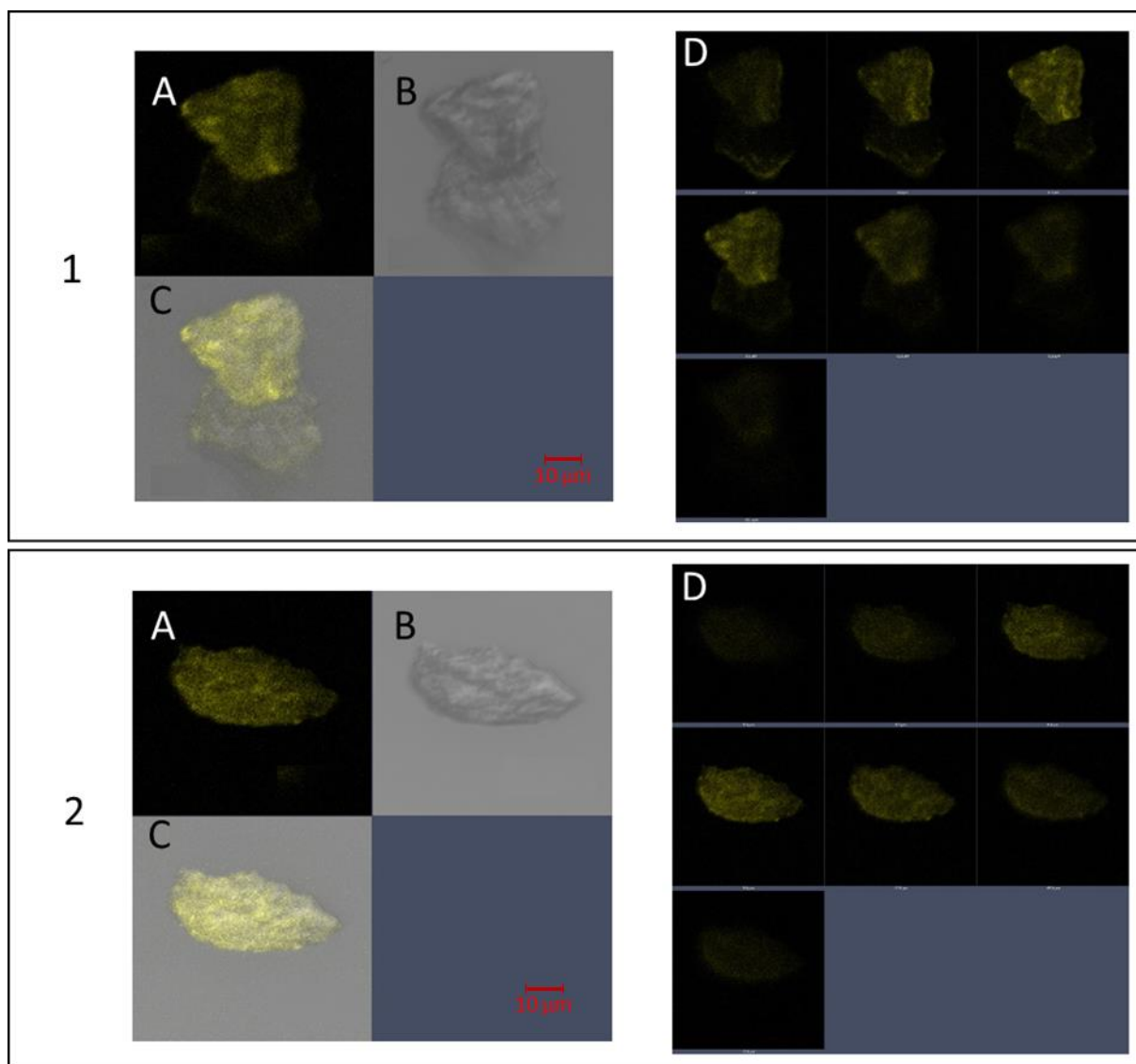
*Figure 4.6: Confocal microscopy pictures of THP1 incubated with (**58**) (1) and with (**58**)-PLGA (2). A) sensor fluorescence; B) white field; C) superposition of A and B; D) sensor fluorescence at different focal plans (0 µm, 2.3 µm, 4.6 µm, 6.9 µm, 9.2 µm, 11.5 µm and 13.8 µm).*

Similarly, both NPs-conjugated and stand-alone (**15a**) are able to penetrate the cells (Fig. 4.7). The internalisation of stand-alone sensor seems more efficient than the corresponding NPs-supported sensor. Some brighter spots seem to indicate that the localisation of the nanosensors in the cells is restricted to certain compartments. A deeper characterization should be useful to show where sensors are accumulated by referencing the differencing the different organelles withs labels.
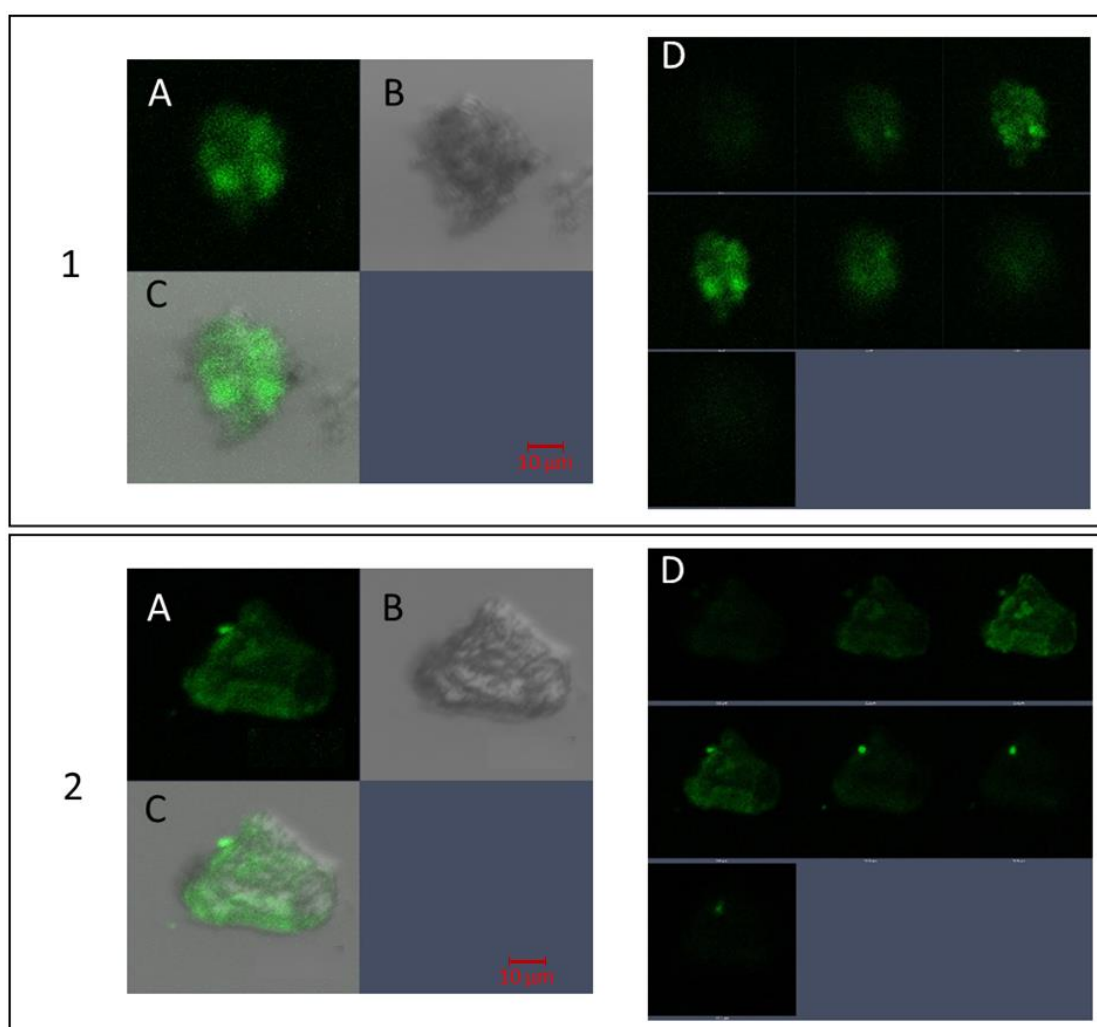
*Figure 4.7: Confocal microscopy pictures of THP1 incubated with (**15a**) (1) and with (**15a**)-PLGA (2). A) sensor fluorescence; B) white field; C) superposition of A and B; D) sensor fluorescence at different focal plans (0 µm, 2.3 µm, 4.6 µm, 6.9 µm, 9.2 µm, 11.5 µm and 13.8 µm).*

As above, (**1a**) proves able to penetrate cells both as stand-alone sensor and associated to NPs (Fig. 4.8). In this case, the nanosensors seem to be internalised more efficiently.
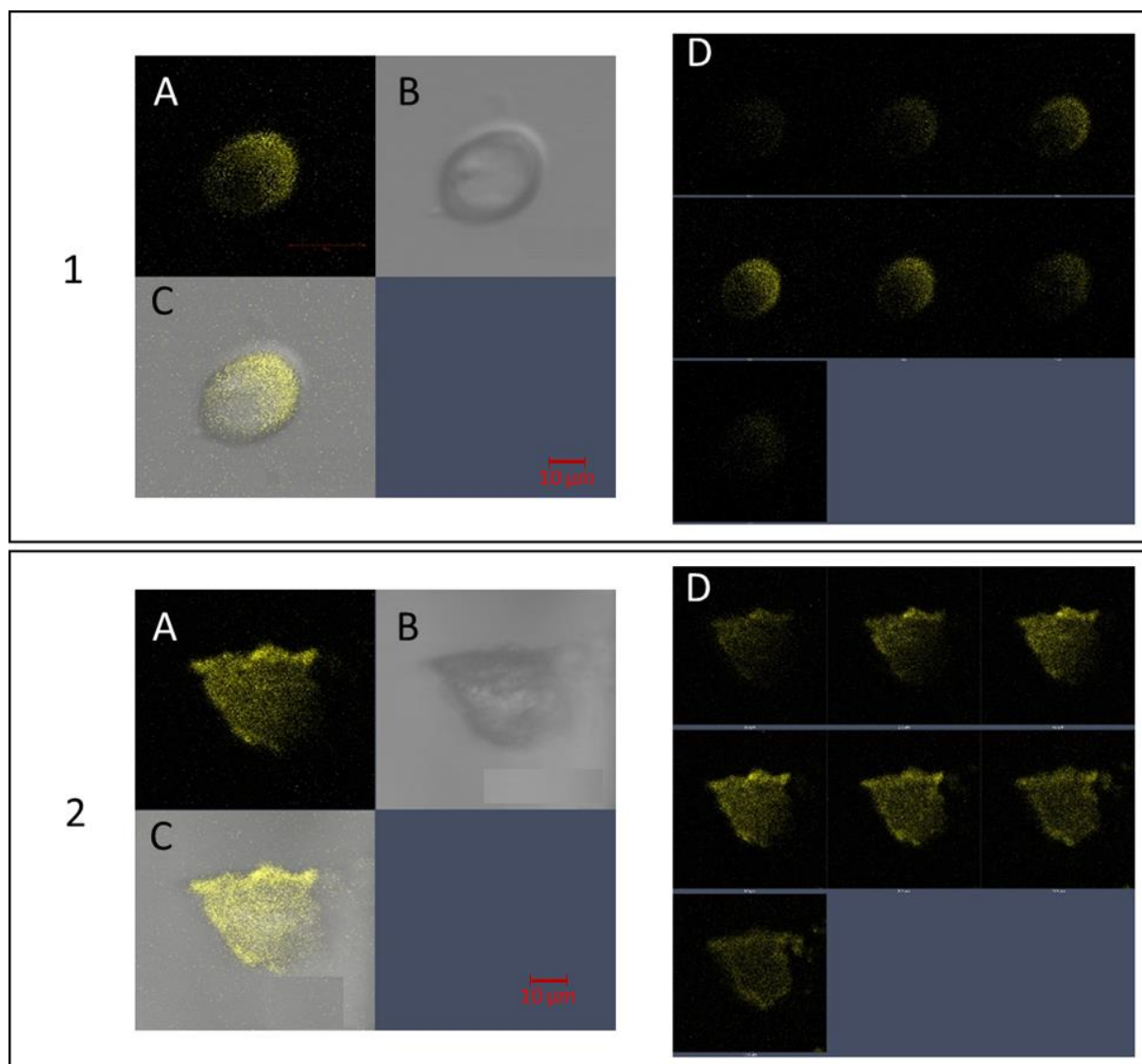
*Figure 4.8: Confocal microscopy pictures of THP1 incubated with (**1a**) (1) and with (**1a**)-PLGA (2). A) sensor fluorescence; B) white field; C) superposition of A and B; D) the location of sensor at different local plan (0 µm, 2.3 µm, 4.6 µm, 6.9 µm, 9.2 µm, 11.5 µm and 13.8 µm).*

Finally, for (**73**), we can observe that the internalisation is achieved when the sensor is free (Fig. 4.9(1)). (**73**)-PLGA NPs are internalised but they seem to localise only in some organelles (Fig. 4.9(2)) but as for (**15a**) a deeper investigation should help for this interpretation and to be precise.
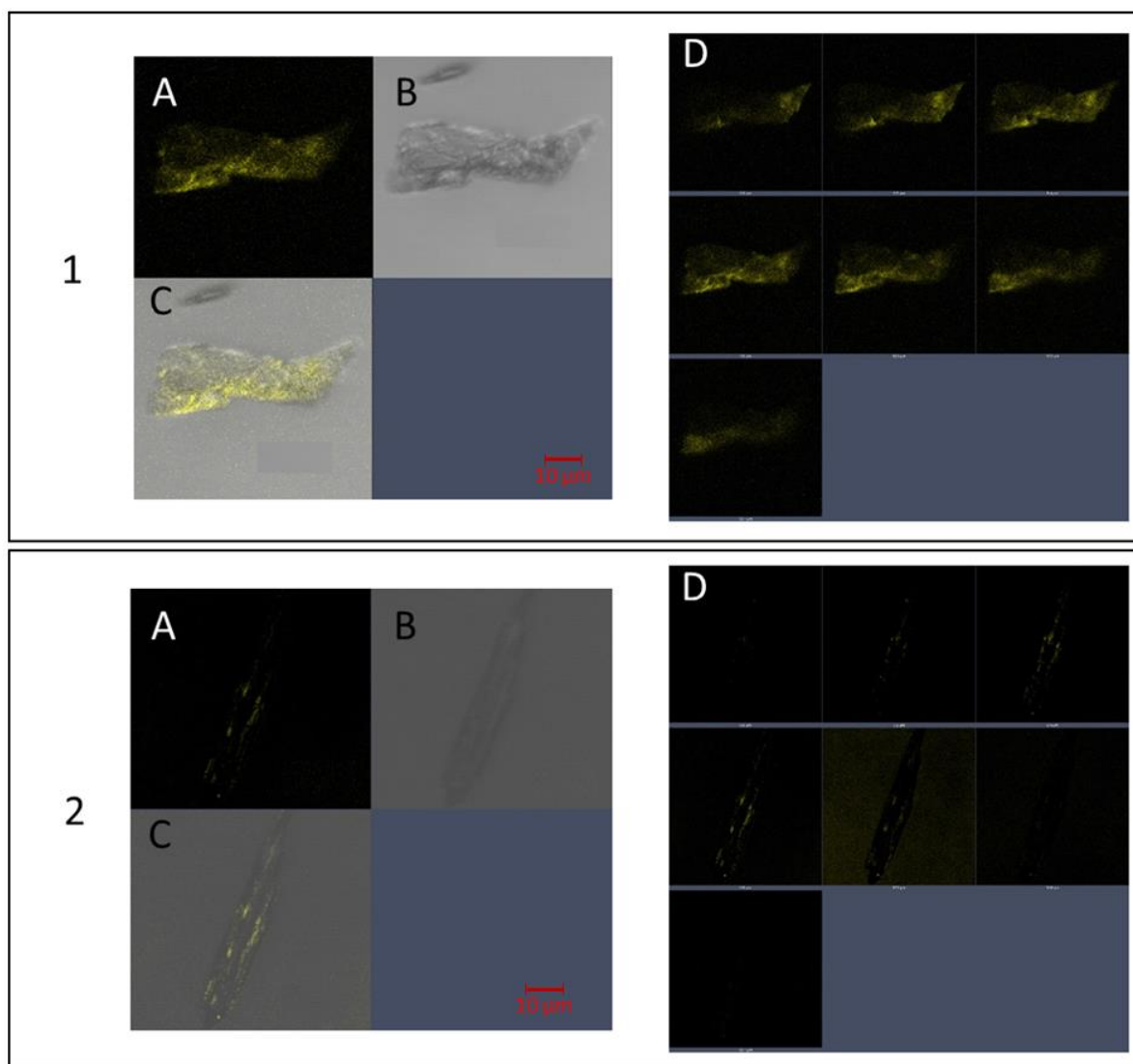
*Figure 4.9: Confocal microscopy pictures of THP1 incubated with (**73**) (1) and with (**73**)-PLGA (2). A) sensor fluorescence; B) white field; C) superposition of A and B; D) sensor fluorescence at different focal plans (0 µm, 2.3 µm, 4.6 µm, 6.9 µm, 9.2 µm, 11.5 µm and 13.8 µm).*

4.5. Cytotoxicity

We next investigated the effect of the sensors on cell viability. The cytotoxicity of the stand-alone sensors and of the nanosensors was evaluated.

To this end, 100 µL TPH-1 cells were incubated with NPs or stand-alone sensors over a volume range of 0 to 200 µL of solution at 1 mg/mL in PBS. Although the addition of sensor solution will dilute the cells in the sample, this will not affect the outcome of the experiment because flow cytometer counts the number of cells regardless of the sample concentration. The viability of cells was evaluated by flow cytometry by analysing the distribution between viable cells (P4) and apoptotic cells (P5) given on cytogram (Fig. 4.10).

V_{PLGA} = 0 mL

H11 Cells
Gate: P3

P5
1,2%

P4
97,3%

V_{PLGA} = 50 mL

F01 PLGA 50
Gate: P3

P5
2,8%

P4
95,8%

V_{PLGA} = 100 mL

F02 PLGA 100
Gate: P3

P5
1,7%

P4
96,7%

V_{PLGA} = 200 mL

F03 PLGA 200
Gate: P3

P5
4,3%

P4
93,4%
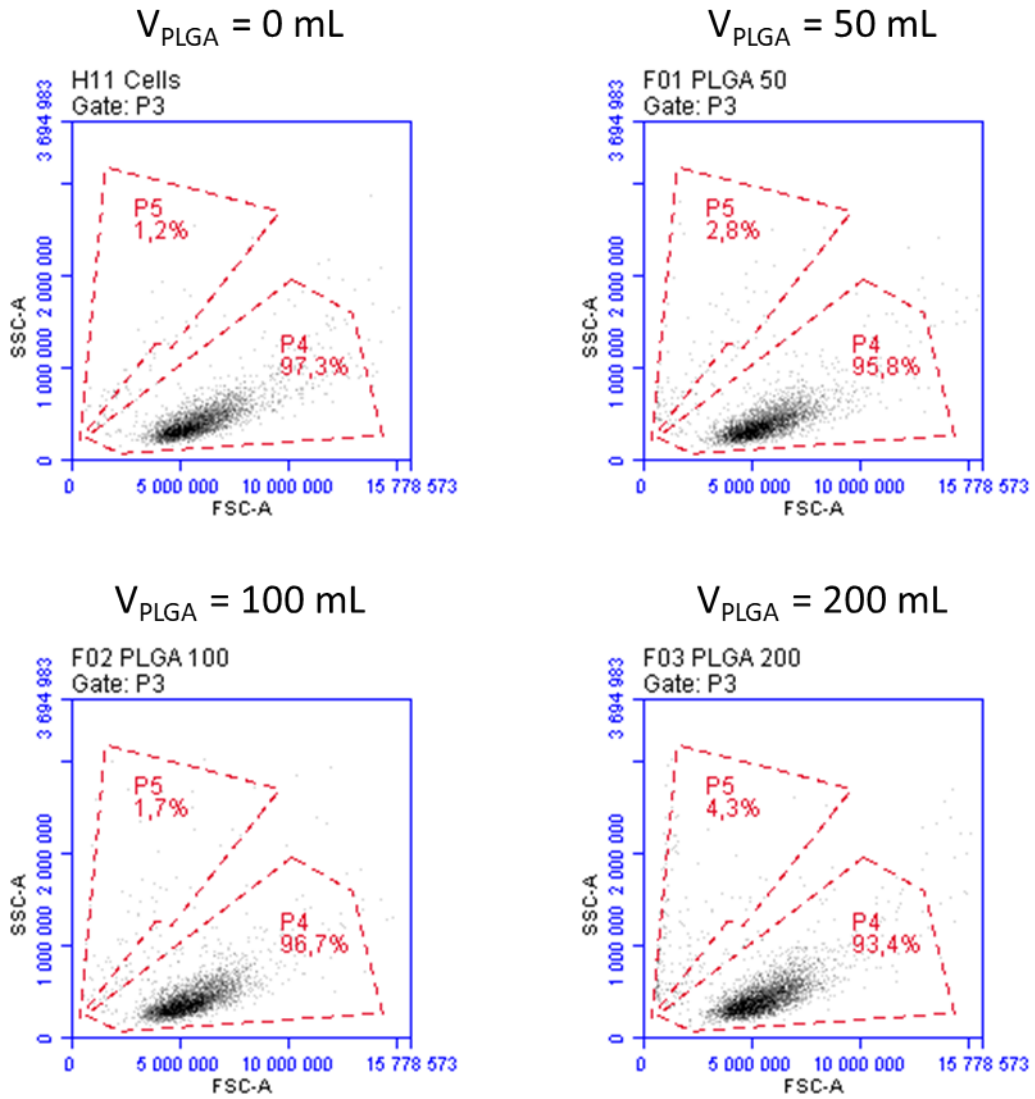
Figure 4.10: Example of distribution to analyse cytotoxicity of PLGA on THP1 cells

First, the effect of PLGA alone is on cell viability was assessed. Cell viability remained constant as the concentration of polymer increased (Fig. 4.11) and PLGA was not particularly toxicity for THP1 cells.
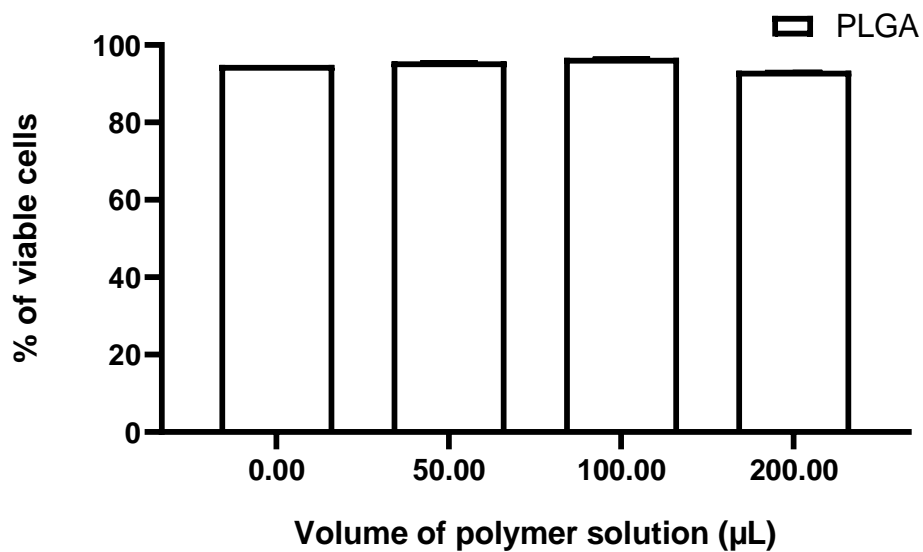
Figure 4.11: Cytotoxicity of PLGA (N = 3)

As shown in Figures 4.12 to 4.16, the percentage of viable cells is constant both in the presence of stand-alone sensors and PLGA-sensor NPs, thus demonstrating the low toxicity of sensors and nanosensors for THP1 with apoptosis pathway.
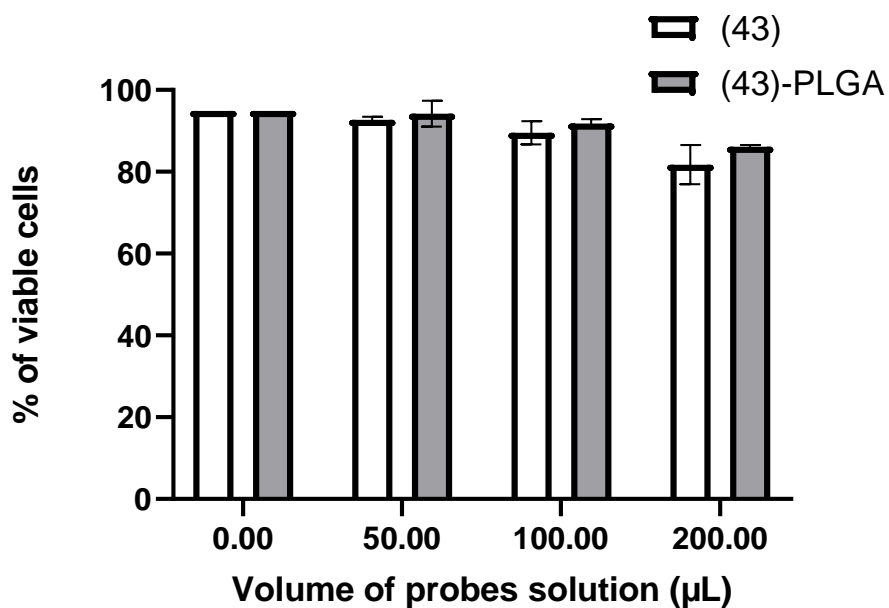
*Figure 4.12: Cytotoxicity of (**43**) (stand-alone sensor and nanosensors) (N = 3)*
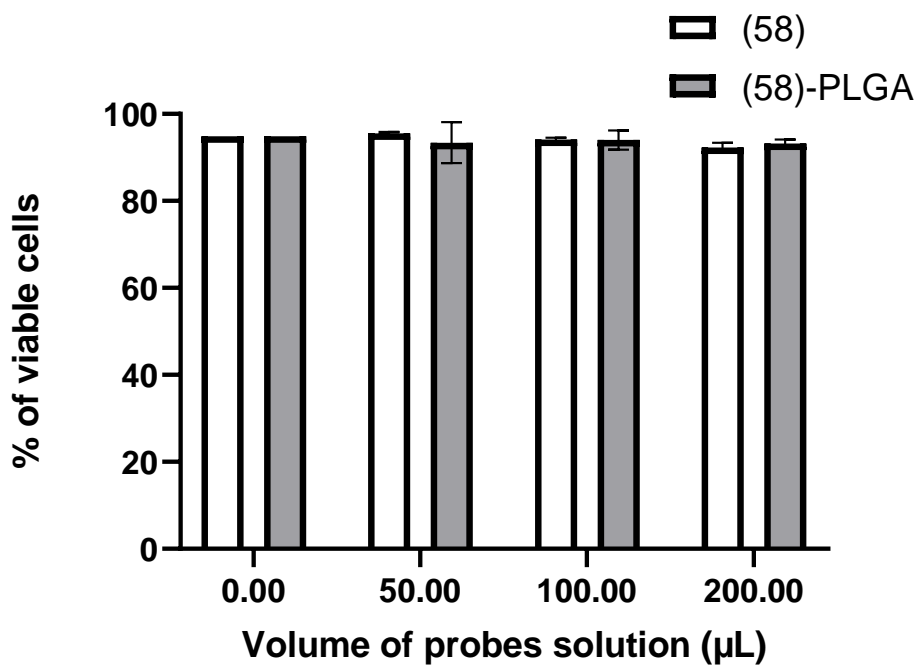
*Figure 4.13: Cytotoxicity of (**58**) (stand-alone sensor and nanosensors) (N = 3)*
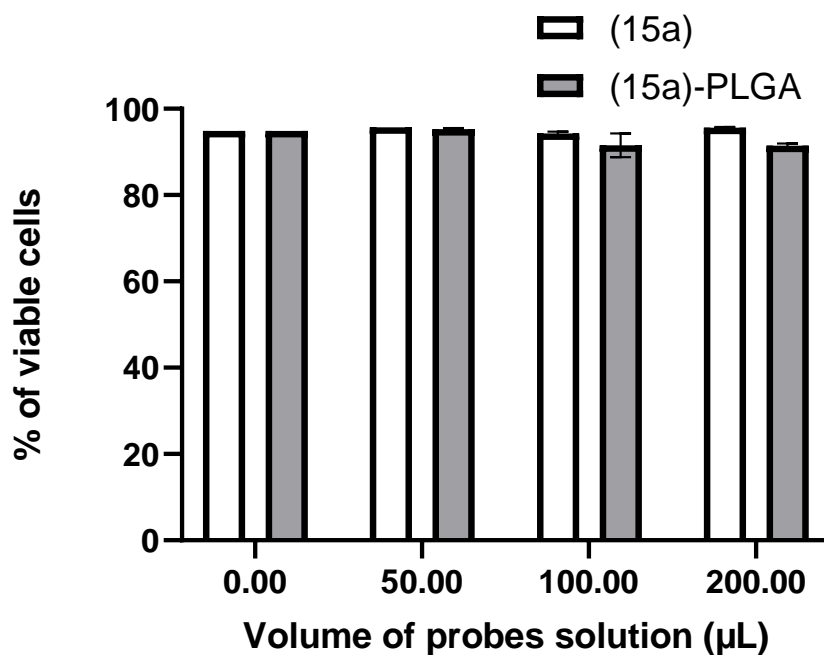
*Figure 4.14: Cytotoxicity of (**15a**) (stand-alone sensor and nanosensors) (N = 3)*
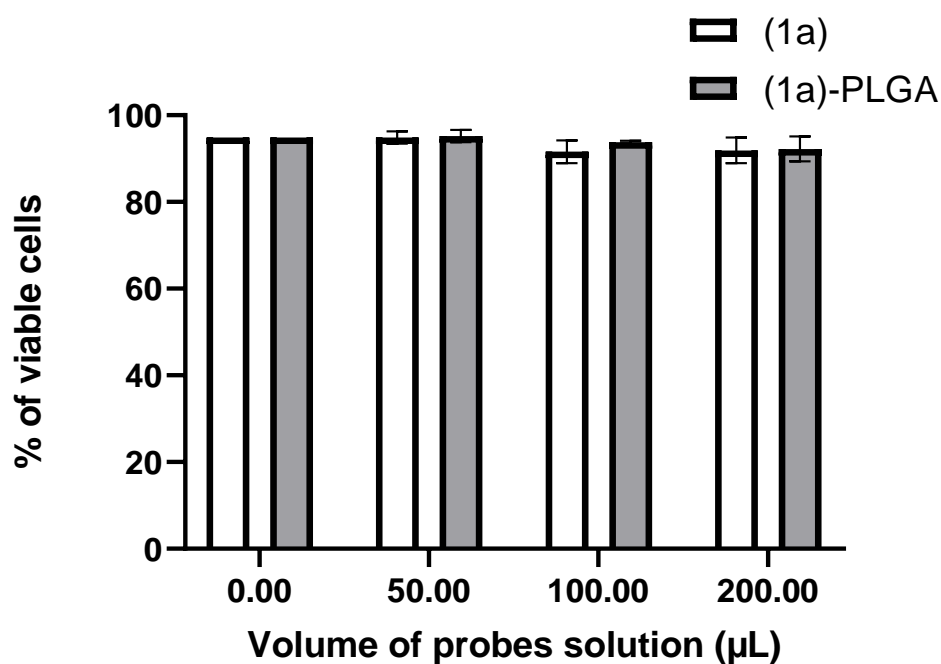
*Figure 4.15: Cytotoxicity of (**1a**) (stand-alone sensor and nanosensors) (N = 3)*
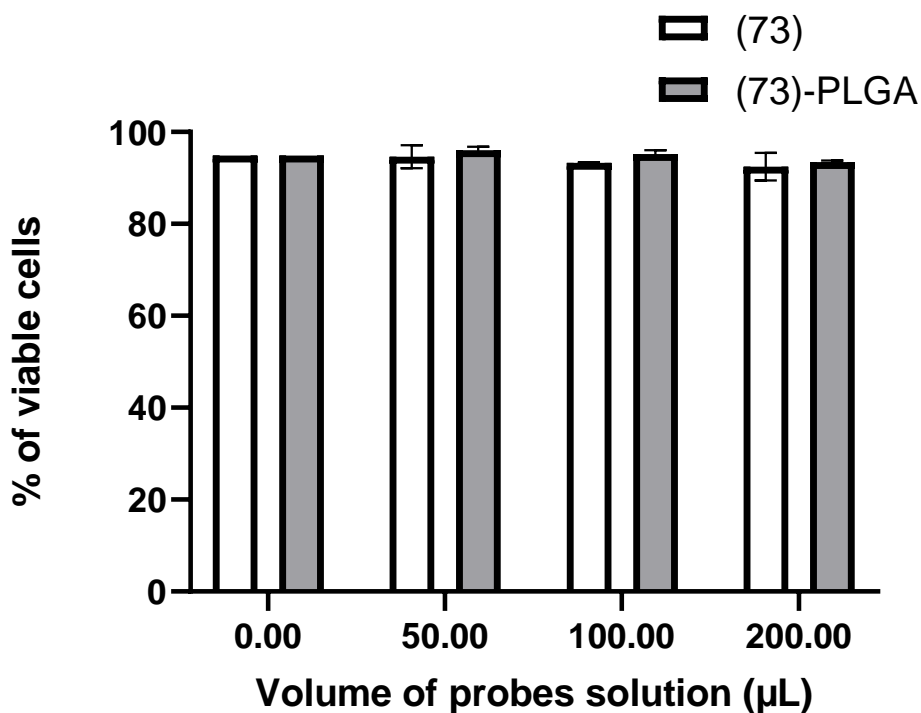
*Figure 4.16: Cytotoxicity of (**73**) (stand-alone sensor and nanosensors) (N = 3)*

We have compared the density of all cells with apoptotic cells, represented by the number of events per volume injected to see if this value is constant. As shown of the fig 4.17, this value is decreasing in all case and in the same way. This behaviour can be explained by cell death following a necrosis pathway. But in our case, PLGA has the same behaviour than our probes. That can be due to the limit of our method and the dilution of the sample. To see this kind of toxicity, it is important to keep the same volume by adding the same volume of probes solution but at different concentration.
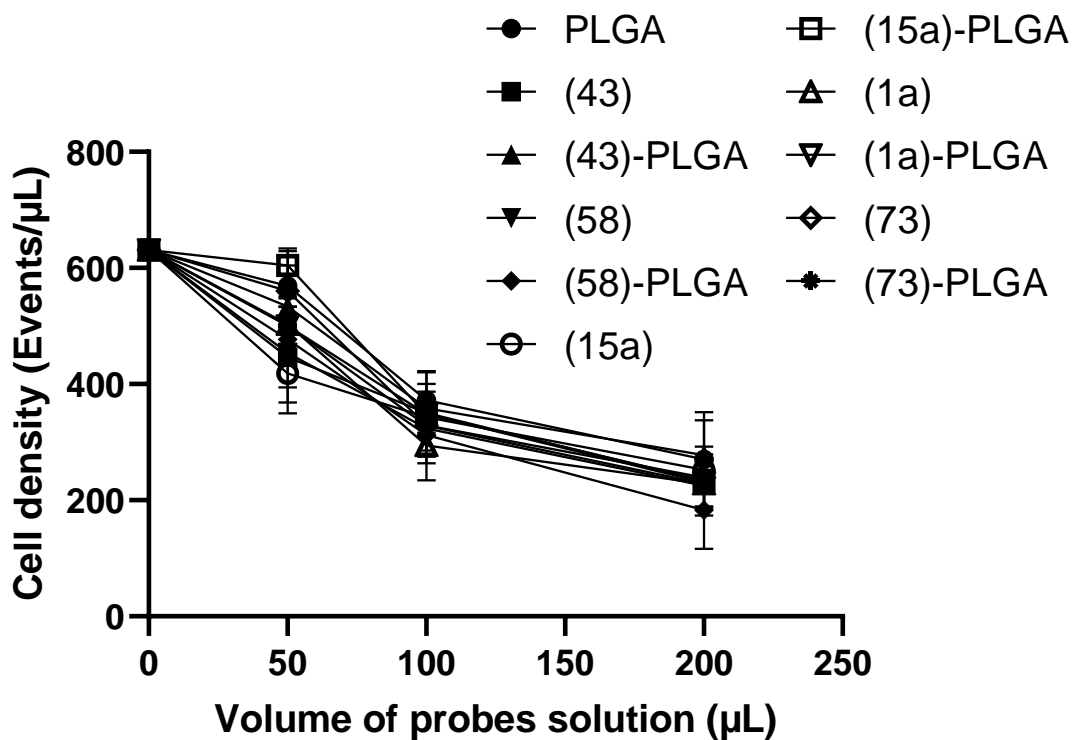
Figure 4.17 Cell density through flow cytometer depending on the addition

4.6. Responsiveness of sensors in cells depending on PMA exposure time

PMA induced cell differentiation by generating superoxide. Superoxide is transformed into hydrogen peroxide by SOD presents in cell. This study described in this section aimed to investigate the dependence of sensor response in cells on time of exposure to those two ROS.

THP1 cells were incubated with the different sensors at 1 mg/mL in PBS for 30 min and then exposed to a fixed amount of PMA at 2.5 µM for different lengths of time. The changes in the fluorescence emission between 533 nm and 630 nm were monitored by flow cytometry[302]. All data are rationalised with values of cells with same concentration of PMA and sensors.

Figure 4.18 shows the increase of fluorescence intensity over time for cells containing stand-alone (**43**) and (**43**) nanosensors which is the expected behaviour because PMA induced superoxide anion. (**43**)-PLGA fluorescence increases quickly for 5-10 min and then it increases slowly probably because of the consumption of sensors is close to be complete. For stand-alone (**43**), the increment is less important at the beginning, probably because of a lake of stability in front of some enzyme as observed in chapter 2 (section 2.1.2.2.).
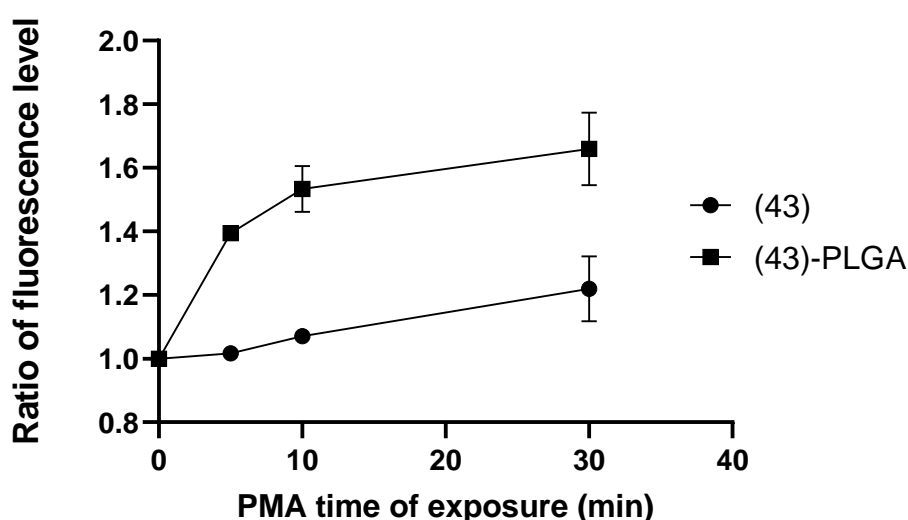
*Figure 4.18: Fluorescence evolution for (**43**) (stand-alone sensor and nanosensors) in THP1 cells with PMA-induced ROS generation over time (N = 3)*

Figure 4.19 shows the increase of fluorescence during 10 min for cells containing stand-alone (**58**) and (**58**) nanosensors which is the expected behaviour. Then, we can observe that stand-alone (**58**) increases slowly and (**58**)-PLGA decreases a bit due to the consumption of sensors less present in NPs. Both are following a similar curve for their increment. Importantly, in these experiments, in contrast with the behaviour displayed by (**58**) sensor in solution, the expected increase of fluorescence intensity was observed in response to ROS for both stand-alone (**58**) and nanosensors. That

can be due to some enzymes presents in cells or in the media that can stabilized our sensor.
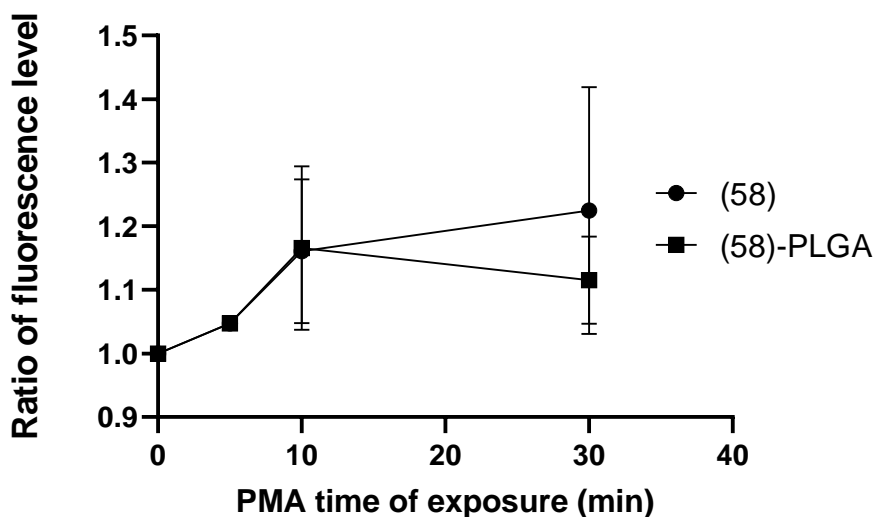
*Figure 4.19: Fluorescence evolution of (**58**) (stand-alone sensor and nanosensors) in THP1 cells with PMA-induced ROS generation over time (N = 3)*

Fig 4.20 shows that stand-alone (**15a**) has an unexpected behaviour with a high increment at the beginning while normally (**15a**) has to react only with singlet oxygen. Exposure of (**15a**) nanosensors containing cells with PMA does not lead to fluorescence variations as expected (Fig. 4.20). The use of NPs for (**15a**) is very important to avoid any side reactions with enzymes for example.
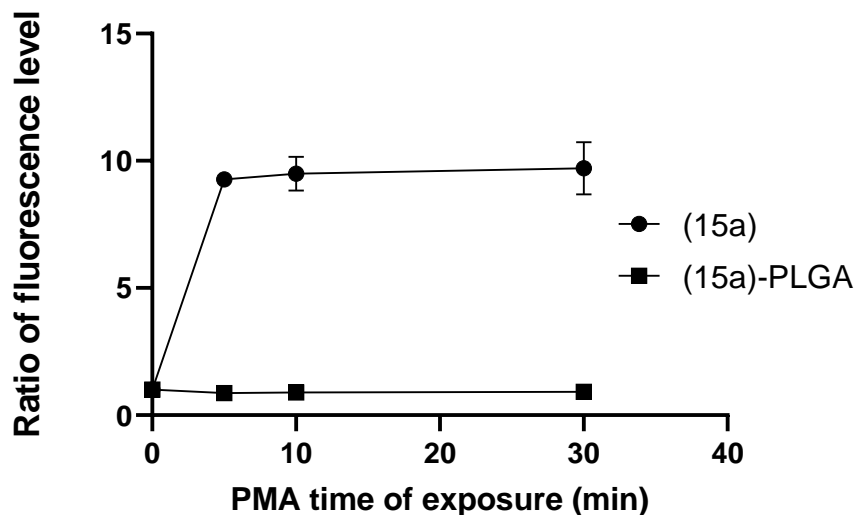
*Figure 4.20: Fluorescence evolution of (**15a**) (stand-alone sensor and nanosensors)*

in THP1 cells with PMA-induced ROS generation over time (N = 3)

Figure 4.21 shows that stand-alone (**1a**) and (**1a**)-PLGA have an expecting increment when this sensor is exposed to superoxide anion. Moreover, they look like linear if (**1a**) is stand alone or in NPs. Because (**1a**) is not attached on PLGA but just encapsulated, seeing the same behaviour is understandable because the structure of (**1a**) is not affected. Same observations can be made on (**73**) and (**73**)-PLGA on figure 4.22 with expected increment and not a lot of difference between stand-alone or NPs (**73**).
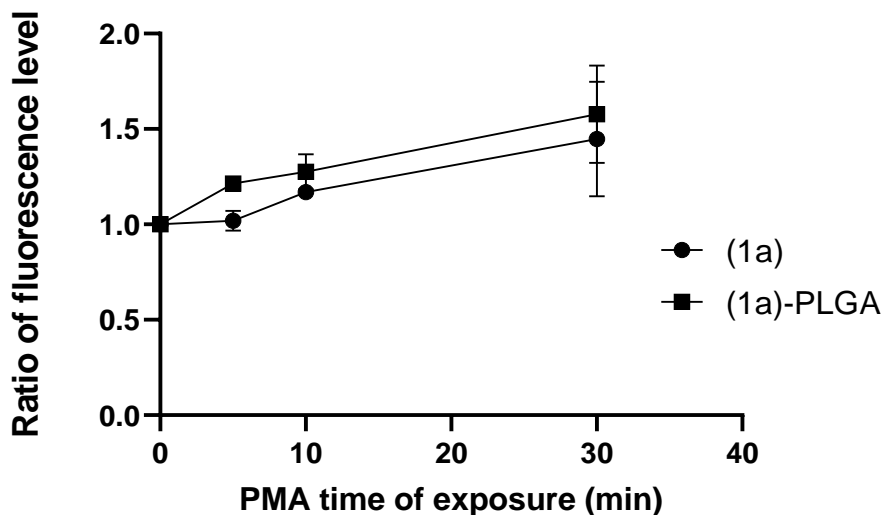
*Figure 4.21: Fluorescence evolution of (**1a**) (stand-alone sensor and nanosensors) in THP1 cells with PMA-induced ROS generation over time (N = 3)*
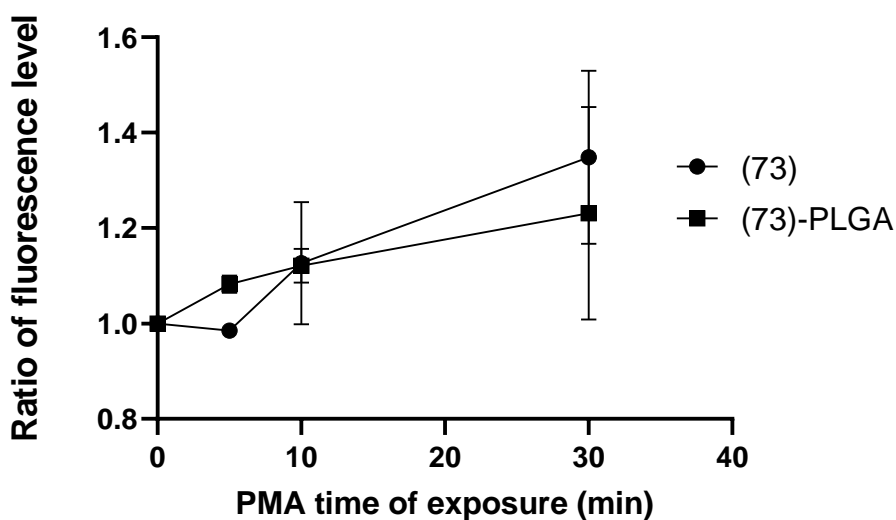
*Figure 4.22: Fluorescence evolution of (**73**) (stand-alone sensor and nanosensors) in THP1 cells with PMA-induced ROS generation over time (N = 3)*

To summarize, all sensors except stand-alone (**15a**) display the expected behaviour in the presence of ROS: (**43**), (**58**), (**1a**) and (**73**) show an increase of fluorescence in the presence of superoxide anion and hydrogen peroxide, while (**15a**)-PLGA stay stable.

(**58**), (**1a**), and (**73**) show a similar behaviour either is stand-alone or NPs form. For (**43**) and (**15a**), better responses are observed when they are under NPs form. One of the limits of this method is that we cannot estimate the level of hydrogen peroxide and of superoxide because both are linked. So, there is not proof if (**43**) and (**1a**) reacts only with superoxide and (**58**) and (**73**) only with hydrogen peroxide.

4.7. Responsiveness of sensors in cells depending on PMA concentration

To confirm our results, we wanted to see if the differentiation induced by PMA has an impact on the fluorescence results. To try and establish the effect of differentiation, we studied the fluorescence response in function of the PMA concentration.

THP1 cells were incubated with sensors solution at 1 mg/mL in PBS for 30 min and exposed to different amounts of PMA solution at 2.5 µM for further 30 min. The changes in the fluorescence emission between 533 nm and 630 nm were monitored by flow cytometry[302].

As previously observed and as expected (Fig. 4.23 to 4.26), (**43**), (**58**), (**1a**) and (**73**) has an increment of fluorescence. (**43**) is better when it is under NPs form because PLGA protects it from enzymes, while (**58**) is better without because it is stabilized by enzymes. (**1a**) and (**73**) has similar behaviour if it is stand-alone or under NPs form. That can be explained by the fact that they are not linked with PLGA.
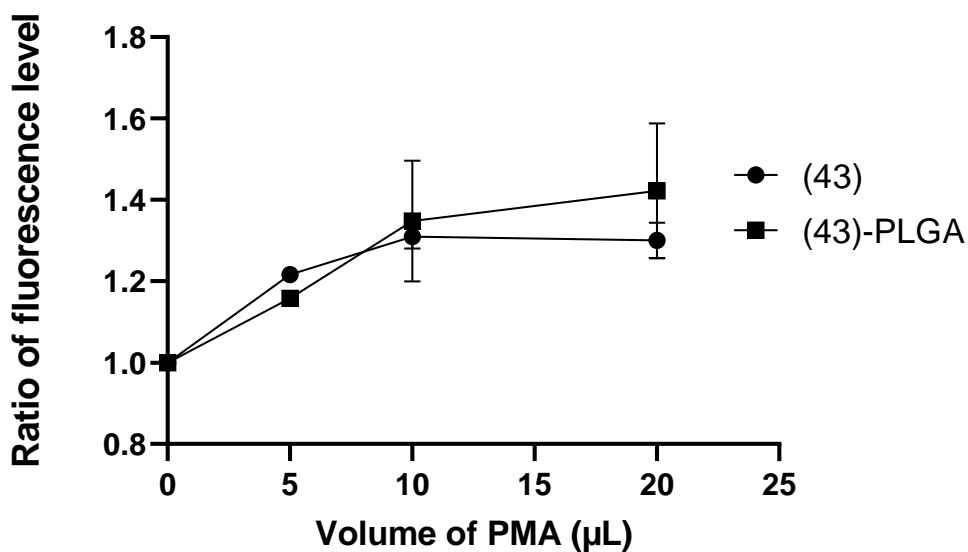
*Figure 4.23: Concentration dependent fluorescence evolution of (**43**) (molecular sensor and nanosensors) in THP1 cells following PMA-induced ROS generation (N = 3)*
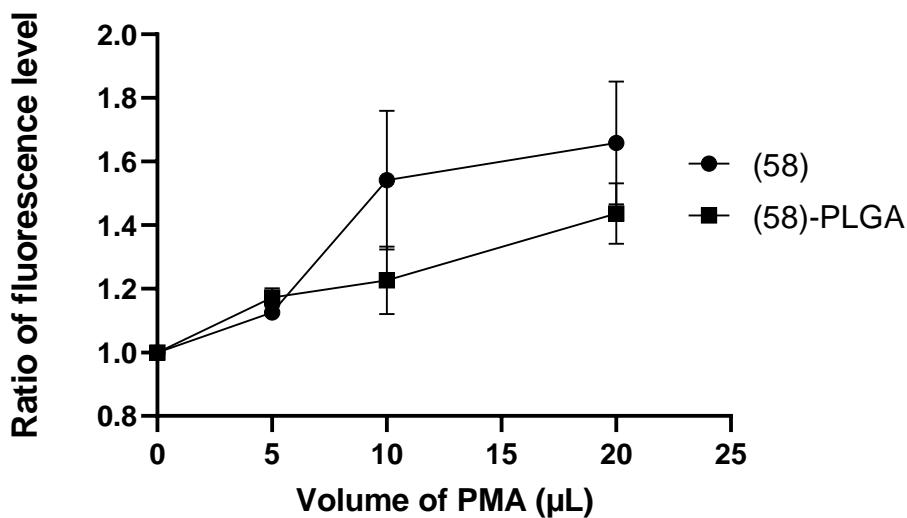
*Figure 4.24: Concentration dependent fluorescence evolution of (**58**) (molecular sensor and nanosensors) in THP1 cells following PMA-induced ROS generation (N = 3)*
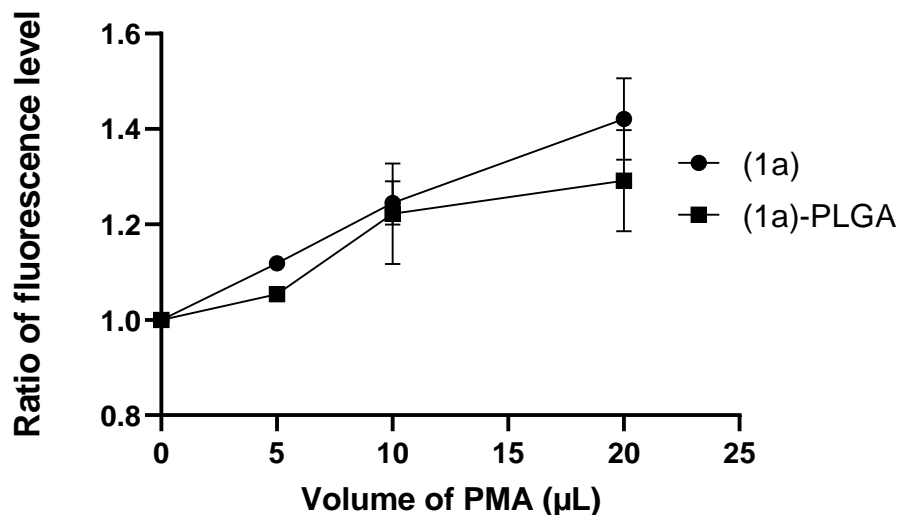
*Figure 4.25: Concentration dependent fluorescence evolution of (**1a**) (molecular sensor and nanosensors) in THP1 cells following PMA-induced ROS generation (N = 3)*
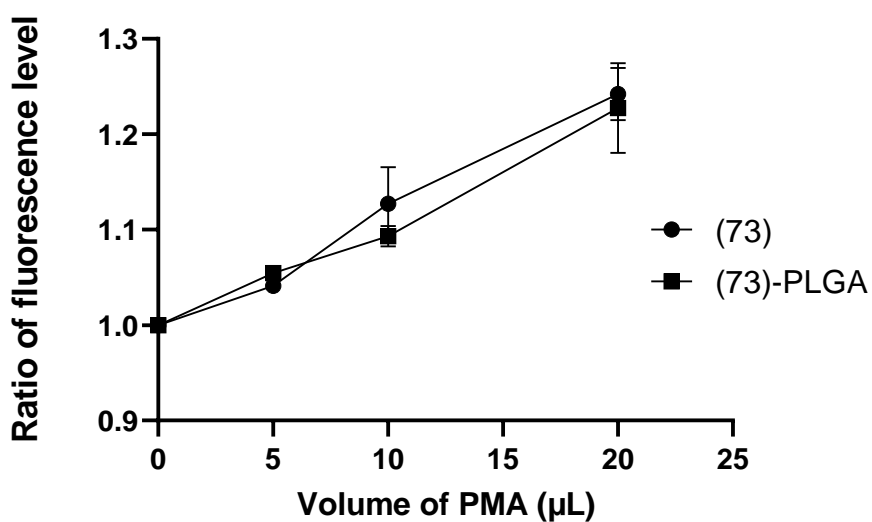
*Figure 4.26: Concentration dependent fluorescence evolution of (**73**) (molecular sensor and nanosensors) in THP1 cells following PMA-induced ROS generation (N = 3)*

We observed a normal behaviour for (**15a**) with a stable fluorescence over PMA concentration because (**15a**) is not sensible with superoxide and hydrogen peroxide generated (Fig. 4.27). (**15a**) associated on PLGA is more stable than stand-alone one.
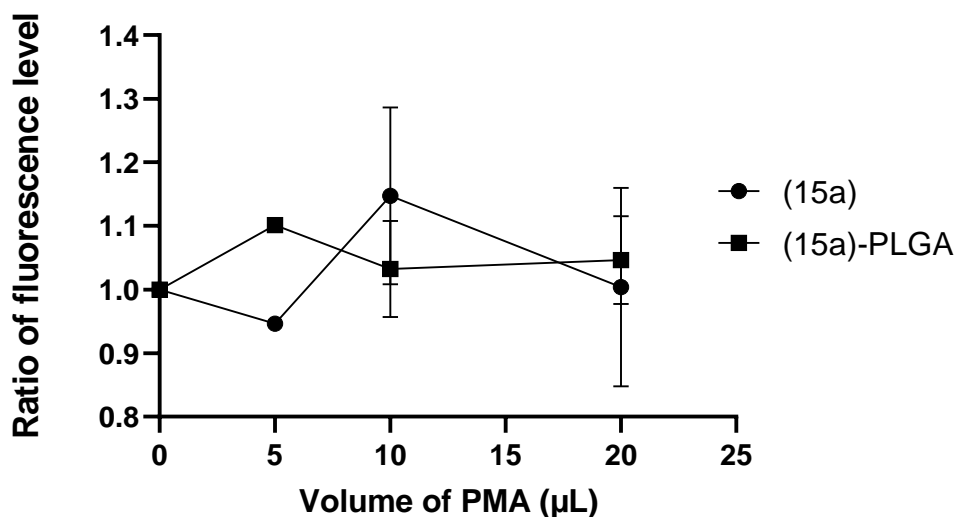
*Figure 4.27: Concentration dependent fluorescence evolution of (**15a**) (molecular sensor and nanosensors) in THP1 cells following PMA-induced ROS generation (N = 3)*

4.8. Responsiveness of sensors in cells with singlet oxygen

The intracellular generation of singlet oxygen is achieved by incubation of the cells with solution of sensors at 1 mg/mL in PBS and a photosensitiser. Cells are irradiated with blue light for different times (from 10 to 60 sec) and are analysed by flow cytometry. In these experiments, the induced differentiation of the cells will not be an element affecting the response of the cell population, but because of the potential of causing photodynamic cell killing, more cells will appear as apoptotic and they will appear in a different section of the cytogram.

As shown on figure 4.28 to 4.31, a decrement is observed on (**43**), (**58**), (**1a**) and (**73**) (stand-alone or NPs). This is probably due to the bleaching of sensors under room or blue light. This phenomenon is more pronounced on (**58**)-PLGA. As shown in chapter 2, (**58**) does not have the expected behaviour in PBS solution but in chapter 4, we have seen that (58) has the expected behaviour. Probably, this molecule is stabilized with enzymes and this property is less visible when (**58**) is attached on PLGA. Future work could be interesting to determine which enzymes stabilize (**58**) by adding in them in PBS separately.
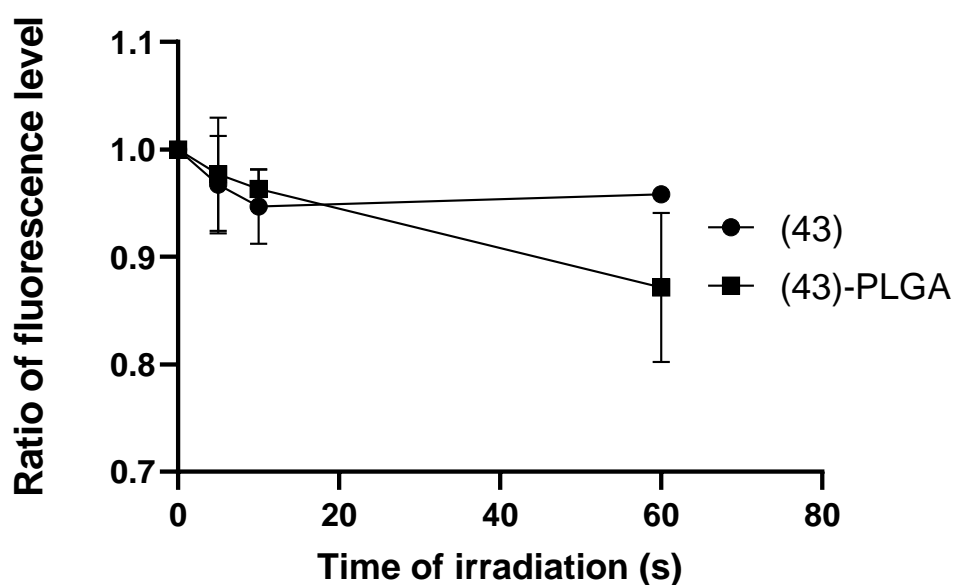
*Figure 4.28: Fluorescence evolution of (**43**) (molecular sensor and nanosensors) in*

THP1 cells following exposure singlet oxygen (N = 3)
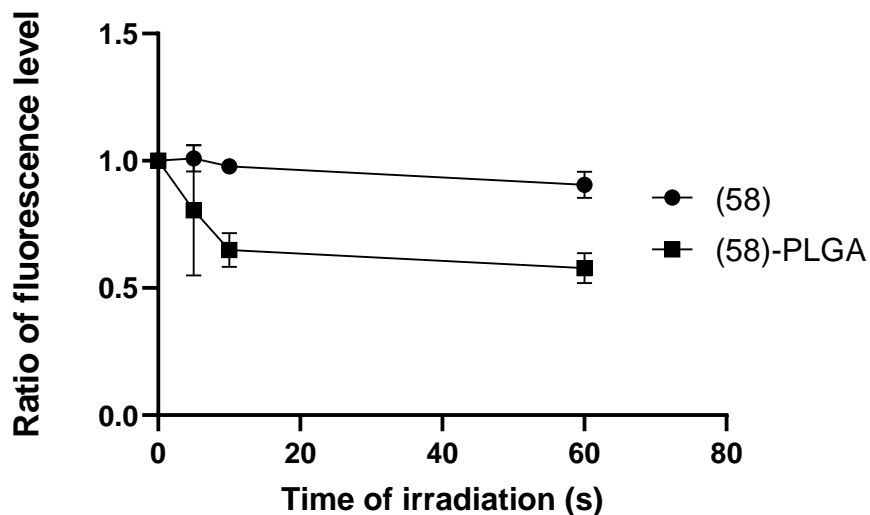
*Figure 4.29: Fluorescence evolution of (**58**) (molecular sensor and nanosensors) in*

THP1 cells following exposure singlet oxygen (N = 3)
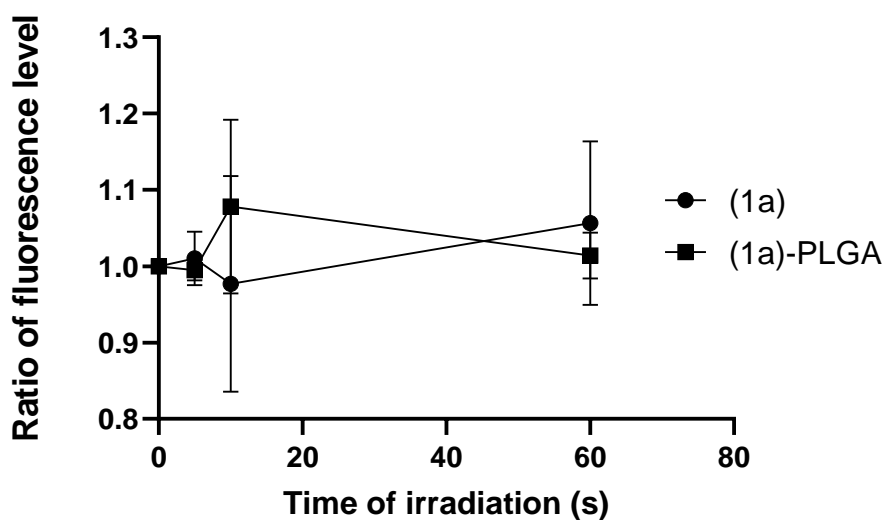
*Figure 4.30: Fluorescence evolution of (**1a**) (molecular sensor and nanosensors) in*

THP1 cells following exposure singlet oxygen (N = 3)
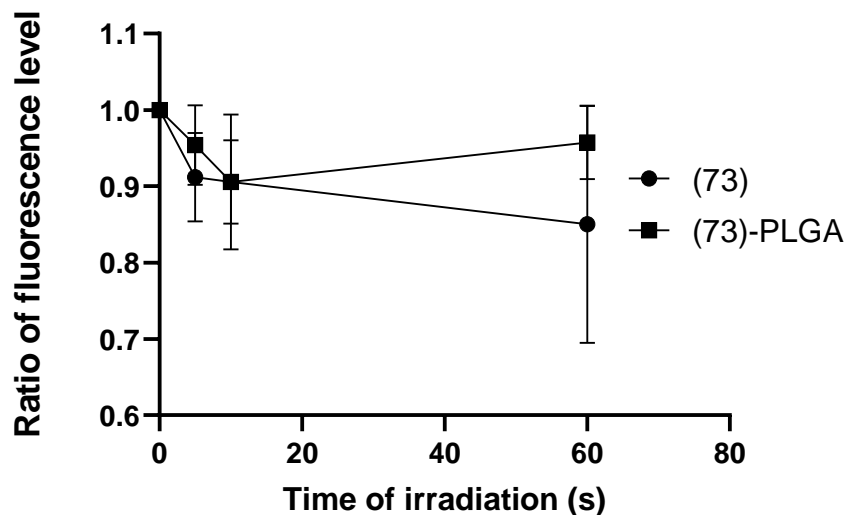
*Figure 4.31: Fluorescence evolution of (**73**) (molecular sensor and nanosensors) in THP1 cells following exposure singlet oxygen (N = 3)*

(**15a**)-based sensors respond as expected to singlet oxygen with an increase of fluorescence intensity. The behaviour is shown in figure 4.32, where it appears that (**15a**) give a more intense response as a stand-alone sensor than when incorporated in the nanosensors. The (**15a**)-PLGA nanosensors display a better increment of fluorescence as observed with NanoSOSG from Ruiz-Gonzµlez *et al.*[133].
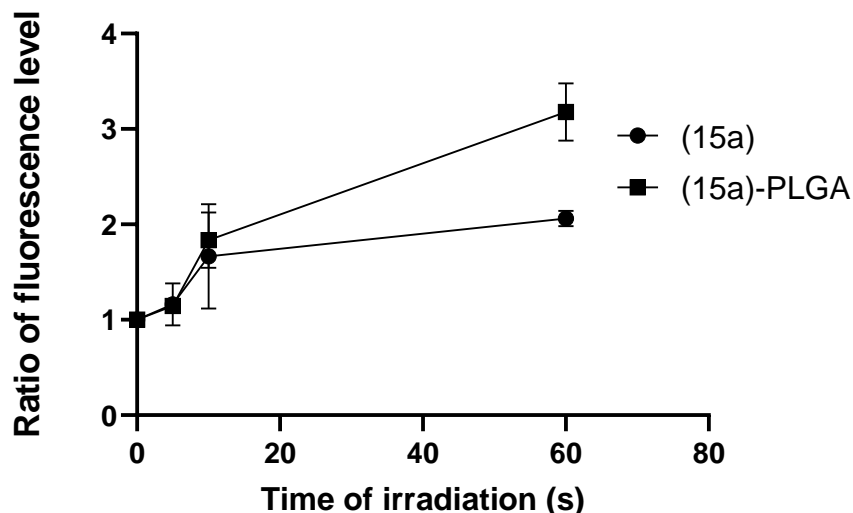
*Figure 4.32: Fluorescence evolution of (**15a**) (stand-alone sensor and nanosensors)*

in THP1 cells following exposure singlet oxygen (N = 3)

4.9. Chapter conclusion

All sensors and nanosensors responded to changing levels of intracellular ROS by increasing their fluorescence emission. Preliminary experiments confirmed that the sensors and nanosensors are not toxic to THP1 cells in the concentrations used in this work. In the case of (**43**), limited toxicity is observed at high concentrations of the stand-alone sensor, but this is not observed with the nanosensors. (**43**)-PLGA shows great potential to determine level of ROS in cells, unfortunately, we cannot determine its efficiency between superoxide or hydrogen peroxide because both are present inside cells. In the experiments described in this section, (**58**) demonstrated good potential as hydrogen peroxide sensor, despite its unpromising behaviour observed in PBS, with a good response to ROS in cells and a good selectivity against singlet oxygen. Its response is better when (**58**) is stand-alone, that is probably due to enzyme stabilization. For (**15a**), the use of NPs improves response and selectivity. For (**1a**) and

(**73**) which are not conjugated to PLGA, no major differences are observed between stand-alone or NPs sensors.

General conclusion and perspective of future work

In this study, a number of sensors for different ROS have been synthesised. The aim was to obtain sensors bearing a conjugatable function to allow covalent anchoring to polymers to obtain nanosensors. We obtained three new target sensors by multi-steps synthesis: (**43**) for superoxide radical anion, (**58**) for hydrogen peroxide and (**72b**) for singlet oxygen.

The behaviour of the sensors in the presence of the target analytes was studied. Despite some limitations (*e.g.*, (**43**) suffered from instability in solution and an unexpected decrease in the fluorescence intensity of (**58**) following exposure to hydrogen peroxide), the sensors responded with fluorescence variations to ROS. (**43**) and (**72b**) showed a great potential to be sensors for superoxide and singlet oxygen. As previously reported by the Nagano group, minor modification of the molecular structure of the sensor can result in a drastic alteration of its responsiveness and selectivity[147], which we observed for (**43**) and (**58**).

PLGA conjugates of the sensors were obtained and a library of corresponding nanoparticles was prepared by single emulsion-based methods. The species were uniform in size and we confirmed that the presence of the polymer did not alter the responsiveness of the sensors to the ROS analytes. In particular we observed a promising responsiveness from the (**43**) nanosensors. The unexpected decrease of fluorescence of the (**58**) in the presence of hydrogen peroxide was maintained on the nanosensors. (**72b**) responded to singlet oxygen but the intrinsic loss of fluorescence in the presence of the target analyte makes it a "switch-off" sensor, which we considered not to be ideal to develop further.

Although we obtained nanoparticles containing two different sensors ((**43**) and (**72b**)), we verified that their fluorescence signals in response to the different analytes suffered from interference, thereby limiting their use. Other nanospecies were prepared, containing combinations of commercially available sensors; due to the lack of suitable functional group, the commercial sensors were encapsulated in the particles rather than conjugated to the polymer.

To compare those results, the same study was performed with (**15a**) for singlet oxygen, (**1a**) for superoxide anion and (**73**) hydrogen peroxide. While (**15a**) was linked to PLGA NPs, (**1a**) and (**73**) were simply encapsulated in NPs. Although the response to the target analyte was as expected, we observed a lack of selectivity and, importantly, of interference between the signals.

The behaviour of the stand-alone sensors and the NPs was characterised in THP1 cells. Crucially, (**58**) displayed an increase of fluorescence intensity emission, which is the expected behaviour but in contrast to what we observed in solution. (**43**) nanosensors, on the contrary, gave a more intense response than the stand-alone (**43**).

The choice of the nanosensor matrix is important because the polymer must not be toxic and not interfere with the light absorption/emission. The approach to generate intracellular ROS also needs to be carefully chosen: the method used in this work had the potential to interfere with the analysis by inducing cell differentiation and division.

This work confirms the suitability of luminescent nanosensors for the intracellular monitoring of ROS. Our results show that if nanosensors containing more than one label are to be synthesised, care must be taken in the selection of the fluorophores in

order to avoid interferences of the signals and lack of selectivity in the response to different analytes.

Experimental

Reagents were purchased from Fluorochem, Sigma Aldrich, Fischer Scientific or Tokyo Chemical Industries, and were used as received unless otherwise specified. (78) have been provided by Dr Giuntini's group. All solvents, either analytical or HPLC grade, were purchased from Fisher Scientific and used as received, unless otherwise specified. TLC analysis was performed using Fluorochem Silica Gel 60Å, 20X20 cm, F254 plates. Silica gel chromatography was performed employing silica gel 60 Å purchased from Fluorochem. Mass spectrometer analyses were performed on a Waters Micromass LCT equipped with an electrospray ionization (ESI) source and time of flight (ToF) detector. HPLC analyses were performed on a Waters separations module 2695. The separations were performed on a Gemini C18, 5 μm, 150x4.6 mm, 110 Å (Phenomenex, UK) at a flow rate of 0.8 mL/min. Method employed depending on the nature of the compound. Method: the mobile phase consisted of water (solvent A) and acetonitrile (solvent B). Gradient: 0-2 min, 5% B; 2-18 min, 5-95% B; 18-21 min, 95% B; 21-22 min, 95-5% B, 22-28 min 5%B. NMR analyses were performed employing either a Bruker 300 MHz (operating at 300.18 MHz for 1H and 75.48 MHz for 13C) or a Bruker 600 MHz (operating at 600.3 1MHz for 1H and 150.95 MHz for 13C) spectrometers. $CDCl_3$, DMSO-d_6, CD_3OD, and D_2O were purchased either from Sigma-Aldrich or Fluorochem. $CDCl_3$, CD_3OD and D_2O were employed as received, DMSO-d_6 was dried over 3Å molecular sieves and stored under argon. Chemical shifts were reported in ppm, referenced to either $CHCl_3$ (1H, 7.26 ppm; 13C, 77.16 ppm), DMSO (1H, 2.50 ppm; 13C, 39.52 ppm), MeOH (1H, 3.31 ppm; 13C 49.00 ppm) or D_2O (1H, 4.79 ppm). Coupling constants (J) were reported in Hertz (Hz) and significant multiplicities were described by singlet (s), doublet (d), triplet (t), quartet (q), doublet of

doublets (dd), doublet of triplets (dt), triplet of doublets (td), multiplet (m), broad singlet (bs) or broad (br). Fluorescence analyses in solution were performed employing a Varian Cary Eclipse Fluorescence Spectrometer. NPs size and zeta potential were performed on Zetasizer Nano-ZS. Cell culture were a kind gift of Dr Sexton's research group at Liverpool John Moores University, and were obtained by growing THP1 in RPMI1640 medium[310]. Flow cytometry analysis were performed on a BD Accuri C6 flow cytometer. Transmittance FTIR spectra were obtained on an Agilent Cary 630 FTIR (Agilent Technology, UK). Confocal microscopy was performed on a Zeiss LSM 700. Centrifugation was performed by Hermle Z400 and a C0383-75 rotor for speed under than 1,000 rpm or by Beckman Coulter Optima XPN-80 with a 70.1 Ti fixed-angle titanium rotor for speed more than 1000 rpm.

Synthesis of di-*tert*-butyl (6-phenylphenanthridine-3,8-diyl)dicarbamate (**25**)
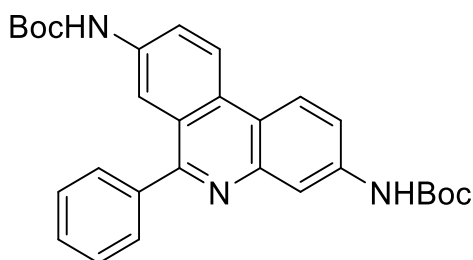
6-phenyl-5,6-dihydrophenanthridine-3,8-diamine (484 mg, 1.70 mmol) was added to saturated aqueous sodium carbonate aqueous solution (10 mL) in a round bottom flask. A solution of di-*tert*-butyldicarbonate (2.6 g, 11.90 mmol) in the minimum volume of tetrahydrofuran was added dropwise at 0 °C. The solution was stirred and allowed to reach room temperature overnight. Tetrahydrofuran was evaporated at reduced pressure and the resulting mixture was extracted with ethyl acetate. The organic phase was dried on magnesium sulfate and ethyl acetate was evaporated at reduced pressure to give 562 mg (1.16 mmol) of a red brown solid. (69%).

^{1}H NMR (300 MHz, CDCl$_3$) δ 8.54 (d, J = 9.0 Hz, 1H), 8.45 (d, J = 8.9 Hz, 1H), 8.13 (d, J = 8.7 Hz, 1H), 7.95 (dd, J = 10.1, 5.6 Hz, 2H), 7.73 − 7.66 (m, 3H), 7.52 (t, J = 6.7 Hz, 3H), 6.73 (s, 1H), 6.67 (s, 1H), 1.56 (s, 9H), 1.50 (s, 9H).

^{13}C NMR (75 MHz, DMSO) δ 160.8, 153.4, 143.9, 140.2, 138.8, 130.2, 129.2, 128.8, 124.9, 123.6, 123.4, 123.1, 119.6, 118.9, 117.0, 115.6, 79.9, 28.8, 28.7.

ESI-MS (+ve): 486.4585 [M+H$^+$] (C$_{29}$H$_{32}$N$_3$O$_4^+$ requires 486.2387).

The spectral data are consistent with those reported by Lee *et al.*[224].

Synthesis of 2-(2-(2-iodoethoxy)ethoxy)ethan-1-ol (**30**)
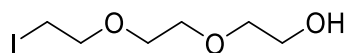
2-(2-(2-chloroethoxy)ethoxy)ethan-1-ol (500 µL, 3.44 mmol) was added to 10 mL of acetone containing sodium iodide (1.03 g, 6.88 mmol) in a round bottom flask equipped with a reflux condenser. The mixture refluxed overnight, then it was allowed to cool to room temperature and filtered through cotton wool. The solvent was evaporated under reduced pressure, the residue was taken in 5 mL of distilled water and extracted with diethyl ether (10 mL). The organic phase was dried on magnesium sulfate and the solvent was evaporated under reduced pressure to give 633 mg (2.43 mmol) of a red brown solid (71%).

^{1}H NMR (300 MHz, CDCl$_3$) δ 3.72-3.68 (m, 4H), 3.62-3.59 (m, 4H), 3.57-3.55 (m, 2H), 3.23-3.19 (m, 2H).

ESI-MS (+ve): 260.9898 [M+H$^+$] (C$_6$H$_{14}$IO$_3$$^+$ requires 260.9909).

The spectral data are consistent with those reported by Tian *et al.*[311].

Synthesis of 2-(2-(2-azidoethoxy)ethoxy)ethan-1-ol (**31**)

2-(2-(2-iodoethoxy)ethoxy)ethan-1-ol (1.2 mg, 4.8 mmol) and sodium azide (940 mg, 14.4 mmol) were dissolved in dry Acetonitrile (5 mL) in a round bottom flask equipped with a reflux condenser. After 2 days of reflux, the mixture was allowed to cool at room temperature and filtered through cotton wool. The solvent was evaporated under reduced pressure. The residue was taken deionised water (5 mL) and extracted with diethyl ether (10 mL). The organic phase was dried on magnesium sulfate and the solvent was evaporated under reduced pressure to give 629 mg (3.6 mmol) of a red brown solid (74%).

^{1}H NMR (300 MHz, CDCl$_3$) δ 3.73-3.64 (m, 8H), 3.59 (t, J = 4.5 Hz, 2H), 3.38 (t, J = 5.0 Hz, 2H).

^{13}C NMR (75 MHz, CDCl$_3$) δ 72.3, 70.2, 70.0, 69.6, 61.1, 50.3.

ESI-MS (+ve): 175.1111 [M+H$^+$] (C$_6$H$_{15}$N$_4$O$_2^+$ requires 175.1099).

The spectral data are consistent with those reported by Dakanali et al.[312]

Synthesis 1-azido-2-(2-(2-chloroethoxy)ethoxy)ethane (**33**)

$$N_3 \diagup\diagdown O \diagup\diagdown O \diagup Cl$$

2-(2-(2-chloroethoxy)ethoxy)ethan-1-ol (2 mL, 13.76 mmol) was dissolved in dry toluene (10 mL) under argon at 0°C in a round bottom flask equipped with a reflux condenser. MsCl (2.1 mL, 15.14 mmol) was added dropwise followed by TEA (1.3 mL, 16.51 mmol). The mixture was stirred at room temperature until TLC showed complete conversion. TBAI (5.6 g, 15.14 mmol) and sodium azide (1 g, 15.14 mmol) were added and the mixture was refluxed for 36 h. The mixture was dried on sodium sulfate and the solvent was evaporated under reduced pressure. The product was isolated by chromatography column (petroleum ether /ethyl acetate, 1/1) to give 2.12 g (10.93 mmol) of a yellow viscous solid (79%).

^{1}H NMR (300 MHz, CDCl$_3$) δ 3.74 – 3.57 (m, 10H), 3.33 (t, J = 6 Hz, 2H).

^{13}C NMR (75 MHz, CDCl$_3$) δ 72.2, 70.2, 69.9, 69.6, 61.2, 50.2.

ESI-MS (+ve): 216.0513 [M+Na$^+$] (C$_6$H$_{12}$ClN$_3$O$_2$Na$^+$ requires 216.0510).

The spectral data are consistent with those reported by Amaral *et al.*[313].

Synthesis 1-azido-2-(2-(2-iodoethoxy)ethoxy)ethane (**34**)

1-azido-2-(2-(2-chloroethoxy)ethoxy)ethane (2.12 g, 10.85 mmol) was dissolved in acetone (10 mL) in a dry round bottom flask equipped with a reflux condenser. Sodium iodide (1.43 g, 22 mmol) was added in the mixture refluxed overnight. The mixture was cooled at room temperature and filtered through cotton wool. The solvent was evaporated under reduced pressure. The resulting solid was taken in deionised water and extracted with diethyl ether. The organic phase was dried on magnesium sulfate and the solvent was evaporated under reduced pressure to give a yellow viscous liquid (3.05 g, 10.70 mmol) (98%).

^{1}H NMR (300 MHz, CDCl$_3$) δ 3.77 (t, J = 6.8 Hz, 2H), 3.71 – 3.68 (m, 6H), 3.4 (t, J = 5.0 Hz, 2H), 3.27 (t, J = 6.8 Hz, 2H).

^{13}C NMR (75 MHz, CDCl$_3$) δ 72.17, 70.84, 70.43, 70.30, 50.87, 3.01.

ESI-MS (+ve): 307.9868 [M+Na$^+$] (C$_6$H$_{12}$IN$_3$O$_2$Na$^+$ requires 307.9866).

The spectral data are consistent with those reported by Deng *et al.*[314].

Synthesis of 3,8-bis((tert-butoxycarbonyl)amino)-5-(3-iodopropyl)-6-phenyl phenanthridin -5-ium (**36**)

(**25**) (0.54 g, 1.10 mmol) and 1,3-diiodopropane (5.1 mL, 44 mmol) were dissolved dry THF (20 mL) under argon. The solution was refluxed at 65 °C for 2 months until MS analysis showed complete conversion. The solvent was evaporated under reduced pressure and the mixture was partitioned between ethyl acetate and water. The organic phase was dried on magnesium sulfate and the solvent was evaporated to give 0.44 g (0.67 mmol) of a yellow solid with (61%).

^{1}H NMR (300 MHz, CDCl$_3$) δ 9.42 (s, 1H), 9.34 (s, 1H), 8.80 (d, J = 9.3 Hz, 1H), 8.61 (dd, J = 9.3, 4.3 Hz, 2H), 8.39 (dd, J = 9.1, 2.1 Hz, 1H), 7.82 – 7.77 (m, 3H), 7.51 – 7.45 (m, 2H), 7.43 (d, J = 2.2 Hz, 1H), 6.99 (s, 1H), 5.16 – 5.02 (m, 2H), 3.51 (t, J = 6.0 Hz, 2H), 2.42 (bs, 2H), 1.57 (s, 9H), 1.47 (s, 9H).

ESI-MS (+ve): 654.0526 [M$^+$] (C$_{32}$H$_{37}$IN$_3$O$_4^+$ requires 654.1823).

Synthesis of 5-(3-azidopropyl)-3,8-bis((tert-butoxycarbonyl)amino)-6-phenyl phenanthridin-5-ium (**26c**)

(**36**) (228 mg, 0.35 mmol) and sodium azide (70 mg, 1.08 mmol) were dissolved in a 3:1 mixture of water and acetone (20 mL) under argon atmosphere in a round bottom flask equipped with a reflux condenser. The mixture was refluxed overnight, then it was cooled at room temperature and acetone was evaporated under reduced pressure. The desired product was extracted from the aqueous solution with ethyl acetate. Organic phase was dried on magnesium sulfate and the solvent was evaporated under reduced pressure to give 174 mg (0.31 mmol) of a yellow solid (89%).

^{1}H NMR (600 MHz, CDCl$_3$) δ 9.54 (s, 1H), 9.39 (s, 1H), 8.83 (d, J = 9.2 Hz, 1H), 8.61 (dd, J = 15.9, 9.2 Hz, 2H), 8.37 (d, J = 8.7 Hz, 1H), 7.80 (dd, J = 14.1, 6.7 Hz, 3H), 7.51 – 7.41 (m, 4H), 5.02 (s, 2H), 3.67 (t, J = 5.8 Hz, 2H), 2.25 (d, J = 23.8 Hz, 2H), 1.58 (s, 9H), 1.47 (s, 9H).

ESI-MS (+ve): 569.1661 [M$^+$] (C$_{32}$H$_{37}$N$_6$O$_4^+$ requires 569.2870).

<u>Synthesis of 3,11-dihydroxy-3'-oxo-3'H-spiro[dibenzo[c,h]xanthene-7,1'-benzo furan]-5'(or 6')-carboxylic acid (**39a** and **39b**)</u>

Benzene-1,2,4-tricarboxylic acid (0.66 g, 3.14 mmol) was dissolved in 7 mL of pure methanesulfonic acid in a round bottom flask equipped with a reflux condenser. Naphthalene-1,6-diol (1 g, 6.25 mmol) was added. The mixture was heated at 100 °C and stirred overnight then it was cooled to room temperature and poured onto 8 volumes of ice-cold water. The red precipitate was collected and dried under reduced pressure. Flash chromatography (10% MeOH in DCM) afforded the product as a red solid (1.37 g, 2.37 mmol, 75.47%). The solid (300 mg, 0.63 mmol) was treated with copper (II) chloride (0.11 g, 0.82 mmol) in deionised water (10 mL). The solution was stirred and sodium persulfate (0.15 g, 0.64 mmol) was slowly added over 30 min. The mixture was heated at 90 °C overnight then cooled down and HCl was added to obtain a precipitate that was filtrated and dried under reduced pressure. A red solid was obtained that was dissolved in methanol and the resulting solution was filtered to remove impurities. The filtrate was evaporated under reduced pressure to give a red solid (207 mg, 0.36 mmol) with a yield of 43%.

1H NMR (300 MHz, d_6-acetone) δ 8.79 (d, J = 1.8 Hz, 2H), 8.76 (d, J = 1.9 Hz, 2H), 8.43 – 8.35 (m, 3H), 7.42 (d, J = 2.4 Hz, 2H), 6.87 (d, J = 3.3 Hz, 2H), 6.84 (d, J = 3.3 Hz, 2H).

ESI-MS (+ve): 477.2195 [M$^+$] ($C_{29}H_{17}O_7^+$ requires 477.0968).

Synthesis of tert-butyl (2-(2-hydroxyethoxy)ethyl)carbamate (**45**)

BocHN⌒⌒O⌒⌒OH

2-(2-aminoethoxy)ethan-1-ol (1.6 mL, 15.2 mmol) was diluted in saturated aqueous sodium hydrogenocarbonate (50 mL) and the mixture was cooled at 0 °C in an ice bath. Di-*tert*-butyldicarbonate (3.63 g, 16.65 mmol) was added to the mixture dissolved in the minimum volume of tetrahydrofuran. The solution was stirred for 30 min at 0 °C and overnight at room temperature. The toluene was evaporated and the product was extracted with ethyl acetate. Organic phase was dried with magnesium sulfate and the solvent was evaporated. The desired compound was purified by flash chromatography (2:1 ethyl acetate/petroleum ether). 2.044 g (9.97 mmol) of yellow oil were obtained (66%).

^{1}H NMR (600 MHz, CDCl$_3$) δ 5.58 (s, 1H), 3.94 (s, 1H), 3.35 (s, 2H), 3.24 – 3.15 (m, 4H), 2.94 (d, *J* = 3.9 Hz, 2H), 1.08 (s, 9H).

^{13}C NMR (150 MHz, CDCl$_3$) δ 155.83, 79.24, 71.75, 69.56, 60.62, 39.75, 27.79.

ESI-MS (+ve): 206.1006 [M+H$^+$] (C$_9$H$_{20}$NO$_4^+$ requires 206.1386).

The spectral data are consistent with those reported by Steinebach *et al.*[315].

<u>Synthesis of tert-butyl (2-(2-azidoethoxy)ethyl)carbamate (**46**)</u>

BocHN⌒⌒O⌒⌒N$_3$

(2-(2-hydroxyethoxy)ethyl)carbamate (2 mL, 9.9 mmol) was dissolved in DCM (10 mL) in a dry round bottom flask, at 0°C under argon. MsCl (2.12 mL, 15.14 mmol) was added dropwise followed by TEA (1.28 mL, 16.51 mmol). The mixture was stirred for 2 h, it was diluted with DCM (10 mL) and deionised water (10 mL). The organic phase was dried with magnesium sulfate and the solvent was evaporated under reduced pressure. The crude was taken in DMF (10 mL), sodium azide (1.95 g ,30 mmol) was added and the mixture was stirred overnight at 120 °C. The solvent was evaporated under reduced pressure and the residue was partitioned between water and DCM. The organic phase was dried with magnesium sulfate and the solvent was evaporated under reduced pressure to give a 2.2 g of yellow liquid (9.57 mmol) with a yield of 97%.

^{1}H NMR (300 MHz, CDCl$_3$) δ 4.96 (s, 1H), 3.70 – 3.59 (m, 2H), 3.55 (t, J = 5.2 Hz, 2H), 3.42 – 3.36 (m, 2H), 3.33 (q, J = 5.5 Hz, 2H), 1.45 (s, 9H).

^{13}C NMR (75 MHz, CDCl$_3$) δ 155.87, 78.89, 72.39, 69.75, 41.24, 40.11, 28.16

ESI-MS (+ve): 253.2239 [M+Na$^+$] (C$_9$H$_{18}$N$_4$O$_3$Na$^+$ requires 253.149).

The spectral data are consistent with those reported by Steinebach *et al.*[315].

Synthesis of 2,5-dioxopyrrolidin-1-yl 3,11-dihydroxy-3'-oxo-3'H-spiro[dibenzo [c,h] xanthene-7,1'-benzofuran]-5'(or 6')-carboxylate (**41**)

(**39**) (598 mg, 1.24 mmol) was dissolved in THF (10 mL) in a dry round bottom flask under nitrogen and the solution was cooled at 0°C. NHS (0.2 g, 1.73 mmol) and DIC (0.25 g, 1.98 mmol) were added and the mixture was allowed reach room temperature. After stirring overnight, the solution was treated with *n*-heptane to induce the precipitation of the desired compound. The solid was collected by filtration and dried under reduced pressure to get a red solid (576 mg, 1.21 mmol, 98%).

^{1}H NMR (300 MHz, CDCl$_3$) δ 8.26 (d, J = 9.2 Hz, 2H), 8.11 (dd, J = 9.1, 3.5 Hz, 2H), 7.74 (s, 1H), 7.72 – 7.63 (m, 2H), 7.57 (s, 1H), 7.53 (s, 1H), 7.26 (d, J = 8.2 Hz, 2H), 7.12 (s, 2H), 2.94 – 2.86 (m, 4H).

ESI-MS (+ve): 595.2572 [M+Na$^+$] (C$_{33}$H$_{18}$NO$_9$Na$^+$ requires 595.0873).

Synthesis of N-(2-(2-azidoethoxy)ethyl)-3,11-dihydroxy-3'-oxo-3'H-spiro[dibenzo[c,h]xanthene-7,1'-benzofuran]-5'(or 6')-carboxamide (**42**)

Compound (**46**) (4.2 g, 7.17 mmol) was dissolved in a 2:5 mixture of TFA/DCM (10 mL) in a round bottom flask and the solution was stirred at room temperature until TLC showed complete conversion. The solvent was evaporated under reduced pressure and the residue was washed with diethyl ether. The dried crude was dissolved in a 5:1 mixture of DCM and DMF (10 mL) and treated with compound (**41**) (1.37 g, 2.39 mmol) at 0°C under argon. TEA (967 mg, 9.56 mmol) was slowly added, the mixture was allowed to reach room temperature and it was stirred overnight. The solvent was removed under reduced pressure and the resulting solid was dissolved in MeOH and filtered through paper. The filtrate was evaporated to dryness to give a red solid (869 mg, 1.48 mmol, 62%).

^{1}H NMR (300 MHz, MeOD) δ 8.53 (s, 1H), 8.16 – 8.19 (m, 2H), 7.76 (s, 1H), 7.70 – 7.61 (m, 2H), 7.41 – 7.44 (m, 4H), 7.12 (d, J = 11.8 Hz, 2H), 6.72 (dd, J = 8.7, 3.8 Hz, 2H), 3.73 – 3.68 (m, 2H), 3.56 – 3.51 (m, 2H), 3.20 (d, J = 5.1 Hz, 2H), 1.29 (bs, 2H).

ESI-MS (+ve): 589.2330 [M+H$^+$] (C$_{33}$H$_{25}$N$_4$O$_7^+$ requires 589.1717).

Synthesis of 5'(or 6')-((2-(2-azidoethoxy)ethyl)carbamoyl)-3'-oxo-3'H-spiro[dibenzo[c,h]xanthene-7,1'-isobenzofuran]-3,11-diyl bis(diphenylphosphinate) (**43**)

Compound (**42**) (62 mg, 0.11 mmol) was dissolved in dry THF (20 mL) in a round bottom flask under argon atmosphere and the solution was cooled at 0 °C. TEA (50 µL, 3.62 mmol) was added to the solution dropwise followed by a solution of $Ph_2P(O)Cl$ (54.3 mg, 0.23 mmol) in dry THF (5 mL). The mixture was stirred overnight and allowed to reach room temperature. The solution was filtered and evaporated under reduced pressure. The crude was dissolved in benzene (10 mL) and washed twice with of diluted ammonia (10 mL) and twice with deionised water (10 mL). The organic phase was dried on magnesium sulfate and the solvent was evaporated under reduced pressure to give a red solid (25 mg, 0.03 mmol) with a yield of 23%.
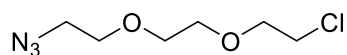
^{1}H NMR (300 MHz, CDCl$_3$) δ 8.49 (dd, J = 9.0, 2.8 Hz, 1H), 7.85 (dd, J = 12.2, 7.4 Hz, 8H), 7.76 – 7.67 (m, 3H), 7.41 – 7.37 (m, 8H), 7.16 (s, 2H), 6.88 (d, J = 0.5 Hz, 10H), 6.65 (dd, J = 8.7, 4.3 Hz, 2H), 3.80 – 3.74 (m, 2H), 3.67 (d, J = 11.1 Hz, 2H), 3.58 – 3.54 (m, 2H), 1.96 – 1.92 (m, 2H).

^{13}C NMR (75 MHz, CDCl$_3$) δ 132.72, 131.91, 131.77, 131.62, 128.83, 128.65, 128.50, 128.34, 125.52, 124.60, 124.19, 67.04, 67.02, 53.41, 37.12.

ESI-MS (+ve): 989.2875 [M+H$^+$] (C$_{57}$H$_{43}$N$_4$O$_9$P$_2$$^+$ requires 989.2499).
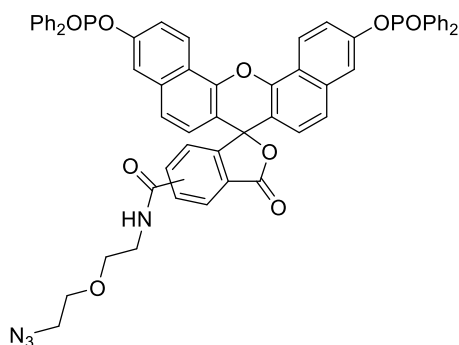
Synthesis of 2-(2,4-dihydroxybenzoyl) benzoic acid (**49**)
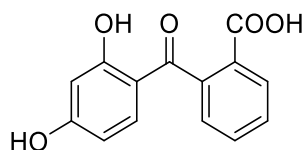
Under an argon atmosphere, resorcinol (2.40 g, 16.89 mmol) and phthalic anhydride (2.34 g, 15.80 mmol) were dissolved in dry nitrobenzene (50 mL). The mixture was cooled to 0°C and aluminium (III) chloride (4.90 g, 36.74 mmol) was added. The resulting dark olive slurry was allowed to warm to room temperature and stirred for an additional 16 h under argon. The reaction was poured into a vigorously stirring mixture of petroleum ether (360 mL) and 1 M HCl (150 mL). The precipitate was filtered and recrystallized twice from MeOH and water (1:1) to afford benzophenone as a pale green powder (2.4 g, 9.3 mmol) with 60% of yield.

^{1}H NMR (300 MHz, DMSO-d$_6$) δ 13.19 (s, 1H), 12.24 (s, 1H), 10.71 (s, 1H), 8.00 (dd, J= 7.7 Hz, 0.9 Hz, 1H), 7.74-7.67 (m, 1H), 7.65-7.61 (m, 1H),7.42 (dd, J= 7.5, 1.0 Hz, 1H), 6.95-6.90 (m, 1H), 6.33 (d, J= 2.3 Hz, 1H), 6.29 (dd, J= 8.7, 2.3 Hz, 1H).

^{13}C NMR (75 MHz, DMSO-d$_6$) δ 200.51, 166.76, 165.01, 164.42, 140.00, 134.75, 132.32, 129.99, 129.74, 129.48, 127.45, 113.29, 108.34, 102.55.

ESI-MS (-ve): 257.110 [M+H$^+$] (C$_{14}$H$_9$O$_5^-$ requires 257.0455).

The spectral data are consistent with those reported by Zhao *et al.*[316].

Synthesis of Fmoc-piperazine rhodol (51)
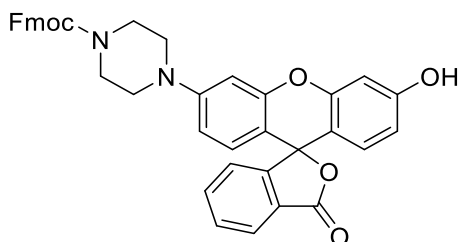
(49) (618 mg, 2.39 mmol) and 1-(3-hydroxyphenyl)-piperazine (427 mg, 2.39 mmol) were added to a round bottomed flask and dissolved in 10 mL of TFA under a gentle stream of argon. The reaction was stirred for 3 hours at 95 °C. After cooling, the reaction mixture was poured into 300 mL of diethyl ether under vigorous stirring. The resulting precipitate was collected, immediately dissolved in methanol, and then evaporated to dryness under reduced pressure to yield a red solid. The crude product was used without further purification. The crude fluorophore (1.2 g), Fmoc-Cl (930 mg, 3.63 mmol), and $NaHCO_3$ (755 mg, 8.99 mmol) were added to a dry round bottomed flask under argon atmosphere. Acetonitrile (20 mL) was added and the reaction was stirred at room temperature overnight. The product was then poured into ethyl acetate (150 mL), washed with water (x5), with brine (x5) and dried over Na_2SO_4 and evaporated. Purification by flash chromatography (1:1 petroleum ether/ethyl acetate) afforded a red solid (628 mg, 1mmol) with 42% of yield.

^{1}H NMR (300 MHz, CDCl$_3$): δ 7.99 (d, J = 7.6 Hz, 1H), 7.74 (d, J = 7.6 Hz, 2H), 7.66-7.57 (m, 2H), 7.55 (d, J = 7.6 Hz, 2H), 7.37 (t, J = 7.2 Hz, 2H), 7.29 (t, J = 7.2 Hz, 2H), 7.14 (d, J = 7.6 Hz, 1H), 6.71 (d, J = 2.0 Hz, 1H), 6.65 (d, J = 2.0 Hz, 1H), 6.63-6.29 (m, 4H), 4.47 (d, J = 6.4 Hz, 2H), 4.22 (t, J = 6.4 Hz, 1H), 3.55 (bs, 4H), 3.14 (bs, 4H).

^{13}C NMR (75 MHz, CDCl$_3$): δ 170.03, 159.59, 155.23, 152.82, 152.65, 152.58, 152.41, 143.76, 141.29, 134.92, 129.63, 129.15, 128.81, 127.73, 127.07, 127.00, 125.06,

124.82, 124.18, 129.97, 112.59, 112.18, 110.35, 109.87, 102.82, 102.33, 67.37, 47.99, 47.25, 43.20.

ESI-MS (+ve): 623.2182 [M+H$^+$] (C$_{39}$H$_{31}$N$_2$O$_6^+$ requires 623.2176).

The spectral data are consistent with those reported by Dickinson *et al.*[101].
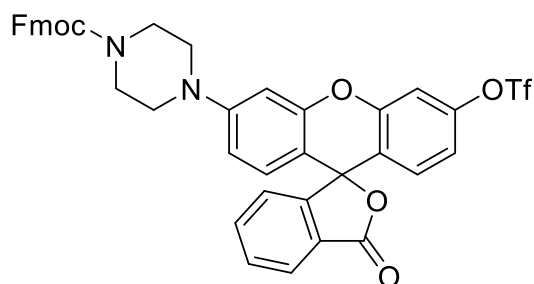
(**50**) (622 mg, 1 mmol), N-phenyl bis(trifluoromethanesulfonamide) (628 mg, 1.01 mmol), and sodium carbonate (535 mg, 5.05 mmol) were added to a dry round bottomed flask. Dry DMF (15 mL) was added *via* syringe. The reaction mixture changed colour from red to orange within 15 minutes and it was allowed to stir under argon atmosphere at room temperature overnight. The reaction mixture was poured into 100 mL of ethyl acetate, washed with water (x5), dried over magnesium sulfate, filtered and evaporated. Purification by column chromatography (petroleum ether/ethyl acetate, 1:1) afforded a white solid (297.4 mg, 0.4 mmol) in 39% of yield.

1H NMR (300 MHz, CDCl$_3$): δ 8.04 (d, J = 7.2 Hz, 1H), 7.76 (d, J = 7.6 Hz, 2H), 7.69 (dt, J = 1.2, 7.6 Hz, 1H), 7.64 (dt, J = 7.6, 1.2 Hz, 1H), 7.57 (d, J = 7.2 Hz, 2H), 7.38 (t, J = 7.2 Hz, 2H), 7.30 (dt, J = 1.2, 7.2 Hz, 2H), 7.23 (d, J = 2.4 Hz, 1H), 7.16 (d, J = 7.2 Hz, 1H), 6.94 (dd, J = 2.4, 8.8 Hz, 1H), 6.88 (d, J = 8.8 Hz, 1H), 6.70 (d, J = 2.0 Hz, 1H), 6.66 (d, J = 8.8 Hz, 1H), 6.61 (dd, J = 2.0, 8.8 Hz, 1H), 4.48 (d, J = 2.4 Hz, 2H), 4.23 (t, J = 2.4 Hz, 1H), 3.56 (bs, 4H), 3.16 (bs, 4H).

13C NMR (75 MHz, CDCl$_3$): δ 169.18, 155.09, 152.77, 152.49, 152.18, 151.85, 149.93, 143.83, 141.31, 135.37, 130.14, 130.06, 128.73, 127.73, 127.07, 126.36, 125.23, 124.86, 123.87, 119.98, 119.86, 116.52, 112.78, 110.42, 108.77, 102.23, 81.96, 67.29, 47.87, 47.30, 43.33.

ESI-MS (+ve): 777.1501 [M+Na$^+$] (C$_{40}$H$_{29}$F$_3$N$_2$O$_8$SNa$^+$ requires 777.1494).

The spectral data are consistent with those reported by Dickinson *et al.*[101].

<u>Synthesis of Fmoc-piperazine rhodol boronate (**53**)</u>
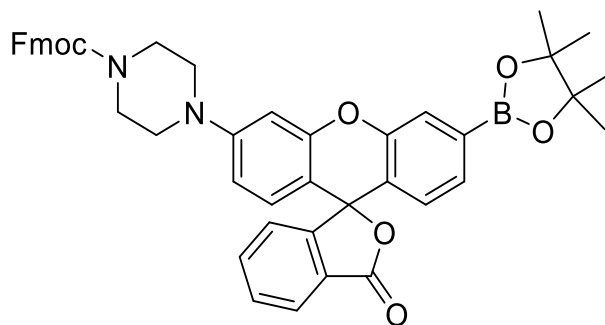
(**52**) (180 mg, 0.23mmol), bis(pinacolato)diboron (58.19 mg, 0.23 mmol), sodium acetate (53.77 mg, 0.65 mmol), and toluene (20 mL) were placed in a dry microwave tube and the mixture was purged with argon for 10 minutes. Pd(dppf)Cl$_2$· CH$_2$Cl$_2$ (58.65 mg, 0.07 mmol) was then added, the tube was sealed and microwave-heated for 4 hours at 110 °C. After cooling the reaction to room temperature, the contents of the tube were washed into a round bottom flask with dichloromethane and evaporated to dryness. Purification by column chromatography (petroleum ether/ethyl acetate, 2:3) afforded a white solid (100 mg, 0.13 mmol, 60%).

^{1}H NMR (300 MHz, CDCl$_3$): δ 8.02 (d, J = 6.4 Hz, 1H), 7.77 (t, J = 7.6 Hz, 3H), 7.68-7.56 (m, 4H), 7.45-7.37 (m, 3H), 7.33 (t, J = 8.0 Hz, 2H), 7.22 (d, J = 6.8 Hz, 1H), 6.81 (d, J = 8.0 Hz, 1H), 6.69 (d, J = 7.6 Hz, 2H), 6.59 (dd, J = 2.4, 8.8 Hz, 1H), 4.50 (d, J = 6.8 Hz, 2H), 4.26 (t, J = 6.4 Hz, 2H), 3.60 (bs, 4H), 3.16 (bs, 4H), 1.35 (s, 12H).

^{13}C NMR (75 MHz, CDCl$_3$): δ 169.65, 155.09, 153.44, 152.69, 152.31, 150.84, 143.88, 141.34, 153.09, 129.70, 129.27, 128.73, 128.04, 127.75, 127.25, 127.09, 126.37, 125.07, 124.90, 123.82, 123.44, 121.60, 120.01, 112.27, 109.47, 102.60, 84.20, 82.85, 67.29, 48.13, 47.34, 24.86.

ESI-MS (+ve): 733.3085 [M+H$^+$] (C$_{45}$H$_{42}$BN$_2$O$_7$$^+$ requires 733.3082).

The spectral data are consistent with those reported by Dickinson *et al.*[101].

Synthesis of 4-oxo-4-(4-(3-oxo-3'-(4,4,5,5-tetramethyl-1,3,2-dioxaborolan-2-yl)-3H-spiro[isobenzofuran-1,9'-xanthen]-6'-yl)piperazin-1-yl)butanoic acid (**54**)

(**53**) (90 mg, 0.12 mmol) was dissolved in 12 mL of 15% piperidine in acetonitrile and stirred at room temperature for 40 minutes. The reaction was then dried under reduced pressure and left 10 minutes under argon stream. Then chloroform (2 mL) and DIPEA (0.194 g, 1.5 mmol) were added. The mixture was cooled to 0°C and succinic anhydride (0.015 g, 0.15 mmol) was added slowly. The reaction mixture was warmed to room temperature and stirred overnight. The solvent was removed under reduced pressure and 70 mg of crude product were obtained.

ESI-MS (+ve): 611.6241 [M+H$^+$] (C$_{34}$H$_{36}$BN$_2$O$_8^+$ requires 611.2466).

Synthesis of 4-(4-(3'-hydroxy-3-oxo-3H-spiro[isobenzofuran-1,9'-xanthen]-6'-yl)piperazin-1-yl)-4-oxobutanoic acid (**56**)

(**49**) (309 mg, 1.19 mmol) and 1-(3-hydroxyphenyl)-piperazine (213.5 mg, 1.2 mmol) were added to a round bottomed flask and dissolved in 10 mL of TFA under a stream of argon. The reaction was stirred for 3 hours at 95 °C, then it was cooled and poured in 300 mL of diethyl ether under vigorous stirring. The resulting precipitate was collected, dissolved in methanol and evaporated to dryness under reduced pressure to yield a red solid. The solid was dissolved in DMF (20 mL) at 0 °C under nitrogen and treated with succinic anhydride (263 mg, 3.63 mmol) and DIPEA (1 mL, 5 μmol). After stirring overnight, DMF was evaporated under reduced pressure. The solid was dissolved in ethyl acetate and washed with water and solvent evaporated to give a red solid (320 mg, 0.64 mmol, 54%).

^{1}H NMR (300 MHz, CDCl$_3$) δ 7.99 (s, 2H), 7.33 – 7.25 (m, 4H), 7.06 (dd, J = 10.5, 4.2 Hz, 2H), 7.00 – 6.93 (m, 4H), 1.50 – 1.46 (m, 4H), 1.40 (d, J = 6.6 Hz, 4H), 0.84 (dd, J = 9.8, 5.3 Hz, 4H).

ESI-MS (+ve): 501.1702 [M+H$^+$] (C$_{28}$H$_{25}$N$_2$O$_7^+$ requires 501.1656).

Synthesis of 4-oxo-4-(4-(3-oxo-3'-((4-(4,4,5,5-tetramethyl-1,3,2-dioxaborolan-2-yl)benzyl)oxy)-3H-spiro[isobenzofuran-1,9'-xanthen]-6'-yl)piperazin-1-yl)butanoic acid (**58**)

(**56**) (172 mg, 0.34 mmol) was mixed in a dry round bottom flask with potassium carbonate (84 mg, 0.61 mmol) and 2-(3-(bromomethyl)phenyl)-4,4,5,5-tetramethyl-1,3,2-dioxaborolane (102 mg, 0.35 mmol) in DMF (10 mL) under nitrogen. The mixture was stirred overnight and the solvent was evaporated under reduced pressure. The solid was partitioned between DCM and deionised water. The organic phase was dried on magnesium sulfate and the solvent evaporated under reduced pressure to afford a red solid (101 mg, 0.13 mmol, 38%).

^{1}H NMR (300 MHz, CDCl$_3$) δ 7.53 (d, J = 4.8 Hz, 1H), 6.70 (d, J = 2.3 Hz, 3H), 6.59 (s, 2H), 6.26 (dd, J = 7.7, 0.9 Hz, 3H), 6.19 (d, J = 7.3 Hz, 3H), 6.10 (d, J = 9.6 Hz, 3H), 4.38 (dd, J = 15.0, 6.3 Hz, 4H), 4.24 (q, J = 12.1 Hz, 4H), 2.96 (d, J = 2.0 Hz, 6H), 0.63 (s, 12H).

^{13}C NMR (75 MHz, CDCl$_3$) δ 185.47, 173.52, 170.03, 165.33, 158.86, 154.43, 153.75, 150.24, 137.36, 135.02, 134.43, 132.63, 131.36, 130.51, 130.36, 130.18, 129.73, 129.58, 129.10, 128.95, 127.23, 126.50, 118.88, 116.51, 112.96, 111.52, 105.58, 100.15, 84.31, 83.95, 70.18, 46.83, 44.60, 28.98, 27.90, 25.01.

ESI-MS (+ve): 755.3011 [M+K$^+$] (C$_{41}$H$_{41}$BN$_2$O$_9$K$^+$ requires 755.0540).

Synthesis of phenyl(2,4,5-trimethylphenyl)ketone (**61**)

Benzoyl chloride (19 mL, 164 mmol) was dissolved in DCM (30 mL) at 0 °C in a round bottom flask under nitrogen. AlCl$_3$ (26.17 g, 196.8 mmol) was added. 1,2,4-trimethylbenzene (19.43 mL, 141 mmol) was added dropwise. The mixture was allowed to reach room temperature and stirred for 6 h, then it was poured on ice bath containing 25 mL of concentrated HCl. The organic phase was separated, dried with magnesium sulfate and the solvent was evaporated under reduced pressure to give a brown solid (33.82 g, 138 mmol, 98%).

^{1}H NMR (300 MHz, CDCl$_3$) δ 7.83 – 7.70 (m, 2H), 7.53 – 7.29 (m, 4H), 6.99 (s, 1H), 2.26 (s, 3H), 2.21 (s, 3H), 2.15 (s, 3H).

^{13}C NMR (75 MHz, CDCl$_3$) δ 198.2, 138.9, 138.0, 135.8, 134.2, 133.0, 132.5, 132.2, 129.9, 129.7, 129.1, 128.5, 128.1, 19.35, 19.29, 18.8.

ESI-MS (+ve): 247.0574 [M+Na$^+$] (C$_{16}$H$_{16}$ONa$^+$ requires 247.1093).

The spectral data are consistent with those reported by Lohier *et al.*[249]*.*

Synthesis of 5-benzoylbenzene-1,2,4-tricarboxylic acid (**62**)

(**61**) (2.08 g, 9.29 mmol), KMnO$_4$ (16 g, 101.26 mmol) and pyridine (7 mL, 86.84 mmol) were dissolved in deionised water (20 mL) in a round bottom flask. The mixture was stirred at 50 °C for 5 days and filtered while hot. The solid was taken in deionised water (50 mL), boiled for 6 h and filtered again. The two filtrates were combined, the water was evaporated to half its volume and concentrated HCl was added to reach pH = 1 to induce the precipitation of the product. The solid was collected by filtration and dried under reduced pressure to give a brown solid (2.74 g, 8.71 mmol, 94%).

^{1}H NMR (300 MHz, (CD$_3$)$_2$CO) δ 8.49 (s, 1H), 7.80 – 7.76 (6, 3H), 7.64 – 7.51 (m, 3H).

^{13}C NMR (75 MHz, (CD$_3$)$_2$CO) δ 181.4, 167.6, 137.5, 134.9, 134.2, 132.9, 127.0, 126.9.

ESI-MS (-ve): 313.1055 [M+H$^+$] (C$_{16}$H$_9$O$_7^-$ requires 313.0354).

The spectral data are consistent with those reported by Lohier *et al.*[249].

Alternative synthesis of 5-benzoylbenzene-1,2,4-tricarboxylic acid (**62**)

(**61**) (1 g, 4.46 mmol), $KMnO_4$ (5.4 g, 34.18 mmol) and $NaHCO_3$ (0.2 g, 2.38 mmol) were dissolved in deionised water (25 mL) in a round bottom flask equipped with a reflux condenser and refluxed overnight. The mixture was filtered, the filtrate was treated with 12 M HCl to pH = 1 and the desired product was extracted with DCM. The organic phase was dried with sodium sulfate and the solvent was evaporated under reduced pressure to give a brown solid (203 mg, 0.65 mmol, 15%).

^{1}H NMR (300 MHz, $(CD_3)_2CO$) δ 8.49 (s, 1H), 7.80 – 7.76 (6, 3H), 7.64 – 7.51 (m, 3H).

^{13}C NMR (75 MHz, $(CD_3)_2CO$) δ 181.4, 167.6, 137.5, 134.9, 134.2, 132.9, 127.0, 126.9.

ESI-MS (-ve): 313.1055 [M+H$^+$] ($C_{16}H_9O_7^-$ requires 313.0354).

The spectral data are consistent with those reported by Lohier *et al.*[249].

Synthesis of 9,10-dioxo-9,10-dihydroanthracene-2,3-dicarboxylic acid (**63**)

(**62**) (550 mg, 1.75 mmol) was refluxed in concentrated sulfuric acid (20 mL) for 3 h in a round bottom flask equipped with a reflux condenser. The solution was cooled to room temperature, poured on ice stirred for 2 days at room temperature. The solid was filtered and dried to give a brown solid (277 mg). The product was purified by a flash chromatography (petroleum ether/ethyl acetate 1:1) to give a brown solid (206 mg, 0.70 mmol, 40%).

^{1}H NMR (300 MHz, (CD$_3$)$_2$CO) δ 8.61 (s, 2H), 8.36 – 8.32 (m, 2H), 8.01 – 7.94 (m, 2H).

^{13}C NMR (75 MHz, (CD$_3$)$_2$CO) δ 181.4, 167.6, 137.5, 134.9, 134.2, 132.9, 127.0, 126.9.

ESI-MS (-ve): 295.0963 [M+H$^+$] (C$_{16}$H$_7$O$_6^-$ requires 295.0248).

The spectral data are consistent with those reported by Lohier *et al.*[249].

Synthesis of anthra[2,3-c]furan-1,3,5,10-tetraone (**64**)

(**63**) (100 mg, 0.34 mmol) was mixed with 10 mL of glacial acetic acid for 1 day in a dry round bottom flask under nitrogen. The solid was filtered, rinsed with petroleum ether and dried under reduced pressure to give a green solid (58.6 mg, 0.21 mmol, 62%).

^{1}H NMR (600 MHz, (CD$_3$)$_2$CO), δ: 8.83 (s, 2H), 8.39 (dd, J = 5.8, 3.3 Hz, 2H), 8.06 (dd, J = 5.9, 3.2 Hz, 2H).

ESI-MS (-ve): 278.6817 [M+H$^+$] (C$_{16}$H$_6$O$_5$$^+$ requires 279.0288).
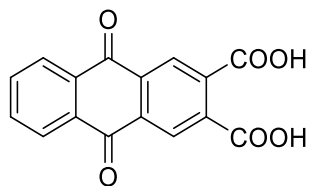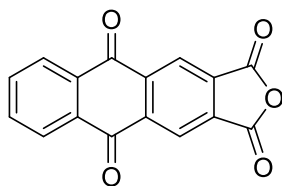
Synthesis of 9,10-bis(bromomethyl)anthracene (**71**)
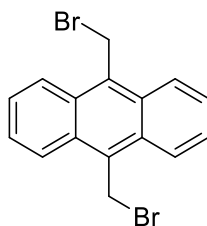
Dimethylanthracene (282 mg, 1.37 mmol), NBS (487 mg, 2.75 mmol) and AIBN (0.1 ml, 0.7 mmol) were dissolved in acetonitrile (50 mL) in a round bottom flask under nitrogen. The mixture was refluxed for 1.5 h. The solid was collected by filtration, dissolved in DCM and washed with saturated aqueous $NaHCO_3$, water and brine. The organic phase was dried on sodium sulfate and the solvent was evaporated under reduced pressure.

^{1}H NMR (300 MHz, CDCl$_3$) δ 8.45 – 8.30 (m, 4H), 7.73 – 7.64 (m, 4H), 5.52 (s, 4H).

^{13}C NMR (75 MHz, CDCl$_3$) δ 126.70, 124.38, 75.89.

ESI-MS (+ve): 280.1359 [M-Br$^-$] (C$_{16}$H$_9$Br$^+$ requires 280.9817).

The spectral data are consistent with those reported by Martinez *et al.*[269].

Synthesis of 3,3'-(anthracene-9,10-diyl)dipropionic acid (**72b**)
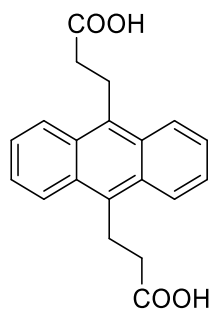
Sodium (750 mg, 32.61 mmol) was dissolved in EtOH (125 mL) in a round bottom flask equipped with a reflux condenser under nitrogen. Dry diethyl malonate (10 mL) was added while the mixture was kept at 5 °C to avoid precipitation and stirred for an hour. A solution of (71) (248 mg, 0.68 mmol) in benzene (175 mL) was added. The mixture was refluxed for 4 h then it was allowed to cool at room temperature. The solution was neutralized with concentrated HCl. The organic phase was separated and the solvent was evaporated under reduced pressure. The solid was treated with 6 M NaOH (10 mL) in methanol and 5 mL of chloroform and the resulting solution was refluxed for 3 hours. Concentrated HCl was added to reach pH = 1 and the resulting suspension as filtered. The solid was dried for 5 days under reduced pressure at 120 °C to give a green solid (46 mg, 0.12 mmol, 18%)

^{1}H NMR (600 MHz, DMSO) δ 13.16 – 12.43 (s, 2H), 8.38 – 8.30 (m, 4H), 7.57 – 7.31 (m, 4H), 4.10 (d, J = 7.0 Hz, 4H), 3.51 – 3.41 (m, 4H).

^{13}C NMR (125 MHz, CDCl$_3$) δ 130.23, 129.57, 126.65, 124.33, 45.86, 26.66.

ESI-MS (-ve): 321.2177 [M-H$^+$] (C$_{20}$H$_{17}$O$_4^-$ requires 321.12).

Synthesis of (**58**)- and (**72b**)-PLGA

PLGA from Sigma Aldrich (M = 86,500 g/mol) (500 mg) was dissolved in DCM (10 mL) and the solution was cooled at 0°C. An excess of NHS (2.7 mg) and DIC (2.9 mg) were added and the mixture was stirred overnight at room temperature. An excess of 1,3-diaminopropane (1.4 mg) was added and the solution was stirred overnight. The solution was divided between two centrifuge tubes, diethyl ether (40 mL) was added to each tube and the resulting suspension was centrifuged (3000 rpm, 620 G, 5 min). The pellet was dissolved in DCM (5 mL), precipitated with diethyl ether and centrifuged (3000 rpm, 620 G, 5 min) for three times. The polymer was dried under reduced pressure to collect 497 mg. The sensor (7.44 mg of (**72**) or 16.56 mg (**58**)) was dissolved in THF or DCM (10 mL), respectively, at 0°C. An excess of NHS (5.36 mg) and DIC (5.84 mg) were added and the mixture was stirred at room temperature overnight. The amino-functionalised PLGA was added, followed by overnight stirring. The precipitate was collected by centrifugation (3000 rpm, 620 G, 5 min) The pellet was dissolved in DCM (5 mL), precipitated with diethyl ether and centrifuged (3000 rpm, 620 G, 5 min) for three times. The polymer was dried and gave a yellow pellet for (**72b**) and a pink pellet for (**58**). For 500 mg of PLGA, 465 mg of (**72b**) PLGA were created and 105 mg of (**58**) PLGA.

(**58**)-PLGA: FTIR (C=O stretch) 1638 cm^{-1}, (N-H stretch) 3306 cm^{-1}.

(**72b**)-PLGA: FTIR (C=O stretch) 1640 cm^{-1}, (N-H stretch) 3300 cm^{-1}.

<u>Synthesis of (**43**)-PLGA</u>

PLGA (500 mg) was dissolved in DCM (10 mL) and cooled at 0 °C. An excess of NHS (2.68 mg) and DIC (2.92 mg) were added and the mixture was stirred overnight at room temperature. An excess of aza-dibenzocyclooctyne (ADIBO) amine (6.38 mg) was added, followed by overnight stirring. The solution was divided between two centrifuge tubes, diethyl ether (40 mL) was added to each tube and the resulting suspension was centrifuged (3000 rpm, 620 G, 5 min). The pellet was dissolved in DCM (5 mL), precipitated with diethyl ether and centrifuged (3000 rpm, 620 G, 5 min) for three times. The polymer was dried under reduced pressure to collect 457 mg. (**43**) (22.84 mg) was dissolved in DCM (10 mL) and the cyclooctyne-modified PLGA was added and the mixture was stirred overnight. The solid was precipitated with diethyl ether, collected by centrifugation and further purified by washing with diethyl ether to give 122 mg of a pink solid.

(**43**)-PLGA: FTIR (C-H stretch) 3064 cm^{-1}, (N-H stretch) 3494 cm^{-1}.

<u>Synthesis of (**15a**)-PLGA</u>

PLGA (50 mg) was dissolved in DCM (10 mL) and cooled at 0 °C. NHS (0.3 mg) and DIC (0.3 mg) were added and the mixture was stirred overnight at room temperature. An excess of 1,3-propanediamine (0.2 mg) was added and stirring was continued overnight. The solution was divided between two centrifuge tubes, diethyl ether (40 mL) was added to each tube and the resulting suspension was centrifuged (3000 rpm, 620 G, 5 min). The pellet was dissolved in DCM (5 mL), precipitated with diethyl ether and centrifuged (3000 rpm, 620 G, 5 min) for three times. The resulting white pellet was dried under reduced pressure to collect 48 mg. (**15a**) (1 mg) was dissolved in 10 mL THF at 0 °C and NHS (0.6 mg) and DIC (0.6 mg) were added stirring was continued overnight at room temperature. The amino-modified PLGA was added and stirring was continued overnight. The solution was divided between two centrifuge tubes, diethyl ether (40 mL) was added to each tube and the resulting suspension was centrifuge (3000 rpm, 620 G, 5 min). The pellet was dissolved in DCM (5 mL), precipitated with diethyl ether and centrifuged (3000 rpm, 620 G, 5 min) for three times. The polymer was dried and give 45 mg of (**15a**)-PLGA.

General procedure for preparation of PLGA, (**43**)-, (**72b**)-, (**58**)- and (**15a**)-PLGA NPs via single emulsion solvent evaporation

10 mg of PLGA was dissolved in 0.4 mL of DCM. 4 mL of 1 % PVA in water was placed in an ice bath. The cooled PVA solution was ultra-sonicated, and the PLGA solution was added dropwise during the first 30 sec of sonication for a total of 2 min with 65% of amplitude. The solution was then mechanically stirred at 500 rpm and 52 G fat room temperature. For sensor-PLGA this step was carried out in the dark and under nitrogen. After 1 hour the solution was ultra-centrifuged at 35,000 rpm and 84,378 G at -4 °C for 40 min. The supernatant was discarded and deionised water was added, the solid was suspended and another centrifugation carried out. The supernatant was discarded and the particles suspended in 10 mL of PBS solution to have approximatively 1 mg/mL suspension of polymer in PBS.

General procedure for encapsulation of (**1a**) and (**73**) in PLGA NPs

10 mg of PLGA and 1 mg of (**1a**) or (**73**) were dissolved in 0.4 mL of DCM. 4 mL of 1% PVA in water was cooled and then ultra-sonicated. The DCM solution was added dropwise during the first 30 sec of sonication for a total of 2 min with 65% of amplitude. The solution was then mechanically stirred at 500 rpm and 52 G at room temperature. For polymer with sensors this step carried out in the dark and under nitrogen. After 1 hour the solution was centrifuged at 35,000 rpm and 84,378 G at -4 °C for 40 min. The supernatant was discarded and the solid was resuspended in deionised water and second centrifugation carried out. The supernatant was discarded and the polymer was suspended in 10 mL of PBS solution to have approximatively 1 mg/mL suspension of polymer in PBS.

General procedure for PLGA NP formulation using double emulsion solvent evaporation

A 1% PVA solution in water (100 µL) was added over 30 seconds to a solution of 10 mg of PLGA in 0.4 mL of DCM maintained in an ice bath and sonication (65% of amplitude) for 2 minutes. The resultant water-in-oil suspension was added to 4 mL of 1% aqueous PVA in an ice bath under the same sonication conditions described above.

The emulsion was then mechanically stirred at 500 rpm at room temperature. After 1 hour the solution was centrifuged at 35,000 rpm and 84,378 G at -4 °C for 40 min. The supernatant was discarded and deionised water was added, the solid was suspended and another centrifugation carried out. The supernatant was discarded and the polymer was suspended in 10 mL of PBS solution to have approximatively 1 mg/mL suspension of polymer in PBS.

Response to ROS:

Superoxide anion

1 mg of (**43**) was dissolved in a mixture of 1 mL of DMSO and 9 mL of PBS (pH = 7.4). A 10 µM solution of Xa was prepared in PBS. In a cuvette, 3 mL of the sensor solution was mixed with 100 µL of Xa solution and 2 µL of catalase (10-40 kU/mg) (to remove hydrogen peroxide as it forms in order to avoid interferences). Different volumes (0-20 µL) of XO were added and the emission spectra ($\lambda_{exc}/\lambda_{em}$ = 490/540 nm) were recorded in function of the XO concentration.

Hydrogen peroxide

1 mg (**58**) was dissolved in a mix of 1 mL of DMSO and 9 mL of PBS (pH = 7.4). A solution of 2.2 µM of hydrogen peroxide was prepared in PBS. 3 mL of the sensor solution were placed in a cuvette and different concentrations (0-2.94 µmol) of hydrogen peroxide solution were added. Emission spectra ($\lambda_{exc}/\lambda_{em}$ = 515/540 nm) were recorded for different hydrogen peroxide concentration.

Singlet oxygen

1 mg of (**72**) was dissolved 10 mL of EtOH and 5 mg of porphyrin was diluted in 10 mL ethanol. In a cuvette, 3 mL of sensor solution were mixed with 3 µL of the solution with porphyrin. The mixture was then exposed to blue light at different time (0-150 sec) and the emission spectra ($\lambda_{exc}/\lambda_{em}$ = 325/425 nm) were recorded.

<u>Fluorescence characterization of NPs:</u>

<u>Superoxide anion</u>

1 mL of sensor solution at 1 mg/mL of sensor on PLGA was dissolved in a mix of 1 mL of dimethylsulfoxide (DMSO) and 9 mL of phosphate buffer solution (PBS) at a pH of 7.4. A solution of 10 µM of Xa was prepared in PBS. In a cuvette for fluorimeter, 3 mL of the sensor solution was mixed with 100 µL of Xa solution and 2 µL of catalase that transforms the resulted hydrogen peroxide into water to avoid interferences. Then different volumes of XO were added to give fluorescent spectra depending on XO concentration.

<u>Hydrogen peroxide</u>

1 mL of sensor solution at 1 mg/mL of sensor on PLGA was dissolved in a mix of 1 mL of DMSO and 9 mL of PBS at a pH of 7.4. A solution of 2.2 µM of hydrogen peroxide was prepared in PBS. In a cuvette for fluorometer, 3 mL of the sensor solution was added. Then, different volumes of hydrogen peroxide solution were added to give fluorescent spectra depending on hydrogen peroxide concentration.

<u>Singlet oxygen</u>

1 mL of sensor solution at 1 mg/mL of sensor on PLGA of sensor was dissolved 10 mL of EtOH and 5 mg of this porphyrin was diluted in 10 mL ethanol. In a cuvette for fluorimeter, 3 mL of sensor solution was added with 3 µL of the solution with porphyrin. The mixture was then exposed under blue light at different time and the intensity was taken.

<u>Sample preparation for confocal microscopy</u>

Nanosensors (1 mg/mL in PBS, pH = 7.4) or stand-alone sensors (2 mg/mL in DMSO diluted in 9.5 mL of PBS, pH = 7.4) were used. 300 µL of cells suspension was mixed with 100 µL of sensors solution in an Eppendorf vial. The mixture was incubated at 37°C with 5% of CO_2 for 30 min. 50 µL of PMA at 2.5 µM was added and the solution was incubated with the same condition of temperature and atmosphere for 10 min. The solution was centrifuged at 5,000 rpm and 1,722 G for 5 min. The supernatant was discarded and 5 ml PBS was added to make a new suspension and wash cells, which was centrifuged and washed one more time. Cells were suspended in 1 mL of PBS, a drop of the suspension was placed on a microscope slide and a coverslip with a 1.5 focal was slowly deposited on the sample, which was examined at the microscope.

Parameters: laser intensity at 1.2 %, filter between 493 and 630 nm, pinhole at 47 µm, gain at 866, pixel dwell time at 1.58 µs.

<u>Sample preparation for flow cytometry tests</u>

<u>Cytotoxicity</u>

To 100 µL of cells suspension, different volumes of sensor solution (1 mg/mL) were added. Cells were incubated for 30 min at 37°C with 5% of CO_2 and the suspension was analysed on the flow cytometer.

<u>PMA exposure time</u>

100 µL of cells in media were incubated with 50 µL of sensors solution (1 mg/mL) at 37 °C in 5% of CO_2. After 30 min, 20 µL of PMA at 2.5 µM were added. The mixture was incubated in the same condition described above for different times (0-30 min). Measurement of the fluorescence though the filter between 533 nm and 630 nm were taken to follow the evolution of the fluorescence.

<u>PMA concentration</u>

100 µL of cells in media were incubated with 50 µL of sensors solution at 1 mg/mL at 37 °C in 5% of CO2 for 30 min. Different volumes (0-20 µL) of PMA at 2.5 µM were added. The mixture was incubated in the same condition described above for 30 min. Measurement of the fluorescence though the filter between 533 nm and 630 nm were taken to follow the evolution of the fluorescence.

Literature

(1)   Murrant, C. L.; Reid, M. B. Detection of Reactive Oxygen and Reactive Nitrogen Species in Skeletal Muscle. *Microsc. Res. Tech.* **2001**, *55* (4), 236–248.

(2)   Pardini, R. S. Toxicity of Oxygen from Naturally Occurring Redox-active Pro-oxidants. *Arch. Insect Biochem. Physiol.* **1995**, *29* (2), 101–118.

(3)   Gomes, A.; Fernandes, E.; Lima, J. L. F. C. Fluorescence Probes Used for Detection of Reactive Oxygen Species. *J. Biochem. Biophys. Methods* **2005**, *65* (2–3), 45–80.

(4)   Bartosz, G. Reactive Oxygen Species: Destroyers or Messengers? *Biochem. Pharmacol.* **2009**, *77* (8), 1303–1315.

(5)   Chen, Q.; Vazquez, E. J.; Moghaddas, S.; Hoppel, C. L.; Lesnefsky, E. J. Production of Reactive Oxygen Species by Mitochondria: Central Role of Complex III. *J. Biol. Chem.* **2003**, *278* (38), 36027–36031.

(6)   Murphy, M. P. How Mitochondria Produce Reactive Oxygen Species. *Biochem. J.* **2009**, *417* (1), 1–13.

(7)   Sullivan, L. B.; Gui, D. Y.; Van Der Heiden, M. G. Altered Metabolite Levels in Cancer: Implications for Tumour Biology and Cancer Therapy. *Nat. Rev. Cancer* **2016**, *16* (11), 680–693.

(8)   Li, L.; Ishdorj, G.; Gibson, S. B. Reactive Oxygen Species Regulation of Autophagy in Cancer: Implications for Cancer Treatment. *Free Radic. Biol. Med.* **2012**, *53* (7), 1399–1410.

(9)   Brand, M. D. Mitochondrial Generation of Superoxide and Hydrogen Peroxide

as the Source of Mitochondrial Redox Signaling. *Free Radic. Biol. Med.* **2016**, *100*, 14–31.

(10)   Onyango, A. N. Endogenous Generation of Singlet Oxygen and Ozone in Human and Animal Tissues: Mechanisms, Biological Significance, and Influence of Dietary Components. *Oxid. Med. Cell. Longev.* **2016**, *2016*, 1–22.

(11)   Pollak, N.; Dölle, C.; Ziegler, M. The Power to Reduce: Pyridine Nucleotides - Small Molecules with a Multitude of Functions. *Biochem. J.* **2007**, *402* (2), 205–218.

(12)   Kim, K. S.; Lee, D.; Song, C. G.; Kang, P. M. Reactive Oxygen Species-Activated Nanomaterials as Theranostic Agents. *Nanomedicine* **2015**, *10* (17), 2709–2723.

(13)   Winterbourn, C. C. Reconciling the Chemistry and Biology of Reactive Oxygen Species. *Nat. Chem. Biol.* **2008**, *4* (5), 278–286.

(14)   Murphy, M. P. How Mitochondria Produce Reactive Oxygen Species. *Biochem. J.* **2009**, *417* (1), 1–13.

(15)   Holzerová, E.; Prokisch, H. Mitochondria: Much Ado about Nothing? How Dangerous Is Reactive Oxygen Species Production? *Int. J. Biochem. Cell Biol.* **2015**, *63*, 16–20.

(16)   Yadav, N.; Sharma, S. Reactive Oxygen Species, Oxidative Stress and ROS Scavenging System in Plants. *Available online www.jocpr.com J. Chem. Pharm. Res.* **2016**, *8* (5), 595–604.

(17)   Emerit, J.; Edeas, M.; Bricaire, F. Neurodegenerative Diseases and Oxidative Stress. *Biomed. Pharmacother.* **2004**, *58* (1), 39–46.

(18) Schumacker, P. Reactive Oxygen Species in Cancer: A Dance with the Devil. *Cancer Cell* **2015**, *27* (2), 156–157.

(19) Barrera, G. Oxidative Stress and Lipid Peroxidation Products in Cancer Progression and Therapy. *ISRN Oncol.* **2012**, *2012*, 1–21.

(20) COOKE, M. S. Oxidative DNA Damage: Mechanisms, Mutation, and Disease. *FASEB J.* **2003**, *17* (10), 1195–1214.

(21) Zhang, W.; Xiao, S.; Ahn, D. U. Protein Oxidation: Basic Principles and Implications for Meat Quality. *Crit. Rev. Food Sci. Nutr.* **2013**, *53* (11), 1191– 1201.

(22) Amici, A.; Levine, R. L.; Tsai, L.; Stadtman, E. R. Conversion of Amino Acid Residues in Proteins and Amino Acid Homopolymers to Carbonyl Derivatives by Metal-Catalyzed Oxidation Reactions. *J. Biol. Chem.* **1989**, *264* (6), 3341–3346.

(23) Refsgaard, H. H. F.; Tsai, L.; Stadtman, E. R. Modifications of Proteins by Polyunsaturated Fatty Acid Peroxidation Products. *Proc. Natl. Acad. Sci. U. S. A.* **2000**, *97* (2), 611–616.

(24) Steenken, S. Addition-Elimination Paths in Electron-Transfer Reactions between Radicals and Molecules. Oxidation of Organic Molecules by the OH Radical. *J. Chem. Soc. Faraday Trans. 1 Phys. Chem. Condens. Phases* **1987**, *83* (1), 113– 124.

(25) Halliwell, B. Free Radicals and Antioxidants - Quo Vadis? *Trends Pharmacol. Sci.* **2011**, *32* (3), 125–130.

(26) Lushchak, V. I. Free Radicals, Reactive Oxygen Species, Oxidative Stress and

Its Classification. *Chem. Biol. Interact.* **2014**, *224*, 164–175.

(27)   Semchyshyn, H. M.; Lozinska, L. M. Fructose Protects Baker's Yeast against Peroxide Stress: Potential Role of Catalase and Superoxide Dismutase. *FEMS Yeast Res.* **2012**, *12* (7), 761–773.

(28)   Demple, B. Introduction : Reactive Oxygen and Its. *DNA Repair (Amst).* **1991**.

(29)   Lushchak, V. I. Adaptive Response to Oxidative Stress: Bacteria, Fungi, Plants and Animals. *Comp. Biochem. Physiol. - C Toxicol. Pharmacol.* **2011**, *153* (2), 175–190.

(30)   Birben, E.; Sahiner, U. M.; Sackesen, C.; Erzurum, S.; Kalayci, O. Oxidative Stress and Antioxidant Defense. *World Allergy Organ. J.* **2012**, *5* (1), 9–19.

(31)   McCord, J. M.; Fridovich, I. Superoxide Dismutase An Enzymic Function for Erythrocuprein (Hemocuprein). *J. Biol. Chem.* **1969**, *244* (25), 6049.

(32)   D'Autréaux, B.; Toledano, M. B. ROS as Signalling Molecules: Mechanisms That Generate Specificity in ROS Homeostasis. *Nat. Rev. Mol. Cell Biol.* **2007**, *8* (10), 813–824.

(33)   Chen, Y.; Zhang, H.; Jenny, H.; Ji, W.; Min, W. Mitochondrial Redox Signaling and Tumor Progression. *Cancers (Basel).* **2016**, *8* (4), 1–15.

(34)   Redza-Dutordoir, M.; Averill-Bates, D. A. Activation of Apoptosis Signalling Pathways by Reactive Oxygen Species. *Biochim. Biophys. Acta - Mol. Cell Res.* **2016**, *1863* (12), 2977–2992.

(35)   Mittler, R. ROS Are Good. *Trends Plant Sci.* **2017**, *22* (1), 11–19.

(36) Pani, G.; Galeotti, T.; Chiarugi, P. Metastasis: Cancer Cell's Escape from Oxidative Stress. *Cancer Metastasis Rev.* **2010**, *29* (2), 351–378.

(37) Márquez-Jurado, S.; Díaz-Colunga, J.; Das Neves, R. P.; Martinez-Lorente, A.; Almazán, F.; Guantes, R.; Iborra, F. J. Mitochondrial Levels Determine Variability in Cell Death by Modulating Apoptotic Gene Expression. *Nat. Commun.* **2018**, *9* (1).

(38) Dickinson, B. C.; Chang, C. J. Chemistry and Biology of Reactive Oxygen Species in Signaling or Stress Responses. *Nat. Chem. Biol.* **2011**, *7* (8), 504–511.

(39) Ray, P. D.; Huang, B. W.; Tsuji, Y. Reactive Oxygen Species (ROS) Homeostasis and Redox Regulation in Cellular Signaling. *Cell. Signal.* **2012**, *24* (5), 981–990.

(40) Polyak, K.; Xia, Y.; Zweier, J. L.; Kinzler, K. W.; Vogelstein, B. A Model for P53-Induced Apoptosis. *Nature* **1997**, *389* (6648), 300–305.

(41) Tsang, W. P.; Chau, S. P. Y.; Kong, S. K.; Fung, K. P.; Kwok, T. T. Reactive Oxygen Species Mediate Doxorubicin Induced P53-Independent Apoptosis. *Life Sci.* **2003**, *73* (16), 2047–2058.

(42) Simon, H.-U.; Haj-Yehia, A.; Levi-Schaffer, F. Role of Reactive Oxygen Species (ROS) in Apoptosis Induction. *APOPTOSIS* **2000**, *5* (5), 415–418.

(43) Bellezza, I.; Riuzzi, F.; Chiappalupi, S.; Arcuri, C.; Giambanco, I.; Sorci, G. Reductive Stress in Striated Muscle Cells. *Cell. Mol. Life Sci.* **2020**, No. 0123456789.

(44)   Lloret, A.; Fuchsberger, T.; Giraldo, E.; Vina, J. Reductive Stress: A New Concept in Alzheimer's Disease. *Curr. Alzheimer Res.* **2015**, *13* (2), 206–211.

(45)   Oyagbemi, A. A.; Azeez, O. I.; Saba, A. B. Interactions between Reactive Oxygen Species and Cancer: The Roles of Natural Dietary Antioxidants and Their Molecular Mechanisms of Action. *Asian Pacific J. Cancer Prev.* **2009**, *10* (4), 535–544.

(46)   Schumacker, P. T. Reactive Oxygen Species in Cancer Cells: Live by the Sword, Die by the Sword. *Cancer Cell* **2006**, *10* (3), 175–176.

(47)   Galadari, S.; Rahman, A.; Pallichankandy, S.; Thayyullathil, F. Reactive Oxygen Species and Cancer Paradox: To Promote or to Suppress? *Free Radic. Biol. Med.* **2017**, *104*, 144–164.

(48)   Finkel, T.; Serrano, M.; Blasco, M. A. The Common Biology of Cancer and Ageing. *Nature* **2007**, *448* (7155), 767–774.

(49)   McMurray, F.; Patten, D. A.; Harper, M. E. Reactive Oxygen Species and Oxidative Stress in Obesity—Recent Findings and Empirical Approaches. *Obesity* **2016**, *24* (11), 2301–2310.

(50)   Kaneto, H.; Katakami, N.; Matsuhisa, M.; Matsuoka, T. A. Role of Reactive Oxygen Species in the Progression of Type 2 Diabetes and Atherosclerosis. *Mediators Inflamm.* **2010**, *2010*.

(51)   Fakhruddin, S.; Alanazi, W.; Jackson, K. E. Diabetes-Induced Reactive Oxygen Species: Mechanism of Their Generation and Role in Renal Injury. *J. Diabetes Res.* **2017**, *2017*.

(52) Davalli, P.; Mitic, T.; Caporali, A.; Lauriola, A.; D'Arca, D. ROS, Cell Senescence, and Novel Molecular Mechanisms in Aging and Age-Related Diseases. *Oxid. Med. Cell. Longev.* **2016**, *2016*.

(53) Liochev, S. I. Reactive Oxygen Species and the Free Radical Theory of Aging. *Free Radic. Biol. Med.* **2013**, *60*, 1–4.

(54) Chandrasekaran, A.; Idelchik, M. del P. S.; Melendez, J. A. Redox Control of Senescence and Age-Related Disease. *Redox Biol.* **2017**, *11* (November 2016), 91–102.

(55) Datla, S. R.; Griendling, K. K. Reactive Oxygen Species, NADPH Oxidases, and Hypertension. *Hypertension* **2010**, *56* (3), 325–330.

(56) Lassègue, B.; Griendling, K. K. Reactive Oxygen Species in Hypertension: An Update. *Am. J. Hypertens.* **2004**, *17* (9), 852–860.

(57) Liou, G.-Y.; Storz, P. Reactive Oxygen Species in Cancer. *Free Radic. Res.* **2010**, *44* (5), 479–496.

(58) Zitka, O.; Skalickova, S.; Gumulec, J.; Masarik, M.; Adam, V.; Hubalek, J.; Trnkova, L.; Kruseova, J.; Eckschlager, T.; Kizek, R. Redox Status Expressed as GSH:GSSG Ratio as a Marker for Oxidative Stress in Paediatric Tumour Patients. *Oncol. Lett.* **2012**, *4* (6), 1247–1253.

(59) Zhou, Y.; Liang, X.; Dai, Z. Porphyrin-Loaded Nanoparticles for Cancer Theranostics. *Nanoscale* **2016**, *8* (25), 12394–12405.

(60) Zhou, Z.; Song, J.; Nie, L.; Chen, X. Reactive Oxygen Species Generating Systems Meeting Challenges of Photodynamic Cancer Therapy. *Chem. Soc.*

Rev. **2016**, *45* (23), 6597–6626.

(61) Boëns, B.; Faugeras, P. A.; Vergnaud, J.; Lucas, R.; Teste, K.; Zerrouki, R. Iodine-Catalyzed One-Pot Synthesis of Unsymmetrical Meso-Substituted Porphyrins. *Tetrahedron* **2010**, *66* (11), 1994–1996.

(62) Mroz, P.; Yaroslavsky, A.; Kharkwal, G. B.; Hamblin, M. R. Cell Death Pathways in Photodynamic Therapy of Cancer. *Cancers (Basel).* **2011**, *3* (2), 2516–2539.

(63) Price, M.; Reiners, J. J.; Santiago, A. M.; Kessel, D. Monitoring Singlet Oxygen and Hydroxyl Radical Formation with Fluorescent Probes during Photodynamic Therapy. *Photochem. Photobiol.* **2009**, *85* (5), 1177–1181.

(64) Lowe, S. W.; Lin, A. W. Apoptosis in Cancer. *Carcinogenesis* **2000**, *21* (3), 485–495.

(65) Gallardo-Villagrán, M.; Leger, D. Y.; Liagre, B.; Therrien, B. Photosensitizers Used in the Photodynamic Therapy of Rheumatoid Arthritis. *Int. J. Mol. Sci.* **2019**, *20* (13).

(66) Zhang, Y.; Chen, X.; Gueydan, C.; Han, J. Plasma Membrane Changes during Programmed Cell Deaths. *Cell Res.* **2018**, *28* (1), 9–21.

(67) Dikalov, S. I.; Harrison, D. G. Methods for Detection of Mitochondrial and Cellular Reactive Oxygen Species. *Antioxid. Redox Signal.* **2014**, *20* (2), 372–382.

(68) Zhang, Y.; Dai, M.; Yuan, Z. Methods for the Detection of Reactive Oxygen Species. *Anal. Methods* **2018**, *10* (38), 4625–4638.

(69) Dikalov, S. I.; Nazarewicz, R. R. Measurements of Reactive Oxygen Species in Cardiovascular Studies. *Syst. Biol. Free Radicals Antioxidants* **2007**, *49* (4),

1437–1450.

(70) Finkelstein, E.; Rosen, G. M.; Rauckman, E. J. Spin Trapping of Superoxide and

Hydroxyl Radical: Practical Aspects. *Arch. Biochem. Biophys.* **1980**, *200* (1), 1–

16.

(71) Münzel, T.; Afanas'ev, I. B.; Kleschyov, A. L.; Harrison, D. G. Detection of

Superoxide in Vascular Tissue. *Arterioscler. Thromb. Vasc. Biol.* **2002**, *22* (11),

1761–1768.

(72) Zhao, H.; Joseph, J.; Fales, H. M.; Sokoloski, E. A.; Levine, R. L.; Vasquez-Vivar,

J.; Kalyanaraman, B. Detection and Characterization of the Product of

Hydroethidine and Intracellular Superoxide by HPLC and Limitations of

Fluorescence. *Proc. Natl. Acad. Sci. U. S. A.* **2005**, *102* (16), 5727–5732.

(73) Zwicker, K.; Dikalov, S.; Matuschka, S.; Mainka, L.; Hofmann, M.; Khramtsov,

V.; Zimmer, G. Oxygen Radical Generation and Enzymatic Properties of

Mitochondria in Hypoxia/Reoxygenation. *Arzneimittel-Forschung/Drug Res.*

1998, *48* (6), 629–636.

(74) Hardy, M.; Rockenbauer, A.; Vásquez-Vivar, J.; Felix, C.; Lopez, M.; Srinivasan,

S.; Avadhani, N.; Tordo, P.; Kalyanaraman, B. Detection, Characterization, and

Decay Kinetics of ROS and Thiyl Adducts of Mito-DEPMPO Spin Trap. *Chem.*

Res. Toxicol. **2007**, *20* (7), 1053–1060.

(75) Hardy, M.; Poulhés, F.; Rizzato, E.; Rockenbauer, A.; Banaszak, K.; Karoui, H.;

Lopez, M.; Zielonka, J.; Vasquez-Vivar, J.; Sethumadhavan, S.; Kalyanaraman,

B.; Tordo, P.; Ouari, O. Mitochondria-Targeted Spin Traps: Synthesis,

Superoxide Spin Trapping, and Mitochondrial Uptake. *Chem. Res. Toxicol.*

2014, *27* (7), 1155–1165.

(76) Kurtoglu, M.; Lampidis, T. J. From Delocalized Lipophilic Cations to Hypoxia: Blocking Tumor Cell Mitochondrial Function Leads to Therapeutic Gain with Glycolytic Inhibitors. *Mol. Nutr. Food Res.* **2009**, *53* (1), 68–75.

(77) Keszler, A.; Kalyanaraman, B.; Hogg, N. Comparative Investigation of Superoxide Trapping by Cyclic Nitrone Spin Traps: The Use of Singular Value Decomposition and Multiple Linear Regression Analysis. *Free Radic. Biol. Med.* **2003**, *35* (9), 1149–1157.

(78) Khan, N.; Wilmot, C. M.; Rosen, G. M.; Demidenko, E.; Sun, J.; Joseph, J.; O'Hara, J.; Kalyanaraman, B.; Swartz, H. M. Spin Traps: In Vitro Toxicity and Stability of Radical Adducts. *Free Radic. Biol. Med.* **2003**, *34* (11), 1473–1481.

(79) Abou-Khalil, S.; Abou-Khalil, W. H.; Planas, L.; Tapiero, H.; Lampidis, T. J. Interaction of Rhodamine 123 with Mitochondria Isolated from Drug-Sensitive and -Resistant Friend Leukemia Cells. *Biochem. Biophys. Res. Commun.* **1985**, *127* (3), 1039–1044.

(80) Vásquez-Vivar, J.; Hogg, N.; Pritchard, K. A.; Martasek, P.; Kalyanaraman, B. Superoxide Anion Formation from Lucigenin: An Electron Spin Resonance Spin-Trapping Study. *FEBS Lett.* **1997**, *403* (2), 127–130.

(81) Maskiewicz, R.; Sogah, D.; Bruice, T. C. Chemiluminescent Reactions of Lucigenin. 1. Reactions of Lucigenin with Hydrogen Peroxide. *J. Am. Chem. Soc.* **1979**, *101* (18), 5347–5354.

(82) Faulkner, K.; Fridovich, I. Luminol and Lucigenin as Detectors for $O_2^{\cdot-}$. *Free Radic. Biol. Med.* **1993**, *15* (4), 447–451.

(83) Tarpey, M. M.; Fridovich, I. Methods of Detection of Vascular Reactive Species: Nitric Oxide, Superoxide, Hydrogen Peroxide, and Peroxynitrite. *Circ. Res.* **2001**, *89* (3), 224–236.

(84) Merényi, G.; Lind, J.; Eriksen, T. E. The Equilibrium Reaction of the Luminol Radical with Oxygen and the One-Electron-Reduction Potential of 5-Aminophthalazine-1,4-Dione. *J. Phys. Chem.* **1984**, *88* (11), 2320–2323.

(85) Arias-Barreiro, C. R.; Okazaki, K.; Koutsaftis, A.; Inayat-Hussain, S. H.; Tani, A.; Katsuhara, M.; Kimbara, K.; Mori, I. C. A Bacterial Biosensor for Oxidative Stress Using the Constitutively Expressed Redox-Sensitive Protein RoGFP2. *Sensors* **2010**, *10* (7), 6290–6306.

(86) Maulucci, G.; Labate, V.; Mele, M.; Panieri, E.; Arcovito, G.; Galeotti, T.; Østergaard, H.; Winther, J. R.; De Spirito, M.; Pani, G. High-Resolution Imaging of Redox Signaling in Live Cells through an Oxidation-Sensitive Yellow Fluorescent Protein. *Sci. Signal.* **2008**, *1* (43), 1–16.

(87) Björnberg, O.; Østergaard, H.; Winther, J. R. Measuring Intracellular Redox Conditions Using GFP-Based Sensors. *Antioxidants Redox Signal.* **2006**, *8* (3–4), 354–361.

(88) Hansen, R. E.; Østergaard, H.; Winther, J. R. Increasing the Reactivity of an Artificial Dithiol-Bisulfide Pair through Modification of the Electrostatic Milieu. *Biochemistry* **2005**, *44* (15), 5899–5906.

(89) Ermakova, Y. G.; Bilan, D. S.; Matlashov, M. E.; Mishina, N. M.; Markvicheva, K. N.; Subach, O. M.; Subach, F. V.; Bogeski, I.; Hoth, M.; Enikolopov, G.; Belousov, V. V. Red Fluorescent Genetically Encoded Indicator for Intracellular

Hydrogen Peroxide. *Nat. Commun.* **2014**, *5*, 1–9.

(90) ThermoFisher Scientific. Probes for Reactive Oxygen Species , Including Nitric Oxide Fluorophores. *Mol. Probes ® Handb.* **2010**, Chapter 18.

(91) Nzambe Ta Keki, J. K.; Ouk, T. S.; Zerrouki, R.; Faugeras, P. A.; Sol, V.; Brouillette, F. Synthesis and Photobactericidal Properties of a Neutral Porphyrin Grafted onto Lignocellulosic Fibers. *Mater. Sci. Eng. C* **2016**, *62*, 61–67.

(92) Topete, A.; Alatorre-Meda, M.; Iglesias, P.; Villar-Alvarez, E. M.; Barbosa, S.; Costoya, J. A.; Taboada, P.; Mosquera, V. Fluorescent Drug-Loaded, Polymeric-Based, Branched Gold Nanoshells for Localized Multimodal Therapy and Imaging of Tumoral Cells. *ACS Nano* **2014**, *8* (3), 2725–2738.

(93) Fan, W.; Shen, B.; Bu, W.; Chen, F.; He, Q.; Zhao, K.; Zhang, S.; Zhou, L.; Peng, W.; Xiao, Q.; Ni, D.; Liu, J.; Shi, J. A Smart Upconversion-Based Mesoporous Silica Nanotheranostic System for Synergetic Chemo-/Radio-/Photodynamic Therapy and Simultaneous MR/UCL Imaging. *Biomaterials* **2014**, *35* (32), 8992–9002.

(94) Zielonka, J.; Vasquez-Vivar, J.; Kalyanaraman, B. Detection of 2-Hydroxyethidium in Cellular Systems: A Unique Marker Product of Superoxide and Hydroethidine. *Nat. Protoc.* **2008**, *3* (1), 8–21.

(95) Dickinson, B. C.; Srikun, D.; Chang, C. J. Mitochondrial-Targeted Fluorescent Probes for Reactive Oxygen Species. *Curr. Opin. Chem. Biol.* **2010**, *14* (1), 50–56.

(96) Zielonka, J.; Kalyanaraman, B. Hydroethidine- and MitoSOX-Derived Red Fluorescence Is Not a Reliable Indicator of Intracellular Superoxide Formation:

Another Inconvenient Truth. *Free Radic. Biol. Med.* **2010**, *48* (8), 983–1001.

(97) Zhao, H.; Kalivendi, S.; Zhang, H.; Joseph, J.; Nithipatikom, K.; Vásquez-Vivar, J.; Kalyanaraman, B. Superoxide Reacts with Hydroethidine but Forms a Fluorescent Product That Is Distinctly Different from Ethidium: Potential Implications in Intracellular Fluorescence Detection of Superoxide. *Free Radic. Biol. Med.* **2003**, *34* (11), 1359–1368.

(98) Winterbourn, C. C. The Challenges of Using Fluorescent Probes to Detect and Quantify Specific Reactive Oxygen Species in Living Cells. *Biochim. Biophys. Acta - Gen. Subj.* **2014**, *1840* (2), 730–738.

(99) Kalyanaraman, B.; Darley-Usmar, V.; Davies, K. J. A.; Dennery, P. A.; Forman, H. J.; Grisham, M. B.; Mann, G. E.; Moore, K.; Roberts, L. J.; Ischiropoulos, H. Measuring Reactive Oxygen and Nitrogen Species with Fluorescent Probes: Challenges and Limitations. *Free Radic. Biol. Med.* **2012**, *52* (1), 1–6.

(100) Kalyanaraman, B.; Hardy, M.; Podsiadly, R.; Cheng, G.; Zielonka, J. Recent Developments in Detection of Superoxide Radical Anion and Hydrogen Peroxide: Opportunities, Challenges, and Implications in Redox Signaling. *Arch. Biochem. Biophys.* **2017**, *617*, 38–47.

(101) Dickinson, B. C.; Lin, V. S.; Chang, C. J. Preparation and Use of MitoPY1 for Imaging Hydrogen Peroxide in Mitochondria of Live Cells. *Nat. Protoc.* **2013**, *8* (6), 1249–1259.

(102) Soh, N. Recent Advances in Fluorescent Probes for the Detection of Reactive Oxygen Species. *Anal. Bioanal. Chem.* **2006**, *386* (3), 532–543.

(103) Wang, H. S. Development of Fluorescent and Luminescent Probes for Reactive

Oxygen Species. *TrAC - Trends Anal. Chem.* **2016**, *85*, 181–202.

(104) Robinson, K. M.; Janes, M. S.; Beckman, J. S. The Selective Detection of Mitochondrial Superoxide by Live Cell Imaging. *Nat. Protoc.* **2008**, *3* (6), 941–947.

(105) Li, A.; Liu, H.; Ouyang, P.; Yang, P. H.; Cai, H. H.; Cai, J. A Sensitive Probe for Detecting Intracellular Reactive Oxygen Species via Glutathione-Mediated Nanoaggregates to Enhance Resonance Rayleigh Scattering Signals. *Sensors Actuators, B Chem.* **2017**, *246*, 190–196.

(106) Carloni, P.; Damiani, E.; Greci, L.; Stipa, P.; Tanfani, F.; Tartaglini, E.; Wozniak, M. On the Use of 1,3-Diphenylisobenzofuran (DPBF). Reactions with Carbon and Oxygen Centered Radicals in Model and Natural Systems. *Res. Chem. Intermed.* **1993**, *19* (5), 395–405.

(107) Chen, X.; Tian, X.; Shin, I.; Yoon, J. Fluorescent and Luminescent Probes for Detection of Reactive Oxygen and Nitrogen Species. *Chem. Soc. Rev.* **2011**, *40* (9), 4783–4804.

(108) Xu, K.; Liu, X.; Tang, B. A Phosphinate-Based Red Fluorescent Probe for Imaging the Superoxide Radical Anion Generated by RAW264.7 Macrophages. *ChemBioChem* **2007**, *8* (4), 453–458.

(109) Xu, K.; Liu, X.; Tang, B.; Yang, G.; Yang, Y.; An, L. Design of a Phosphinate-Based Fluorescent Probe for Superoxide Detection in Mouse Peritoneal Macrophages. *Chem. - A Eur. J.* **2007**, *13* (5), 1411–1416.

(110) Xu, K.; Tang, B.; Huang, H.; Yang, G.; Chen, Z.; Li, P.; An, L. Strong Red Fluorescent Probes Suitable for Detecting Hydrogen Peroxide Generated by

Mice Peritoneal Macrophages. *Chem. Commun.* **2005**, No. 48, 5974–5976.

(111) Chen, X.; Wang, F.; Hyun, J. Y.; Wei, T.; Qiang, J.; Ren, X.; Shin, I.; Yoon, J. Recent Progress in the Development of Fluorescent, Luminescent and Colorimetric Probes for Detection of Reactive Oxygen and Nitrogen Species. *Chem. Soc. Rev.* **2016**, *45* (10), 2976–3016.

(112) Luo, Y.; Wang, D.; Abbruzzese, J. L.; Lu, W. Measurement of Reactive Oxygen Species by Fluorescent Probes in Pancreatic Cancer Cells. In *Methods in molecular biology (Clifton, N.J.)*; Humana Press, New York, NY, 2019; Vol. 1882, pp 207–219.

(113) Griendling, K. K.; Touyz, R. M.; Zweier, J. L.; Dikalov, S.; Chilian, W.; Chen, Y. R.; Harrison, D. G.; Bhatnagar, A. *Measurement of Reactive Oxygen Species, Reactive Nitrogen Species, and Redox-Dependent Signaling in the Cardiovascular System: A Scientific Statement from the American Heart Association*; 2016; Vol. 119.

(114) Terai, T.; Nagano, T. Small-Molecule Fluorophores and Fluorescent Probes for Bioimaging. *Pflugers Arch. Eur. J. Physiol.* **2013**, *465* (3), 347–359.

(115) Zhou, M.; Diwu, Z.; Panchuk-Voloshina, N.; Haugland, R. P. A Stable Nonfluorescent Derivative of Resorufin for the Fluorometric Determination of Trace Hydrogen Peroxide: Applications in Detecting the Activity of Phagocyte NADPH Oxidase and Other Oxidases. *Anal. Biochem.* **1997**, *253* (2), 162–168.

(116) Barja, G. The Quantitative Measurement of H2O2 Generation in Isolated Mitochondria. *J. Bioenerg. Biomembr.* **2002**, *34* (3), 227–233.

(117) Loschen, G.; Flohé, L.; Chance, B. Respiratory Chain Linked H2O2 Production

in Pigeon Heart Mitochondria. *FEBS Lett.* **1971**, *18* (2), 261–264.

(118) Pastor, I.; Esquembre, R.; Micol, V.; Mallavia, R.; Mateo, C. R. A Ready-to-Use Fluorimetric Biosensor for Superoxide Radical Using Superoxide Dismutase and Peroxidase Immobilized in Sol-Gel Glasses. *Anal. Biochem.* **2004**, *334* (2), 335–343.

(119) Towne, V.; Will, M.; Oswald, B.; Zhao, Q. Complexities in Horseradish Peroxidase-Catalyzed Oxidation of Dihydroxyphenoxazine Derivatives: Appropriate Ranges for PH Values and Hydrogen Peroxide Concentrations in Quantitative Analysis. *Anal. Biochem.* **2004**, *334* (2), 290–296.

(120) Staniek, K.; Nohl, H. H2O2 Detection from Intact Mitochondria as a Measure for One-Electron Reduction of Dioxygen Requires a Non-Invasive Assay System. *Biochim. Biophys. Acta - Bioenerg.* **1999**, *1413* (2), 70–80.

(121) Werner, E. Determination of Cellular H2O2 Production. *Sci. STKE* **2003**, *2003* (168), 901–909.

(122) Urano, Y.; Kamiya, M.; Kanda, K.; Ueno, T.; Hirose, K.; Nagano, T. Evolution of Fluorescein as a Platform for Finely Tunable Fluorescence Probes. *J. Am. Chem. Soc.* **2005**, *127* (13), 4888–4894.

(123) Xu, Z.; Xu, L. Fluorescent Probes for the Selective Detection of Chemical Species inside Mitochondria. *Chem. Commun.* **2015**, *52* (6), 1094–1119.

(124) Crow, J. P. Dichlorodihydrofluorescein and Dihydrorhodamine 123 Are Sensitive Indicators of Peroxynitrite in Vitro: Implications for Intracellular Measurement of Reactive Nitrogen and Oxygen Species. *Nitric Oxide - Biol. Chem.* **1997**, *1* (2), 145–157.

(125) Royall, J. A.; Ischiropoulos, H. Evaluation of 2′,7′-Dichlorofluorescin and Dihydrorhodamine 123 as Fluorescent Probes for Intracellular H2O2 in Cultured Endothelial Cells. *Archives of Biochemistry and Biophysics.* 1993, pp 348–355.

(126) Corby, E. j.; Taylor, W. C. A Study of the Peroxidation of Organic Compounds by Externally Generated Singlet Oxygen Molecules. *J. Am. Chem. Soc.* **1964**, *86* (18), 3881–3882.

(127) Lavi, A.; Weitman, H.; Holmes, R. T.; Smith, K. M.; Ehrenberg, B. The Depth of Porphyrin in a Membrane and the Membrane's Physical Properties Affect the Photosensitizing Efficiency. *Biophys. J.* **2002**, *82* (4), 2101–2110.

(128) Wilkinson, F.; Brummer, J. G. Rate Constants for the Decay and Reactions of the Lowest Electronically Excited Singlet State of Molecular Oxygen in Solution. *J. Phys. Chem. Ref. Data* **1981**, *10* (4), 809–999.

(129) Umezawa, N.; Tanaka, K.; Urano, Y.; Kikuchi, K.; Higuchi, T.; Nagano, T. Novel Fluorescent Probes for Singlet Oxygen. *Angew. Chemie - Int. Ed.* **1999**, *38* (19), 2899–2901.

(130) Pedersen, S. K.; Holmehave, J.; Blaikie, F. H.; Gollmer, A.; Breitenbach, T.; Jensen, H. H.; Ogilby, P. R. Aarhus Sensor Green: A Fluorescent Probe for Singlet Oxygen. *J. Org. Chem.* **2014**, *79* (7), 3079–3087.

(131) Garcia-Diaz, M.; Huang, Y. Y.; Hamblin, M. R. Use of Fluorescent Probes for ROS to Tease Apart Type I and Type II Photochemical Pathways in Photodynamic Therapy. *Methods* **2016**, *109*, 158–166.

(132) Filatov, M. A.; Senge, M. O. Molecular Devices Based on Reversible Singlet Oxygen Binding in Optical and Photomedical Applications. *Mol. Syst. Des. Eng.*

2016, *1* (3), 258–272.

(133) Ruiz-González, R.; Bresolí-Obach, R.; Gulías, Ò.; Agut, M.; Savoie, H.; Boyle, R. W.; Nonell, S.; Giuntini, F. NanoSOSG: A Nanostructured Fluorescent Probe for the Detection of Intracellular Singlet Oxygen. *Angew. Chemie - Int. Ed.* **2017**, *56* (11), 2885–2888.

(134) Bresolí-Obach, R.; Nos, J.; Mora, M.; Sagristà, M. L.; Ruiz-González, R.; Nonell, S. Anthracene-Based Fluorescent Nanoprobes for Singlet Oxygen Detection in Biological Media. *Methods* **2016**, *109*, 64–72.

(135) Yang, X. F.; Guo, X. Q. Investigation of the Anthracene-Nitroxide Hybrid Molecule as a Probe for Hydroxyl Radicals. *Analyst* **2001**, *126* (10), 1800–1804.

(136) Blough, N. V.; Simpson, D. J. Chemically Mediated Fluorescence Yield Switching in Nitroxide-Fluorophore Adducts: Optical Sensors of Radical/Redox Reactions. *J. Am. Chem. Soc.* **1988**, *110* (6), 1915–1917.

(137) Green, S. A.; Simpson, D. J.; Zhou, G.; Ho, P. S.; Blough, N. V. Intramolecular Quenching of Excited Singlet States by StableNitroxyl Radicals. *J. Am. Chem. Soc.* **1990**, *112* (20), 7337–7346.

(138) Tai, C.; Gu, X.; Zou, H.; Guo, Q. A New Simple and Sensitive Fluorometric Method for the Determination of Hydroxyl Radical and Its Application. *Talanta* **2002**, *58* (4), 661–667.

(139) Tang, B.; Zhang, L.; Geng, Y. Determination of the Antioxidant Capacity of Different Food Natural Products with a New Developed Flow Injection Spectrofluorimetry Detecting Hydroxyl Radicals. *Talanta* **2005**, *65* (3), 769–775.

(140) Gopakumar, K.; Kini, U. R.; Ashawa, S. C. Gamma Irradiation of Coumarin in Aqueous Solution. *Radiat. Eff.* **1977**, *32* (3–4), 199–203.

(141) Ashawa, S. C.; Kini, U. R.; Madhvanath, U. The Aqueous Coumarin System as a Low Range Chemical Dosimeter. *Int. J. Appl. Radiat. Isot.* **1979**, *30* (1), 7–10.

(142) Crosby, D. G.; Berthold, R. V. Fluorescence Spectra of Some Simple Coumarins. *Anal. Biochem.* **1962**, *4* (5), 349–357.

(143) Sherman, W. R.; Robins, E. Fluorescence of Substituted 7-Hydroxycoumarins. *Anal. Chem.* **1968**, *40* (4), 803–805.

(144) Makrigiorgos, G. M.; Folkard, M.; Huang, C.; Bump, E.; Baranowska-Kortylewicz, J.; Sahu, S. K.; Michael, B. D.; Kassis, A. I. Quantification of Radiation-Induced Hydroxyl Radicals within Nucleohistones Using a Molecular Fluorescent Probe. *Radiat. Res.* **1994**, *138* (2), 177.

(145) Makrigiorgos, G. M.; Bump, E.; Huang, C.; Baranowska-Kortylewicz, J.; Kassis, A. I. A Fluorimetric Method for the Detection of Copper-Mediated Hydroxyl Free Radicals in the Immediate Proximity of DNA. *Free Radic. Biol. Med.* **1995**, *18* (4), 669–678.

(146) Chakrabarti, S.; Mahmood, A.; Kassis, A. I.; Bump, E. A.; Jones, A. G.; Makrigiorgos, G. M. Generation of Hydroxyl Radicals by Nucleohistone-Bound Metal-Adriamycin Complexes. *Free Radic. Res.* **1996**, *25* (3), 207–220.

(147) Setsukinai, K. ichi; Urano, Y.; Kakinuma, K.; Majima, H. J.; Nagano, T. Development of Novel Fluorescence Probes That Can Reliably Detect Reactive Oxygen Species and Distinguish Specific Species. *J. Biol. Chem.* **2003**, *278* (5), 3170–3175.

(148) Ou, B.; Hampsch-Woodill, M.; Flanagan, J.; Deemer, E. K.; Prior, R. L.; Huang, D. Novel Fluorometric Assay for Hydroxyl Radical Prevention Capacity Using Fluorescein as the Probe. *J. Agric. Food Chem.* **2002**, *50* (10), 2772–2777.

(149) Khan, I.; Saeed, K.; Khan, I. Nanoparticles: Properties, Applications and Toxicities. *Arab. J. Chem.* **2019**, *12* (7), 908–931.

(150) Laurent, S.; Forge, D.; Port, M.; Roch, A.; Robic, C.; Vander Elst, L.; Muller, R. N. Magnetic Iron Oxide Nanoparticles: Synthesis, Stabilization, Vectorization, Physicochemical Characterizations, and Biological Applications. *Chem. Rev.* **2008**, *108* (6), 2064–2110.

(151) Rao, J. P.; Geckeler, K. E. Polymer Nanoparticles: Preparation Techniques and Size-Control Parameters. *Prog. Polym. Sci.* **2011**, *36* (7), 887–913.

(152) Astefanei, A.; Núñez, O.; Galceran, M. T. Characterisation and Determination of Fullerenes: A Critical Review. *Anal. Chim. Acta* **2015**, *882*, 1–21.

(153) Franskevych, D.; Palyvoda, K.; Petukhov, D.; Prylutska, S.; Grynyuk, I.; Schuetze, C.; Drobot, L.; Matyshevska, O.; Ritter, U. Fullerene C60Penetration into Leukemic Cells and Its Photoinduced Cytotoxic Effects. *Nanoscale Res. Lett.* **2017**, *12* (1).

(154) Ibrahim, K. S. Carbon Nanotubes-Properties and Applications: A Review. *Carbon Lett.* **2013**, *14* (3), 131–144.

(155) Dreaden, E. C.; Alkilany, A. M.; Huang, X.; Murphy, C. J.; El-Sayed, M. A. The Golden Age: Gold Nanoparticles for Biomedicine. *Chem. Soc. Rev.* **2012**, *41* (7), 2740–2779.

(156) Sigmund, W.; Yuh, J.; Park, H.; Maneeratana, V.; Pyrgiotakis, G.; Daga, A.; Taylor, J.; Nino, J. C. Processing and Structure Relationships in Electrospinning of Ceramic Fiber Systems. *J. Am. Ceram. Soc.* **2006**, *89* (2), 395–407.

(157) Moreira, A. F.; Dias, D. R.; Correia, I. J. Stimuli-Responsive Mesoporous Silica Nanoparticles for Cancer Therapy: A Review. *Microporous Mesoporous Mater.* **2016**, *236*, 141–157.

(158) Hu, Z.; Tan, J.; Lai, Z.; Zheng, R.; Zhong, J.; Wang, Y.; Li, X.; Yang, N.; Li, J.; Yang, W.; Huang, Y.; Zhao, Y.; Lu, X. Aptamer Combined with Fluorescent Silica Nanoparticles for Detection of Hepatoma Cells. *Nanoscale Res. Lett.* **2017**, *12* (1).

(159) van Elk, M.; Murphy, B. P.; Eufrásio-da-Silva, T.; O'Reilly, D. P.; Vermonden, T.; Hennink, W. E.; Duffy, G. P.; Ruiz-Hernández, E. Nanomedicines for Advanced Cancer Treatments: Transitioning towards Responsive Systems. *Int. J. Pharm.* **2016**, *515* (1–2), 132–164.

(160) Shirshahi, V.; Soltani, M. Solid Silica Nanoparticles: Applications in Molecular Imaging. *Contrast Media Mol. Imaging* **2015**, *10* (1), 1–17.

(161) Ali, S.; Khan, I.; Khan, S. A.; Sohail, M.; Ahmed, R.; Rehman, A. ur; Ansari, M. S.; Morsy, M. A. Electrocatalytic Performance of Ni@Pt Core–Shell Nanoparticles Supported on Carbon Nanotubes for Methanol Oxidation Reaction. *J. Electroanal. Chem.* **2017**, *795*, 17–25.

(162) Astete, C. E.; Sabliov, C. M. Synthesis and Characterization of PLGA Nanoparticles. *J. Biomater. Sci. Polym. Ed.* **2006**, *17* (3), 247–289.

(163) Crucho, C. I. C.; Barros, M. T. Formulation of Functionalized PLGA Polymeric

Nanoparticles for Targeted Drug Delivery. *Polymer (Guildf).* **2015**, *68*, 41–46.

(164) Ding, D.; Zhu, Q. Recent Advances of PLGA Micro/Nanoparticles for the Delivery of Biomacromolecular Therapeutics. *Mater. Sci. Eng. C* **2018**, *92*, 1041–1060.

(165) Gentile, P.; Chiono, V.; Carmagnola, I.; Hatton, P. V. An Overview of Poly(Lactic-Co-Glycolic) Acid (PLGA)-Based Biomaterials for Bone Tissue Engineering. *Int. J. Mol. Sci.* **2014**, *15* (3), 3640–3659.

(166) Liu, Z.; Jiao, Y.; Wang, Y.; Zhou, C.; Zhang, Z. Polysaccharides-Based Nanoparticles as Drug Delivery Systems. *Adv. Drug Deliv. Rev.* **2008**, *60* (15), 1650–1662.

(167) Mashaghi, S.; Jadidi, T.; Koenderink, G.; Mashaghi, A. Lipid Nanotechnology. *Int. J. Mol. Sci.* **2013**, *14* (2), 4242–4282.

(168) Wang, Y.; Xia, Y. Bottom-up and Top-down Approaches to the Synthesis of Monodispersed Spherical Colloids of Low Melting-Point Metals. *Nano Lett.* **2004**, *4* (10), 2047–2050.

(169) Commission, E. SCIENTIFIC COMMITTEE ON EMERGING AND NEWLY IDENTIFIED HEALTH RISKS (SCENIHR) Modified Opinion (after Public Consultation) on The Appropriateness of Existing Methodologies to Assess the Potential Risks Associated with Engineered and Adventitious. **2006**, No. March.

(170) Eustis, S.; El-Sayed, M. A. Why Gold Nanoparticles Are More Precious than Pretty Gold: Noble Metal Surface Plasmon Resonance and Its Enhancement of the Radiative and Nonradiative Properties of Nanocrystals of Different Shapes. *Chem. Soc. Rev.* **2006**, *35* (3), 209–217.

(171) Cao, Y. C.; Jin, R.; Mirkin, C. A. Nanoparticles with Raman Spectroscopic Fingerprints for DNA and RNA Detection. *Science* **2002**, *297* (5586), 1536–1540.

(172) Lee, S.; Choi, S. U.-S.; Li, S.; Eastman, J. A. Measuring Thermal Conductivity of Fluids Containing Oxide Nanoparticles. *J. Heat Transfer* **1999**, *121* (2), 280–289.

(173) Priyadarshana, G.; Kottegoda, N.; Senaratne, A.; de Alwis, A.; Karunaratne, V. Synthesis of Magnetite Nanoparticles by Top-Down Approach from a High Purity Ore. *J. Nanomater.* **2015**, *2015*, 1–8.

(174) Faivre, D.; Bennet, M. Magnetic Nanoparticles Line Up. *Nature* **2016**, *535* (7611), 235–236.

(175) Guo, D.; Xie, G.; Luo, J. Mechanical Properties of Nanoparticles: Basics and Applications. *J. Phys. D. Appl. Phys.* **2014**, *47* (1), 013001.

(176) Khlebtsov, N.; Dykman, L. Biodistribution and Toxicity of Engineered Gold Nanoparticles: A Review of in Vitro and in Vivo Studies. *Chem. Soc. Rev.* **2011**, *40* (3), 1647–1671.

(177) Bahadar, H.; Maqbool, F.; Niaz, K.; Abdollahi, M. Toxicity of Nanoparticles and an Overview of Current Experimental Models. *Iran. Biomed. J.* **2016**, *20* (1), 1–11.

(178) Loureiro, A.; G. Azoia, N.; C. Gomes, A.; Cavaco-Paulo, A. Albumin-Based Nanodevices as Drug Carriers. *Curr. Pharm. Des.* **2016**, *22* (10), 1371–1390.

(179) Martis, E.; Badve, R.; Degwekar, M. Nanotechnology Based Devices and Applications in Medicine: An Overview. *Chronicles Young Sci.* **2012**, *3* (1), 68.

(180) Nikalje, A. P. Nanotechnology and Its Applications in Medicine. *Med. Chem.*

(Los. Angeles). **2015**, *5* (2), 1–9.

(181) Alexis, F.; Pridgen, E.; Molnar, L. K.; Farokhzad, O. C. Factors Affecting the Clearance and Biodistribution of Polymeric Nanoparticles. *Mol. Pharm.* **2008**, *5* (4), 505–515.

(182) Dong, H.; Wen, B.; Melnik, R. Relative Importance of Grain Boundaries and Size Effects in Thermal Conductivity of Nanocrystalline Materials. *Sci. Rep.* **2015**, *4* (1), 7037.

(183) Ma, E. Controlling Plastic Instability. *Nat. Mater.* **2003**, *2* (1), 7–8.

(184) Todescato, F.; Fortunati, I.; Minotto, A.; Signorini, R.; Jasieniak, J.; Bozio, R. Engineering of Semiconductor Nanocrystals for Light Emitting Applications. *Materials (Basel).* **2016**, *9* (8), 672.

(185) Weiss, J.; Takhistov, P.; McClements, D. J. Functional Materials in Food Nanotechnology. *J. Food Sci.* **2006**, *71* (9), R107–R116.

(186) *Biotechnology and Nanotechnology Risk Assessment: Minding and Managing the Potential Threats around Us*; Ripp, S., Henry, T. B., Eds.; ACS Symposium Series; American Chemical Society: Washington, DC, 2011; Vol. 1079.

(187) Golobič, M.; Jemec, A.; Drobne, D.; Romih, T.; Kasemets, K.; Kahru, A. Upon Exposure to Cu Nanoparticles, Accumulation of Copper in the Isopod Porcellio Scaber Is Due to the Dissolved Cu Ions Inside the Digestive Tract. *Environ. Sci. Technol.* **2012**, *46* (21), 12112–12119.

(188) Masciangioli, T.; Zhang, W.-X. Peer Reviewed: Environmental Technologies at the Nanoscale. *Environ. Sci. Technol.* **2003**, *37* (5), 102A-108A.

(189) Holzinger, M.; Le Goff, A.; Cosnier, S. Nanomaterials for Biosensing Applications: A Review. *Front. Chem.* **2014**, *2*, 63.

(190) Shaalan, M.; Saleh, M.; El-Mahdy, M.; El-Matbouli, M. Recent Progress in Applications of Nanoparticles in Fish Medicine: A Review. *Nanomedicine Nanotechnology, Biol. Med.* **2016**, *12* (3), 701–710.

(191) Cushing, B. L.; L. Kolesnichenko, V.; O'Connor, C. J. Recent Advances in the Liquid-Phase Syntheses of Inorganic Nanoparticles. **2004**.

(192) Kim, G.; Lee, Y.-E. K.; Kopelman, R. Hydrogen Peroxide (H2O2) Detection with Nanoprobes for Biological Applications: A Mini-Review. *Oxidative Stress Nanotechnol. Methods Mol. Biol.* **2013**, *1028*, 101–114.

(193) Aylott, J. W. Optical Nanosensors - An Enabling Technology for Intracellular Measurements. *Analyst* **2003**, *128* (4), 309–312.

(194) Uusitalo, L. M.; Hempel, N. Recent Advances in Intracellular and in Vivo ROS Sensing: Focus on Nanoparticle and Nanotube Applications. *Int. J. Mol. Sci.* **2012**, *13* (9), 10660–10679.

(195) Koo Lee, Y.-E.; Smith, R.; Kopelman, R. Nanoparticle PEBBLE Sensors in Live Cells and In Vivo. *Annu. Rev. Anal. Chem.* **2009**, *2* (1), 57–76.

(196) Kim, G.; Koo, Y. E. L.; Xu, H.; Philbert, M. A.; Kopelman, R. Nanoencapsulation Method for High Selectivity Sensing of Hydrogen Peroxide inside Live Cells. *Anal. Chem.* **2010**, *82* (6), 2165–2169.

(197) Cao, Y.; Koo, Y.-E. L.; Koo, S. M.; Kopelman, R. Ratiometric Singlet Oxygen Nano-Optodes and Their Use for Monitoring Photodynamic Therapy

Nanoplatforms. *Photochem. Photobiol.* **2005**, *81* (6), 1489.

(198) King, M.; Kopelman, R. Development of a Hydroxyl Radical Ratiometric Nanoprobe. *Sensors Actuators, B Chem.* **2003**, *90* (1–3), 76–81.

(199) Tian, J.; Chen, H.; Zhuo, L.; Xie, Y.; Li, N.; Tang, B. A Highly Selective, Cell-Permeable Fluorescent Nanoprobe for Ratiometric Detection and Imaging of Peroxynitrite in Living Cells. *Chem. - A Eur. J.* **2011**, *17* (24), 6626–6634.

(200) Hammond, V. J.; Aylott, J. W.; Greenway, G. M.; Watts, P.; Webster, A.; Wiles, C. An Optical Sensor for Reactive Oxygen Species: Encapsulation of Functionalised Silica Nanoparticles into Silicate Nanoprobes to Reduce Fluorophore Leaching. *Analyst* **2008**, *133* (1), 71–75.

(201) Lee, D.; Khaja, S.; Velasquez-Castano, J. C.; Dasari, M.; Sun, C.; Petros, J.; Taylor, W. R.; Murthy, N. In Vivo Imaging of Hydrogen Peroxide with Chemiluminescent Nanoparticles. *Nat. Mater.* **2007**, *6* (10), 765–769.

(202) Lee, D.; Erigala, V. R.; Dasari, M.; Yu, J.; Dickson, R. M.; Murthy, N. Detection of Hydrogen Peroxide with Chemiluminescent Micelles. *Int. J. Nanomedicine* **2008**, *3* (4), 471–476.

(203) Dasari, M.; Lee, D.; Erigala, V. R.; Murthy, N. Chemiluminescent PEG-PCL Micelles for Imaging Hydrogen Peroxide. *J. Biomed. Mater. Res. - Part A* **2009**, *89* (3), 561–566.

(204) Hu, Y.; Chen, R.; Zhang, L.; Gao, J.; Wu, W.; Jiang, X. Chemiluminescent Nanomicelles for Imaging Hydrogen Peroxide and Self-Therapy in Photodynamic Therapy. *J. Biomed. Biotechnol.* **2011**, *2011*.

(205) Wen, F.; Dong, Y.; Feng, L.; Wang, S.; Zhang, S.; Zhang, X. Horseradish Peroxidase Functionalized Fluorescent Gold Nanoclusters for Hydrogen Peroxide Sensing. *Anal. Chem.* **2011**, *83* (4), 1193–1196.

(206) Shiang, Y. C.; Huang, C. C.; Chang, H. T. Gold Nanodot-Based Luminescent Sensor for the Detection of Hydrogen Peroxide and Glucose. *Chem. Commun.* **2009**, No. 23, 3437–3439.

(207) Casanova, D.; Bouzigues, C.; Nguyn, T. L.; Ramodiharilafy, R. O.; Bouzhir-Sima, L.; Gacoin, T.; Boilot, J. P.; Tharaux, P. L.; Alexandrou, A. Single Europium-Doped Nanoparticles Measure Temporal Pattern of Reactive Oxygen Species Production inside Cells. *Nat. Nanotechnol.* **2009**, *4* (9), 581–585.

(208) Lee, H.; Lee, K.; Kim, I. K.; Park, T. G. Fluorescent Gold Nanoprobe Sensitive to Intracellular Reactive Oxygen Species. *Adv. Funct. Mater.* **2009**, *19* (12), 1884–1890.

(209) Auchinvole, C. A. R.; Richardson, P.; McGuinnes, C.; Mallikarjun, V.; Donaldson, K.; McNab, H.; Campbell, C. J. Monitoring Intracellular Redox Potential Changes Using SERS Nanosensors. *ACS Nano* **2012**, *6* (1), 888–896.

(210) Koo Lee, Y. E.; Kopelman, R. *Nanoparticle PEBBLE Sensors in Live Cells*, 1st ed.; Elsevier Inc., 2012; Vol. 504.

(211) Buck, S. M.; Koo, Y. E. L.; Park, E.; Xu, H.; Philbert, M. A.; Brasuel, M. A.; Kopelman, R. Optochemical Nanosensor PEBBLEs: Photonic Explorers for Bioanalysis with Biologically Localized Embedding. *Curr. Opin. Chem. Biol.* **2004**, *8* (5), 540–546.

(212) Yang, L.; Li, N.; Pan, W.; Yu, Z.; Tang, B. Real-Time Imaging of Mitochondrial

Hydrogen Peroxide and PH Fluctuations in Living Cells Using a Fluorescent Nanosensor. *Anal. Chem.* **2015**, *87* (7), 3678–3684.

(213) Yang, L.; Chen, Y.; Yu, Z.; Pan, W.; Wang, H.; Li, N.; Tang, B. Dual-Ratiometric Fluorescent Nanoprobe for Visualizing the Dynamic Process of PH and Superoxide Anion Changes in Autophagy and Apoptosis. *ACS Appl. Mater. Interfaces* **2017**, *9* (33), 27512–27521.

(214) Zielonka, J.; Srinivasan, S.; Hardy, M.; Ouari, O.; Lopez, M.; Vasquez-Vivar, J.; Avadhani, N. G.; Kalyanaraman, B. Cytochrome C-Mediated Oxidation of Hydroethidine and Mito-Hydroethidine in Mitochondria: Identification of Homo- and Heterodimers. *Free Radic. Biol. Med.* **2008**, *44* (5), 835–846.

(215) MACH, R.; MINTUN, M.; CHU, W.; DUGAN, L. DIHYDROETHIDINE ANALOGUES AND USES THEREOF, July 15, 2011.

(216) Huber, R.; Amann, N.; Wagenknecht, H. A. Synthesis of DNA with Phenanthridinium As An Artificial DNA Base. *J. Org. Chem.* **2004**, *69* (3), 744–751.

(217) Lewis, W. G.; Green, L. G.; Grynszpan, F.; Radić, Z.; Carlier, P. R.; Taylor, P.; Finn, M. G.; Sharpless, K. B. Click Chemistry in Situ: Acetylcholinesterase as a Reaction Vessel for the Selective Assembly of a Femtomolar Inhibitor from an Array of Building Blocks. *Angew. Chemie - Int. Ed.* **2002**, *41* (6), 1053–1057.

(218) Kalyanaraman, B.; Dranka, B. P.; Hardy, M.; Michalski, R.; Zielonka, J. HPLC-Based Monitoring of Products Formed from Hydroethidine-Based Fluorogenic Probes — The Ultimate Approach for Intra- and Extracellular Superoxide Detection. *Biochim. Biophys. Acta - Gen. Subj.* **2014**, *1840* (2), 739–744.

(219) Manetsch, R.; Krasiński, A.; Radić, Z.; Raushel, J.; Taylor, P.; Sharpless, K. B.; Kolb, H. C. In Situ Click Chemistry: Enzyme Inhibitors Made to Their Own Specifications. *J. Am. Chem. Soc.* **2004**, *126* (40), 12809–12818.

(220) Chu, W.; Chepetan, A.; Zhou, D.; Shoghi, K. I.; Xu, J.; Dugan, L. L.; Gropler, R. J.; Mintun, M. A.; Mach, R. H. Development of a PET Radiotracer for Non-Invasive Imaging of the Reactive Oxygen Species, Superoxide, in Vivo. *Org. Biomol. Chem.* **2014**, *12* (25), 4421–4431.

(221) Cheng, J.; Teply, B. A.; Sherifi, I.; Sung, J.; Luther, G.; Gu, F. X.; Levy-Nissenbaum, E.; Radovic-Moreno, A. F.; Langer, R.; Farokhzad, O. C. Formulation of Functionalized PLGA-PEG Nanoparticles for in Vivo Targeted Drug Delivery. *Biomaterials* **2007**, *28* (5), 869–876.

(222) Baughman, T. W.; Sworen, J. C.; Wagener, K. B. The Facile Preparation of Alkenyl Metathesis Synthons. *Tetrahedron* **2004**, *60* (48), 10943–10948.

(223) Kele, P.; Mezö, G.; Achatz, D.; Wolfbeis, O. S. Dual Labeling of Biomolecules by Using Click Chemistry: A Sequential Approach. *Angew. Chemie - Int. Ed.* **2009**, *48* (2), 344–347.

(224) Lee, M. R.; Shin, I. Fabrication of Chemical Microarrays by Efficient Immobilization of Hydrazide-Linked Substances on Epoxide-Coated Glass Surfaces. *Angew. Chemie - Int. Ed.* **2005**, *44* (19), 2881–2884.

(225) Dhumure, A. B.; Patil, A. B.; Kulkarni, A. S.; Voevodina, I.; Scandola, M.; Shinde, V. S. Thermoresponsive Copolymers with Pendant D-Galactosyl 1,2,3-Triazole Groups: Synthesis, Characterization and Thermal Behavior. *New J. Chem.* **2015**, *39* (10), 8179–8187.

(226) Steiger, S. A.; Li, C.; Backos, D. S.; Reigan, P.; Natale, N. R. Dimeric Isoxazolyl-1,4-Dihydropyridines Have Enhanced Binding at the Multi-Drug Resistance Transporter. *Bioorganic Med. Chem.* **2017**, *25* (12), 3223–3234.

(227) Bunting, J. W.; Moors, R. G. PH Dependence of the Elimination of Isoquinolines from N-(2-Cyanoethyl)Isoquinolinium Cations. *J. Am. Chem. Soc.* **1989**, *111* (6), 2258–2262.

(228) Albericio, F.; Isidro-Llobet, A.; Mercedes, A. Amino Acid-Protecting Groups. **2009**, 2455–2504.

(229) Nikishin, G.; Svitanko, I.; Troyansky, E. Direct Oxidation of Alkanoic Acids and Their Amides to γ-Lactones by Peroxydisulphate-Containing Systems. *J. Chem. Soc., Perkin Trans. 2* **1983**, No. I, 595.

(230) Yang, J.; Fu, X.; Jia, Q.; Shen, J.; Biggins, J. B.; Jiang, J.; Zhao, J.; Schmidt, J. J.; Wang, P. G.; Thorson, J. S. Studies on the Substrate Specificity of Escherichia Coli Galactokinase. *Org. Lett.* **2003**, *5* (13), 2223–2226.

(231) Martin, V. V.; Rothe, A.; Gee, K. R. Fluorescent Metal Ion Indicators Based on Benzoannelated Crown Systems: A Green Fluorescent Indicator for Intracellular Sodium Ions. *Bioorganic Med. Chem. Lett.* **2005**, *15* (7), 1851–1855.

(232) Xue, J.; Song, W.; Yao, H.; Hou, S.; Liu, S.; Wang, Y.; Pei, D.; Zhu, X.; Qin, D.; Ren, L. Effects of Cholic Acid Modified Glucosamine on Chondrogenic Differentiation. *RSC Adv.* **2016**, *6* (73), 69586–69594.

(233) Lau, Y. Y.; Zhai, H.; Schafer, L. L. Catalytic Asymmetric Synthesis of Morpholines. Using Mechanistic Insights to Realize the Enantioselective Synthesis of Piperazines. *J. Org. Chem.* **2016**, *81* (19), 8696–8709.

(234) Hiza, A.; Tsukaguchi, Y.; Ogawa, T.; Inai, M.; Asakawa, T.; Hamashima, Y.; Kan, T. Synthetic Studies of Fisetin, Myricetin and Nobiletin Analogs and Related Probe Molecules. *Heterocycles* **2014**, *8* (2), 1371–1396.

(235) Santhosh, K. C.; De Clercq, E.; Pannecouque, C.; Witvrouw, M.; Loftus, T. L.; Turpin, J. A.; Buckheit, R. W.; Cushman, M. Anti-HIV Activity of a Series of Cosalane Amino Acid Conjugates. *Bioorganic Med. Chem. Lett.* **2000**, *10* (22), 2505–2508.

(236) De Biasi, S.; Gibellini, L.; Bianchini, E.; Nasi, M.; Pinti, M.; Salvioli, S.; Cossarizza, A. Quantification of Mitochondrial Reactive Oxygen Species in Living Cells by Using Multi-Laser Polychromatic Flow Cytometry. *Cytom. Part A* **2016**, *89* (12), 1106–1110.

(237) Żamojć, K.; Zdrowowicz, M.; Jacewicz, D.; Wyrzykowski, D.; Chmurzyński, L. Fluorescent Probes Used for Detection of Hydrogen Peroxide under Biological Conditions. *Crit. Rev. Anal. Chem.* **2016**, *46* (3), 171–200.

(238) Dickinson, B. C.; Huynh, C.; Chang, C. J. A Palette of Fluorescent Probes with Varying Emission Colors for Imaging Hydrogen Peroxide Signaling in Living Cells. **2010**.

(239) Smith, G. A.; Metcalfe, J. C.; Clarke, S. D. The Design and Properties of a Series of Calcium Indicators Which Shift from Rhodamine-like to Fluorescein-like Fluorescence on Binding Calcium. *J. Chem. Soc. Perkin Trans. 2* **1993**, No. 6, 1195–1204.

(240) Ignat'ev, N. V.; Barthen, P.; Kucheryna, A.; Willner, H.; Sartori, P. A Convenient Synthesis of Triflate Anion Ionic Liquids and Their Properties. *Molecules* **2012**,

17 (5), 5319–5338.

(241) Bhuniya, S.; Maiti, S.; Kim, E. J.; Lee, H.; Sessler, J. L.; Hong, K. S.; Kim, J. S. An Activatable Theranostic for Targeted Cancer Therapy and Imaging. *Angew. Chemie - Int. Ed.* **2014**, *53* (17), 4469–4474.

(242) Yuan, L.; Lin, W.; Xie, Y.; Chen, B.; Zhu, S. Single Fluorescent Probe Responds to H2O2, NO, and H2O2/NO with Three Different Sets of Fluorescence Signals. *J. Am. Chem. Soc.* **2012**, *134* (2), 1305–1315.

(243) Lu, Y.; Shi, X.; Fan, W.; Black, C. A.; Lu, Z.; Fan, C. A Fast-Response Two-Photon Fluorescent Probe for Imaging Endogenous H2O2in Living Cells and Tissues. *Spectrochim. Acta - Part A Mol. Biomol. Spectrosc.* **2018**, *190*, 353–359.

(244) Lippert, A. R.; Van De Bittner, G. C.; Chang, C. J. Boronate Oxidation as a Bioorthogonal Reaction Approach for Studying the Chemistry of Hydrogen Peroxide in Living Systems. *Acc. Chem. Res.* **2011**, *44* (9), 793–804.

(245) Martin, M. M.; Lindqvist, L. The PH Dependence of Fluorescein Fluorescence. *J. Lumin.* **1975**, *10* (6), 381–390.

(246) Song, L.; Hennink, E. J.; Young, I. T.; Tanke, H. J. Photobleaching Kinetics of Fluorescein in Quantitative Fluorescence Microscopy. *Biophys. J.* **1995**, *68* (6), 2588–2600.

(247) Queiroz, N. L.; Nascimento, J. A. M.; Nascimento, M. L.; Nascimento, V. B.; Oliveira, S. C. B. Oxidation Mechanism of Fluorescein at Glassy Carbon Electrode. *Electroanalysis* **2017**, *29* (2), 489–496.

(248) Tanaka, K.; Miura, T.; Umezawa, N.; Urano, Y.; Kikuchi, K.; Higuchi, T.; Nagano, T. Rational Design of Fluorescein-Based Fluorescence Probes. Mechanism-Based Design of a Maximum Fluorescence Probe for Singlet Oxygen. *J. Am. Chem. Soc.* **2001**, *123* (11), 2530–2536.

(249) Lohier, J. F.; Wright, K.; Peggion, C.; Formaggio, F.; Toniolo, C.; Wakselman, M.; Mazaleyrat, J. P. Synthesis of Protected Derivatives and Short Peptides of AntAib, a Novel Cα-Tetrasubstituted α-Amino Acid of the Ac5c Type Possessing a Fused Anthracene Fluorophore. *Tetrahedron* **2006**, *62* (26), 6203–6213.

(250) Cooper, C. R.; James, T. D. Selective D-Glucosamine Hydrochloride Fluorescence Signalling Based on Ammonium Cation and Diol Recognition. *Chem. Commun.* **1997**, No. 15, 1419–1420.

(251) Ciaccio, J. A.; Drahus, A. L.; Meis, R. M.; Tingle, C. T.; Smrtka, M.; Geneste, R. "Instant Methylide" Modification of the Corey-Chaykovsky Epoxide Synthesis. *Synth. Commun.* **2003**, *33* (12), 2135–2143.

(252) Vedejs, E. Clemmensen Reduction of Ketones in Anhydrous Organic Solvents. In *Organic Reactions*; John Wiley & Sons, Inc.: Hoboken, NJ, USA, 2011; pp 401–422.

(253) Corey, E. J.; Suggs, J. W. Pyridinium Chlorochromate. An Efficient Reagent for Oxidation of Primary and Secondary Alcohols to Carbonyl Compounds. *Tetrahedron Lett.* **1975**, *16* (31), 2647–2650.

(254) Schauer, D. J.; Helquist, P. Mild Zinc-Promoted Horner-Wadsworth-Emmons Reactions of Diprotic Phosphonate Reagents. *Synthesis (Stuttg).* **2006**, No. 21, 3654–3660.

(255) Hallman, J. L.; Bartsch, R. A. Synthesis of Naphtho[f]Ninhydrin. *J. Org. Chem.* **1991**, *56* (21), 6243–6245.

(256) Chiong, H. A.; Pham, Q. N.; Daugulis, O. Two Methods for Direct Ortho-Arylation of Benzoic Acids. *J. Am. Chem. Soc.* **2007**, *129* (32), 9879–9884.

(257) Choi, W. K.; El-Gamal, M. I.; Choi, H. S.; Baek, D.; Oh, C. H. New Diarylureas and Diarylamides Containing 1,3,4-Triarylpyrazole Scaffold: Synthesis, Antiproliferative Evaluation against Melanoma Cell Lines, ERK Kinase Inhibition, and Molecular Docking Studies. *Eur. J. Med. Chem.* **2011**, *46* (12), 5754–5762.

(258) Borisov, A. V.; Maizlish, V. E.; Shaposhnikov, G. P. Tetraanthraquinonoporphyrazines: I. Substituted 2,3-Dicarboxyanthraquionones. *Russ. J. Gen. Chem.* **2005**, *75* (7), 1151–1156.

(259) Kang, S.; Lee, S.; Yang, W.; Seo, J.; Han, M. S. A Direct Assay of Butyrylcholinesterase Activity Using a Fluorescent Substrate. *Org. Biomol. Chem.* **2016**, *14* (37), 8815–8820.

(260) Cooper, C. R.; James, T. D. Synthesis and Evaluation of D-Glucosamine-Selective Fluorescent Sensors. *J. Chem. Soc. Perkin Trans. 1* **2000**, *1* (6), 963–969.

(261) Botta, M. C.; Biava, H. D.; Spanevello, R. A.; Mata, E. G.; Suárez, A. G. Development of Polymer-Supported Chiral Aminoalcohols Derived from Biomass and Their Application to Asymmetric Alkylation. *Tetrahedron Lett.* **2016**, *57* (20), 2186–2189.

(262) Varazo, K.; Xie, F.; Gulledge, D.; Wang, Q. Synthesis of Triazolyl Anthracene as a Selective Fluorescent Chemosensor for the Cu(II) Ion. *Tetrahedron Lett.* **2008**,

49 (36), 5293–5296.

(263) Mahmoodi, N. O.; Mirkhaef, S.; Ghavidast, A. Synthesis of Anthracene Derivatives of 1,3-Diazabicyclo[3.1.0]Hex-3-Ene. *J. Mol. Struct.* **2015**, *1081*, 248–253.

(264) Lin, Y. i.; Lang, S. A.; Seifert, C. M.; Child, R. G.; Morton, G. O.; Fabio, P. F. Aldehyde Syntheses. Study of the Preparation of 9,10-Anthracenedicarboxaldehyde. *J. Org. Chem.* **1979**, *44* (25), 4701–4703.

(265) Doty, B. J.; Morrow, G. W. Conjugate Reduction of Quinone Derivatives. A Route to Phenol Keto-Tautomer Equivalents. *Tetrahedron Lett.* **1990**, *31* (43), 6125–6128.

(266) Taber, D. F.; Sheth, R. B. A Three-Step Route to a Tricyclic Steroid Precursor. *J. Org. Chem.* **2008**, *73* (20), 8030–8032.

(267) Andrus, M. B.; Ye, Z.; Zhang, J. Highly Selective Glycine Phase-Transfer Catalysis Using Fluoroanthracenylmethyl Cinchonidine Catalysts. *Tetrahedron Lett.* **2005**, *46* (22), 3839–3842.

(268) Zara, C. L.; Jin, T.; Giguere, R. J. Microwave Heating in Organic Synthesis: Decarboxylation of Malonic Acid Derivatives in Water. *Synth. Commun.* **2000**, *30* (12), 2099–2104.

(269) Martinez, G. R.; Garcia, F.; Catalani, L. H.; Cadet, J.; Oliveira, M. C. B.; Ronsein, G. E.; Miyamoto, S.; Medeiros, M. H. G.; Mascio, P. Di. Synthesis of a Hydrophilic and Non-Ionic Anthracene Derivative, the N,N′-Di-(2,3-Dihydroxypropyl)-9,10-Anthracenedipropanamide as a Chemical Trap for Singlet Molecular Oxygen Detection in Biological Systems. *Tetrahedron* **2006**,

62 (46), 10762–10770.

(270) Kapoor, R. C.; Jain, M. K.; Mishra, V. N. Fluorescence and Absorption Spectra of Rose-Bengal Dye in the Presence of Surfactants. *J. Lumin.* **1981**, *22* (4), 429–439.

(271) Giuntini, F.; Foglietta, F.; Marucco, A. M.; Troia, A.; Dezhkunov, N. V.; Pozzoli, A.; Durando, G.; Fenoglio, I.; Serpe, L.; Canaparo, R. Insight into Ultrasound-Mediated Reactive Oxygen Species Generation by Various Metal-Porphyrin Complexes. *Free Radic. Biol. Med.* **2018**, *121*, 190–201.

(272) Kolemen, S.; Ozdemir, T.; Lee, D.; Kim, G. M.; Karatas, T.; Yoon, J.; Akkaya, E. U. Remote-Controlled Release of Singlet Oxygen by the Plasmonic Heating of Endoperoxide-Modified Gold Nanorods: Towards a Paradigm Change in Photodynamic Therapy. *Angew. Chemie - Int. Ed.* **2016**, *55* (11), 3606–3610.

(273) Bertozzi, C. R.; Bednarski, M. D. The Synthesis of Heterobifunctional Linkers for the Conjugation of Ligands to Molecular Probes. *J. Org. Chem.* **1991**, *56* (13), 4326–4329.

(274) Martins, C.; Sousa, F.; Araújo, F.; Sarmento, B. Functionalizing PLGA and PLGA Derivatives for Drug Delivery and Tissue Regeneration Applications. *Adv. Healthc. Mater.* **2018**, *7* (1), 1–24.

(275) Mir, M.; Ahmed, N.; Rehman, A. ur. Recent Applications of PLGA Based Nanostructures in Drug Delivery. *Colloids Surfaces B Biointerfaces* **2017**, *159*, 217–231.

(276) Crucho, C. I. C.; Barros, M. T. Formulation of Functionalized PLGA Polymeric Nanoparticles for Targeted Drug Delivery. *Polymer (Guildf).* **2015**, *68*, 41–46.

(277) Danhier, F.; Ansorena, E.; Silva, J. M.; Coco, R.; Le Breton, A.; Préat, V. PLGA-Based Nanoparticles: An Overview of Biomedical Applications. *J. Control. Release* **2012**, *161* (2), 505–522.

(278) Parker, F. S.; Parker, F. S. Amides and Amines. *Appl. Infrared Spectrosc. Biochem. Biol. Med.* **1971**, *1*, 165–172.

(279) Pucci, A.; Locatelli, E.; Ponti, J.; Uboldi, C.; Molinari, V.; Comes Franchini, M. Click Chemistry on the Surface of PLGA-b-PEG Polymeric Nanoparticles: A Novel Targetable Fluorescent Imaging Nanocarrier. *J. Nanoparticle Res.* **2013**, *15* (8), 1818.

(280) Arumugam, S.; Chin, J.; Schirrmacher, R.; Popik, V. V.; Kostikov, A. P. [18F]Azadibenzocyclooctyne ([18F]ADIBO): A Biocompatible Radioactive Labeling Synthon for Peptides Using Catalyst Free [3+2] Cycloaddition. *Bioorg. Med. Chem. Lett.* **2011**, *21* (23), 6987–6991.

(281) Debets, M. F.; Van Berkel, S. S.; Schoffelen, S.; Rutjes, F. P. J. T.; Van Hest, J. C. M.; Van Delft, F. L. Aza-Dibenzocyclooctynes for Fast and Efficient Enzyme PEGylation via Copper-Free (3+2) Cycloaddition. *Chem. Commun.* **2010**, *46* (1), 97–99.

(282) Ben El Ayouchia, H.; Bahsis, L.; Anane, H.; Domingo, L. R.; Stiriba, S.-E. Understanding the Mechanism and Regioselectivity of the Copper(I) Catalyzed [3 + 2] Cycloaddition Reaction between Azide and Alkyne: A Systematic DFT Study. *RSC Adv* **2018**, *8*, 7670–7678.

(283) Lemoine, D.; Préat, V. Polymeric Nanoparticles as Delivery System for Influenza Virus Glycoproteins. *J. Control. Release* **1998**, *54* (1), 15–27.

(284) Song, C. .; Labhasetwar, V.; Murphy, H.; Qu, X.; Humphrey, W. .; Shebuski, R. .; Levy, R. . Formulation and Characterization of Biodegradable Nanoparticles for Intravascular Local Drug Delivery. *J. Control. Release* **1997**, *43* (2–3), 197– 212.

(285) Swider, E.; Koshkina, O.; Tel, J.; Cruz, L. J.; de Vries, I. J. M.; Srinivas, M. Customizing Poly(Lactic-Co-Glycolic Acid) Particles for Biomedical Applications. *Acta Biomater.* **2018**, *73*, 38–51.

(286) Hakkimane, S. S.; Shenoy, V. P.; Gaonkar, S. L.; Bairy, I.; Guru, B. R. Antimycobacterial Susceptibility Evaluation of Rifampicin and Isoniazid Benz-Hydrazone in Biodegradable Polymeric Nanoparticles against Mycobacterium Tuberculosis H37Rv Strain. *Int. J. Nanomedicine* **2018**, *13*, 4303–4318.

(287) Al Meslmani, B. M.; Mahmoud, G. F.; Bakowsky, U. Development of Expanded Polytetrafluoroethylene Cardiovascular Graft Platform Based on Immobilization of Poly Lactic-Co-Glycolic Acid Nanoparticles Using a Wet Chemical Modification Technique. *Int. J. Pharm.* **2017**, *529* (1–2), 238–244.

(288) Julbe, A.; Drobek, M.; Européen, I.; De, U. Encyclopedia of Membranes. *Encycl. Membr.* **2016**.

(289) Shkodra-Pula, B.; Grune, C.; Traeger, A.; Vollrath, A.; Schubert, S.; Fischer, D.; Schubert, U. S. Effect of Surfactant on the Size and Stability of PLGA Nanoparticles Encapsulating a Protein Kinase C Inhibitor. *Int. J. Pharm.* **2019**, *566* (May), 756–764.

(290) Peek, L. J.; Roberts, L.; Berkland, C. Poly(D,L-Lactide-Co-Glycolide) Nanoparticle Agglomerates as Carriers in Dry Powder Aerosol Formulation of

Proteins. *Langmuir* **2008**, *24* (17), 9775–9783.

(291) Greish, K. Enhanced Permeability and Retention (EPR) Effect for Anticancer Nanomedicine Drug Targeting. *Methods Mol. Biol.* **2010**, *624* (1), 25–37.

(292) Godbey, W. T.; Godbey, W. T. Fluorescence. *An Introd. to Biotechnol.* **2014**, 173–186.

(293) Reineck, P.; Gómez, D.; Ng, S. H.; Karg, M.; Bell, T.; Mulvaney, P.; Bach, U. Distance and Wavelength Dependent Quenching of Molecular Fluorescence by Au@SiO2 Core-Shell Nanoparticles. *ACS Nano* **2013**, *7* (8), 6636–6648.

(294) Clegg, R. M. The History of FRET : From Conception through the Labors of Birth. *Rev. Fluoresc.* **2006**, *3*, 1–45.

(295) Shi, J.; Tian, F.; Lyu, J.; Yang, M. Nanoparticle Based Fluorescence Resonance Energy Transfer (FRET) for Biosensing Applications. *J. Mater. Chem. B* **2015**, *3* (35), 6989–7005.

(296) Tsuchiya, S.; Yamabe, M.; Yamaguchi, Y.; Kobayashi, Y.; Konno, T.; Tada, K. Establishment and Characterization of a Human Acute Monocytic Leukemia Cell Line (THP-1). Int J Cancer. 1980; 26:171–176. DOI: 10.1002/ljc.2910260208. *Int. J. Cancer* **1980**, *176* (2), 171–176.

(297) Chao, T. L.; Wang, T. Y.; Lee, C. H.; Yiin, S. J.; Ho, C. Te; Wu, S. H.; You, H. L.; Chern, C. L. Anti-Cancerous Effect of Inonotus Taiwanensis Polysaccharide Extract on Human Acute Monocytic Leukemia Cells through ROS-Independent Intrinsic Mitochondrial Pathway. *Int. J. Mol. Sci.* **2018**, *19* (2).

(298) Auwerx, J. The Human Leukemia Cell Line, THP-1: A Multifacetted Model for the

Study of Monocyte-Macrophage Differentiation. *Experientia* **1991**, *47* (1), 22–31.

(299) Starr, T.; Bauler, T. J.; Malik-Kale, P.; Steele-Mortimer, O. The Phorbol 12-Myristate-13-Acetate Differentiation Protocol Is Critical to the Interaction of THP-1 Macrophages with Salmonella Typhimurium. *PLoS One* **2018**, *13* (3), 1–13.

(300) Smith, M.; Young, H.; Hurlstone, A.; Wellbrock, C. Differentiation of THP1 Cells into Macrophages for Transwell Co-Culture Assay with Melanoma Cells. *Bio-Protocol* **2015**, *5* (21), 1–7.

(301) Park, E. K.; Jung, H. S.; Yang, H. I.; Yoo, M. C.; Kim, C.; Kim, K. S. Optimized THP-1 Differentiation Is Required for the Detection of Responses to Weak Stimuli. *Inflamm. Res.* **2007**, *56* (1), 45–50.

(302) Kuwabara, W. M. T.; Zhang, L.; Schuiki, I.; Curi, R.; Volchuk, A.; Alba-Loureiro, T. C. NADPH Oxidase-Dependent Production of Reactive Oxygen Species Induces Endoplasmatic Reticulum Stress in Neutrophil-like HL60 Cells. *PLoS One* **2015**, *10* (2), e0116410.

(303) Chen, R. J.; Chen, P. C.; Prasannan, A.; Vinayagam, J.; Huang, C. C.; Chou, P. Y.; Weng, C. C.; Tsai, H. C.; Lin, S. Y. Formation of Gold Decorated Porphyrin Nanoparticles and Evaluation of Their Photothermal and Photodynamic Activity. *Mater. Sci. Eng. C* **2016**, *63*, 678–685.

(304) Brown, M.; Wittwer, C. Flow Cytometry: Principles and Clinical Applications in Hematology. *Clin. Chem.* **2000**, *46* (8 II), 1221–1229.

(305) Elmore, S. Apoptosis: A Review of Programmed Cell Death. *Toxicol. Pathol.* **2007**, *35* (4), 495–516.

(306) Confocal Microscopy | Principle & Applications | ibidi https://ibidi.com/content/216-confocal-microscopy (accessed Dec 7, 2019).

(307) Vadakkan, M. V.; Annapoorna, K.; Sivakumar, K. C.; Mundayoor, S.; Kumar, G. S. V. Dry Powder Cationic Lipopolymeric Nanomicelle Inhalation for Targeted Delivery of Antitubercular Drug to Alveolar Macrophage. *Int. J. Nanomedicine* **2013**, *8* (September 2014), 2871–2885.

(308) Held, P. Sample Preparation for Fluorescence Microscopy: An Introduction - Concepts and Tips for Better Fixed Sample Imaging Results. *BioTek* **2015**, 1.

(309) Gatto, F.; Cagliani, R.; Catelani, T.; Guarnieri, D.; Moglianetti, M.; Pompa, P. P.; Bardi, G. PMA-Induced THP-1 Macrophage Differentiation Is Not Impaired by Citrate-Coated Platinum Nanoparticles. *Nanomaterials* **2017**, *7* (10), 1–10.

(310) Campwala, H.; Sexton, D. W.; Crossman, D. C.; Fountain, S. J. P2Y6 Receptor Inhibition Perturbs CCL2-Evoked Signalling in Human Monocytic and Peripheral Blood Mononuclear Cells. *J. Cell Sci.* **2014**, *127* (22), 4964–4973.

(311) Tian, T.; Qian, T.; Jiang, T.; Deng, Y.; Li, X.; Yuan, W.; Chen, Y.; Wang, Y. X.; Hu, W. A Donor-Acceptor Type Macrocycle: Toward Photolyzable Self-Assembly. *Chem. Commun.* **2020**, *56* (28), 3939–3942.

(312) Dakanali, M.; Do, T. H.; Horn, A.; Chongchivivat, A.; Jarusreni, T.; Lichlyter, D.; Guizzunti, G.; Haidekker, M. A.; Theodorakis, E. A. Self-Calibrating Viscosity Probes: Design and Subcellular Localization. *Bioorganic Med. Chem.* **2012**, *20* (14), 4443–4450.

(313) Amaral, S. P.; Fernandez-Villamarin, M.; Correa, J.; Riguera, R.; Fernandez-Megia, E. Efficient Multigram Synthesis of the Repeating Unit of Gallic Acid-

Triethylene Glycol Dendrimers. *Org. Lett.* **2011**, *13* (17), 4522–4525.

(314) Deng, L.; Norberg, O.; Uppalapati, S.; Yan, M.; Ramström, O. Stereoselective Synthesis of Light-Activatable Perfluorophenylazide- Conjugated Carbohydrates for Glycoarray Fabrication and Evaluation of Structural Effects on Protein Binding by SPR Imaging. *Org. Biomol. Chem.* **2011**, *9* (9), 3188–3198.

(315) Steinebach, C.; Sosič, I.; Lindner, S.; Bricelj, A.; Kohl, F.; Ng, Y. L. D.; Monschke, M.; Wagner, K. G.; Krönke, J.; Gütschow, M. A MedChem Toolbox for Cereblon-Directed PROTACs. *Medchemcomm* **2019**, *10* (6), 1037–1041.

(316) Zhao, Q.; Huo, F.; Kang, J.; Zhang, Y.; Yin, C. A Novel FRET-Based Fluorescent Probe for the Selective Detection of Hydrogen Sulfide (H2S) and Its Application for Bioimaging. *J. Mater. Chem. B* **2018**, *6* (30), 4903–4908.